MINISTÉRIO DA CIÊNCIA, TECNOLOGIA E INOVAÇÃO
INSTITUTO NACIONAL DE PESQUISAS ESPACIAIS

sid.inpe.br/mtc-m21b/2016/06.08.16.27-TDI

BIO-OPTICAL CHARACTERIZATION OF AMAZON FLOODPLAIN LAKES AND EVALUATION OF THE RETRIEVAL OF OPTICALLY ACTIVE CONSTITUENT USING REMOTE SENSING

Lino Augusto Sander de Carvalho

Doctorate Thesis Course Graduate in Remote Sensing, guided by Drs. Cláudio Clemente Faria Barbosa and Evlyn Márcia Leão de Moraes Novo, approved in April 18, 2016.

URL of the original document:
<http://urlib.net/ 8JMKD3MGP3W34P/3LRECPB>

INPE
São José dos Campos
2016

PUBLISHED BY:

Instituto Nacional de Pesquisas Espaciais - INPE
Gabinete do Diretor (GB)
Serviço de Informação e Documentação (SID)
Caixa Postal 515 - CEP 12.245-970
São José dos Campos - SP - Brasil
Tel.:(012) 3208-6923/6921
Fax: (012) 3208-6919
E-mail: pubtc@inpe.br

COMMISSION OF BOARD OF PUBLISHING AND PRESERVATION OF INPE INTELLECTUAL PRODUCTION (DE/DIR-544):
Chairperson:
Maria do Carmo de Andrade Nono - Conselho de Pós-Graduação (CPG)
Members:
Dr. Plínio Carlos Alvalá - Centro de Ciência do Sistema Terrestre (CST)
Dr. André de Castro Milone - Coordenação de Ciências Espaciais e Atmosféricas (CEA)
Dra. Carina de Barros Melo - Coordenação de Laboratórios Associados (CTE)
Dr. Evandro Marconi Rocco - Coordenação de Engenharia e Tecnologia Espacial (ETE)
Dr. Hermann Johann Heinrich Kux - Coordenação de Observação da Terra (OBT)
Dr. Marley Cavalcante de Lima Moscati - Centro de Previsão de Tempo e Estudos Climáticos (CPT)
Silvia Castro Marcelino - Serviço de Informação e Documentação (SID) **DIGITAL LIBRARY:**
Dr. Gerald Jean Francis Banon
Clayton Martins Pereira - Serviço de Informação e Documentação (SID)
DOCUMENT REVIEW:
Simone Angélica Del Ducca Barbedo - Serviço de Informação e Documentação (SID)
Yolanda Ribeiro da Silva Souza - Serviço de Informação e Documentação (SID)
ELECTRONIC EDITING:
Marcelo de Castro Pazos - Serviço de Informação e Documentação (SID)
André Luis Dias Fernandes - Serviço de Informação e Documentação (SID)

MINISTÉRIO DA CIÊNCIA, TECNOLOGIA E INOVAÇÃO
INSTITUTO NACIONAL DE PESQUISAS ESPACIAIS

sid.inpe.br/mtc-m21b/2016/06.08.16.27-TDI

BIO-OPTICAL CHARACTERIZATION OF AMAZON FLOODPLAIN LAKES AND EVALUATION OF THE RETRIEVAL OF OPTICALLY ACTIVE CONSTITUENT USING REMOTE SENSING

Lino Augusto Sander de Carvalho

Doctorate Thesis Course Graduate in Remote Sensing, guided by Drs. Cláudio Clemente Faria Barbosa and Evlyn Márcia Leão de Moraes Novo, approved in April 18, 2016.

URL of the original document:
<http://urlib.net/ 8JMKD3MGP3W34P/3LRECPB>

INPE
São José dos Campos
2016

Cataloging in Publication Data

Carvalho, Lino Augusto Sander de.

C253b Bio-optical characterization of Amazon floodplain lakes and evaluation of the retrieval of optically active constituent using remote sensing / Lino Augusto Sander de Carvalho. – São José dos Campos : INPE, 2016.

xxvi + 175 p. ; (sid.inpe.br/mtc-m21b/2016/06.08.16.27-TDI)

Thesis (Doctorate in Remote Sensing) – Instituto Nacional de Pesquisas Espaciais, São José dos Campos, 2016.

Guiding : Drs. Cláudio Clemente Faria Barbosa and Evlyn Márcia Leão de Moraes Novo.

1. Amazon floodplain lakes. 2. Hydrological optics. 3. Lakes Biooptical Properties. 4. Semi-Analytical modeling. I.Title.

CDU 528.8:551.435.12(811)

Esta obra foi licenciada sob uma Licença Creative Commons Atribuição-NãoComercial 3.0 Não Adaptada.

This work is licensed under a Creative Commons Attribution-NonCommercial 3.0 Unported License.

Aluno (a): ***Lino Augusto Sander de Carvalho***

Título: " BIO-OPTICAL CHARACTERIZATION OF AMAZON FLOODPLAIN LAKES AND EVALUATION OF THE RETRIEVAL OF OPTICALLY ACTIVE CONSTITUENT USING REMOTE SENSING".

Aprovado (a) pela Banca Examinadora em cumprimento ao requisito exigido para obtenção do Título de ***Doutor(a)*** em

Sensoriamento Remoto

Dr. Cláudio Clemente Faria Barbosa

Presidente / Orientador(a) / INPE / SJCampos - SP

Dra. Evlyn Márcia Leão de Moraes Novo

Orientador(a) / INPE / SJCampos - SP

Dr. João Antonio Lorenzzetti

Membro da Banca / INPE / SJCampos - SP

Dra. Natália de Moraes Rudorff

Membro da Banca / INPE / Cachoeira Paulista - SP

Dr. Mauricio Almeida Noernberg

Convidado(a) / UFPR / Paraná - PR

Dr. Emmanuel Boss

Convidado(a) / Univ. Of Maine / Estados Unidos - USA

Este trabalho foi aprovado por:

( ) maioria simples

( ) unanimidade

São José dos Campos, 18 de Abril de 2016

ACKNOWLEDGEMENTS

Aos Orientadores Cláudio Clemente Faria Barbosa e Evlyn Márcia Leão de Moraes Novo pela valiosa orientação, suporte, crédito depositado em mim e pela oportunidade de trabalho em uma área repleta de desafios.

Ao Programa de Pós-Graduação no INPE, professores e funcionários, pela oportunidade de estudos e utilização de suas instalações.

Ao Professor Emmanuel Boss e à Universidade de Maine pelo período de doutorado sanduiche.

À Coordenação de Aperfeiçoamento de Pessoal de Nível Superior (CAPES) que proveu a bolsa de estudos.

Ao Conselho Nacional de Desenvolvimento Científico e Tecnológico (CNPq) através do Programa Ciência sem Fronteiras que me possibilitou o doutorado sanduiche.

À FAPESP e ao Programa de Pós-Graduação em Sensoriamento Remoto pelo suporte financeiro aos trabalhos de campo para coletas de dados.

À NASA, pelo suporte financeiro e à Curtis Mobley e Emmanuel Boss pela indicação para a participação no curso *Calibration and Validation for Ocean Color Remote Sensing* nos anos de 2013 e 2015.

À todos os meus amigos pelos bons momentos vividos.

À meus pais, por todo o carinho e suporte.

À minha esposa, pelo carinho e paciência.

ABSTRACT

Amazon floodplain lakes play a substantial role in global and regional biogeochemical Amazonian processes. Due to their size, sampling strategies usually applied in limnological studies are not suitable and therefore, Remote Sensing (RS) techniques figure as an alternative due to the high temporal and synoptic characteristics. However, the use of RS demands precise lake bio-optical characterization in order to provide reliable estimates of optical active components (OAC).This work focused on the study of *Curuai Lake* which is a suitable example of a Brazilian Amazon floodplain lake. Curuai lake was sampled in four field campaigns (September/2012, February and August/2013 and April/2014) where Apparent Optical Properties-AOP (R_{rs} and K-functions), *in situ* Inherent Optical Properties-IOP (Attenuation, Absorption, Backscattering profiles and Particle Size Distribution (PSD)) as well as laboratory analysis (AOC concentration and absorption) were measured. A data quality assessment was performed to test the suitability of commercial instrumentation (ACS and Hydroscat) for turbid environments as well as commonly used AOP/IOP measurement methodologies. The optical characterization compared datasets from each fieldcampaign for surface and profile measurements. Also three semi-analytical inverse models (*Nechad* Algorithm (NECHAD et al., 2010), Quasi-Analytical Algorithm (QAA) (LEE et al., 2002) and Generalized ocean color inversion model (GIOP) (WERDELL et al., 2013)) were tested using measured AOP and IOPs. Data quality assessment show that sun/skyglint effects have the highest impact on above water remote sensing measurements R_{rs} (R_{rs}^{Ab}). Highest errors were found for In-water derived AOPs (R_{rs}^{Iw} and K-functions), but despite the the different tested approaches their differences are commonly in the 10 to 15 % interval. For *in situ* IOPs, the Hydrolight IOP/AOP closure experiments resulted in mismatches from 50 % to 100% depending on the field campaign. Among the corrections tested for ACS/Hydroscat errors, the Doxaran (DOXARAN et al., 2013) and Rottgers (RöTTGERS et al., 2013) methods were the most suitable. For Laboratory absorption measurements, differences range from 10% to 80% but were below 15 % for biogeochemical variables concentration measurements. Curuai Lake Bio-optical characterization show that K-functions go from 1 to 12 m^{-1} in 676 nm depending on the season but can go as high as $\approx$ 20 m^{-1} in the blue range. For IOPs, total attenuation, absorption and scattering coefficients were higher for February/2013 ($\approx$ 25, 4 and 21 m^{-1} respectively for 550 nm) and similar for August/2013 and April/2014 ($\approx$ 12, 2.5 and 10 m^{-1} respectively for 550 nm). Backscattering coefficients also were higher for February/2013 ($\approx$ 0.6 m^{-1} in 700 nm) and similar for August/2013 and April/2014 ($\approx$ 0.3 m^{-1} in 700 nm). However, the backscattering to scattering ratio ($^{b_{b_p}}/_{b_p}$) was similar for February/2013, August/2013 and April/2014 (Median of 0.04), indicating low particle type variability. However, differences were found for the exponent of scattering coefficient (γ_b) (Median = 1.3 to 1.5) and for specific scattering b_p^* (0.42 to 0.67 m^2g^{-1}) showing a possible dominance of smaller inorganic particles for February/2013. Specific absorption coefficients for particulate (a_p), non-algal particles (a_{nap}) and phytoplankton (a_ϕ) were within literature values but particularly

high for a_{nap} (up to $\approx 6\ m^{-1}$ in the blue range). Particle Size Distribution shows a bimodal behavior with most of particles in the 10-15 μm range. Results for Inverse Models were not satisfactory for most of retrieved IOPs and biogeochemical variables (Chla and TSM). Best results for GIOP presented errors of at least 20 % while for QAA errors can reach more than 100 %. The Nechad algorithm shows errors that reaches 30 % for TSM estimates which may be considered reasonable. The main source of errors for semi-analytical inverse models rely on uncertainties of input parameters but further investigation is needed to understand the main source of error in the current dataset as well as help guiding future data acquisition.

Keywords: Amazon floodplain lakes. Hydrological Optics. Lakes Biooptical Properties. Semi-Analytical modeling.

CARACTERIZAÇÃO BIO-OPTICA DE LAGOS DA PLANÍCIE INUNDÁVEL AMAZÔNICA E AVALIAÇÃO DA RECUPERAÇÃO DE CONSTITUINTES OPTICAMENTE ATIVOS UTILIZANDO SENSORIAMENTO REMOTO

RESUMO

Lagos de várzea amazônico desempenha um papel importante nos processos biogeoquímicos globais e regionais da Amazonia. Devido ao seu tamanho, estratégias de amostragem normalmente aplicados em estudos limnológicos não são adequadas e, portanto, técnicas de sensoriamento remoto (SR) se apresentam como uma alternativa devido às sua alta resolução temporal e visão sinóptica. No entanto, o uso de SR exige uma caracterização bio-óptica precisa, a fim de fornecer estimativas confiáveis de componentes ativos ópticos (COA). Este trabalho teve como foco de estudo o *Lago Curuai* que é um exemplo representativo de lagos de planície de inundação da Amazônia brasileira. O Lago Curuai foi amostrado em quatro campanhas de campo (setembro/2012, fevereiro e agosto/2013 e abril/2014) em que Propriedades Ópticas Aparentes - POA (R_{rs} e K-functions), Propriedades Ópticas Inerentes POI *in situ* (coeficientes de atenuação, absorção, retroespalhamento e além de distribuição de tamanho de partículas (DTP)), bem como análises de laboratório (concentração e absorção de COA) foram medidos. Uma avaliação da qualidade dos dados foi realizada para testar a capacidade de instrumentação comercial (ACS e Hydroscat) para a extração de informações em ambientes túrbidos, bem como os métodos de medição POA / POI comumente usados. A caracterização bio-optica comparou conjuntos de dados de cada campanha de campo, para medições de superfície e do perfil. Além disto, três modelos inversos semi-analíticos (Algoritmo de *Nechad* (NECHAD et al., 2010), Quasi-Analytical Algorithm (QAA) (LEE et al., 2002) e Generalized ocean color inversion model (GIOP) (WERDELL et al., 2013)) foram testados utilizando as POA e POI medidas . A avaliação da qualidade demonstrou que os efeitos do sol/skyglint têm o maior impacto sobre as medições de sensoriamento remoto acima da água r_{rs} (R_{rs}^{Ab}). Erros mais altos foram encontrados para as POA derivados dentro da água (In-Water) (R_{rs}^{Iw} e K-funções), mas, apesar das diferentes abordagens testadas, suas diferenças estão comumente no intervalo de 10 a 15%. Para as *in situ* POI, os experimentos de fechamento (Closure) utilizando o Hydrolight entre POA e POI resultaram em erros de 50 % a 100 %, dependendo da campanha de campo. Entre as correções testadas para erros dos equipamentos ACS/Hydroscat, as correções de Doxaran (DOXARAN et al., 2013) e Rottgers (RöTTGERS et al., 2013) foram as mais adequados. Para medidas de absorção em laboratório, as diferenças variam de 10 % a 80 %, mas ficaram abaixo de 15 % para variáveis biogeoquímicos. A caracterização Bio-óptica do Lago Curuai mostrou que a K-functions vão de 1 a 12 m^{-1} em 676 nm, dependendo da época, mas pode chegar até $\approx$ 20 m^{-1} na faixa azul. Para as POI, coeficientes de atenuação total, absorção e espalhamento, seus valores foram mais altos em fevereiro / 2013 ($\approx$ 25, 4 e 21 m^{-1}, respectivamente, para 550 nm) e semelhantes para agosto/2013 e abril / 2014 ($\approx$ 12, 2,5 e 10 m^{-1}, respectivamente, para 550 nm). O coeficiente de retroespalhamento também foi maior para fevereiro/2013 ($\approx$ 0,6 m^{-1} em 700 nm) e semelhantes para agosto / 2013 e abril / 2014 ($\approx$ 0,3 m^{-1} em 700 nm). No entanto, a razão retroespalhamento/espalhamento

(b_{b_p}/b_p) foi semelhante para fevereiro / 2013, agosto / 2013 e abril / 2014 (média de 0,04), indicando baixa variabilidade no tipo de partícula. No entanto, foram encontradas diferenças para o expoente do coeficiente de espalhamento (γ_b) (Média = 1,3 a 1,5) e para o coeficiente de espalhamento especifico b_p^* (0,42-0,67 m^2g^{-1}) mostrando uma possível dominância de partículas inorgânicas de menor raio para fevereiro / 2013. O coeficiente de absorção específica para o material particulado particulado (a_p), partículas não-algais (a_{nap}) e fitoplâncton (a_ϕ) se apresentaram altos dentro dos valores da literatura, mas particularmente elevados para a_{nap} (até $\approx 6\ m^{-1}$ na faixa azul). A distribuição de tamanho de partículas apresentou um comportamento bimodal, com a maioria das partículas em 10-15 μm . Os resultados para os modelos inversos não foram satisfatórios para a maioria de POI e variáveis biogeoquímicas (chla e TSM) recuperadas. Os melhores resultados para o algoritmo GIOP apresentaram erros de pelo menos 20 %, enquanto para o algoritmo QAA os erros podem chegar a mais de 100 %. O algoritmo de Nechad mostram erros que chegam a 30 % para as estimativas do TSM, o que podem ser considerados razoáveis. Os resultados demonstraram que a principal fonte de erros para os modelos inversos semi-analíticos foram as incertezas nos parâmetros de entrada, entretanto, mais estudos são necessários para entender a principal fonte de erros no conjunto de dados atual, bem como para guiar futuras aquisição de dados.

Keywords: Lagos de Varzea Amazonica. Optica Hidrológica. Propriedades Bio-Ópticas de Lagos. Modelagem Semi-Analítica.

LIST OF FIGURES

Page

3.1 Coordinates System 9

4.1 Study Area - Curuai Floodplain Lake 31
4.2 Daily mean water level above the sea level for the 2012 - 2014 period. Red marks indicate the period of each field campaign performed in this work. 32
4.3 Field Campaign Sample Stations in Curuai Lake 33
4.4 Structure for Trios Measurements in *September* and *February* 36
4.5 Riverboat used in All Field Campaigns 37
4.6 Trios Cage for All In-Water Measurements 40
4.7 ACS Frame 43
4.8 Flowchart of the Above Water Correction Methodology 51
4.9 Flowchart of the In-Water Correction Methodology - I 53
4.10 Flowchart of the In-Water Correction Methodology - II 53

5.1 *August* and *April* Non-Corrected (NC) and ρ_{sky} corrected 64
5.2 *August* and *April* $R^{Ab}_{rs-QC1}(0^+, \lambda)$ 65
5.3 *August* and *April* R_{rs-RC} 65
5.4 *August* and *April* $R^{Ab}_{rs-QC2}(0^+, \lambda)$ 66
5.5 Above Water Corrections Statistical Indexes 67
5.6 Example of Irradiance (E_d) and Radiance (L_u) profiles 68
5.7 Statistical Indexes comparing Non-Linear, Linear,Weighted and Standard for K_d (a,b,c) and K_{lu} (d,e,f) . $K_{d-NonLin}$ and $K_{lu-NonLin}$ were taken as reference. 70
5.8 Depth comparison for Non-Linear (a,b,c) and Linear (d,e,f) K_d 71
5.9 Depth comparison for Non-Linear (a,b,c) and Linear (d,e,f) K_{lu} 72
5.10 Comparison of $R_{rs}(0^-)$ derived from Linear and Non-Linear K-functions approaches 73
5.11 Depth comparison $R_{rs}(0-)$ from Non-Linear (a,b,c) and Linear (d,e,f) K-function approaches 74
5.12 Comparison of Above Derived $R^{Ab}_{rs}(0^-, \lambda)$ and In-Water Non-Linear derived $R^{Iw}_{rs}(0^-, \lambda)$ for *August* + *April* (All samples from *August* and *April*) 75
5.13 Absorption Tube Scattering Correction Effect on ACS Absorption and Backscattering Measurements for a selected station from *February* 77

5.14 Sigma correction parameter K_{scat} variability for a selected station from *February* . . . 78
5.15 Comparison ACS and LISST (670 nm) - *April* . . . 81
5.16 Results for Polynomial Fitting applied for Morel's and Gordon's First and Second Order models. . . . 83
5.17 Statistical Indexes for Laboratory Spectrophotometer Absorption Particulate Material, Non-algal Particles and Phytoplankton (a_p, a_{nap}, a_ϕ) - *April* . . . 85
5.18 Comparison of Total Absorption Coefficients from ACS (a_{T-w}) and Laboratory ($a_{T-w} = a_p + a_{cdom}$) for *April* . . . 86

6.1 TSM, DOC and Chla Variability among stations . . . 89
6.2 Biogeochemical Variables Ratios . . . 91
6.3 Diffuse Attenuation Coefficients (K_d and K_{lu}) for the 500 to 800 nm interval. K-function calculated from the Non-Linear Approach . . . 92
6.4 Total Median Spectral IOPs (Particulate + CDOM) Measured with ACS 94
6.5 Inter-campaign variability of backscattering . . . 95
6.6 LogLog transformed of Suspended Matter (TSM, TSOM and TSIM) and Selected IOPs (b_{b_p}, b_p, $c_{(p+CDOM)}$) . . . 99
6.7 Type II Linear Regressions for Chla Concentration Samples and $a_\phi(676)$ 100
6.8 (a) Backscattering Ratio ${}^{b_{b_p}}/_{b_p}(HS6/ACS)$ and ${}^{TSOM}/_{TSM}$ Ratio and (b) Clorophyll- a concentration [Chl-a]/Attenuation $c^*_{(p+CDOM)}(660)$ for All samples. . . . 102
6.9 Median Scattering (b_p (700 nm)) Profiles . . . 103
6.10 Median Scattering Gama Factors Profiles . . . 104
6.11 Median Chlorophyll-a Absorption Profiles . . . 105
6.12 Spectrophotometer Absorption Measurements . . . 107
6.13 Specific Spectrophotometer Absorption Measurements . . . 110
6.14 Particle Size Distributions for *April* . . . 111
6.15 Comparison of (a) ξ_{psd}/γ_b (b) Junge Model/Measured PSD . . . 112

7.1 Statistical Indexes comparing GIOP derived and Laboratory Measured $a_{T-w}(\lambda)$ ($a_{T-w}(\lambda) = a_p(\lambda) + a_{cdom}(\lambda)$), $a_\phi(\lambda)$ and $a_{nap+cdom}(\lambda)$ for *April* . 113
7.2 Statistical Indexes comparing GIOP derived and ACS/Hydroscat Measured $a_{T-w}(\lambda)$ and $b_{bp}(\lambda)$ . . . 115
7.3 Specific Absorption (a^*_{ph}) comparison . . . 117
7.4 Comparison of Measured and Derived a_{T-w}, $a_{nap+cdom}$, a_{ph} and b_{bp} . . . 119
7.5 Comparison of $a_{nap+cdom}$ and b_{b_p} exponents derived from for median solutions presented in Figure 7.4 . . . 120

7.6 Statistical Indexes comparing QAA-(Mishra and V5) derived and Laboratory Measured $a_T(\lambda)$ ($a_T(\lambda) = a_p(\lambda) + a_{cdom}(\lambda) + a_w$), $a_\phi(\lambda)$ and $a_{nap+cdom}(\lambda)$ for *April* 122
7.7 Statistical Indexes comparing QAA-(Mishra and V5) derived and ACS Measured $a_T(\lambda)$ 124
7.8 Statistical Indexes comparing QAA-(Mishra and V5) derived and Hydroscat Measured $b_{bp}(\lambda)$ 125
7.9 Comparison of Nechad derived and measured $a_p^*(\lambda)$ and $b_{b_p}^*(\lambda)$. 127
7.10 Statistical Indexes comparing measured TSM concentration and derived from both: (1) Nechad model with A^p and C^p tabulated parameters from Nechad et al. (2010) (Dashed Line) and (2) Nechad model with A^p and C^p parameters calculated from $a_{nap}^*(\lambda)$, $a_{cdom}(\lambda)$ and $b_{b_p}^*(\lambda)$ from *February* (Solid Line) 128
7.11 Comparison of A^p parameters 129
7.12 Statistical Indexes comparing Nechad Model calculated with A^p and C^p parameters from Nechad et al. (2010) and calculate from Linear regressed A^p and C^p 130

B.1 Statistical Indexes for Particulate Absorption a_p and TSM/TSOM/TSIM Linear Fitting 165
B.2 Statistical Indexes for Particulate Absorption a_{nap} and TSM/TSOM/TSIM Linear Fitting 166
B.3 Statistical Indexes for Particulate Absorption a_ϕ and TSM/TSOM/TSIM Linear Fitting 167

C.1 Hidrolight Experiment - *February* 169
C.2 Hidrolight Experiment - *August* 170
C.3 Hidrolight Experiment - *April* 171

E.1 Diffuse Attenuation Coefficients (K_d and K_{lu}) for the 400 to 800 nm interval 175

LIST OF TABLES

Page

3.1 Summary of Specific Coefficients and Derived Parameters Available for Use in GIOP - Table adapted from Werdell et al. (2013) 29

4.1 Field Campaign Dates and Number of Stations 34
4.2 Measurements carried out in each season 34
4.3 Parameters Used for GIOP Tests 60
4.4 Parameters Used for GIOP Sensitivity Analysis 61

5.1 Best ACS/Hydroscat correction for each field campaign for the tested AOPs. Color in the table are colors from curves in Appendix C. 79
5.2 LISST Statistical Indexes 81
5.3 Derived coefficients for R_{rs}/IOPs models by Non-Linear Fitting 83
5.4 Indexes for Biogeochemical Variables - Replicas 87

6.1 Statistics for the Non-Linear K-functions (K_d, K_u and K_{lu},) at 676 nm . 93
6.2 ${}^{b_{b_p}}/b_p(HS6/ACS)$ in 700 nm statistics for surface measurements 96
6.3 Exponent γ_b and γ_{b_b} calculated for scattering and backscattering coefficients for all stations (for each field campaign) calculated within 0.5 to 1.0 meters depth 97
6.4 Mass-Specific coefficients for TSM and TSIM calculated from the Type II Linear Regression with Attenuation Coefficient $c^*_{(p+CDOM)}(660)$, Scattering Coefficient $b^*_p(700)$ and Backscattering coefficient $b^*_{b_p}(700)$ 100
6.5 Statistics for Chla Concentration and $a_\phi(676)$ 101
6.6 Exponents S_{cdom} and S_{nap} 109
6.7 Specific Absorptions in 676 nm for the division a_p over TSM and a_ϕ over Chla;- Particulate (a^*_p) and Phytoplankton (a^*_ϕ) 110
6.8 Statical Indexes for fitted Junge Model Exponent (ξ_{psd}) 112

7.1 Statistical Indexes comparing Measured and Derived TSM/Chl-a - Inputs: b_{bp} Exponent from April (1.35); $a_{nap+cdom}$ Exponent from April (0.015), Linear Regressed a^*_ϕ from April; Overconstrained Linear matrix inversion using QR decomposition. 116

A.1 Descriptive Statistics of the Surface Optically Active Substances used for IOP relationships (23, 31 and 25 Stations for *February*, *August* and *April* respectively) 163

A.2 Descriptive Statistics of the Surface Optically Active Substances - All Samples 164

D.1 Statistical Indexes for TSM and IOPs. For UPD, RPD and RMSE, TSM was taken as reference. 173
D.2 Statistical Indexes for TSIM and IOPs. For UPD, RPD and RMSE, TSIM was taken as reference. 174
D.3 Statistical Indexes for TSOM and IOPs. For UPD, RPD and RMSE, TSOM was taken as reference. 174

LIST OF ABBREVIATIONS

AC-9	–	Absorption and Attenuation meters -9
ACS	–	Absorption and Attenuation meters
AOP	–	Apparent Optical Properties
CDM	–	Colored Dissolved Matter
CDOM	–	Colored Dissolved Organic Matter
CFS	–	Constant Fraction of Scattering
Chla	–	Chlorophyll -a
CTD	–	Conductivity-Temperature-Depth
CV	–	Coefficient of Variation
DIC	–	Dissolved Inorganic Carbon
DOC	–	Dissolved Organic Carbon
DTC	–	Dissolved Total Carbon
FEOF	–	Feofitine
FOV	–	Field Of View
GEOMA	–	Thematic Network for Amazon Research and Environmental Modeling
GF/F	–	Glass Fiber Filter/G
GIOP	–	The Generalized Ocean Color Inversion Model
IIE	–	International Institute of Ecology
IOP	–	Inherent Optical Properties
LBA-HIBAM	–	Large-Scale Biosphere-Atmosphere Experiment-Hydrology of the Amazonian B
LGC	–	Lago Grande de Curuai
LMI	–	Linear Matrix Inversion
LSP	–	Lambertian Spectralon Plaque
MVCO	–	Martha's Vineyard Coastal Observatory
NAP	–	Non-Algal Particles
NASA	–	National Aeronautics and Space Administration
NN	–	Neural Networks
OAC	–	Optical Active Components
OD	–	Optical density
OD nap	–	Optical density of Non-Algal Particles
PSD	–	Particle Size Distribution
QAA	–	Quasi-Analytical Algorithm
QAA-Mishra	–	Quasi-Analytical Algorithm-Mishra Version
QAA-V5	–	Quasi-Analytical Algorithm- Version 5
QC1	–	Quality Control 1 for R_{rs}^{Ab}
QC2	–	Quality Control 2 for R_{rs}^{Ab}
RPD	–	Modular Relative Percent Difference
RTE	–	Radiative Transfer Equation
RMSE	–	Root Mean Squared Error
SAA	–	Semi-Analytic Algorithms
SD	–	Standard deviation

SOC	–	Spectral Optimization Class
SZA	–	Solar Zenith Angle
T-R method	–	Transmittance-Reflectance quantitative technique
TSIM	–	Total Suspended Inorganic Matter
TSM	–	Total Suspended Matter
TSOM	–	Total Suspended Organic Matter
UPD	–	Unbiased Percent Difference
UV	–	Ultraviolet
VIS	–	Visible
VSF	–	Volume Scattering Function
PSD	–	Particle Size Distribution

LIST OF SYMBOLS

λ	–	Wavelength
$\hat{\xi}$	–	Unity Vector
ϕ	–	*Azimuthal* angle
θ	–	*Zenital* angle
$\Omega(\hat{\xi})$	–	solid angle in the $\hat{\xi}$ direction
$d\Omega(\hat{\xi})$	–	$\sin(\theta)d\theta d\phi$
(ΔA)	–	Instrument Detector Area
(ΔQ)	–	Radiant Power
Ω	–	Solid Angle
$(\Delta\lambda)$	–	Wavelength Interval
θ_{SZA}	–	Solar Zenith Angle
β	–	Volume Scattering Function
ΔV	–	Arbitrary Volume
ΔI	–	Intensity Interval
ψ	–	Scattering angle from the beam propagation direction
$\widetilde{\beta}$	–	*Scattering Phase Function*
ω_0	–	*Single Scattering Albedo*
ξ_{psd}	–	Slope of the Particle Size Distribution
σ_x	–	particle geometrical cross-sectional area
$\bar{\rho}$	–	Air-Water Fresnel reflectance factor for sun+sky E_d reflected on the surface
ρ	–	Fresnel reflectance factor of the water for the upward radiance
ρ_{sky}	–	Mobley (1999) proportionality factor
γ_b	–	Particulate Scattering power law model exponent
γ_{b_b}	–	Particulate Backscattering power law model exponent
a	–	*Absorption Coefficient*
a_ϕ	–	Phytoplankton absorption coefficient
a_{Chla}	–	Chlorophyll-a absorption coefficient
a_p	–	Particulate Absorption coefficient
a_{nap}	–	Non-Algal Particles Absorption coefficient
a_w	–	Pure water Absorption Coefficient
a_{CDOM}	–	CDOM Absorption coefficient
a^*_ϕ	–	Specific Phytoplankton absorption coefficient
a^*_{nap}	–	Specific Non-Algal Particles absorption coefficient
a^*_p	–	Specific Particulate Particles absorption coefficient
a_T	–	Total Absorption coefficient
a_{T-w}	–	a_T - a_w
$a_{nap-fit}$	–	a_{nap} fitted to model described in equation 3.28 Bricaud et al. (2010) Method
$a_{\phi-fit}$	–	a_ϕ fitted to model described in equation 3.28 Bricaud et al. (2010) Method
a_{Flat}	–	ACS Absorption corrected for Flat Correction
a_{Zan}	–	ACS Absorption corrected for Zaneveld Correction

a_{Kirk}	–	ACS Absorption corrected for Kirk Correction
a_{roth}	–	ACS Absorption corrected for Rottgers Correction
b	–	Scattering Coefficient
b_f	–	Foward Scattering Coefficient
b_b	–	*Backward Scattering (Backscaterring)*
$\frac{b_b}{b}$	–	*Backscattering to Scattering Ratio*
b_w	–	Pure water Scattering Coefficient
b_{b_w}	–	Pure water Backscattering Coefficient
b_{CDOM}	–	CDOM Scattering coefficient
b_T	–	Total Scattering Coefficients
b_{b_T}	–	Total Backscattering Coefficients
b_p	–	Particulate Scattering Coefficient
b_{b_p}	–	Particulate Backscattering Coefficient
b_p^*	–	Particulate Scattering Coefficient
$b_{b_p}^*$	–	Specific Particulate Backscattering Coefficient
c	–	Beam Attenuation Coefficient
D	–	diameter of each particle
D_o	–	reference diameter
E_d	–	Downwelling Irradiances
E_u	–	Upwelling Irradiances
f	–	Factor Relating $R(0^-)$ and $\frac{b_b}{a}$
f'	–	Factor Relating $R(0^-)$ and $\frac{b_b}{a+b_b}$
g0	–	proportionality factor for Gordon et al. (1988) model
g1	–	proportionality factor for Gordon et al. (1988) model
k	–	differential number concentration at D_o
k-functions	–	Diffuse Attenuation Coefficients
k_d	–	Downwelling Irradiance Diffuse Attenuation Coefficient
k_{lu}	–	Upwelling Radiance Diffuse Attenuation Coefficients
k_u	–	Upwelling Irradiance Diffuse Attenuation Coefficients
L_u	–	Upwelling Radiances
L_d	–	Downwelling Radiances
L_r	–	surface-reflected part of the incident sun/sky radiance
L_{sky}	–	radiance measured by a detector pointed to the sky
L_T	–	$L_r + L_u$
L_w	–	L_T - $\rho_{sky} \cdot L_{sky}$
N	–	Number Concentration
$N(D, \xi_{psd})$	–	Number Particle Size distribution (PSD)
$N'(D)$	–	Differential distribution per unit size, (Density unction of the PSD)
n_w^2	–	water refractive index
Q_x	–	Efficiency factor for each coefficient
Q	–	Factor Relating $L_u(0^-)$ and $E_u(0^-)$
R	–	Irradiance Reflectance

R_{rs}	–	Remote Sensing Reflectance
R_{rs}^{Ab}	–	Above Water Remote Sensing Reflectance
R_{rs-NC}^{Ab}	–	Non-Corrected Above Water Remote Sensing Reflectance
$R_{rs-\rho_{sky}}^{Ab}$	–	R_{rs-NC}^{Ab} corrected by (MOBLEY, 2015) factor
R_{rs-RC}^{Ab}	–	$R_{rs-\rho_{sky}}^{Ab}$ corrected by Residual Correction strategy + (MOBLEY, 2015)
R_{rs-QC1}^{Ab}	–	$R_{rs-\rho_{sky}}^{Ab}$ corrected by Quality Control (1) criteria + (MOBLEY, 2015)
R_{rs-QC2}^{Ab}	–	$R_{rs-\rho_{sky}}^{Ab}$ corrected by Quality Control (2) criteria + (MOBLEY, 2015)
$\mathscr{R}$	–	Surface Transmittance Factor
$\bar{r}$	–	mean water-air Fresnel reflectance factor for the diffuse upward flux surface
R_{rs}^{Iw}	–	In-Water Remote Sensing Reflectance
R^{Iw}	–	In-Water Irradiance Reflectance
$R_{rs-NonLin}^{Iw}$	–	In-Water Remote Sensing Reflectance derived from Non-Linear Fitting
R_{rs-Lin}^{Iw}	–	In-Water Remote Sensing Reflectance derived from Linear Fitting
R_{NonLin}^{Iw}	–	In-Water Irradiance Reflectance derived from Non-Linear Fitting
R_{Lin}^{Iw}	–	In-Water Irradiance Reflectance derived Linear Fitting
L_T	–	Total radiance signal that leaves the water body
L_r	–	surface-Reflected part of the incident sun/sky radiance
S_{cdom}	–	CDOM exponential absorption model exponent
$S_{nap+cdom}$	–	Nap+CDOM exponential absorption model exponent
S_{nap}	–	Non-Algal Particles exponential absorption model exponent
V(D)	–	Particle Volume Size Distribution
$z = 0^-$	–	Below the water surface (Subsurface)
$z = 0^+$	–	Above the water surface
$[TSM]$	–	Total Suspended Matter Concentration
$[Chl - a]$	–	Chlorophyll-a Concentration

CONTENTS

Page

1 INTRODUCTION 1

2 HYPOTHESIS AND OBJECTIVES 7

2.0.1 Hypothesis of the Work 7

2.0.2 Main Objective 7

2.0.3 Specific Objectives 7

3 THEORETICAL BACKGROUND 9

3.1 Fundamental Definitions 9

3.1.1 Radiometric Quantities 9

3.1.2 Inherent Optical Properties - IOP 10

3.1.3 Apparent Optical Properties - AOP 13

3.1.4 Surface Effects 14

3.2 Optically Active Constituents - OACs 16

3.2.1 Pure Water 16

3.2.2 Colored Dissolved Organic Matter - CDOM 16

3.2.3 The Particulate Material 17

3.2.3.1 Photosynthetically Active Biota Phytoplankton/Chlorophyll-a 17

3.2.3.2 Non-Algal Particles - NAP 19

3.2.3.3 Total and Specific IOPs 20

3.3 Radiative Transfer in Waters Bodies 21

3.3.1 Forward Model Approximations 21

3.3.2 Inverse Models 23

3.3.2.1 Quasi-Analitical Model (QAA) 24

3.3.2.2 The Nechad Algorithm 26

3.3.2.3 The Generalized ocean color inversion model - GIOP 28

4 MATERIAL AND METHODS 31

4.1 Study Area 31

4.2 Field Campaign Description 33

4.3 Measurements Methods 35

4.3.1 In-Situ Radiometric Measurements 35

4.3.1.1 Above Water Approach 35

4.3.1.2 In-water Approach . . . 39
4.3.2 In-situ IOP Measurements . . . 41
4.3.2.1 Attenuation and Absorption Measurements - ACS . . . 42
4.3.2.2 Backscattering Measurements - Hydroscat . . . 45
4.3.2.3 Size Distribution Measurements - LISST . . . 46
4.3.3 Laboratory Measurements . . . 47
4.3.3.1 Determination of Limnological Parameter Concentrations . . . 47
4.3.3.2 Absorption Measurements . . . 48
4.4 Data Quality Assessment . . . 49
4.4.1 In-Situ Radiometric Measurements . . . 50
4.4.1.1 Above Water Approach . . . 50
4.4.1.2 In-Water Approach . . . 50
4.4.1.3 Comparing Above Water ($R_{rs}^{Ab}(0^+, \lambda)$) and In-water ($R_{rs}^{Iw}(0^-, \lambda)$) Approaches . . . 54
4.4.2 In-Situ IOPs . . . 54
4.4.2.1 Hydrolight Experiments - ACS and Hydroscat Measurements . . . 54
4.4.2.2 LISST Quality Analysis . . . 56
4.4.2.3 Testing Forward Model Approximations . . . 56
4.4.3 Laboratory Measurements . . . 56
4.5 Curuai Lake Bio-Optical Variability . . . 57
4.5.1 IOPs Seasonal Comparison . . . 57
4.5.2 The *April* Field Campaign . . . 58
4.5.2.1 Absorption Analysis . . . 58
4.5.2.2 LISST Analysis . . . 59
4.6 Inverse Models . . . 59
4.6.1 GIOP . . . 60
4.6.2 QAA . . . 61
4.6.3 Nechad . . . 62

5 DATA QUALITY ASSESSMENT . . . 63
5.1 In-Situ Radiometric Measurements . . . 63
5.1.1 Above Water Approach . . . 63
5.1.2 In-Water Approach . . . 67
5.1.3 Comparing Above and In Water R_{rs} Approaches . . . 75
5.2 In-Situ IOPs . . . 76
5.2.1 ACS and Hydroscat Corrections - Hydrolight Experiments . . . 76
5.2.2 Lisst Experiments . . . 80
5.2.3 Forward Models Performance . . . 82

5.3 Laboratory Measurements Uncertainty 84

6 CURUAI LAKE BIO-OPTICAL VARIABILITY 89
6.1 Seasonal variations of biogeochemical variables 89
6.2 AOPs Seasonal Inter-comparison 91
6.3 IOPs Seasons Inter-comparison 93
6.3.1 Spectral Dependence of Surface IOPs 93
6.3.2 Relationships between IOPs and biogeochemical parameters 97
6.3.3 IOPs Profiles 102
6.4 The *April* Field Campaign 106
6.4.1 Laboratory Measurement Results 106
6.4.2 LISST Results 111

7 INVERSE MODELS 113
7.0.1 GIOP 113
7.0.2 QAA 120
7.0.3 Nechad 126

8 CONCLUSIONS AND FINAL CONSIDERATIONS 133

REFERENCES 137

Appendix A 163
A.1 Descriptive Statistics of the Biogeochemical used for IOP relationships . 163

Appendix B 165
B.1 Absorption Measurements and its respectively Statistical Indexes for is relation to biogeochemical components for *April* 165

Appendix C 169
C.1 Results for Hydrolight Experiments 169

Appendix D 173
D.1 Statistical Indexes for TSM, TSIM and TSOM and IOPs 173

Appendix E 175
E.1 Measured AOPs 175

1 INTRODUCTION

Historically, the use of Remote Sensing techniques to retrieve optical properties from water bodies has mainly been developed for oceanic waters. However, the need for information to support the rational use of fresh water has led to an increased demand for Remote Sensing studies applied to inland waters (Rivers and Lakes).Inland waters are mainly characterized as Case 2 Waters, in which the correlation among Optically Active Components (OACs) is weak, different from deep ocean waters, where Chlorophyll-a (Chla) dominates OAC composition and co-vary with the remaining components (BUKATA et al., 1995; KIRK, 2010). Particularly, Amazon basin waters are a singular case of inland waters, due to their high concentration of Organic/Inorganic Suspended, dissolved organic material and diversity of phytoplankton species (SIOLI, 1984; RICHEY et al., 1986; MEADE, 1994). Such characteristics demand studies to increase the OAC retrieval accuracy via remote sensing.

Amazon floodplain lakes have been the focus of relevant national and international multidisciplinary scientific projects (Thematic Network for Amazon Research and Environmental Modeling *GEOMA*, and Large-Scale Biosphere-Atmosphere Experiment-Hydrology of the Amazonian Basin *LBA-HIBAM*) in the recent decades. This interest stems from the role they play in global and regional processes, given the size of the Amazon region (approximately 6.5 million km^2), biodiversity and natural resources (JUNK et al., 2011). Their biogeochemistry is mainly driven by the hydrology of the Amazon River, characterized by a seasonal flood pulse (JUNK et al., 1989), which causes water level changes throughout the hydrological year as well as sediment exchanges between the river and floodplain lakes, influencing processes and composition of OACs pools (RUDORFF et al., 2014a). Particularly, light availability, required for photosynthesis and other photo-chemical processes, depends directly on the distribution of particulate and dissolved materials in the water column. Those components are comprised mainly by dissolved and suspended organic forest by-products as well as Andean suspended minerals (RICHEY et al., 1986; MEADE, 1994; LEITE et al., 2011; COSTA et al., 2012). In that sense, the study of Amazon floodplain lakes OACs contributes not only for providing additional information on biogeochemical processes but, crucially, to the development of satellite Remote Sensing algorithms. These algorithms tuned to Amazon optical environment would help to build a synoptic multi-temporal database to improve the understating of this peculiar ecosystem (LEE et al., 2002; WANG et al., 2005; IOCCG, 2006; WERDELL et al., 2013; MISHRA et al., 2014).

The first classification of Amazonian waters was based on the connection between optical (color) and chemical properties by Sioli (1984). According to this classification, Amazonian waters can be grouped into three major types: *black waters* with a high concentration of humic substances; *white water* with high concentration of suspended inorganic particles; and *clear water* with relatively low concentration of inorganic particulate matter and dissolved humic substances. However, this classification is too general to support OACs estimates via remote sensing methods. Such estimates require the description of the ambient light field structure in terms of Inherent Optical Properties (IOPs) and Apparent Optical Properties (AOPs) of the studied aquatic system (MOUW et al., 2015).

Measuring IOPs and AOPs, however, is not trivial. Although these properties are routinely measured in ocean waters, they are scarce in very turbid inland waters because their measurement represents a significant endeavor. Efforts have been made to expand inland waters IOP/AOPs database (GLOBALLAKESWEBSITE, 2015) using standard measurement methods, but definitive protocols have not yet been achieved (MOUW et al., 2015). Due to the lack of a reliable protocol to measure *Laboratory* and *in situ* IOPs/AOPs, NASA Protocols for ocean waters (MUELLER et al., 2003) are currently being used (WANG et al., 2009; SHI et al., 2014). However, some methods are not suitable for turbid inland waters resulting in notable errors.

As an example of such errors, IOPs laboratory absorption measurements (particulate total absorption (a_p), phytoplankton (a_ϕ), non-algal particles (a_{nap}) and Colored Dissolved Organic Matter (CDOM) absorption (a_{cdom})), are mainly performed through bench-top spectrophotometer techniques, which are subject to several sources of uncertainties (STRAMSKI et al., 2015). Filter-pad technique uncertainties, for instance include, among others, pathlength amplification due to light scattering within the sample+filter ensemble and effects related to particle distribution and particle load. Those uncertainties are enhanced by the high particulate concentrations in Case 2 waters. Additional sources of uncertainty, also highlighted by Stramski et al. (2015), are filtration, freezing, and storage procedures. In addition, for a_{cdom}, cuvette lengths could constrain absorption measurements, especially in Ultraviolet (UV) and Visible (VIS) blue range (NELSON; COBLE., 2009).

Regarding *in situ* IOP measurements, equipment designed for ocean waters optical characterization is generally not suitable for highly turbid waters (MCKEE et al., 2009; BOSS et al., 2009). Commonly used *in situ* Absorption and Attenuation meters (ACS) are subject to scattering errors (acceptance angle effects and absorption tube

scattering errors) which increase directly with OAC concentrations. Also *in situ* Backscattering meters are affected by both, pathlength loss of signal and saturation. Despite the efforts made to correct those effects, they are still a significant source of error in *in situ* measurements (MCKEE; CUNNINGHAM, 2006; LEYMARIE et al., 2010; Sander de Carvalho et al., 2015).

Uncertainties are also caused by *in situ* radiometric measurement approach. The two most common ones, *above-water* and *in-water* are both influenced by particular sources of uncertainties which are typical of turbid waters. For instance, for the *above-water* approach, AOPs are influenced by the strong signal in the Near-Infrared which limits sky/sunglint correction (LEE et al., 2011; GLEASON et al., 2012). Regarding *in-water* approach, Mueller et al. (2003) methodology does not hold because of the high turbidity causing light extinction in the first meter depth, which demands measurements to be taken carefully at very low sink/depth rates. Unfortunately, measurements in the first meter depth are also susceptible to wave interference as well as shadowing effects. Therefore, the reduction of one source of uncertainty (light extinction) implies an increase with regard to other uncertainties (shadow and wave focusing) (LEE et al., 2013). Also, for shallow lakes, *free fall* strategies commonly used in the ocean are limited, since sink/depth rate are hardly controlled.

Despite those constraints, there are reports of measurements of IOPs and AOPs around the world, using the current methodology (SUN et al., 2009; MA et al., 2009; CAMPBELL et al., 2011; CHERUKURU et al., 2014; DOGLIOTTI et al., 2015). Bio-optical properties of Amazon floodplain lakes, however, are not comparable to most of those water bodies, due the particular combination of fine inorganic particles and a wide variety of dissolved and suspended organic matter. Nevertheless, Chinese and Australian Lakes properties are amongst the most similar to those of the Amazon floodplain lakes. Particularly, Chinese lakes (Poyang and Taihu) have concentrations of inorganic suspended matter comparable to those within Brazilian Floodplain lakes. Some of the reported data comes from environments which present even more extreme Chlorophyll-a concentrations (AUGUSTO-SILVA et al., 2014; CAMPBELL et al., 2011; WU et al., 2011; MATTHEWS; BERNARD, 2013), or dissolved organic matter (KUTSER et al., 2005; KUTSER, 2012) but not the combination of both OACs coupled with high concentration of suspended sediments as in the case of Amazon waters.

In this research a Brazilian Amazon floodplain lake, named *Curuai Lake* is under study. Curuai Lake is a suitable example of floodplain Amazon lakes because it presents high variability of Total Suspended Organic and Inorganic Matter (TSOM

and TSIM) (≈ 5 to $\geq 1000\ mgL^{-1}$), Dissolved Organic and Inorganic Matter (DOC and DIC) (≥ 5 ppm) and Chlorophyll-a (0.8 to $\geq 300\ mgL^{-1}$) in four distinct phases of the hydrological year (BARBOSA et al., 2009). Several studies have already described the hydrology of the lake (RUDORFF et al., 2014a; RUDORFF et al., 2014b), AOPs and Remotely Sensed radiometric measurements (NOVO et al., 2004; RUDORFF et al., 2009; Lobo et al., 2012; FERREIRA et al., 2012; LOBO et al., 2014). However, the lake has not yet been optically characterized. Also, no Remote Sensing study has focused on testing the suitability of semi-analytical algorithms, which have, allegedly, higher accuracy when compared to empirical algorithms.

Semi-analytical algorithms have been currently applied to Case 2 inland waters(ODERMATT et al., 2012; ZHU et al., 2014; PALMER et al., 2015). Some authors claim that semi-analytical algorithms are more stable then empirical algorithms and, if well parametrized, could be applied in a wide range of OAC types and concentrations (MOUW et al., 2015). In that sense, numerous algorithms developed for Case 1 waters have been re-parametrized for the retrieval of OAC concentrations for Case 2 waters. Particularly, three algorithms widely used for ocean waters, have been the focus of studies on Case 2 waters: the *Nechad* Algorithm (NECHAD et al., 2010), Quasi-Analytical Algorithm (QAA) (LEE et al., 2002) and the recently developed Generalized ocean color inversion model (GIOP) (WERDELL et al., 2013). *Nechad* has been applied and used as a standard form to retrieve Total Suspended Matter (TSM) in very turbid waters (DOGLIOTTI et al., 2015; KNAEPS et al., 2015), whilst QAA has been focused on Chlorophyll-a concentration and CDOM absorption (MISHRA et al., 2013; MISHRA et al., 2014). GIOP approach, which has been included in free NASA/ESA platforms(WERDELL et al., 2013), focuses on bio-optical inputs which can be chosen from a list of standard IOPs but also allows local measured inputs acquired from *in situ* measurements.

This research reports the measurements of both, IOPs and AOPs at Curuai Lake in four different phases of the hydrological year (September/2012, February and August/2013 and April/2014). Apparent Optical Properties (R_{rs} and K-functions), *in situ* Inherent Optical Properties (Attenuation, Absorption, Backscattering profiles and Particle Size Distribution (PSD)) as well as laboratory analysis (AOC concentration and absorption) were measured using different strategies in each field campaign. A comprehensive data quality analysis was carried out in order to assess the quality of protocols for both, acquisition and correction of optical properties as well as to investigate the suitability of commercial instrumentation (ACS and Hydroscat) for an inland turbid environments. Also, an optical characteriza-

tion comparing datasets from each field campaign, for surface and profiles measurements, investigating IOP/AOPs differences among seasons was performed. At last, three semi-analytical inverse models (*Nechad* Algorithm (NECHAD et al., 2010), Quasi-Analytical Algorithm (QAA) (LEE et al., 2002) and Generalized ocean color inversion model (GIOP) (WERDELL et al., 2013)) were tested, aiming the development of reliable remote sensing techniques to monitor Amazon basin turbid lakes. The document is divided as follow: Chapter 2 presents the Objectives of this work; Chapter 3 presents a brief Theoretical Background; Chapter 4 presents the *Material and Methods*; Results and discussion are presented in three Chapters, *Data Quality Assessment* (Chapter 5), *Curuai Lake Bio-Optical Variability* (Chapter 6) and *Inverse Models* (Chapter 7).

2 HYPOTHESIS AND OBJECTIVES

2.0.1 Hypothesis of the Work

The existing protocols of data collection, processing and correction, as well as semi-analytical bio-optical algorithms, are suitable for application in very turbid and particular Amazon water bodies.

2.0.2 Main Objective

Optically characterize the Curuai Lake and identify the best fitted semi-analytical model to retrieve reliable OACs from Remote Sensing Reflectance

2.0.3 Specific Objectives

a) Analyze the uncertainties in *insitu* radiometric measurements, identifying the main sources of errors in derived AOPs and test different correction schemes. Identify the most acceptable approach for radiometric measurements in *Curuai Lake*.

b) Analyze the measured IOPs correction schemes and identify which is the most acceptable. Compare IOPs *insitu*, laboratory measurements as well as derived quantities from IOPs measurements aiming at an uncertainties analysis. Indicate the limitations in the used approaches.

c) Describe and analyze *Curuai Lake* bioptical properties and identify the variability of measured IOPs.

d) Test and parametrize three semi-analytical algorithms, using measured *insitu* data. Identify the most suitable set of parameters as well the most reliable algorithm to retrieve TSM, Chlorophyll-a and CDOM optical properties and concentrations.

3 THEORETICAL BACKGROUND

In this chapter a brief review of hydrological optics theory is presented. Fundamental definitions of Radiometric Quantities, Inherent and Apparent Optical Properties (IOPs and AOPs) and well as surface effects are discussed. Optical properties of dominant water bodies components (Pure Water, dissolved and particulate material) are also discussed. At last, Radiative Transfer Models (Foward and Inverse Models) are discussed and the three Inverse Models tested in this research are presented.

3.1 Fundamental Definitions

3.1.1 Radiometric Quantities

Figure 3.1 presents the directions and solid angles used in this research. The unity vector ($\hat{\xi}$) represents the direction and θ and ϕ are the *zenith* and *azimuth* angles respectively. $\Omega(\hat{\xi})$ is the solid angle in the $\hat{\xi}$ direction ($d\Omega(\hat{\xi}) = \sin(\theta)d\theta d\phi$).

Figure 3.1 - Coordinates System

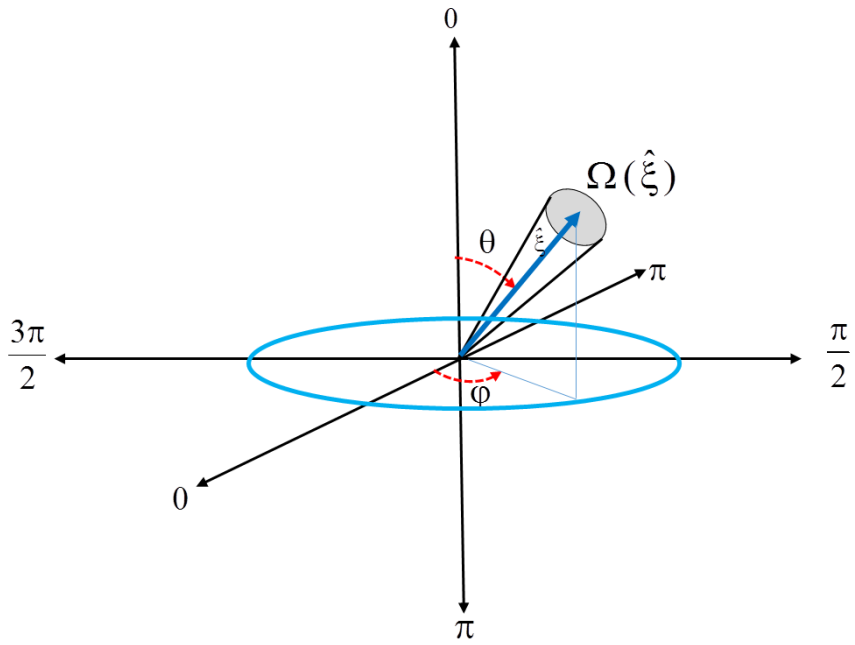

The fundamental radiometric quantities, *Radiance* and *Plane Irradiance* are defined as (equations (3.1) and (3.2)):

$$L(\hat{\xi}, \lambda) \equiv \frac{\Delta Q}{\Delta A \Delta \Omega \Delta \lambda} \; (Wm^{-2}sr^{-1}nm^{-1}) \tag{3.1}$$

$$E(\lambda) \equiv \frac{\Delta Q}{\Delta A \Delta \lambda} \; (Wm^{-2}nm^{-1}) \tag{3.2}$$

where (ΔA) is the instrument detector area, (ΔQ) is the radiant power, Ω is the solid angle and $(\Delta\lambda)$ is the wavelength interval. *Radiance* and *Plane Irradiance* are related as :

$$E_d(\lambda) \equiv \int_{\phi=0}^{2\pi} \int_{\theta=0}^{\frac{\pi}{2}} L(\theta, \phi, \lambda) \, |\cos\theta| \sin\theta d\theta d\phi \tag{3.3}$$

$$E_u(\lambda) \equiv \int_{\phi=0}^{2\pi} \int_{\theta=\frac{\pi}{2}}^{\pi} L(\theta, \phi, \lambda) \, |\cos\theta| \sin\theta d\theta d\phi \tag{3.4}$$

where E_d and E_u are referred to as the *downwelling* and *upwelling irradiances*. The *downwelling* and *upwelling radiances* (L_d and L_u) are defined as measured in any direction within $\frac{\pi}{2} \leq \theta \leq \pi$ for $L_u(\theta, \phi)$ and within $0 \leq \theta \leq \frac{\pi}{2}$ for $L_d(\theta, \phi)$ in the $0 \leq \phi \leq 2\pi$ interval. Those quantities can also be defined just above water surface (0^+) or just below the water surface (subsurface) (0^-).

Another key radiometric quantity is the *Radiant Intensity* which is denoted by:

$$I(\hat{\xi}, \lambda) \equiv \frac{\Delta Q}{\Delta \Omega \Delta \lambda} \; (Wsr^{-1}nm^{-1}) \tag{3.5}$$

The Solar Zenith Angle, which is a key variable for radiometric measurements is defined as θ_{sza}.

3.1.2 Inherent Optical Properties - IOP

The Inherent Optical Properties (IOPs) are those which depend only on the aquatic environment and are not affected by the ambient light field within the medium (PREISENDORFER, 1976; MOBLEY, 1994). Considering an incident irradiance parallel beam $E(\lambda)$; if $\Delta E(\lambda)$ is the irradiance that leaves the beam (by absorption or scattering), after crossing the Δl length, the *Beam Attenuation Coefficient* is defined by :

$$c(\lambda) \equiv \frac{\Delta E_i(\lambda)}{E_i(\lambda)\Delta l} \ \left(m^{-1}\right) \tag{3.6}$$

The *Volume Scattering Function* (β) is defined by :

$$\beta(\psi, \lambda) \equiv \frac{\Delta I(\psi, \lambda)}{E_i(\lambda)\Delta V} \ \left(m^{-1} sr^{-1}\right) \tag{3.7}$$

where ΔV is an arbitrary volume, ΔI is the intensity and ψ is an scattering angle from the beam propagation direction. From the β, the Scattering coefficient (b) is defined by:

$$b(\lambda) \equiv 2\pi \int_0^{\pi} \beta(\psi, \lambda) \sin \psi d\psi \ \left(m^{-1}\right) \tag{3.8}$$

The scattering coefficient can be split in two fractions, *Foward Scattering Coefficient* (b_f) and the *Backward Scattering (Backscaterring) Coefficient* (b_b)

$$b_f(\lambda) \equiv 2\pi \int_0^{\frac{\pi}{2}} \beta(\psi, \lambda) \sin(\psi) d\psi \ \left(m^{-1}\right) \tag{3.9}$$

$$b_b(\lambda) \equiv 2\pi \int_{\frac{\pi}{2}}^{\pi} \beta(\psi, \lambda) \sin(\psi) d\psi \ \left(m^{-1}\right) \tag{3.10}$$

The *Scattering Phase Function* ($\widetilde{\beta}$) is defined as :

$$\widetilde{\beta}(\psi, \lambda) \equiv \frac{\beta(\psi, \lambda)}{b(\lambda)} \ \left(sr^{-1}\right) \tag{3.11}$$

From the attenuation and scattering coefficient definition, the *Absorption Coefficient* (a), is defined as :

$$a(\lambda) = c(\lambda) - b(\lambda) \tag{3.12}$$

Two derived IOPs worth mentioning are the *Single Scattering Albedo* $\left(\omega_0 = \frac{b(\lambda)}{c(\lambda)}\right)$, which is the percentage of Attenuation (c) that is attributed to Scattering (b) and the

backscattering to scattering ratio $\left(\frac{b_b(\lambda)}{b(\lambda)}\right)$, which states the backscattering probability in the aquatic medium. Both are dimensionless and closely related to properties of each component of the aquatic medium.

All the above defined optical properties depend on particle shape and inhomogeneity, composition, particle size distribution (PSD), and on the particle number concentration (N). Therefore, Attenuation, Absorption and Scattering coefficients can be calculated as:

$$Coef_x = \int_{D_{Min}}^{D_{Max}} \sigma_x(D) \cdot Q_x(D, m, \lambda) \cdot N(D, \xi_{psd}) dD \tag{3.13}$$

where σ_x is the particle geometrical cross-sectional area perpendicular to the light beam, Q_x is the efficiency factor for each coefficient ($Coef_x$ with x = c, a, b and also b_b) and $N(D, \xi_{psd})$ is the concentration number (see below) and D is the diameter of each particle (CLAVANO et al., 2007; KOSTADINOV et al., 2009). The product inside the integral directly depends on the particle's complex index of refraction ($m = n + i \cdot k$; where n is the real and k the imaginary part) relative to the medium in which the particle is immersed, the size of the particle with respect to the wavelength of the incident light and the shape of the particle.

The refraction index is related to the physical-chemical properties of the material and its real part is proportional to the ratio of the speed of light within a reference medium to that within the particle, whilst the imaginary part represents the absorption of light as it propagates through the particle (MOBLEY, 1994). In aquatic media, mineral particles generally show higher values for the real part of the refraction index as opposed to living organisms due to their lower water content. Regarding the imaginary parts, pigments and high absorbing organic particles present the highest values(TWARDOWSKI et al., 2001). Regarding particle shape, the number of phytoplankton groups (Taxonomic groups) is associated to a variety of shapes (KARP-BOSS et al., 2007) while for non-living particles, the variability of diverse crystalline structures (Clay, Sand or Silt) and the possibility of aggregation, increases the range of shape possibilities (SLADE et al., 2011; HILL et al., 2011). In relation to particle size, the group of particles that are relevant to optics in marine and freshwater range from sub-micron (colloids and viruses) to aggregates and zooplankton that can reach up to centimeters (CLAVANO et al., 2007). A way of defining the particle size distribution (PSD)as the number of particles within a given size class of width ΔD for a unit volume of suspension (m^{-3}) is:

$$N(D) = N'(D) \cdot \Delta D \tag{3.14}$$

where $N(D)$ is the number of particles per unit volume in the size interval $D \pm 0.5 \cdot \Delta D$. In this formulation, D represents the midpoint diameter of each size class. $N'(D)$ represents the differential distribution per unit size, also referred to as the density function of the PSD (REYNOLDS et al., 2010). The size distribution can sometimes be approximated by the *Junge* distribution (MOBLEY, 1994), although several other distributions have been already reported. The *Junge* distribution is given by:

$$N'(D) = k \cdot \left(\frac{D}{D_o}\right)^{-\xi_{psd}} \tag{3.15}$$

where D_o is a reference diameter, k is the differential number concentration at D_o, and ξ_{psd} is the slope of the distribution.

3.1.3 Apparent Optical Properties - AOP

According to Mobley (1994) the Apparent optical properties (AOPs) are those properties that depend both on the medium (the IOPs) and on the geometric (directional) structure of the ambient light field, and that display enough regular features and stability to be useful descriptors of the water body optical characteristics.

The main AOPs for Remote Sensing applications are the Diffuse Attenuation Coefficient ($K - functions$), the Irradiance Reflectance (R) and the Remote Sensing Reflectance (R_{rs}).

The Diffuse Attenuation Coefficients is defined as :

$$K_x \equiv -\frac{1}{RQ_x(z,\lambda)} \frac{dRQ_x(z,\lambda)}{dz} \tag{3.16}$$

where the K_x stands for any $K - functions$ (K_u, K_d, K_{lu}), z stands for the depth and the radiometric quantities (radiances and irradiances) decrease *approximately* exponentially with depth :

$$RQ_x(z,\lambda) \equiv RQ_x(0,\lambda) \exp\left[-\int_0^z K_x(z,\lambda)dz\right] \tag{3.17}$$

where $RQ_x(z, \lambda)$ stands for the upwelling (u) and downwelling (d) radiometric quantities (E_u, E_d, L_u, etc).

Irradiance Reflectance (R) and the Remote Sensing Reflectance (R_{rs}) are defined as:

$$R(z, \lambda) \equiv \frac{E_u(z, \lambda)}{E_d(z, \lambda)} \tag{3.18}$$

$$R_{rs}(z, \theta, \phi, \lambda) \equiv \frac{L(z, \theta, \phi, \lambda)}{E_d(z, \lambda)} \tag{3.19}$$

with $0 \leq \theta \leq \frac{\pi}{2}$ and $0 \leq \phi \leq 2\pi$ i.e. L_u. The $R(z, \lambda)$, $R_{rs}(z, \theta, \phi, \lambda)$ can be also be measured below $z = 0^-$ and above $z = 0^+$ the water surface.

3.1.4 Surface Effects

In order to relate measurements done at different position relative to the air-water interface, two main surface effects should be considered in this work, the *Sun/sky specular reflection* and the *air-water/water-air* interface effects. For the *air-water/water-air* effect, the approximations of Morel and Gentili (1996), also described in Mueller et al. (2003), were currently used. To derive $E_d(0^+, \lambda)$ from $E_d(0^-, \lambda)$ the following approach was used:

$$E_d(0^+, \lambda) = E_d(0^-, \lambda) \cdot \frac{1 - \bar{r} \cdot R(0^-, \lambda)}{1 - \bar{\rho}} \tag{3.20}$$

where $\bar{r}$ is the mean water-air Fresnel reflectance factor for the diffuse upward flux ($E_u(0^-, \lambda)$), and $\bar{\rho}$ is the bulk air-water Fresnel reflectance factor for the downward irradiance of sun and sky reflected on the surface.

Similarly, to derive $L_u(0^+, \lambda)$ from $L_u(0^-, \lambda)$ or $L_d(0^+, \lambda)$ from $L_d(0^-, \lambda)$ the following approaches were used:

$$L_u(0^+, \theta, \lambda) = L_u(0^-, \lambda) \cdot \frac{(1 - \rho(\theta, \theta_{SZA}))}{n_w^2} \tag{3.21}$$

$$L_d(0^+, \theta, \lambda) = \frac{L_d(0^-, \lambda)}{(1 - \rho(\theta, \theta_{SZA})) \cdot n_w^2} \tag{3.22}$$

where ρ is the Fresnel reflectance factor of the water for the upward radiance and n_w^2 is the water refractive index.

From equations 3.20 and 3.21 the $R_{rs}(0^+)$ is related to $R_{rs}(0^-)$ by:

$$R_{rs}(0^+) = \mathscr{R} \cdot R_{rs}(0^-) \tag{3.23}$$

where the $\mathscr{R}$ is equal to :

$$\mathscr{R} = \left(\frac{(1-\bar{\rho}) \cdot (1-\rho(\theta, \theta_{SZA}))}{(1-\bar{r} \cdot R(0^-, \lambda)) \cdot n_w^2} \right) \tag{3.24}$$

Following Morel and Gentili (1996), $(1-\bar{\rho})$ is equal to 0.957; $(1-\bar{r} \cdot R(0^-, \lambda))$ is equal to 0.985 where $\bar{r} \approx 0.48$ and $R(0^-, \lambda) \approx 0.03$. The index of refraction of the water is assumed 1.33 and therefore $n_w^{-2} = 0.556$. (1-$\rho(\theta, \theta_{SZA})$ varies from 0.979 to 0.939 depending on the viewing angle and the SZA ($0° \leq \theta \leq 60°; \theta_{SZA} = 60°$). Therefore, for a nadir view, a $\mathscr{R} \approx 0.529$ is currently assumed.

For the *Sun/sky specular reflection*, following Mobley (1999) and Mobley (2015) the total radiance signal that leaves the water body is defined as:

$$L_T(\theta, \phi, \lambda) = L_r + L_u(0^+, \theta, \phi, \lambda) \tag{3.25}$$

where L_r is the surface-reflected part of the incident sun/sky radiance. To minimize the effects of L_r, simulations by Mobley (1999) and Mobley (2015) shows that the geometry of acquisition of $\theta \approx 40°$ and $\phi \approx 137°$ from the Sun will minimize the effects of Sun glint and nonuniform sky radiance while avoiding instrument shading. For the remaining sky radiance Mobley (1999) suggests the measurement of L_{sky}, which is the radiance measured by a detector pointed to the sky, at the same plane (same ϕ) but rotated 90° from $L_T(\theta, \phi, \lambda)$. That would result in:

$$L_r(\lambda) = \rho_{sky} \cdot L_{Sky}(\lambda) \tag{3.26}$$

ρ_{sky} is the proportionality factor which depends on the several factors θ, ϕ, θ_{SZA}, Ω_0, wind speed, sky radiance distribution). From simulations from Mobley (1999), for the viewing direction described above ($\theta \approx 40°$ and $\phi \approx 137°$), a value of $\rho_{sky} \approx 0.028$

is acceptable for wind speeds smaller than 5 ms^{-1}. However ρ_{sky} also depends on polarization (MOBLEY, 2015) with improved table values available for each viewing directions.

3.2 Optically Active Constituents - OACs

3.2.1 Pure Water

Absorption by pure water (a_w) is weak in the blue/green spectral region, preceded by a very high absorption in the untraviolet (UV below 400 nm) and followed by a high absorption in the red/NIR region (POPE; FRY, 1997). The measurement of pure water absorption is difficult due to the limits posed by purifying techniques in the set up for measuring the absorption. Pure water absorption has been currently measured in different wavelength intervals: (200 to 400 nm) (QUICKENDEN; IRVIN, 1980); 366 nm, (BOIVIN et al., 1986); 730 to 800 nm, (SMITH; BAKER, 1981) with the 380 to 700 nm interval (POPE; FRY, 1997), being the most important for Inland Remote Sensing studies. Pure water absorption also varies in shape and magnitude with temperature, especially in the red and Near-InfraRed (NIR). Also, the addition ions affect the fundamental and harmonics from water molecular vibrations (PEGAU et al., 1997; SULLIVAN et al., 2006).

Pure water scattering properties (b_w) follow the Einstein-Smoluchowski theory, which states a scattering behavior similar to the Rayleigh Scattering for an ideal gas (MOBLEY, 1994). The pure water volume scattering function (VSF) is symmetric in 90° resulting in equivalent forward and back scattering ($b_{f_w} = b_{b_w}$). Table values are generally used to parametrize bio-optical models. It is also important to state that, different from oceanic waters which are strongly affected by dissolved salts, inland waters are less affected and its behavior is closer to that of laboratory measurements

3.2.2 Colored Dissolved Organic Matter - CDOM

The Colored Dissolved Organic Matter (CDOM), composed by humic substances, has a polymeric shape with long chains of aromatic rings that vary from soluble molecules with low molecular weight to insoluble macro-molecules with high molecular weight (KIRK, 2010). Different from open ocean waters, where most of the CDOM comes from degradation and respiration processes of marine organisms, at inland waters, CDOM comes mainly from soil leaching processes, mainly from vegetation decomposition. Leaching process drags surface soil content to the lotic and lentic systems (rivers and lakes) which leads to a mixture of organic matter decom-

position stages increasing the complexity of the environment (JUNK et al., 2011).

The CDOM IOP that mostly affects the optical response of natural water bodies is its absorption coefficient (a_{CDOM}) (KIRK, 2010). The key characteristic of a_{CDOM} is its high absorption in the "blue" wavelengths, which decreases exponentially towards large wavelengths according Equation 3.27.

$$a_{cdom} = a_{cdom}(\lambda_0)e^{(-S_{cdom}(\lambda-\lambda_0))} \tag{3.27}$$

where S_{CDOM} is the exponential wavelength constant and λ_0 is a reference wavelength. The shape of the absorption model can be explained by the superposition of the different π bonds of the long CDOM molecules chains. The simple bonds, which are more frequent in humic compounds, absorb in the shorter wavelengths whereas the less frequent π bonds absorb in longer wavelengths(KIRK, 2010). In the visible part of the spectrum, the S_{cdom} are typically between $0,007$ to $0,026$.

Elastic CDOM scattering in natural waters is still not well understood. Routinely, one assumes that CDOM does not scatter ($b_{cdom} = 0$) (DALL'OLMO; WESTBERRY, 2009). Some authors suggest CDOM scattering in the visible (400 to 750 nm) for ocean waters (STRAMSKI; WOZNIAK, 2005), which would suggest CDOM scattering in inland waters. However, no study provides empirical evidences until the present moment. An Inelastic scattering (or CDOM Fluorescence) has otherwise an excitation peak in the near-UV (355 or 370 nm), with an emission broad peak in the blue region (COBLE, 2007; KIRK, 2010).

3.2.3 The Particulate Material

The particulate material or the Total Suspended Matter (TSM) can be defined as the material retained in a pore-sized filter, which can vary between 1.2 or 0.7 μm of nominal size (Mueller et al 2003). Besides Absorption (a_p) and Scattering properties (b_p or b_{b_p}) TSM can be divided in its Organic and Inorganic counterparts but for IOPs purposes, the particulate material is divided into the Photosynthetically Active Biota (particles containing no soluble pigments) and the Non-Algal Particles.

3.2.3.1 Photosynthetically Active Biota Phytoplankton/Chlorophyll-a

The Photosynthetically Active Biota from rivers and lakes is mainly composed by Phytoplankton which are primary producers and is the base of the food chain of aquatic environments. Phytoplankton is a diverse group, including more than 10

thousands species with a size varying from 0.2 a 1000 μm, in a large diversity of shapes and physiological processes that directly influences its optical response (KIRK, 2010).

The main optical component is the Chlorophyll-a (Chla), although several other pigments influence the optical response, as Chlorophyll-b and c, carotenoids and biliproteins whose occurrence depends on the group that the each organism is part of. The absorption of Chla has a characteristic shape with two peaks, the first at $\approx$ 440 nm and the second at $\approx$ 676 nm. The absorption peak, however, is impacted by both: (1) other pigments that make the absorption band broader, but especially (2) the "packaging effect", which constrains absorption by Chla, making it not linear with Chla concentration ($[Chla]$) (BRICAUD; STRAMSKI, 1990; BRICAUD et al., 1995; CIOTTI et al., 2002; BABIN et al., 2003).

Although Phytoplankton absorption (a_ϕ) is not defined just by Chla absorption (a_{Chla}), the Specific Phytoplankton Absorption (a^*_ϕ) is defined as the ratio $a^*_\phi = \frac{a_\phi}{[Chla]}$ (BRICAUD et al., 1995) which describes the effective area per milligram of Chla that absorbs light. Several efforts have been made to devise global a^*_ϕ models, which could be used particularly for estimating Chla from remote sensing data. However, the development of a^*_ϕ models is affected by the variability in phytoplankton groups, photoadaptation strategies (LOISEL et al., 2010) and phytoplankton physiological state (MOREL; BRICAUD, 1981). Therefore, measuring a^*_ϕ is still necessary, for reliable Remote Sensing estimates (CIOTTI; BRICAUD, 2006; GIARDINO et al., 2007; WERDELL et al., 2013).

Regarding scattering and backscattering properties, the understanding of phytoplankton scattering characteristics remains limited mainly due to the technical constraints of both laboratory and *in situ* measurements. Historically, scattering properties of phytoplankton cells were investigated using theoretical models due to the lack of instrumentation required to measure scattering. Most of those models used Mie theory based on a spherical shape and internal homogeneity, which led to underestimation of the scattering and backscattering coefficients (STRAMSKI et al., 2001). The majority of those studies concluded that phytoplankton scattering and backscattering coefficients are weak compared to other nonliving organic and inorganic particles.

The backscattering is directly related to phytoplankton size, shape, morphology and Chla content although Chla concentration is not a universal predictor of the magnitude of backscattering (BRICAUD; MOREL, 1986; VOLTEN et al., 1998; WHIT-

MIRE et al., 2010). The relationship between b_{bp} and Chla has been shown to be linear for Case 1 waters, although $\frac{b_{b_p}}{[Chla]}$ can exhibit high variability (DALL'OLMO; WESTBERRY, 2009). Whitmire et al. (2010) shows differences in the backscattering properties of cultures, and relate them to differences in cellular structure and composition. Results showed that phytoplankton cell size does not affect the spectral shape of b_{bp} but it is related to both, the backscattering to scattering ratio ($^{b_b}/_{b}$) and backscattering coefficient cross-section.

3.2.3.2 Non-Algal Particles - NAP

Non-Algal Particles (NAP) include mainly non-living organic and inorganic particles. NAP generally derives from dead Phytoplankton cells but also from vegetation byproducts, rock weathering in the catchment or wind resuspension (in shallow waters) which are processes that include organic and inorganic particles in NAP (KIRK, 2010). Human activities which include agricultural and industrial practices also contribute to NAP .

Absorption and Scattering properties from NAP depend on two main properties: the composition and particle size/shape (STRAMSKI et al., 2007). From the ratio of Organic/Inorganic particles and Iron content which control NAP refractive index to the range of PSDs, all that, directly affect NAP IOPs. NAP absorption is estimated by an exponential model (equation 3.28) (BOWERS; BINDING, 2006):

$$a_{nap} = a_{nap}(\lambda_0)e^{(-S_{nap}(\lambda-\lambda_0))} \tag{3.28}$$

where a_{nap} is the specific absorption by NAP and S_{nap} is the exponent for absorption model for $300 < \lambda < 900$ and λ_0 is a reference wavelength.

Stramski et al. (2007) however, highlighted that the model fails to describe both, the shoulders and the slope in the NAP absorption spectra. Therefore equation 3.28 might be inadequate to describe the specific absorption (a^*_{nap}) of mineral particles. In that sense, Iron content is a key factor, because its presence within the mineral structure can increase absorption (BABIN et al., 2003; ESTAPA et al., 2012). However it is important to remember that the internal structure of mineral particles is complex regarding the location and distribution of iron. Iron occurrence in NAP assumes different configuration such as surface coating, elements within mineral structure or even as crystal oxides (STRAMSKI et al., 2007). Each of these configurations impact NAP absorption in different ways.

NAP scattering properties are, however, the main properties when dealing with Remote Sensing Measurements. Similar to particulate absorption, particulate scattering is influenced by particle composition and PSD (as already presented in section 3.1.2). The currently applied model for scattering and and backscattering (and therefore for specific b and b_b) is presented in equation 3.29:

$$x = x(\lambda_0) \cdot \left(\frac{\lambda_{ref}}{\lambda}\right)^{\gamma_x} \tag{3.29}$$

where (x = b or $\mathrm{b_b}$ for both, coefficient and specific coefficient); λ is the wavelength and λ_0 is a the reference wavelengths. The power law exponents (γ_b and γ_{b_b}) were found to correlate with median particle size (SLADE; BOSS, 2015), and by association with the spectral slope of particulate beam attenuation,(e.g. (BOSS et al., 2013) (SLADE; BOSS, 2015)). The smaller the γ_b and γ_{b_b}, the larger the mean particle size.

The specific scattering and backscattering is directly influenced by organic an inorganic contents as already shown in section 3.1.2, by the particle efficiency factor . Babin et al. (2003) shows that high $b^*(555)$ values in case 1 waters are mainly due to the low apparent density, which results from the organic nature of particles and their elevated water content. However Wozniak et al. (2010) and Stavn and Richter (2008) shows cases in which organic dominated waters presents lower values of b^* than mineral dominated waters, showing that the organic influence is still under investigation.

3.2.3.3 Total and Specific IOPs

As a consequence of the separate parts of each component, the Total Absorption coefficient ($a_T(\lambda)$) and the Total Scattering/Backscattering Coefficients ($b_T(\lambda)$) and $b_{b_T}(\lambda)$) are:

$$a_T(\lambda) = a_w(\lambda) + \sum_{i=1}^{N_\phi} A_{\phi_i} \cdot a^*_\phi + \sum_{i=1}^{N_{nap}} A_{nap_i} \cdot a^*_{nap_i} + \sum_{i=1}^{N_{cdom}} A_{cdom_i} \cdot a^*_{cdom} \tag{3.30}$$

$$b_T(\lambda) = b_w(\lambda) + \sum_{i=1}^{N_p} B_{p_i} \cdot b^*_{p_i} \tag{3.31}$$

$$b_{bT}(\lambda) = b_{bw}(\lambda) + \sum_{i=1}^{N_{bp}} B_{bp_i} \cdot b^*_{bp_i} \tag{3.32}$$

where A and B are the concentration or amplitude of each component and a^*s and $b^*_b s$ are their specific absorption and backscattering coefficients. The product $a = A \cdot a^*s$ and $b_b = B \cdot b^*_b s$ for each component gives the absorption and scattering/backscattering coefficients.

The difficulty in separating NAP and CDOM, mostly due to the similarity of its absorption spectral shape (S_{cdom} and S_{nap}), leads to the the combination of both components, and therefore equation 3.30 becomes:

$$a_T(\lambda) = a_w(\lambda) + \sum_{i=1}^{N_\phi} A_{\phi_i} \cdot a^*_\phi + \sum_{i=1}^{N_{nap/cdom}} A_{nap/cdom_i} \cdot a^*_{nap/cdom_i} \tag{3.33}$$

In that case, the same exponential model of equations 3.27 plus 3.28 is used:

$$a_{nap+cdom} = a_{nap+cdom}(\lambda_0) e^{\left(-S_{nap+cdom}(\lambda-\lambda_0)\right)} \tag{3.34}$$

3.3 Radiative Transfer in Waters Bodies

The Radiative Transfer Equation (RTE), which is a complete *Foward Model*, governs the behavior of radiance within natural water bodies linking IOPs to Radiance Distributions (MOBLEY, 1994). The solution of the RTE is a complex mathematical problem, with no explicit analytical solutions. RTE solutions are generally solved by mathematical/numerical techniques (Monte Carlo, Invariant Imbedding *(Hydrolight)*, Neural Network)(OOWB, 2015), or simplified analytical approximations (Gershun's law (MOBLEY, 1994)). However, the most popular simplifications for Remote Sensing techniques are the ones based on the Single and Quasi-single Scattering Approximations (OOWB, 2015), which lead to a variety of approximations to the forward models which are currently used for Remote Sensing Inverse Models. Four of those models will be briefly discussed.

3.3.1 Forward Model Approximations

Primarily studied by Gordon and Brown (1973) , the model shown in equation 3.35 has since been improved. Equation 3.36 shows a variation of equation 3.35 proposed

by Gordon et al. (1975) and Morel and Prieur (1977) for open ocean waters. Those models are widely used in Remote Sensing studies.

$$R_{rs}(\lambda, 0^-) = \frac{f'}{Q} \cdot \left(\frac{b_b(\lambda)}{a(\lambda) + b_b(\lambda)} \right) \tag{3.35}$$

$$R_{rs}(\lambda, 0^-) = \frac{f}{Q} \left(\frac{b_b(\lambda)}{a(\lambda)} \right); \tag{3.36}$$

where f factor is defined as $R(0^-) = f \cdot \frac{b_b(\lambda)}{a}$ and f' factor by $R(0^-) = f' \cdot \frac{b_b(\lambda)}{a+b_b(\lambda)}$. Q is the proportionality factor which relates $L_u(0^-, \lambda)$ and $E_u(0^-, \lambda)$ according to equation: $E_u(0^-, \lambda) = Q \cdot L_u(0^-, \lambda)$. Several studies have focused on the variability of those factors but Morel and Gentili (1996) and Morel et al. (2002), particularly, reported for ocean waters f ranges from 0.3 to 0.5 and Q from 3 to 6. For turbid coastal waters, Loisel and Morel (2001) reported values very different from Open Ocean Case I waters ($\frac{f'}{Q} = 0.13$).

Another widely used model is the second order polynomial, developed by Gordon et al. (1988) (equation 3.37):

$$R_{rs}(\lambda, 0^-) = g_0 \cdot \left(\frac{b_b(\lambda)}{a(\lambda) + b_b(\lambda)} \right) + g_1 \cdot \left(\frac{b_b(\lambda)}{a(\lambda) + b_b(\lambda)} \right)^2 \tag{3.37}$$

the g_0 and g_1 are proportionality factors, which vary with viewing angle, SZA and water bodies IOPs. Currently used values are around $g_0 \approx 0.09$ and $g_1 \approx 0.10$ ((GORDON et al., 1988; MOREL; GENTILI, 1993; LEE et al., 1999; LEE et al., 2002; LEE et al., 2010; LEE et al., 2011).

A slightly more complex model proposed by Park and Ruddick (2005), focus both on Case I and turbid mineral rich Case II waters and includes bidirectional effects. The inclusion of the third and fourth order polynomial terms would account for multiple-scattering effects as well as the variation of particle scattering phase functions in different turbid media.

$$R_{rs}(\lambda, 0^-) = \left[g_0^* \cdot \left(\frac{b_b}{a + b_b} \right) + g_1^* \cdot \left(\frac{b_b}{a + b_b} \right)^2 + g_2^* \cdot \left(\frac{b_b}{a + b_b} \right)^3 + g_3^* \cdot \left(\frac{b_b}{a + b_b} \right)^4 \right] \tag{3.38}$$

The four coefficients, which were tested by Hydrolight simulations and experimental cases are available for a variety of IOPs, SZA and viewing directions (PARK; RUDDICK, 2005; RUDDICK et al., 2006; NECHAD et al., 2010).

3.3.2 Inverse Models

In Hydrological Optics, an *inverse problem* initiates with the use of Radiometric Measurements as inputs to retrieve first IOPs and then the respective OAC concentrations (MOBLEY, 1994). Although inverse problems have conceptual and practical limits (Existence, Uniqueness and Stability of solutions), they have been extensively used in remote sensing applications (GORDON, 2002; IOCCG, 2006; ODERMATT et al., 2012; MOUW et al., 2015). According to Gordon (2002), the variety of algorithms could be divided on those based on *explicit solutions*, where IOPs are an *explicit* function of AOPs (which are mostly based on Foward Models from section 3.3.1) and those based on *implicit solutions*, where the solution is based on recurrent solutions of Foward Models. Explicit solutions include the so called *Semi-Analytic Algorithms* (SAAs) which are not only based on Foward Models from section 3.3.1 but also on empirical assumptions to estimate IOPs.

According to Werdell et al. (2013), SAAs fall into three classes, named as **spectral optimization**, **spectral deconvolution**, and **bulk inversion**. SAAs included in the **spectral optimization** class (SOC) uses predefined specific IOPs and, solutions, are obtained via linear (matrix) or nonlinear (least squares) optimization (ROESLER; PERRY, 1995; HOGE; LYON, 1996; MARITORENA et al., 2002; WANG et al., 2005). The **spectral deconvolution** (SDC) operates in a step-wise fashion to determine the spectral backscattering and absorption coefficients (LEE et al., 2002; SMYTH et al., 2006). In the **bulk inversion class** (BIC) there is no predefined spectral shapes for the absorption or scattering coefficients (LOISEL; STRAMSKI, 2000).

For the *implicit approach*, Neural Networks (NN) have been used extensively and specially for the MERIS algorithms (MERIS Neural Network Algorithm (DOERFFER; SCHILLER, 2007)). Although most of the Neural Network was performed using synthetic data (derived Hydrolight (HYDROLIGHT TECHDOC, 2013) simulations). It is important to point out that there has been an effort to include insitu data on

NN training as a result of the effort to implement global databases for improving Remote Sensing methods (SeaBass).

In this research three Semi-Analytical Algorithms named, Quasi-Analytical Algorithm (QAA) (LEE et al., 2002), *Nechad Algorithm* (NECHAD et al., 2010), and the Generalized ocean color inversion model (GIOP) (WERDELL et al., 2013) (named here after QAA, GIOP and Nechad) were tested. These three algorithms have been widely used for both ocean and inland waters (MOUW et al., 2015) and were chosen because: (1) GIOP and Nechad are *spectral optimization* algorithms which allows the input of both, measured and modeled IOPs in which the measured dataset could be used and tested; (2) QAA, which is a *spectral deconvolution* algorithm, has been developed for Case 1 and 2 waters with versions that could be suitable for turbid environments. Details of each algorithm are discussed on the following.

3.3.2.1 Quasi-Analitical Model (QAA)

The Quasi-Analytical Algorithm (QAA), proposed by (LEE et al., 2002; LEE et al., 2007), aims the retrieval of, first, the total absorption and backscattering coefficients and, second, phytoplankton and CDM (CDOM + NAP) absorption. The algorithm follows a step-by-step structure. The 5th version of QAA, which is applicable for both Case 1 and Case 2 waters, displays the following structure:

a) a_T for $\lambda_0 = 550$, 555 and 560 is derived using an empirical model adjusted with synthetic simulated data (IOCCG, 2006). :

$$a_T(\lambda_0) = a_w(\lambda_0) + 10^{(-1.146-1.366\cdot\chi-0.469\cdot(\chi^2))} \tag{3.39}$$

where:

$$\chi = \log\left(\frac{R_{rs}(0-,443) - R_{rs}(0-,490)}{R_{rs}(0-,\lambda_0) + 5\cdot\frac{R_{rs}(0-,667)}{R_{rs}(0-,490)}\cdot R_{rs}(0-,667)}\right) \tag{3.40}$$

b) To obtain $R_{rs}(0^-\lambda)$ QAA uses:

$$R_{rs}(0^-,\lambda) = \frac{R_{rs}(0^+,\lambda)}{0.52 + 1.7\cdot R_{rs}(0^+,\lambda)} \tag{3.41}$$

which is slightly different from equation 3.23 and 3.24. Subsurface remote-sensing reflectances are related to IOPs by the second order polynomial described in equation 3.37, and coefficients $g_0 = 0.089$ and $g_1 = 0.125$:

$$u'(\lambda) \equiv \frac{b_b(\lambda)}{a(\lambda) + b_b(\lambda)} \equiv \frac{-0.0895 + \sqrt{0.08 + 0.499 R_{sr}(0^-, \lambda)}}{0.249} \tag{3.42}$$

c) Total Backscattering $b_{bT}(\lambda)$ is given by:

$$b_{b_T}(\lambda) = b_{bw}(\lambda) + b_{bp}(\lambda_0)\left(\frac{\lambda_0}{\lambda}\right)^Y \tag{3.43}$$

where $b_{bp}(\lambda_0) = \left(\frac{u'(\lambda_0) \cdot a(\lambda_0)}{1 - u'(\lambda_0)} - b_{bw}(\lambda_0)\right)$ and $b_{bw}(\lambda)$ is taken from (POPE; FRY, 1997). The exponent Y is computed by:

$$Y = 2.0 \cdot \left\{1 - 1.2 \cdot \exp\left[-0.9\left(\frac{R_{sr}(0^-, 443)}{R_{sr}(0^-, \lambda_0)}\right)\right]\right\} \tag{3.44}$$

d) Once all above values are calculated, $a_T(\lambda)$ is calculated by:

$$a_T(\lambda) = \frac{(1 - u'(\lambda))b_b(\lambda)}{u'(\lambda)} \tag{3.45}$$

The second part of QAA algorithm aims to obtain $a_\phi(\lambda)$ and $a_{nap+cdom}(\lambda)$. For that, a system of semi-analytical equations is used:

$$a_{nap+cdom}(\lambda) = \frac{[a_T(411) - \zeta_{QAA} \cdot a_T(443)]}{\xi_{QAA} - \zeta_{QAA}} - \frac{[a_w(411) - \zeta_{QAA} \cdot a_w(443)]}{\xi_{QAA} - \zeta_{QAA}} \tag{3.46}$$

where:

$$\zeta_{QAA} = \frac{a_\phi(411)}{a_\phi(443)} = 0.74 + \frac{0.2}{\frac{0.8 + R_{rs}(0^-, 443)}{R_{rs}(0^-, \lambda_0)}} \tag{3.47}$$

and

$$\xi_{QAA} = \frac{a_\phi(411)}{a_\phi(443)} = e^{S \cdot (\lambda - 443)} \tag{3.48}$$

where:

$$S = 0.015 + \frac{0.002}{0.6 + \frac{R_{rs}(0^-,443)}{R_{rs}(0^-,\lambda_0)}} \tag{3.49}$$

Finally $a_\phi(\lambda)$ is calculated by:

$$a_\phi(443) = a_T(\lambda) - a_{nap+cdom}(\lambda) - a_w(\lambda) \tag{3.50}$$

The applicability of QAA for turbid and high productive waters is controversial for very high Chla and TSM. To overcome this limitation, Lee et al. (2002) suggests the shift of λ_0 to 640 nm when $a_T(440) > 0.3$. Other studies suggest shifting λ_0 to 708 nm (DORON et al., 2007; LE et al., 2009b) and particularly Mishra et al. (2014) proposes a parametrization of equation 3.40 for χ and $a_T(708)$ that would account for turbid lake IOP characteristics.

Mishra et al. (2014) also proposed an alternative method for estimating $a_{nap+cdom}(\lambda)$ based on empirical modeling: $a_{nap+cdom}(\lambda)$ with λ = 381, 443, and 510 nm and $S_{nap+cdom}$ are empirically modeled against $\frac{R_{rs}(0^-,490)}{R_{rs}(0^-,510)}$. This method, however, is only applicable when $\frac{R_{rs}(0^-,490)}{R_{rs}(0^-,510)} < 0.54$ and $\frac{R_{rs}(0^-,413)}{R_{rs}(0^-,443)} > 0.89$.

3.3.2.2 The Nechad Algorithm

The Nechad Algorithm (NECHAD et al., 2010) was developed for TSM concentration retrieval. The method shows that a single band provides a robust and TSM-sensitive algorithm, if a suitable selection of band is made. The algorithm assumes the model described in equation 3.36 and divide backscattering and absorption into two parts: backscattering and absorption from particles (both non-algal and algal) and all other non-particle optically-active substances (equation 3.51):

$$u = \frac{b_{bp} + b_{bnp}}{a_p + a_{np}} \tag{3.51}$$

where $u = \frac{b_b(\lambda)}{a}$ and the subscripts p and np denote the particle and non-particle contributions. To develop the algorithm, some assumptions and approximations regarding IOPs are made in order to relate [TSM] and u. Those assumptions are:

a) Particulate backscattering is proportional to TSM concentration via the constant TSM-specific particulate backscattering coefficient, b^*_{bp}:

$$b_{bp} = b^*_{bp} \cdot [TSM] \tag{3.52}$$

b) Space and time variability of non-particulate absorption, a_{np} are to be negligible.

c) Particulate absorption is proportional to TSM concentration via the constant TSM-specific particulate absorption coefficient, a^*_p:

$$a_p = a^*_p \cdot [TSM] \tag{3.53}$$

d) Non-particulate backscattering is negligible, $b_{bnp} = 0$.

From those four assumptions equation 3.51 can be rewritten as:

$$[TSM] = A \cdot \frac{u}{1 - \frac{u}{C}} (g \cdot m^{-3}) \tag{3.54}$$

where the calibration coefficients A and C are given by:

$$A = \frac{a_{np}}{b^*_{bp}} \tag{3.55}$$

$$C = \frac{b^*_{bp}}{a^*_p} \tag{3.56}$$

Assuming: the First Order Gordon model (equation 3.35), the ***"water-leaving reflectance"*** as $\rho_w = \cdot\mathscr{R} \cdot R_{rs}(0^-)$ (from equation 3.23), $\frac{f}{Q} = 0.13$ for sediment-dominated waters (LOISEL; MOREL, 2001) and $\mathcal{R} = 0{,}529$, ρ_w can be estimated as follows:

$$\rho_w = \gamma \cdot \left(\frac{u}{1 + u} \right) \tag{3.57}$$

where $\gamma = \frac{\pi \mathcal{R} f'}{Q}$ which is ≈ 0.216. When combining equations and it leads to:

$$[TSM] = A^\rho \cdot \frac{\rho_w}{1 - \frac{\rho_w}{C^\rho}} \tag{3.58}$$

where A^ρ and C^ρ are:

$$A^\rho = \frac{A}{\gamma} \tag{3.59}$$

$$C^\rho = \frac{\gamma \cdot C}{(1 + C)} \tag{3.60}$$

3.3.2.3 The Generalized ocean color inversion model - GIOP

The GIOP is part of an effort from NASA towards consensus on a unified Semi-Analytical Algorithm (SAA) that would encompass similarities and uniqueness from the numerous existing SAA. GIOP allows the construction of a set of SAAs, from a collection of options for model parametrization. GIOP also permits isolation and evaluation of specific modeling assumptions, construction of SAAs, development of regionally tuned SAAs, and execution of ensemble inversion modeling (WERDELL et al., 2013).

Some assumptions are made to create a general SAA. To achieve $R_{rs}(0^-\lambda)$ GIOP uses Lee et al. (2002):

$$R_{rs}(0^-\lambda) = \frac{R_{rs}(0^+\lambda)}{0.52 + 1.7 \cdot R_{rs}(0^+\lambda)} \tag{3.61}$$

which is slightly different from equation 3.23 and 3.24. Subsurface remote-sensing reflectances are relate to IOPs by the the second order polynomial described in equation 3.37, and coefficients g_0 and g_1 are user-provided.

GIOP uses absorption and backscattering coefficients as described in equations 3.30 and 3.31 which leads to:

$$u'(\lambda) = \frac{b_{bw}(\lambda) + B_{bp_i} b^*_{bp_i}}{b_{bw}(\lambda) + B_{bp_i} b^*_{bp_i} + a_w(\lambda) + A_{\phi_i} a^*_\phi + a^*_{NAP} + A_{CDOM_i} a^*_{CDOM}} \tag{3.62}$$

The strength of GIOP is the possibility of model parametrization. Table 3.1 shows the set of possibilities that are offered by GIOP (adapted from Werdell et al. (2013)).

Table 3.1 - Summary of Specific Coefficients and Derived Parameters Available for Use in GIOP - Table adapted from Werdell et al. (2013)

Eigenvector	Description
a^*_ϕ	User-provided a^*_ϕ Maritorena et al. (2002) tabulated a^*_ϕ **Bricaud et al. (1998)-derived a^*_ϕ using OC-derived C_a** Ciotti and Bricaud (2006)-derived $a^*\phi$ using user-provided size fraction
a^*_{dg}	**Equation (3.34) with user-provided S_{dg}** Equation (3.34) with Lee et al. (2002)-derived S_{dg} Equation (3.34) with Franz and Werdell (2010)-derived S_{dg} User-provided a^*_{dg}
b^*_{bp}	Equation (3.29) with user-provided S_{dg} Equation (3.29) with Hoge and Lyon (1996)-derived S_{dg} **Equation (3.29) with Lee et al. (2002)-derived S_{dg}** Equation (3.29) with Ciotti et al. (1999)-derived S_{dg} Equation (3.29) with Morel and Maritorena (2001)-derived S_{dg} Equation (3.29) with Loisel and Stramski (2000)-derived S_{dg} User-provided b^*_{bp} Loisel and Stramski (2000)-derived b^*_{bp} Lee et al. (2002)-derived b^*_{bp}

Boldface indicates the parameters used in Werdell et al. (2013) testing (GIOP-DC).

In GIOP two inversion methods are used: the optimization method (previously used by Roesler and Perry (1995)) and a linearized matrix inversion (from Hoge and Lyon (1996)). The optimization techniques are generally based on the minimization of a merit function as follows:

$$\Xi^2 = \sum_{i=1}^{N_\lambda} \frac{(\hat{R}_{rs}(0^-, \lambda_i) - R_{rs}(0^-, \lambda_i))^2}{\sigma^2(\lambda_i)} \tag{3.63}$$

where Ξ^2 is the merit function and $\sigma(\lambda_i)$ is the input uncertainties and $\hat{R}_{rs}$ is an estimated Remote Sensing Reflectance. If values of $\sigma(\lambda_i)$ are not available, they are set to 1.0 and the optimization is unweighted. According to Werdell et al. (2013), in GIOP, the LM method was used but several other optimization techniques can be used.

For the Linear Matrix Inversion (LMI) method, the linearization proposed by Hoge and Lyon (1996) starts with equation 3.64:

$$a_\phi(\lambda) + a_{nap+cdom}(\lambda) + b_{bp_i}(\lambda) \cdot \nu = a_w(\lambda) + b_{bw}(\lambda) \cdot \nu \tag{3.64}$$

where $\nu = 1 - \frac{1}{u'} or \frac{a}{b_b}$. For an exact solution, three different wavelengths are used to form a system of three equations with three unknowns. After spectrally modeling the three IOP variables with values at a reference wavelength ($\lambda_r = 410$ nm) the equation becomes (equation 3.65):

$$a^*_\phi(\lambda) \cdot a_\phi(\lambda) + a^*_{nap+cdom}(\lambda) \cdot a_{nap+cdom}(\lambda) + b^*_{bp_i}(\lambda) \cdot b_{bp_i}(\lambda) \cdot \nu = a_w(\lambda) + b_{bw}(\lambda) \cdot \nu \tag{3.65}$$

Equation 3.65 can now be used to construct the linear matrix that could be inverted to derive the IOPs consistent with the input R_{rs} and the spectral models.

$$\begin{bmatrix} 1 & 1 & \nu(\lambda_r) \\ a^*_\phi(\lambda_2) & a^*_{nap+cdom}(\lambda_2) & b^*_{bp_i}(\lambda_2)\nu(\lambda_2) \\ a^*_\phi(\lambda_3) & a^*_{nap+cdom}(\lambda_3) & b^*_{bp_i}(\lambda_3)\nu(\lambda_3) \end{bmatrix} \cdot \begin{bmatrix} a_\phi(\lambda_r) \\ a_{nap+cdom}(\lambda_r) \\ b_{bp_i}(\lambda_r) \end{bmatrix} = - \begin{bmatrix} a_w(\lambda_r) + b_{bw}(\lambda_r)\nu(\lambda_r) \\ a_w(\lambda_2) + b_{bw}(\lambda_2)\nu(\lambda_2) \\ a_w(\lambda_3) + b_{bw}(\lambda_3)\nu(\lambda_2) \end{bmatrix} \tag{3.66}$$

As mention by Hoge and Lyon (1996), any standard method of solving this system of equations can be used. The Hoge/Lyon inversion algorithm uses lower/upper deconvolution Hoge and Lyon (1996), but other methods uses QR decomposition or an overconstrained solution (WANG et al., 2005).

4 MATERIAL AND METHODS

This chapter presents a brief description of the study area followed by the explanation of *insitu* sampling procedures, equipment characteristics and methods for data processing. Details for closure analysis and uncertainties assessment as well as semi-analytic model parametrization are also discussed.

4.1 Study Area

Lago Grande de Curuai (LGC) floodplain is located on the southern margin of the Amazon River, near Obidos city (Brazil), 900 km upstream from the Atlantic Ocean (Figure 4.1). It is a complex system of about 30 shallow interconnected lakes with spatially and temporally variable hydraulic connectivity among them and with the Amazon River. As described by Barbosa et al. (2009) the effect of the seasonal flood pulse coupled with landforms, leads to complex water flow and mixing patterns within the Curuai floodplain. Figure 4.2 displays a schematic representation of the flooding dynamics of Curuai Floodplain from July-2012 to May-2014.

Figure 4.1 - Study Area - Curuai Floodplain Lake

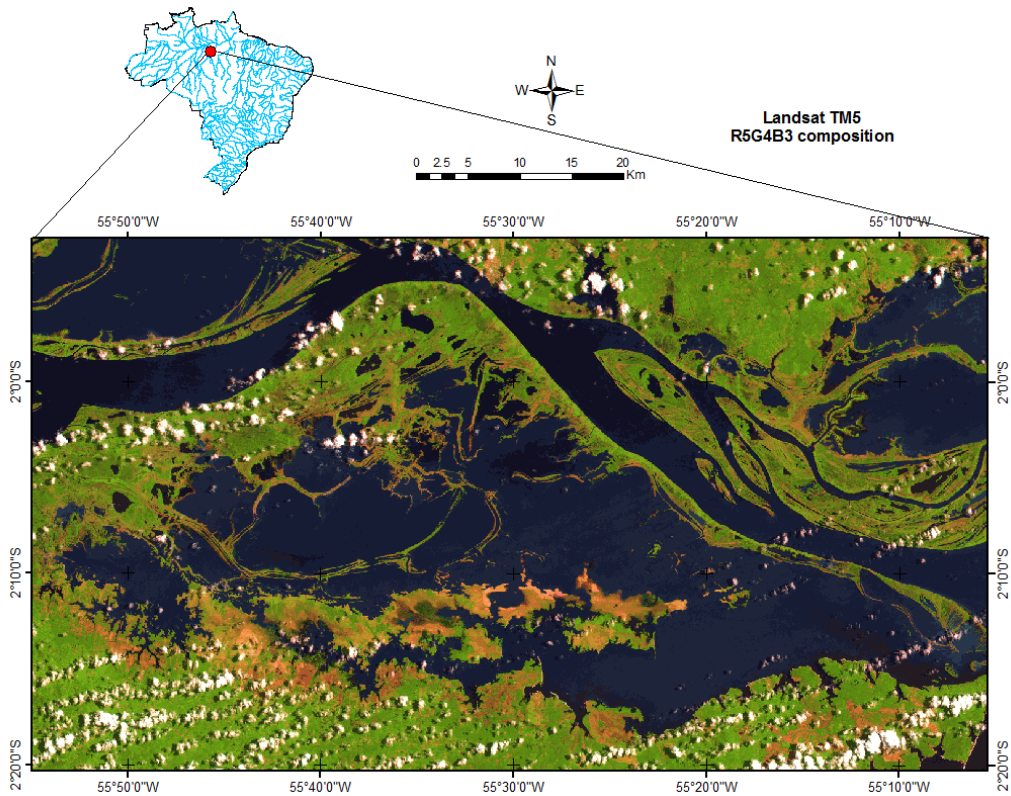

In the rising water period there is an inflow from the Amazon River which brings inorganic sediments to the lake. During peak discharge most of river water enters the floodplain as diffuse overbank flow (RUDORFF et al., 2014a; RUDORFF et al., 2014b). In the high water period, floodplain waters are less turbid than the river as a large portion of the sediments entering the floodplain are trapped near the banks. During the receding period, the lake is sufficiently shallow for fine deposited sediments to be re-suspended by wind effects, resulting in high values and variability of suspended sediment and chlorophyll-a concentrations. Wind-induced mixing, however, modulate the concentration of suspended sediment and chlorophyll-a within a season and spatially depending on the lakes fetch and depth. Low water period is characterized by the highest suspended sediment and chlorophyll concentrations (BARBOSA et al., 2009).

Figure 4.2 - Daily mean water level above the sea level for the 2012 - 2014 period. Red marks indicate the period of each field campaign performed in this work.

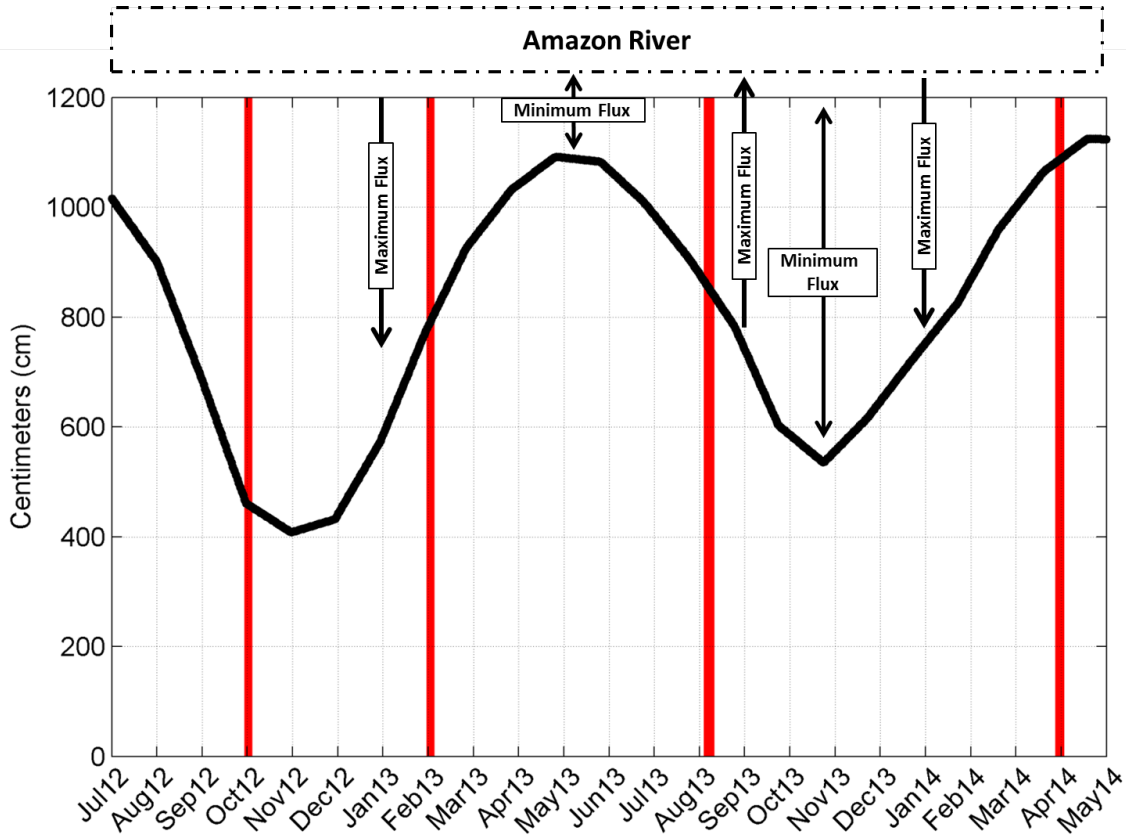

4.2 Field Campaign Description

Four field campaigns, here after named *September*,*February*, *August* and *April* were performed to represent the four states of the Amazon water level, here after named Low Water period, Rising Water Period, Receding Water Period and High Water Period, to cover all the seasonal variability of the Curuai Lake. Dates and number of sampling stations in each field campaign are presented in Table 4.1. Table 4.2 presents the set of measurements taken in each field campaign.

Figure 4.3 - Field Campaign Sample Stations in Curuai Lake

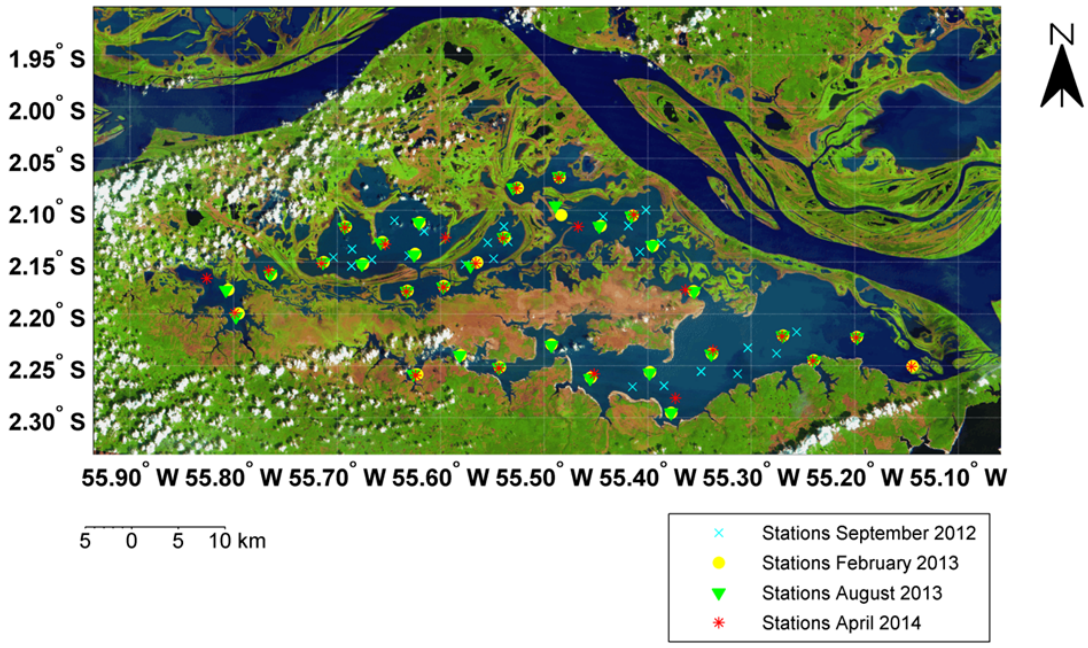

A Landsat-5 image from 11/24/2003 (Low Water Period) was used as background.

The distribution of sampling stations was initially set for *September* and based on a historical dataset of 12 Landsat-TM images acquired in the 2003/2004 period. Each image was classified into six (6) optically distinct water masses using a region-based unsupervised classifier. Map algebra was used to make sure that only perennial regions were sampled. Samples were distributed in order to represent those spectral distinct water masses and at least three (3) samples were set for each of them. Additional sampling stations were included based on previous field work experience.

All measurements were performed in the ≈ 9:30 a.m. to ≈ 3:00 p.m. local time pe-

riod, avoiding large solar zenith angles (θ_{SZA}). Usually 4 to 5 stations were sampled per day in a 30 to 40 minutes period. Each piece of equipment was deployed separately and therefore instruments sampling and water collection were not exactly simultaneous, but as close as possible.

Table 4.1 - Field Campaign Dates and Number of Stations

Field Campaign	**Date** ($DD/MM/YYYY$)	**Number of Stations**
September	30/09/2012 to 05/10/2012	30
February	02/02/2013 to 07/02/2013	32
August	11/08/2013 to 18/08/2013	31
April	04/09/2014 to 04/15/2014	28

Table 4.2 - Measurements carried out in each season

	September	**February**	**August**	**April**
Concentration Analysis				
Chlo-a	X	X	X	X
Feof	X	X	X	X
TSM	X	X	X	X
TSIM	X	X	X	X
TSOM	X	X	X	X
DTC	X	X	X	X
DIC	X	X	X	X
DOC	X	X	X	X
In-Situ				
ACS		X	X	X
Hydroscat		X	X	X
LISST			X	X
E_d Profiles	X	X	X	X
E_u Profiles			X	X
L_u Profiles	X	X	X	X
E_s			X	X
L_w			X	X
L_{Sky}			X	X
Laboratory Spectrophotometer Measurements				
a_{cdom}				X
a_p				X
a_{nap}				X
a_ϕ				X

Concentration Analysis

4.3 Measurements Methods

4.3.1 In-Situ Radiometric Measurements

All radiometric measurements were carried out with intercalibrated TRIOS sensors (TRIOS, 2015). Radiance and Irradiance sensors have a wavelength range of 350-950 nm, sample interval of approximately 3.3 nm. Radiance sensors have a 7° field-of-view (FOV). To check the drift in intercalibration a calibration procedure was performed using a calibrated lamp before *April* field campaign.

Radiometers were mounted on a structure that allows *Above* and *In-water* data collection. In *September* and *February*, measurements were carried out in a small motorboat (figure 4.4) and in *August* and *April* the structure was mounted in a riverboat (figure 4.5). In *September*, E_s was measured from the radiance reflected of a white Lambertian Spectralon Plaque (LSP) ($\pi \cdot L_{plaque}$) and an Irradiance sensor was used for the remaining field campaigns. No L_{sky} was measured in *September* and *February* and only profiles of E_d and L_u were carried out. Table 4.2 presents radiometric measurements taken in each field campaign.

At first, procedures for Radiometric acquisition and data processing followed ocean based NASA (2003) protocol (MUELLER et al., 2003). However due to specific characteristics of turbid inland water systems some of the recommendations were not applicable and new procedures were applied (mainly for In-water measurements). The same was applied for data processing and some methods were tested and adapted. The description of each procedure is presented in the sections below.

All radiometric measurements were aimed to be taken simultaneously. However an automatic integration time for each radiometer was set, which depended on the amount of light reaching the sensor and therefore the differences between each radiometer varied from 256 (milliseconds) to 4 seconds. A *fixed depth approach* (ZIBORDI et al., 2009) (see description below) was used for In-water measurements which also determined the sampling the above water data collection, i.e. at each depth (from the surface to $\approx$ 3 meters depth depending on the field campaign), 10 to 15 measurements were taken for all sensors (Above and In-water). Only one cast was performed for each station.

4.3.1.1 Above Water Approach

Water leaving Radiance (L_T) measurements were carried out with a sensor-viewing geometry of 45° zenith angle and approximately 137° azimuth angle taking the

Figure 4.4 - Structure for Trios Measurements in *September* and *February*

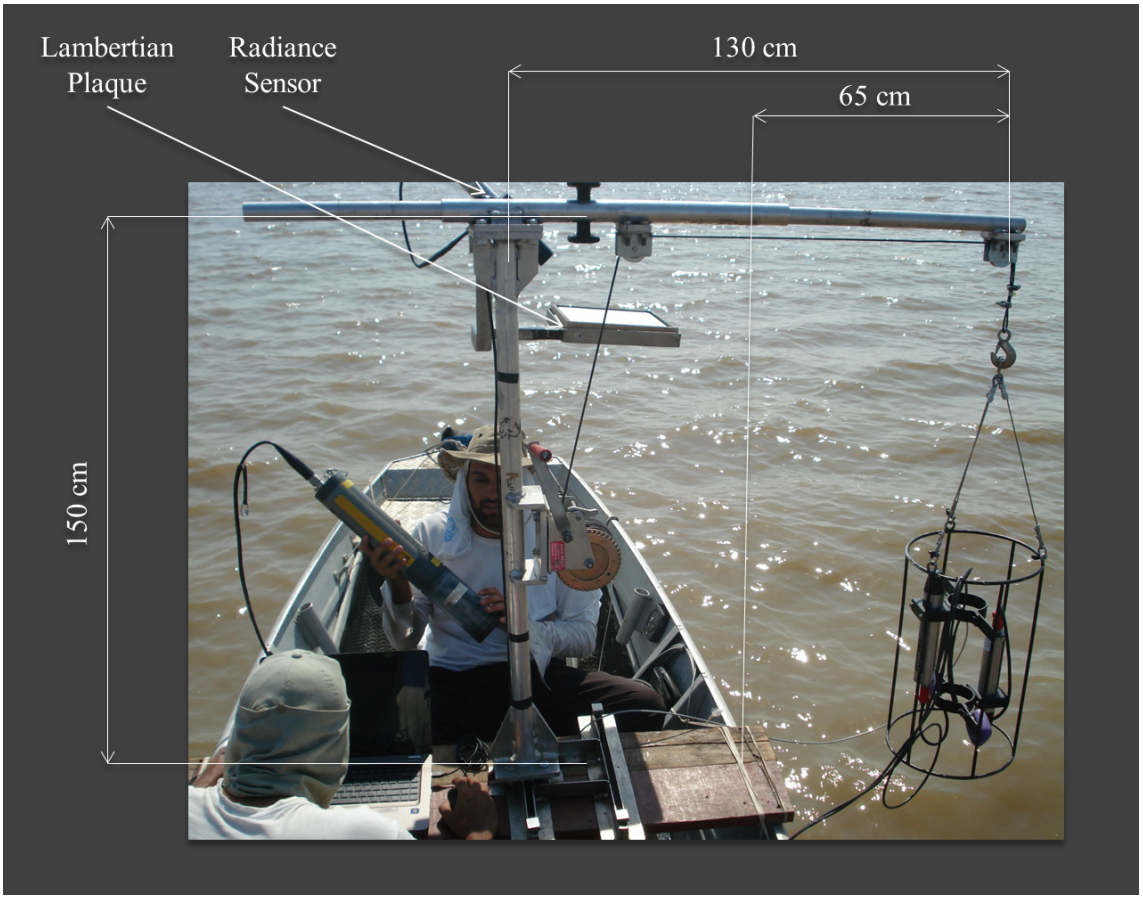

This set up was used for Above and In-Water measurements in *September* and just for Above Water in *February*

Sun direction as reference (MOBLEY, 1999; MOBLEY, 2015) ($L_T(0^+, \theta \approx 45°, \phi \approx 137°, \lambda)$). It is worth mentioning that some variability in the azimuth orientation was expected due to the operational constraints (boat and structure positioning).

To account for skylight surface reflection reaching the L_T sensor, a L_{sky} measurement was taken in the same plane but with a rotation of the mounting pole $\approx 45°$ upward from nadir. For *August* and *April*, the downwelling irradiance ($E_s = E_d(0^+, \lambda)$) was measured on the top of the boat ($\approx$ 5m) to avoid any interference (Figure 4.5) and for *February*, on the top of the structure presented in figure 4.4. As mentioned before, in September, E_s was measured from a white Lambertian Spectralon Plaque (LSP), also presented in figure 4.4.

The correction proposed by Mobley (1999) was used, as follows :

Figure 4.5 - Riverboat used in All Field Campaigns

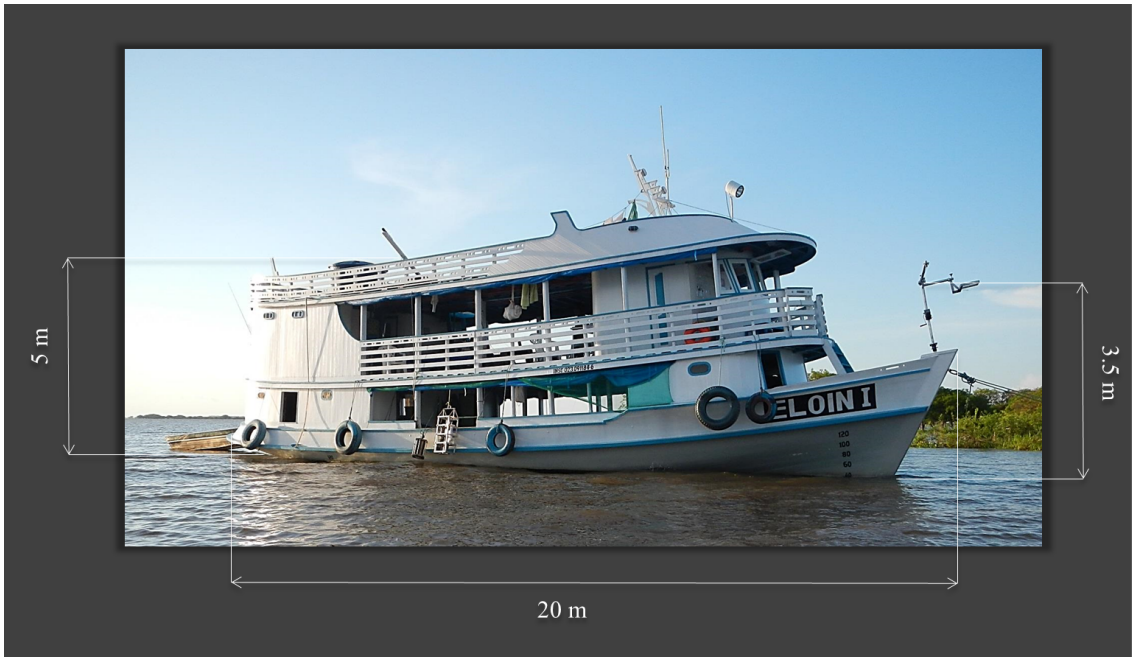

The set up used for radiometric profiles as well as Above Water Measurements is presented in the front

$$L_w = L_T(0^+, \theta \approx 45°, \phi \approx 137°, \lambda) - \rho_{sky} \cdot L_{sky}(0^+, \theta \approx -45°, \phi \approx 137°, \lambda) \quad (4.1)$$

The ρ factor, taken from Mobley (2015), that improves Mobley (1999) suggestion also accounting for polarization, was chosen based on the sea surface roughness (based on the wind speed), the θ_{sza}, and sensor-viewing geometry. Since no L_{sky} was measured in *September* and *February* skylight correction was not possible and therefore no above water $R_{rs}(0^+, \lambda)$ was used for those two field campaigns. The derived $R_{rs}(0^+, \lambda)$ (for *August* and *April*) was therefore calculated as :

$$R^{Ab}_{rs-\rho_{sky}}(0^+, \lambda) = \frac{L_w(0^+, \lambda)}{E_s(0^+, \lambda)} = \frac{L_T(0^+, \lambda) - \rho_{sky} \cdot L_{sky}(0^+, \theta \approx -45°, \phi \approx 137°, \lambda)}{E_s(0^+, \lambda)} \quad (4.2)$$

The chosen geometry of acquisition and correction for skylight reflection, however, does not account for all surface effects that affects L_w signal. Although the ρ factor

can be adequately selected, the complexity of geometrical light field between the target and the sensor, variability of environmental conditions and mainly the tilting and drifting of the boat, input uncertainties in the $R_{rs}^{Ab}(0^+, \lambda)$ that demand further filtering procedures.

Four filtering procedures were tested :

a) a residual correction which normalizes all R_{rs} taken each station by the spectrum that presents the minimum value of R_{rs} at 920 nm (adapted from Doxaran et al. (2007)).

b) the $\frac{L_{sky}}{E_s} < 0.05$ ratio which selects homogeneous sunny skies (low cloud content) (QC1) (RUDDICK et al., 2006; DOGLIOTTI et al., 2015).

c) a coefficient of variation $CV < 20\%$ for $R_{rs}(0^+, \lambda)$ in 765 and 865 nm which discard noisy/out of range spectra (QC2) (RUDDICK et al., 2006; DOGLIOTTI et al., 2015).

The QC1 criteria was applied for all collected spectra while the QC2 was calculated for each cast. The final chosen spectra to represent each station was calculated in two steps: (1) first a median inside each cast and (2) second from a median of the result of (1).

Since above water measurements are taken in a sensor-viewing geometry different from 0° for zenith/azimuth angles, a correction for Bidirectional Effects should be applied (OOWB, 2015). Bidirectional effects occur in reflection and refraction at the air-water interface ($\mathfrak{R}$ factor), in the relationship between AOPs and IOPs (f factor) and at the in-water radiance/irradiance ratio (Q factor) (all of those factors were discussed in section 3.1.4). All factors depend on sensor-viewing geometry and wind speed but particularly for f and Q they depend on atmospheric properties (aerosol optical thickness (τ_a)) and IOPs (especially the scattering phase function) which are challenging to derive from radiometric measurements (OOWB, 2015). The classical Bidirectional Effects correction based on pre-computed look-up-tables Morel and Gentili (1996) and Morel et al. (2002) were not applied in this work since no tables are available for the set of IOPs in Curuai lake. Also, no atmospheric properties were measured in each field campaign.

4.3.1.2 In-water Approach

The *profile* system for E_d, E_u and L_u measurements, was deployed in an open cage (Figure 4.6) following the orientation of the Above Water measurements to minimize effects of platform shading. The choice for a winched system was made due to shallow lake conditions to make it easier to keep control of equipments. However the proximity to the vessel (skiff or riverboat) increased shading effects in a proportion which is difficult to be assessed.

In the *fixed depth approach* used in this work, the cage was lowered and stopped following a "fixed interval" which varied from 0.3 to 0.5 meters depending on each campaign. Measurements started above water (cage above the water surface), followed by a "subsurface measurement" and were lowered/stopped respecting the stated interval. At each depth, 10 to 15 measurements were taken for all variables. The interval was chosen arbitrarily, and it was a source of error as discussed in chapter 5.

Figure 4.6 also presents the dimensions of each radiometer and the position of the pressure sensor, which is a key factor in k-functions calculations in very turbid waters.

Initially, calibration and immersion factors provided by the manufacturer were applied (TRIOS, 2015). A normalization scheme was used to account for illumination variation during each cast. E_d, L_u and E_u profiles were normalized by E_s as (MUELLER et al., 2003) :

$$\hat{R}_{x_N}(\lambda, z) = \frac{\hat{R}(z, \lambda) \cdot E_s(\lambda, t(z(0^+))])}{E_s(\lambda, t(z))} \tag{4.3}$$

where $\hat{R}_{x_N}(\lambda, z)$ is the normalized quantity and $\hat{R}(\lambda, z)$ is the (E_d, L_u or E_u) is the measurement at each depth (z). $E_s(\lambda, t(z))$is irradiance measurement at the time t(z) when the radiometer was at depth z and $E_s(\lambda, t(z(0^+)))$ is the measurement at time $t(z(0^+))$ when the profiler was at the surface.

The diffuse attenuation coefficients (K-functions) were calculated for $\hat{R}_{x_N}(\lambda, z)$ (K_d, K_{lu} and K_u). To account for the effect of sensor size (Figure 4.6) in $\hat{R}_{x_N}(\lambda, z)$ a *real depth* was calculated subtracting the sensor size $\approx 30cm$ from each depth measurement. A tilt filtering was also performed taking 5° as a boundary condition (MUELLER et al., 2003). However for some stations this limit had to be extended to

Figure 4.6 - Trios Cage for All In-Water Measurements

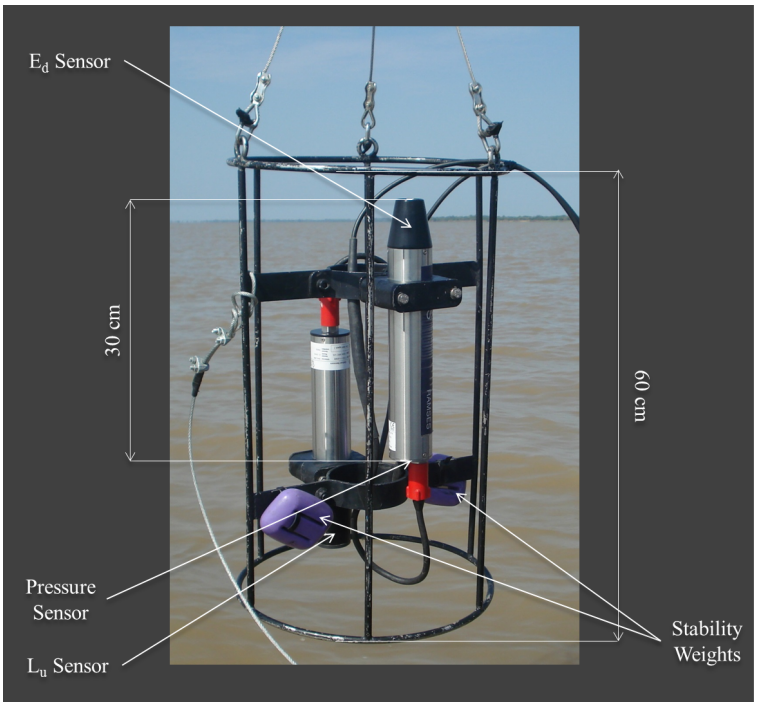

For *August* and *April* a E_u sensor was included

10∘ due to the high variabiliy in sensor position. Four *k-function* approaches were compared :

a) *Standard K-functions* (KIRK, 2010).

$$K_f(\lambda) = \frac{1}{z - z_{ref}} \cdot \ln\left(\frac{\hat{R}_{x_N}(z,\lambda)}{\hat{R}_{x_N}(z_{ref},\lambda)}\right) \tag{4.4}$$

where z_{ref} is the reference depth. For this approach, at each measured interval (30 to 50 cm) one k-function was calculated. The advantage relies in calculating several k-functions per profile, what leads to a better understating of stratified water columns.

b) *Weighted K-functions* adapted from Kirk (2010) for all $\hat{R}_{x_N}(z,\lambda,)$.

For N depth intervals :

$$^{w}K(av) = \frac{\sum_{i=1}^{N} K(z_i, z_{i+2}, \lambda)\hat{R}_{x_N}(z_{i+1},\lambda)}{\sum_{i=1}^{N} \hat{R}_{x_N}(z_{i+1},\lambda)} \tag{4.5}$$

A data smoothing is proposed in Kirk (2010) which leads to a K(z) value calculated as :

$$K(z_i, z_{i+2}, \lambda) = \frac{1}{2\Delta z} \cdot \ln\left(\frac{\hat{R}_{x_N}(z_i, \lambda)}{\hat{R}_{x_N}(z_{i+2}, \lambda)}\right) \tag{4.6}$$

$K(z_i, z_{i+2}, \lambda)$ is multiplied by $\hat{R}_{x_N}(z, \lambda)$, in the depth interval in between, in the numerator of 4.5. The Weighted approach gives one K-function per profile.

c) *Fitting Approach K-functions.*

Two fitting approaches were applied to $\hat{R}_{x_N}(\lambda, z)$ data : The linear approach converted all in-water $\hat{R}_{x_N}(\lambda, z)$ data collected to $\ln \hat{R}_{x_N}(z, \lambda)$ and fitted it to a linear type $y = ax + b$ to described in equation 4.7. A Matlab *Type-I* Linear Regression function ("Regress") (REGRESS, 2015) was used.

$$\ln(\hat{R}_{x_N}(\lambda, z)) = -K_f(\lambda) \cdot z + \ln(\hat{R}_{x_N}(z_{ref}, \lambda)) \tag{4.7}$$

The Non-linear approach aimed to fit an exponential function, described in equation 4.8, to all in-water $\hat{R}_{x_N}(\lambda, z)$ data collected. A minimization Matlab function ("fminsearch") (FMINSEARCH, 2015) was used in the fitting procedure.

$$(\hat{R}_{x_N}(z, \lambda)) = (\hat{R}_{x_N}(z_{ref}, \lambda)) \cdot e^{-K_f \cdot z} \tag{4.8}$$

In both, linear and non-linear approaches $z_{ref} = 0-$, i.e. it gives values of $E_d(0^-, \lambda,)$, $L_u(0^-, \lambda)$ and $E_u(0^-, \lambda)$ $(\hat{R}_{x_N}(0^-, \lambda))$. Those values were used to calculate the $R_{rs}(0^-, \lambda)$ for all field campaigns $(R_{rs}^{Iw}(0^-, \lambda))$ and $R^{Iw}(0^-, \lambda)$ for *August* and *April* (MUELLER et al., 2003).

To account for depth intervals, a test varying the number of depths chosen to calculate k-functions and $\hat{R}_{x_N}(0^-, \lambda)$ was performed.

4.3.2 In-situ IOP Measurements

IOP measurements were carried out with a 10 cm pathlength ACS attenuation-absorption meter with spectral range of 400 to 750 nm and wavelength resolution of ≈ 3.5 nm (smoothed by a ≈ 16 nm bandpass filter) (WETLABS, 2009). Backscattering (b_b) was measured using a HOBILabs HydroScat-6 sensor (MAFFIONE; DANA, 1997),

which allows to estimate (b_b) at six wavelength bands: 420, 442, 470, 510, 590 and 700 nm . Conductivity-Temperature-Depth (CTD) measurements were done using SBE-37SI (Sea-Bird Electronics). At each station, the profile was measured as follows: i) the CTD, ACS and HydroScat-6 instruments were simultaneously lowered until $\approx$ 75% of the lake depth; ii) they were kept at this depth for a warm up period (8 to 10 min) to remove air bubbles, as recommended by the manufacturer; iii) in *February* and *August*, the instruments were slowly raised, stopping for 30 seconds every 50 cm until surface and in *April*, a continuous profile was performed. Sampling rate for ACS and HydroScat-6 was set to 4Hz and 2Hz respectively.

4.3.2.1 Attenuation and Absorption Measurements - ACS

Prior to each field campaign, an ACS air calibration was performed following manufacturer specifications (WETLABS, 2009). The repeatable stabilization factory recommendation values ($\approx$ 0.01 m^{-1}) were not reached but were below 0.05 m^{-1}. However, the uncertainty associated with the calibration is negligible when compared to the high values of our measurements (see below). Pure water calibration was carried out after *April* campaign with a maximal drift in calibration of 0.2 m^{-1}, mainly in the blue region (400 to 500 nm).

First, pure water offsets supplied from the instrument's device file were applied to all vertical profiles to compute lake water total (particulate + dissolved matter) attenuation and absorption, (WETLABS, 2009). A 9x1 median moving window was used to filter spurious data. Temperature correction was made based on WETLabs (2009) and following tables from (SULLIVAN et al., 2006). As discussed in section 3.2.1, effects of temperature in pure water should be removed from ACS measurements.

$$x_{corr} = x_{meas}(\lambda) - (T_i - T_{norm}) \cdot \Psi_T(\lambda) \tag{4.9}$$

where x could be the attenuation (c) and the absorption (a) coefficients, x_{corr} is the attenuation/absorption normalized to a constant temperature, x_{meas} is the attenuation/absorption measured at the in situ temperature, T_i is the *insitu* sample temperature, T_{norm} is the normalization temperature, and $\Psi_T(\lambda)$ is the temperature dependency m^{-1} $^{\circ}C^{-1}$ at the measured wavelength, extracted from Sullivan et al. (2006).

Since salinity in Curuai Lake is negligible, no Salinity correction was applied. After temperature correction (a_{corr} and c_{corr}), the *absorption tube scattering corrections*

Figure 4.7 - ACS Frame

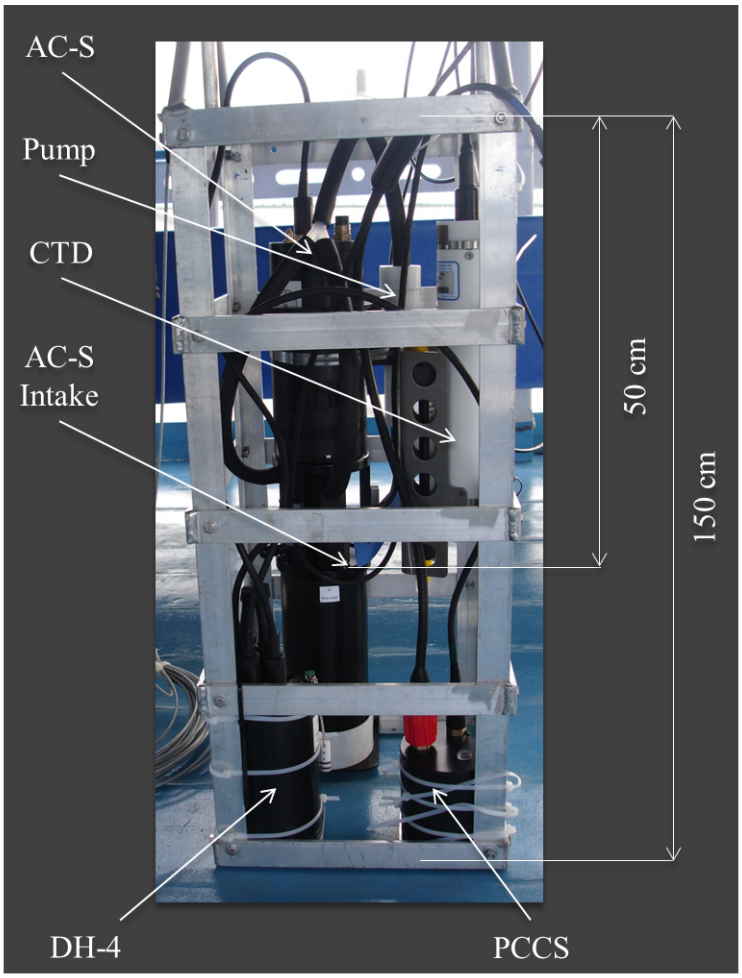

Setup used for *February*, *August* and *April*

were studied and applied. *Absorption tube scattering corrections* account for errors that result from scattering in the absorption tube which are: (1) the increase of the actual photon path length in the tube due to single and multiple scattering and (2) because part of the photons that reach the wall at an angle higher than 41.7°, due to internal reflection at the quartz/air interface of the tube, are assumed to be lost and therefore not detected in the absorption detector. Both effects overestimate the absorption coefficient measurements (LEYMARIE et al., 2010). The impact of those errors in turbid waters is higher due to the highly scattering environment.

Six *absorption tube scattering corrections* were tested.The Flat method, which subtracts a fraction from the absorption measurement at a reference wavelength (Equation (4.10)) :

$$a_{Flat} = a_{corr} - a_{corr}(\lambda_{ref}) \tag{4.10}$$

Where a_{Flat} stands for the ACS absorption corrected by the Flat method, and *ref* is the reference wavelength. Based on Leymarie et al. (2010) instead of the commonly used 715 nm as a reference wavelength we used 750 nm (Interpolated) as an attempt to improve this correction, since the absorption coefficient relative to water is expected to be lower at 750 nm than 715 nm.

The Zaneveld Correction (ZANEVELD et al., 1994; WETLABS, 2009) is described by the equation (4.11) :

$$a_{Zan} = a_{corr} - a_{corr}(\lambda_{ref}) \cdot \frac{b_{corr}(\lambda)}{b_{corr}(\lambda_{ref})} \tag{4.11}$$

Leymarie et al. (2010), based on computer simulations, assessed two reference wavelengths, 715 and 870, for 10 centimeters AC-9. In this study absorption in 750 nm (a_{750}) was tested as reference, due to the spectral range limit imposed by Interpolated ACS. The temperature corrected scattering (b_{corr}), was estimated as a difference between c_{corr} and the a_{corr}.

The here named *Kirk method* (KIRK, 1992; ZANEVELD et al., 1994) is described as (Equation (4.12)):

$$a_{Kirk} = a_{corr} - CFS \cdot b_{corr} \tag{4.12}$$

where the constant fraction of scattering (CFS) proposed by (KIRK, 1992) for coastal water ranges from 0.121 to 0.162. Wet Labs manual (WETLABS, 2009), however, recommends 0.18 for turbid waters.

The absorption tube scattering correction proposed by (RöTTGERS et al., 2013) (*proportional*$_a{}^c$) was also used and tested :

$$a_{rott}(\lambda) = a_m(\lambda) - (a_m(715) - a_{715}) \left(\frac{e_c^{-1} c_{corr}(\lambda) - a_{corr}(\lambda)}{e_c^{-1} c_{corr}(715) - a_{715}} \right) \tag{4.13}$$

where $a_{715} = 0.212 \cdot a_{corr}(715)^{1.135}$ and $e_c = 0.56$. Tests for the acceptance angle

variability were performed in (Sander de Carvalho et al., 2015) showing in general, specifically for tests made for *August* Field Campaign, an induced error of 20 % in the attenuation coefficient does not impact substantially the derived $R_{rs}^{Ab}(\lambda, 0^+)$. These differences tended to zero and therefore, we have chosen not to use the $e_c = 0.56$ correction proposed by (RöTTGERS et al., 2013). Another reason for not using the $e_c = 0.56$ factor, from Boss et al. (2009), is that it is based on low attenuation waters (Darling Marine Center Estuary, Martha's Vineyard Coastal Observatory (MVCO) and a Cross-equatorial open ocean transect) which might not be suitable for high attenuation Curuai waters.

4.3.2.2 Backscattering Measurements - Hydroscat

Sensor calibrations included dark offset and gain ratio measurements and were done following the Backscattering Sensor Calibration Manual (HOBILABS USER'S MANUAL, 2010).Hydroscat Volume Scattering Function ($\beta(140°)$) measurements were subtracted from pure water provided by Zhang and Hu (2009). The corrected backscattering coefficient was calculated using the measured β as (Equation (4.14)) :

$$b_{b_{corr}} = 2 \cdot \pi \cdot \chi \cdot (\beta(140°) \cdot \sigma(K_{bb})) \tag{4.14}$$

Where $\mathrm{b_{b_{corr}}}$ is the corrected backscattering and χ is a non-dimensional variable relating the ($\beta(140°)$) to the backscattering coefficient. Here we assume χ equal to 1.08 as suggested by the manufacturer (HOBILABS USER'S MANUAL, 2010). However, χ can vary according to acquisition angle (OISHI, 1990; BOSS; PEGAU, 2001) and environmental conditions.

Due to high absorption and scattering values presented in the study area, Hydroscat data must be corrected for power losses due to absorption and scattering effects along optical path of the instrument (pathlength effect). Sigma-correction, described in the Hydroscat Manual (HOBILABS USER'S MANUAL, 2010) was adapted to incorporate ACS measurements. The "Sigma" correction ($\sigma(K_{b_b})$) depends on sensor's optical path geometry and is expressed as (Equation (4.15)) :

$$\sigma(K_{bb}) = k1 \cdot \exp\left(k_{exp} \cdot K_{bb}\right) \tag{4.15}$$

where $\mathrm{k_{exp}}$ (the optical pathlength) is characteristic of the specific instrument, and

is included in its calibration file. When the calibration is performed with DI water the term k1 equals *1* at all wavelengths (HOBILABS USER'S MANUAL, 2010). K_{bb} is the attenuation coefficient for light traveling from the sensor to the volume and back to the detector. K_{bb} is related to absorption (a)and scattering (b) coefficients as (Equation (4.16)) :

$$K_{bb} = a + K_{scat} \cdot b \tag{4.16}$$

where K_{scat} has the standard value of 0.4. In this work a new sigma correction was tested, based on Doxaran (personal communication). This correction substitutes the factor K_{scat}, by an expression based on the backscattering probability (b_b/b) (in percentage values), as follows :

$$K_{scat} = 0.0317 \cdot \ln\left(\frac{b_b}{b}\right) + 0.0668 \tag{4.17}$$

As no ($\frac{b_b}{b}$) is available from Hydroscat before sigma correction, backscattering probability was estimated using ACS measurements following (SULLIVAN et al., 2005) :

$$\frac{b_b}{b}(ACS) = 0.11 \cdot \frac{a_{ACS}(715)}{c_{ACS}(715)} - 0.001 \tag{4.18}$$

Where $\frac{b_b}{b}(ACS)$ is the backscattering probability estimated from ACS; $a_{ACS}(715)$ and $c_{ACS}(715)$ are the ACS measured absorption and attenuation coefficients at 715 nm prior to application of the scattering correction to absorption. The ($\frac{b_b}{b}$) calculated from b_b from Hydroscat and b from ACS will be called $\frac{b_b}{b}(^{(HS-6)}/_{(ACS)})$.

4.3.2.3 Size Distribution Measurements - LISST

Size distribution measurements were carried out with a LISST-Portable (LISST, 2015). As shown in table 4.2 measurements were taken only in *April*. Samples (sampled as described in section 4.3.3) were measured in replica within a maximum of three hours after sampling, following the LISST (2015) description. The LISST-Portable estimates the particle size distribution using the forward scattering of a laser beam (670 nm), measured with a series of 32 circled detectors, over a path-length of 5 cm. From LISST-Portable it is also possible to measure the transmitted

light, from which the beam attenuation coefficient of particles, c_p, can be calculated. From the optical scattering angular pattern extracted from the detector, the particle volume concentration, V(D), is calculated from Mie Inversions. The V(D) is divided in a total of 32 size classes that logarithmically increase with diameter (AGRAWAL; POTTSMITH, 2000). The V(D) is calculated using manufacturer provided software and calibration and the transformation to N'(D), described in equations 3.14 and 3.15 from section 3.1.2, was done separately. The effective particle size range measured with this laser is 2.72-460.3 μm, with the width of individual size classes varying from 0.45 to 76 μm over this range.

4.3.3 Laboratory Measurements

At each station, 200 to 300 mL of water were sampled within the Secchi depth. In the field, samples were kept in dark and cooled for a maximum of three hours before filtration. 47-mm Whatman GF/F 0.7 μm pore size filters were used for chlorophyll-a (Chla) and pre-weighted GF/C 1.2 μm pore size filters were used for TSM. The result of 47-mm Whatman GF/F 0.7 μm was used for dissolved total carbon (DTC, DOC and DIC) analysis.

For the determination of particulate absorption, samples were filtered by a 47-mm Whatman GF/F 0.7 μm and for CDOM absorption analysis the filtered water was re-filtered in a 0.2 μm pore size Whatman Membrane filter.

Both, filtered and re-filtered water were stored in light blocking containers to prevent photodegradation. Except for dissolved matter (DTC, DOC, DIC and CDOM absorption) analysis, all measurements were done in replica. Except for CDOM samples, the remaining samples were kept frozen for five (5) days, until laboratory analysis was performed.

4.3.3.1 Determination of Limnological Parameter Concentrations

Limnological Parameter Concentrations were determined by the International Institute of Ecology (IIE) ((IIE, 2015)) according to the following protocol: Chla concentration based on (NUSCH, 1980) with Whatman GF/F 0.7 μm filters soaked in 80% ethanol, heated to 75 °C for 5 min and immediately cooled. After 24 hours in the dark, absorbance at 665 and 750 nm were measured with a UV-2600 Shimadzu spectrophotometer (Shimadzu Corporation, Japan) and the concentration determined. DOC and DIC concentrations were determined according to Farmer and Hansell (2007) using an infrared gas analysis Shimadzu, TOC-5000 analyzer

with high temperature combustion. TSM determination followed Wetzel and Likens (2000) gravimetric protocol. Sample filters were dried at 60 °C for a 24 hour period and weighted to determine TSM concentration. To separate TSIM from TSOM, filters were burned at 480 °C for one hour to eliminate the organic matter and weighed again.

4.3.3.2 Absorption Measurements

Laboratory absorption measurements were performed only for *April* datam (table 4.2), using a dual beam UV-2600 Shimadzu spectrophotometer. CDOM optical density (OD) was measured using a 10 cm pathlength quartz cell cuvette and distilled water at the same ambient temperature as reference. The spectral absorption coefficient, $a_{CDOM}(\lambda)$ was calculated from the measured optical density ($ODs(\lambda)$) according to equation (4.26).

$$a_{CDOM} = \frac{2.3 \cdot (OD_s(\lambda) - OD_{null})}{l} \tag{4.19}$$

where "l" is the cuvette pathlength and OD_{null} is the optical density at a wavelength where absorption by CDOM can be assumed to be zero, in this case, the average over 750-800 nm.

TSM absorption coefficient (a_{TSM}), derived Non-Algal Particles (a_{nap}) and Phytoplankton (a_{ϕ}) absorptions were measured using the Transmittance-Reflectance quantitative technique (T-R Method) (TASSAN; FERRARI, 1995; TASSAN, 2002). As discussed by Stramski et al. (2015) the T-R method overcomes the limitations related to filter scattering (mainly the Reflectance) common to filter-pad approach (Transmittance method).

Although accounting for scattering errors, the T-R also is affected by the pathlength amplification ($\beta - factor$), which is a major source of error for filter-pad methodologies. The multiple scans and the variability of filters, whose properties can vary from each other are other sources of uncertainties. For pathlength amplification correction, the factors described in Tassan (2002) were used. As highlighted by Stramski et al. (2015), T-R method presents results close to those of the most reliable method which is the so called IS method (sample inside the integrating sphere).

Another important step of T-R method is the bleaching process. This process is done by submitting the sample filter for ≈ 20 min to a 10% sodium hypochlorite

(NaClO) solution before being rinsed with distilled water and re-scanned. It has been demonstrated that NaClO bleaching oxidizes phytoplankton pigments faster than other particulate organic matter, enabling the separation of their absorption signals (FERRARI; TASSAN, 1998). NAP absorption fraction (OD_{NAP}) includes unbleached organic detritus (Organic NAP) and mineral sediments (Inorganic NAP).

TSM, NAP and Phytoplankton absorptions measurements were then converted from optical density (OD) to absorption coefficients (m^{-1}) using the following equation (TASSAN, 2002):

$$a_x(\lambda) = \frac{2.33 \cdot OD_{nap}}{R} \tag{4.20}$$

where R is the ratio of the filtered volume to the filter clearance area in meters and x is the component (TSM or NAP). The difference between a_{TSM} and a_{nap} leads to the absorption due to phytoplankton pigments a_ϕ ($a_\phi = a_{TSM} - a_{nap}$).

4.4 Data Quality Assessment

The *Data Quality Assessment* was mostly based on closure exercises that chased the following objectives :

- In-Situ Radiometric Measurements (Above and In Water) tests of literature correction approaches and k-function calculations as well as the sensitivity to environmental conditions and sampling strategies.
- Closure Experiments for ACS and LISST
- Closure Experiments of IOPs (ACS and Hydroscat) and AOPs (R_{rs}, R and K_d) to :(1) identify most suitable set of corrections for ACS and Hydroscat measurements using a "Hydrolight" strategy and (2) test the suitability of forward models for the current dataset.
- Quality control using Laboratory measurement replicas.

The reliability of the measurements and methods were assessed for each set of measurements at each step of data acquisition and processing. The following statistical indexes used for test data quality assessment (ANTOINE et al., 2008; RUDORFF, 2013):

a) Unbiased Percent Difference (UPD),

$$UPD = \frac{\sum_{i=1}^{N} \left[\frac{(x_{test} - x_{ref})}{\frac{(x_{test} + x_{ref})}{2}} \right]}{N} \cdot 100 \tag{4.21}$$

b) Modular Relative Percent Difference (RPD)

$$RPD = \frac{\sum_{i=1}^{N} \left[\frac{|(x_{test} - x_{ref})|}{(x_{ref})} \right]}{N} \cdot 100 \tag{4.22}$$

c) Root Mean Square Error (RMSE)

$$RMSE = \sqrt{\sum_{i=1}^{N} \frac{(x_{test} - x_{ref})}{N}} \tag{4.23}$$

Where x_{test} and x_{ref} are the *tested* and *reference* measurements. Median, Mean, Standard Deviation (SD) and Coefficient of Variation (CV) and correlation coefficient (r) are also computed.

4.4.1 In-Situ Radiometric Measurements

4.4.1.1 Above Water Approach

The Flowchart from Figure 4.8 describes the methodological steps to test the effect of above water correction techniques. The main steps are adapted from Rudorff (2013).

Initially, Mobley (2015) correction was applied to the Non-corrected R_{rs} ($R^{Ab}_{rs-NC} = \frac{L_T}{E_s}$) generating $R^{Ab}_{rs-\rho_{sky}}$ as described in section 4.3.1.1. The three proposed corrections (Residual Correction, QC1 and QC2) were applied to $R^{Ab}_{rs-\rho_{sky}}$ generating R^{Ab}_{rs-RC}, R^{Ab}_{rs-QC1} and R^{Ab}_{rs-QC2}. Statistical indexes were calculated at each step, first taking R^{Ab}_{rs-NC} as reference for Mobley (2015) correction and then taking $R^{Ab}_{rs-\rho_{sky}}$ for the remaining corrections. The correction with the highest impact on R^{Ab}_{rs-NC} (higher difference from R^{Ab}_{rs-NC}) was then chosen.

4.4.1.2 In-Water Approach

K-functions tests were performed for *February*, *August* and *April*, because data acquired in *September* was very noisy. Tests were performed for both: each data set and combining all data from the three field campaigns. Only L_u and E_d profiles were used. A series of tests were performed for In-Water Approach:

Figure 4.8 - Flowchart of the Above Water Correction Methodology

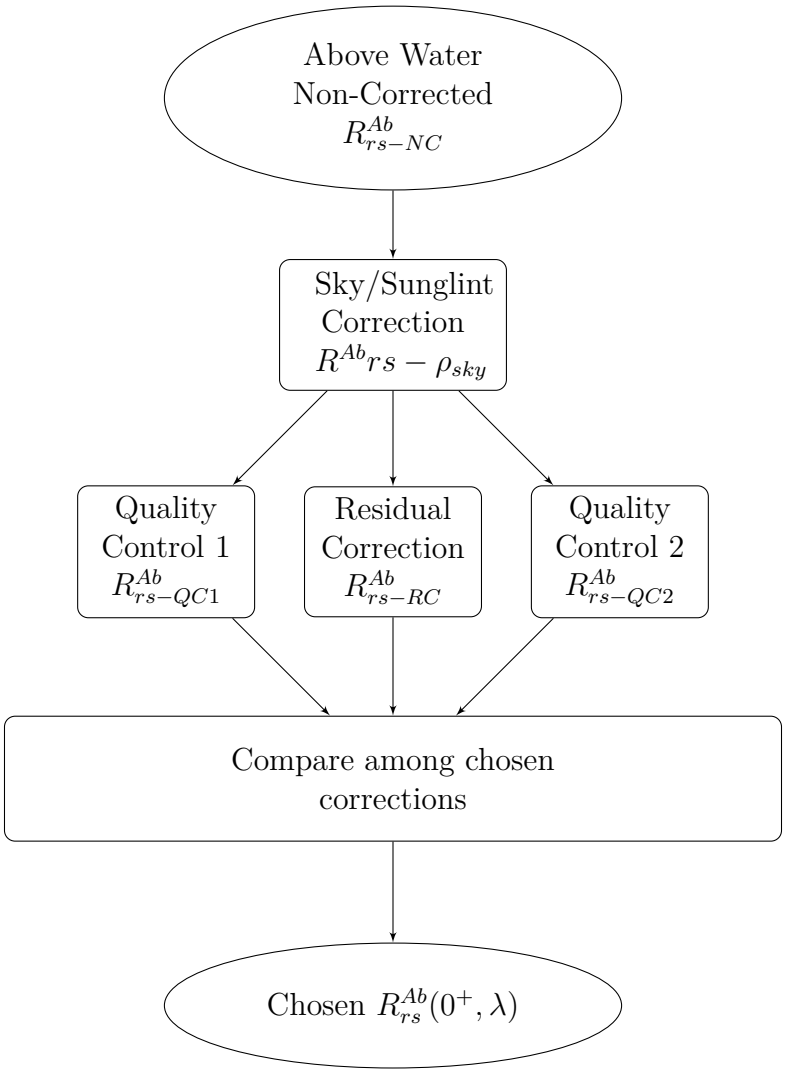

a) *Impact of K-function computing Approaches* : Non-Linear, Linear, Weighted and Standard approaches were compared. For Non-Linear and Linear approaches, all measurements from all depths were used. For Weighted and Standard approaches, K_{lu} and K_d were calculated using data from all depths, divided by number of casts and the median was assumed to represent the entire water column. Non-Linear Approach was assumed as reference against which the remaining approaches were assessed using the statistical indexes (Figure 4.8).

b) *Impact of Number of measurements in the water column on K-functions*: A test varying the number of depths used in the calculation of K_{lu} and K_d, was performed using only the Non-Linear and Linear Approaches. A

step of 1 meter was used, starting from one meter depth and finishing at 5 meters depth. To calculate statistical indexes, K_{lu} and K_d calculated with all measurements (5 meters depth) was used as reference (Figure 4.9).

c) *Impact of computing Approaches on derived* $R_{rs}^{Iw}(0^-, \lambda)$: Non-Linear and Linear approaches were compared. All measurements from all depths were used. Non-Linear Approach was assumed as reference against which the remaining approaches were assessed using the statistical indexes (Figure 4.8).

d) *Impact of Number of measurements in the water column on* $R_{rs}^{Iw}(0^-, \lambda)$: A test varying the number of depths used in the calculation of $R_{rs}^{Iw}(0^-, \lambda)$, was performed using only the Non-Linear and Linear Approaches. A step of 1 meter was used starting from one meter depth and finishing at 5 meters depth. To calculate statistical indexes, $R_{rs}^{Iw}(0^-, \lambda)$ calculated with all measurements (5 meters depth) was used as reference (Figure 4.9).

All tests were performed for the 500-800 nm interval due to unrealistic measurements outside of this interval (i.e. insufficient light levels resulting in high noise/signal affecting negatively the computation of K-functions), as will be discussed in Chapter 5. Tests were performed using only samples from 20 stations acquired *February* due to the extremely high level of noise. All stations from *August* and *April* were used. *September* presented the highest levels of noise and therefore, was not used in the analysis.

Figure 4.9 - Flowchart of the In-Water Correction Methodology - I

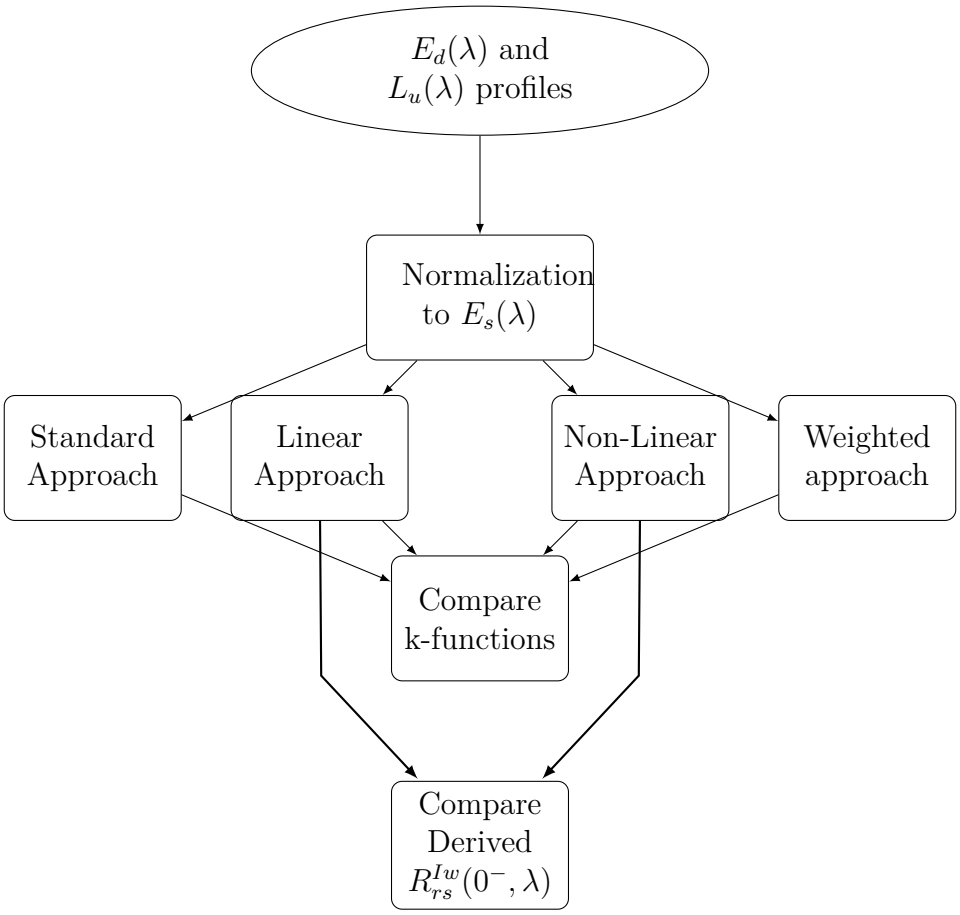

Figure 4.10 - Flowchart of the In-Water Correction Methodology - II

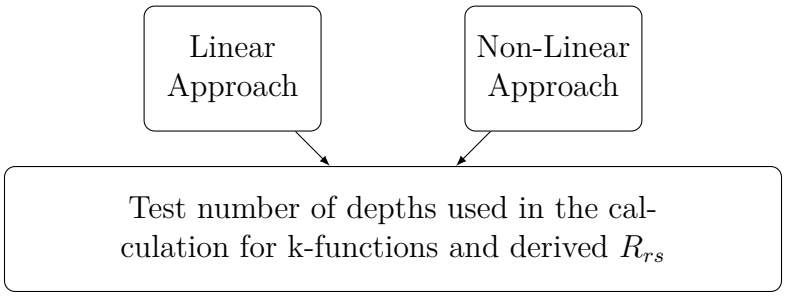

4.4.1.3 Comparing Above Water ($R_{rs}^{Ab}(0^+,\lambda)$) and In-water ($R_{rs}^{Iw}(0^-,\lambda)$) Approaches

To compare In-water Remote Sensing Reflectances, $R_{rs}^{Ab}(0^+,\lambda)$ was converted to $R_{rs}^{Ab}(0^-,\lambda)$ using equation 3.23. Factor $\mathscr{R}$ was calculated for each θ_{sza}, for each R_{rs} measurement. The resulting corrected $R_{rs}^{Ab}(0^-,\lambda)$ ($R_{rs-\rho_{sky}}^{Ab}(0^-,\lambda)$, $R_{rs-RC}^{Ab}(0^-,\lambda)$, $R_{rs-QC1}^{Ab}(0^-,\lambda)$, $R_{rs-QC2}^{Ab}(0^-,\lambda)$), were compared to R_{rs}^{Iw} calculated using Non-Linear approach ($R_{rs-NonLin}^{Iw}(0^-,\lambda)$). Statistical Indexes were calculated taking $R_{rs-NonLin}^{Iw}(0^-,\lambda)$ as reference.

4.4.2 In-Situ IOPs

In order to test the performance of ACS *absorption tube scattering corrections* and Hydroscat *sigma correction*, Hydrolight simulations were performed, according to the steps described in the next section.

4.4.2.1 Hydrolight Experiments - ACS and Hydroscat Measurements

The closure Hydrolight based data quality analysis were performed as follows :

(i) Use Hydrolight default water absorption coefficients (*H2OabDefaults.txt*).

(ii) Input ACS and Hydroscat data profiles for each station, each time varying the ACS scattering corrections for absorption and sigma correction for HS-6 as follows:

  (a) $Zaneveld/0.03$ - Proportional correction for absorption tube scattering correction. Hydrolight chooses the Fournier-Forand VSF based on a wavelength independent $\frac{b_b}{b}(ACS) = 0.03$.

  (b) $Zaneveld/Doxaran$ - Proportional correction for absorption tube scattering correction. Hydrolight chooses the Fournier-Forand VSF based on $\frac{b_b}{b}(ACS)$ calculated from Doxaran based sigma corrected Hydroscat Measurements and ACS scattering coefficient (b).

  (c) $Kirk/0.03$ - Kirk Method with a constant fraction of scattering (CSF) equals to 0.18 for absorption tube scattering correction. Hydrolight chooses the Fournier-Forand VSF based on a wavelength independent $\frac{b_b}{b}(ACS) = 0.03$.

  (d) $0.18/Doxaran$ - Kirk Method with a constant fraction of scattering (CSF) equals to 0.18 for absorption tube scattering correction. Hydrolight chooses the Fournier-Forand VSF based on $\frac{b_b}{b}(ACS)$ calculated

from Doxaran based sigma corrected Hydroscat Measurements and ACS scattering coefficient (b).

(e) *Rottgers*/0.03 - Rottgers Method for absorption tube scattering correction. Hydrolight chooses the Fournier-Forand VSF based on a wavelength independent $\frac{b_b}{b}(ACS) = 0.03$.

(f) *Rottgers/Doxaran* - Rottgers Method for absorption tube scattering correction. Hydrolight chooses the Fournier-Forand VSF based on $\frac{b_b}{b}$ calculated from Doxaran based sigma corrected Hydroscat Measurements and ACS scattering coefficient (b).

(g) *Rottgers*/0.4 - Rottgers Method for absorption tube scattering correction / Hydrolight chooses the Fournier-Forand VSF based on $\frac{b_b}{b}$ calculated from standard 0.4 value sigma corrected Hydroscat Measurements and ACS scattering coefficient (b).

(iii) No bioluminescence or inelastic scattering;

(iv) Default wind speed (5,0 m/s);

(v) Semi-empirical sky model;

(vi) sun zenith angle was the calculated angle at the time of the field observation at each station

(vii) in-situ irradiance (E_s) was used as incident light and

(viii) Simulations were run down to 2.5 meters depth with 0.1 meters depth resolution (waters were assumed to be optically deep) and twenty five wavelengths between 400 and 900 nm, 20 nm wavelength resolution. Simulated AOPs were later interpolated for the same interval as measured AOPs (1 nm).

Before computing the statistical indexes reference AOPs were selected according to the following criteria: (1) The smaller surface effects on derived R_{rs}^{Iw} in relation to R_{rs}^{Ab} and (2) the possibility of computing k_ds. Therefore, the three selected AOPs used as reference were: Irradiance Reflectance $R_{NonLin}^{Iw}(0^-, \lambda)$, Remote Sensing Reflectance $R_{rs-NonLin}^{Iw}(0^-, \lambda)$, Downwelling Diffuse Attenuation Coefficient ($K_{d-NonLin}(\lambda)$. Since Upwelling Irradiance $E_u(0^-, \lambda)$ was not measured in February, $E_u(0^-, \lambda)$ was derived from the simplistic $E_u(\lambda, 0-) = \pi L_u(0^-, \lambda)$. Statistical Indexes were performed for February, August and April separately. As Hydrolight

simulations calculate AOPs for each pre-set depth (each 0.1 meters for the proposed simulations), for Statistical indexes calculations, median values were calculated for the 0 to 1 meter interval for ($K_d(\lambda)$ and from 0 to 0.2 meters for $R^{Iw}_{NonLin}(0^-, \lambda)$ and $R^{Iw}_{rs-NonLin}(0^-, \lambda)$.

4.4.2.2 LISST Quality Analysis

For LISST Quality Analysis, two experiments were performed:(1) Comparison between LISST and ACS attenuation coefficient (c) measurements; (2) Comparison between measurement replicas.

4.4.2.3 Testing Forward Model Approximations

Gordon and Morel approximations (Section 3.3.1) were tested as a strategy to (1) indirectly assess the quality of the AOP and IOP measurements as well as their suitability as input to inverse models, (2) to investigate model performance to the available dataset taking into account that the inverse models are based on both approximations. Tests were made directly (Hydrolight was not used), using models from section 3.3.1 with the inputs: AOP (R^{Ab}_{rs} and R^{Iw}_{rs}) and IOPs (ACS total absorption coefficient and Hydroscat backscattering coefficient) . Only the median of surface measured absorption and backscattering were used.

Two fitting designs were used: (1) first and second order polynomial fitting for each wavelength (POLYFIT, 2016) and (2) Non-Linear fitting to the entire spectra (NLINFIT, 2015). The polynomial fitting provides a set of coefficients for the combination of the entire *August+April* dataset whereas for the Non-Linear fitting a single coefficient is computed for each sampling station. Median and Standard deviation were computed to assess the quality of Non-Linear fitting coefficients for each forward model approximation. Fitting approaches provided the set of coefficients f/Q, f'/Q, g_0 and g_1 which were then compared to values commonly used in the literature.

4.4.3 Laboratory Measurements

Optical Active components (a_p, a_{nap} and a_ϕ) replicas were compared using statistical indexes. First set of samples was taken as reference. The removal of 400 to 520nm and 640 to 700nm intervals from a_{nap} spectra were tested, to prevent phytoplankton pigment contamination as proposed by Bricaud et al. (2010). A Non-Linear fitting procedure (equation 3.28) (NLINFIT, 2015) was applied to the data, to compute the fitted a_{nap} ($a_{nap-fit}$). The $a_{nap-fit}$ was then used to compute $a_{\phi-fit}$ as follows: $a_{\phi-fit} = a_{TSM} - a_{nap-fit}$. Statistical Indexes were also computed for $a_{nap-fit}$, and

$a_{\phi-fit}$ in order to assess efficiency of Bricaud et al. (2010) procedure in removing phytoplankton pigment contamination.

4.5 Curuai Lake Bio-Optical Variability

The seasonal variability of biogeochemical variables, k-functions ($K_d(\lambda)$, $K_{lu}(\lambda)$, $K_u(\lambda)$ and $R_{rs}^{Iw}(0^-, \lambda)$) was assessed just by plotting seasonal changes and computing descriptive statistics: Median, Mean, Maximum, Minimum Standard Deviation and CV.

Regarding the IOPs, however, the analysis focused on their spectral characteristics and on their relationships to each biogeochemical variable concentration. These analysis were carried out as follows: *Seasonal Comparison* and April *Field Campaign*. In the *Seasonal Comparison* ACS and Hydroscat datasets from *February*, *August* and *April* were compared whereas for *April Field Campaign* only laboratory absorption and LISST data-sets were used. Details of both analysis are further discussed in the next sections.

4.5.1 IOPs Seasonal Comparison

The seasonal comparison of IOPs spectra and shape features was based on both surface and profile measurements. Only surface data was used to assess the relationship between IOPs and biogeochemical variables.

For building surface IOPs database used in this analysis, a median of IOPs measurement was taken from 0.5 to 1.0 meters. The common approach of integrating within the first optical depth ($\frac{1}{K_d}$) (GORDON; MCCLUNEY, 1975) was not possible because ACS and Hydroscat size prevented measurements above 0.5 meters. Profiles were performed to different maximum depths (February $\approx$ 2.5 meters; August $\approx$ 5.0 meters; April $\approx$ 4.5 meters) due to the variability in lake maximum depths among periods.

This analysis used a type II linear regression analysis to model the relationship between IOPs and biogeochemical variables, using "lsqbisec" function implemented in MATLAB by Edward T. Peltzer (`http://www.mbari.org/staff/etp3/regress.htm`) based on (SPRENT; DOLBY, 1980).

Linear regression analysis against suspended matter (TSM, TSIM and TSOM) was first run for b_{b_p}, b_p and c_{p+CDOM} for the entire spectra and specific wavelengths ($b_{b_p}(700nm)$, $b_p(700nm)$ and $c_{p+CDOM}(660nm)$) were chosen for comparison with

previous studies. Only 23 stations out of 32 were used for *February* because ACS measurements were above equipment sensitivity (Noise Signal in the Blue (400 to 500 nm). The analysis was performed combining samples from all seasons and for each season. Specific coefficients (c^*_{p+CDOM} b^*_p $b^*_{b_p}$) computed from Type II linear regression analysis were compared to literature values.

The *absorption line height at 676 nm* (BRICAUD et al., 1995) was calculated as in Boss et al. (2007), replacing particulate matter absorption ($a_p(676)$) for ACS $a_{p+CDOM}(676)$, to estimate phytoplankton absorption ($a_\phi(676)$) (Equation 4.24).

$$a_\phi(676) = \left[a_{corr}(676) - \frac{39}{65}a_{corr}(650) - \frac{26}{65}a_{corr}(715)\right](m^{-1}) \tag{4.24}$$

Type II linear regression between $a_\phi(676)$ and Chla concentration was used to retrieve Chla from ACS measurements. This line-height method was used due to the fact that it reduces the influence of dissolved materials as well as non-algal particles on the bulk absorption (ROESLER; BARNARD, 2013). Type II linear regression coefficients provided also estimates of Phytoplankton specific coefficient ($a^*_\phi(676)$).

The following power-law function (equation 4.25) (also described in equation 3.29) was Non-Linearly fitted to ACS and Hydroscat measured scattering $b_p(\lambda)$ and backscattering $b_{b_p}(\lambda)$.

$$x = x(\lambda_{ref}) \cdot \left(\frac{\lambda_{ref}}{\lambda}\right)^{\gamma_x} \tag{4.25}$$

where (x = b or $\mathrm{b_b}$), γ_x is the exponent and λ is the wavelength. The reference wavelengths (λ_{ref}) were chosen as 555 nm and 510 nm respectively). The fitting procedure was made on wavelengths intervals from 550 nm to 750 nm for scattering coefficients and for 510, 590 and 700 nm for backscattering measurements to avoid absorption influence due to high absorption in the blue region (DOXARAN et al., 2009). The indexes γ_b and γ_{b_b} were analyzed among seasons.

4.5.2 The *April* Field Campaign

4.5.2.1 Absorption Analysis

Absorption spectra (a_p, a_{nap}, a_ϕ and a_{cdom}) were filtered to remove null and negative values and then a_{cdom} and a_{nap} spectra were fitted to an exponential (NLINFIT, 2015)

(equations 4.26 and 4.27).

$$a_{CDOM} = a_{CDOM}(\lambda_{ref}) \cdot e^{(-S_{cdom} \cdot (\lambda - \lambda_{ref}))} \tag{4.26}$$

$$a_{nap} = a_{nap}(\lambda_{ref}) \cdot e^{(-S_{nap} \cdot (\lambda - \lambda_{ref}))} \tag{4.27}$$

where $\lambda_{ref} = 440$.

In order to calculate a_p^* and a_ϕ^* two approaches were used: the ratio $\frac{a_p}{[TSM]}$ and $\frac{a_\phi}{[Chla]}$ and similarly to section 4.5.1, type II linear regression was used to calculate spectral a_p^* (using a_p and [TSM]) and spectral a_ϕ^* (using a_ϕ and [Chla]).

4.5.2.2 LISST Analysis

Particle Volume Size ($V(D)$) and Particle Number Size ($N'(D)$) distributions were plotted and replicas were graphically compared. $N'(D)$ distributions were fitted to the *Junge distribution* (equation 3.15).The relation $\xi_{psd} = \gamma_x + 3$ (BOSS; PEGAU, 2001; DOXARAN et al., 2009; SLADE; BOSS, 2015) was used for comparing ξ_{psd} and γ_b.

4.6 Inverse Models

GIOP, QAA and Nechad models, described in section 3.3.2, were submitted to different types of analysis: (1) For GIOP modeling a series of IOP input variables both measured in this research and provided by literature were tested. (2) Two versions of QAA were used only having $R_{rs}(0^+, \lambda)$ as input variable and without any parametrization attempt; (3) Nechad model was tested using as input IOPs both measured in this research and provided by Nechad et al. (2010). An attempt of parametrization was made using TSM concentration as a calibration parameter. Details are provided in the subsections 4.6.1, 4.6.2 and 4.6.3.

Only data from *February*, *August* and *April* were used to test the models due to extremely noisy $R_{rs}(0^-, \lambda)$ in *September*. Attempts to use both $R_{rs}(0^-, \lambda)$ and $R_{rs}(0^+, \lambda)$ as input to GIOP and QAA models indicated that only $R_{rs}(0^+, \lambda)$ provided reliable results i.e. the noise in the blue region made the inversion impossible. Therefore, $R_{rs}(0^-, \lambda)$ dataset was used only for Nechad model. Only 23 stations out of 32 (the same selected for *IOPs Seasonal comparison*) were used in *February*.

April dataset allowed a analysis of all the IOPs necessary to parametrize and test the proposed inverse models ($a_p^*(\lambda)$, $a_{nap}^*(\lambda)$, $a_{cdom}(\lambda)$ and $b_{b_p}^*(\lambda)$). For the remaining seasons, *April* data was used as input to run models for *February* and *August*.

4.6.1 GIOP

Table 4.3 shows the group of entries used to test GIOP. All combinations of values presented in table 4.3, i.e. b_{bp} Exponent, $a_{nap+cdom}$ Exponent, a_ϕ^* and Inversion Methods were tested for *April*, using Laboratory a_{T-w} ($a_{T-w} = a_p + a_{cdom} - a_w$), $a_{nap+cdom}$, a_ϕ as reference. The 400 to 750 interval (with a 1 nm interval) was used for all entries.

The set of GIOP outputs for each station in every season was compared to measured IOPs using RMSE and RPD index. GIOPs a_{T-w}, b_{bp}, Chlorophyl-a for *April*, *August* and the combination of both were compared to ACS, Hydroscat, measured Chlorophyl-a concentration respectively.

Table 4.3 - Parameters Used for GIOP Tests

Air-Water transmission	Lee et al. (2002) (Default)
$a_w(\lambda)$ and $b_{bw}(\lambda)$	Pope and Fry (1997) and Morel (1974) (Default)
AOP-IOP relationship	(0.0895,0.1247) from Lee et al. (2002)
b_{bp} Exponent	*eta* Lee et al. (2002) (Default) *1.03373* from Maritorena et al. (2002) b_{bp} Exponent from February b_{bp} Exponent from August b_{bp} Exponent from April
$a_{nap+cdom}$ Exponent	*0.015* Lee et al. (2002) (Default) *0.02061* from Maritorena et al. (2002) $a_{nap+cdom}$ Exponent from April
a_ϕ^*	Bricaud et al. (1998) Maritorena et al. (2002) Ciotti and Bricaud (2006) Median a_ϕ^* from April Linear Regressed a_ϕ^* from April
Inversion Method	Non-linear inversion using fminsearch Matlab routine Linear matrix inversion using QR decomposition

A b_{bp} and $a_{nap+cdom}$ exponent *sensitivity analysis* was carried out to further test GIOP suitability using Wang et al. (2005) method. A matlab code available from

GIOPSensitivity (2005) was used. Table 4.4 shows test's criteria. Acceptable solutions were: positive values and convergence (ConvCrit) which states that differences between modeled and measured R_{rs} cannot exceed a given threshold.

Each acceptable solution provided a set of IOPs(a_T, $a_{nap+cdom}$, a_ϕ and b_{bp}) as well as the exponents of $a_{nap+cdom}$ and b_{bp}. Modeled IOPs (median, 5 and 95 percentiles of solutions) were compared to measured IOPs for all wavelengths (350 values). Median $a_{nap+cdom}$ and b_{bp} derived exponents and its respective standard deviations were also compared to measured values (Measured $a_{nap+cdom}$ exponent was calculated from fitting an exponential for the sum a_{nap} + a_{cdom}).

Table 4.4 - Parameters Used for GIOP Sensitivity Analysis

Air-Water transmission	Lee et al. (2002) (Default)
$a_w(\lambda)$ and $b_{bw}(\lambda)$	Pope and Fry (1997) and Morel (1974) (Default)
AOP-IOP relationship	(0.0895,0.1247) from Lee et al. (2002)
b_{bp} Exponent	Variation of (0:0.1:3)
$a_{nap+cdom}$ Exponent	Variation of (0.01:0.001:0.03)
a^*_ϕ	Linear Regressed a^*_ϕ from April
Inversion Method	Overconstrained Linear matrix inversion

4.6.2 QAA

Two versions of QAA were used : QAA-V5 which is the Version 5 of QAA developed in Lee et al. (2007) and described in section 3.3.2.1 and the QAA-Mishra developed in Mishra et al. (2014) for algal-bloom-dominated waters. The main difference of QAA-Mishra and QAA-V5 is the use of $a_T(708)$ (equations 4.28 and 4.29) for model parametrization (from equations 3.39 and 3.40 in section 3.3.2.1):

$$a_T(\lambda 0) = a_w(\lambda 0) + 10^{(-0.7153-2.054\cdot\chi-1.047\cdot(\chi^2))} \tag{4.28}$$

$$\chi = \log\left(0.01 \cdot \frac{R_{rs}(0-,443) - R_{rs}(0-,620)}{R_{rs}(0-,\lambda_0) + 0.005 \cdot \frac{R_{rs}(0-,620)}{R_{rs}(0-,443)} \cdot R_{rs}(0-,620)}\right) \tag{4.29}$$

were $\lambda_0 = 708$.

QAA-(Mishra and V5) outputs and Laboratory Measured $a_T(\lambda)$, $a_\phi(\lambda)$ and $a_{nap/cdom}(\lambda)$ were compared using *April* data. QAA-(Mishra and V5) outputs and ACS measured $a_T(\lambda)$ and Hydroscat measured $b_{bp}(\lambda)$ were also compared for *April*, *August* and for the combination of both, using RMSE and RPD index.

4.6.3 Nechad

The *Nechad* model was tested using both: Nechad et al. (2010) A^p and C^p parameters and derived from measured parameters as follows.

a) *For* April *field campaign* : The parameters A^p and C^p were calculated for specific $a_p^*(\lambda)$, $b_{b_p}^*(\lambda)$ and $a_{cdom}(\lambda)$ measured in *April*. A test was made with $a_{nap}^*(\lambda)$ instead of $a_p^*(\lambda)$ for C^p. For $a_p^*(\lambda)$, $a_{nap}^*(\lambda)$ and $b_{b_p}^*(\lambda)$ median and specific coefficients calculated using linear regression were tested (4.5.2.1 and 4.5.1).

b) *February and August* : Similar to *April* A^p and C^p were calculated for *February* and *August* using $a_p^*(\lambda)$, $a_{nap}^*(\lambda)$ and $a_{cdom}(\lambda)$ from *April* and $b_{b_p}^*(\lambda)$ measured in *February* and *August*. Similar to *April* tests, $b_{b_p}^*(\lambda)$ median and specific coefficients calculated using linear regression were tested (4.5.2.1 and 4.5.1). Tests were also performed grouping all stations from *February*, *August* and *April*.

c) *Linear Fitting for* A^p : A type II linear fitting was performed using TSM concentrations and the term $\frac{\rho_w}{1-\frac{\rho_w}{C^p}}$ from equation 3.58 in section 3.3.2.2 to compute A^p. Four fitted A^p were derived (*February*, *August*, *April* and *All Samples*) from $R_{rs}(0^-,\lambda)$, $R_{rs}(0^+,\lambda)$ and respective [TSM]. Half of the stations were used for calibration A^p and the other half for validation

For all tests, estimated TSM were compared to TSM concentrations (Second set of Samples were not used) using the statistical indexes RMSE and RPD.

5 DATA QUALITY ASSESSMENT

This chapter presents the results of the data quality assessment described in section 4.4 as follows: (a) For *In Situ Radiometric Measurements*: Comparison of different corrections of measured $R_{rs}^{Ab}(0^+, \lambda)$; Comparison of K-function approaches and test the impact of the number of measurements in the water column for K-functions and derived $R_{rs}^{Iw}(0^-, \lambda)$; Comparison of $R_{rs}^{Ab}(0^+, \lambda)$ and $R_{rs}^{Iw}(0^-, \lambda)$. (b) For *In-Situ IOPs*: Hydrolight experiments to assess the best set of corrections for the scattering effect in the absorption tube and for Hydroscat Sigma Corrections; comparison of LISST measurement replicas and LISST/ACS; Forward models tested for ACS, Hydroscat and $R_{rs}^{Ab}(0^+, \lambda)$and $R_{rs}^{Iw}(0^-, \lambda)$. (c) Laboratory replicas differences (a_p, a_ϕ and a_{nap}) and biogeochemical variables (TSM, TSOM and TSIM and Chla).

5.1 In-Situ Radiometric Measurements

5.1.1 Above Water Approach

Figure 5.1 presents the Non-corrected ($R_{rs-NC}^{Ab}(0^+, \lambda)$) spectra for *August* and *April* as well as ($R_{rs-\rho_{sky}}^{Ab}(0^+, \lambda)$) corrected for sky/sunglint effects (MOBLEY, 2015). Sky/sunglint correction caused a decrease in $R_{rs-NC}^{Ab}(0^+, \lambda)$ spectra in all wavelengths but particularity in the blue range (400 to 500 nm). As this region is more affected by sky/sunglint effects, this larger decrease in $R_{rs-\rho_{sky}}^{Ab}(0^+, \lambda)$ indicates that the correction was effective in removing them.

However, the correction caused negative values in $R_{rs-\rho_{sky}}^{Ab}(0^+, \lambda)$ below 400 nm and above 850 nm mostly in *April*. Overcast sky conditions or the presence of intermittent clouds were likely the cause of those negative values. Quality Control criteria 1 (QC1) shows that for all measured spectra in *August* and *April*, ≈ 26 % and ≈ 76 % resulted in $\frac{L_{sky}}{E_s} > 0.05$, respectively. For those conditions, values of $\rho_{sky} \cdot L_{Sky}$ can be higher than L_T due to an inadequate characterization of both, the skyglint and the ρ_{sky} factor. Particularity, for this study, the ρ_{sky} factor was based only on the θ_{sza} and on the geometry of acquisition since a full description of sky conditions was not available.

Figure 5.1 - *August* and *April* Non-Corrected (NC) and ρ_{sky} corrected

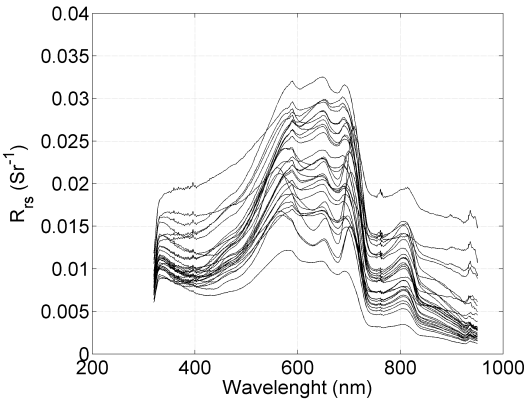

(a) *August* $R^{Ab}_{rs-NC}(0^+, \lambda)$

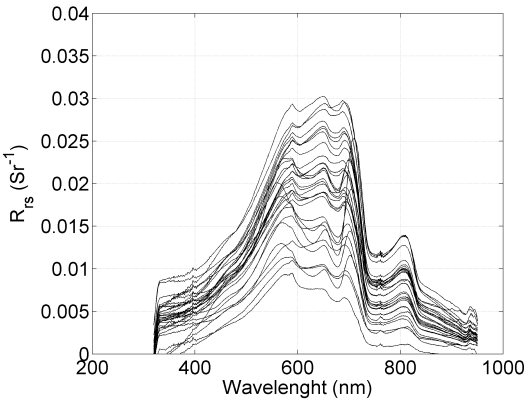

(b) *August* $R^{Ab}_{rs-\rho_{sky}}(0^+, \lambda)$

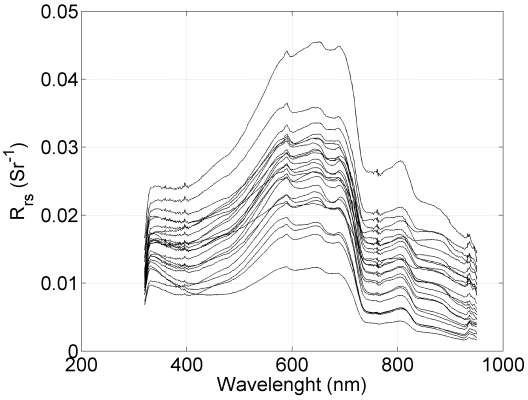

(c) *April* $R^{Ab}_{rs-NC}(0^+, \lambda)$

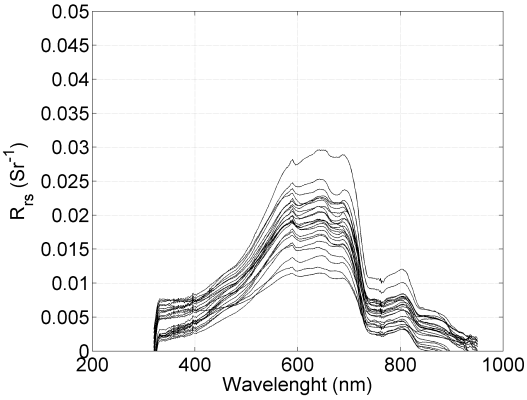

(d) *April* $R^{Ab}_{rs-\rho_{sky}}(0^+, \lambda)$

Spectra that passed the QC1 ($R^{Ab}_{rs-QC1}(0^+, \lambda)$) test are presented in Figure 5.2. All the spectra which violated QC1 were removed (five stations were removed from *August*, and fourteen from *April*). It is also worth mentioning that even after QC1, which supposedly presented only clear sky measurements, some spectra still presented high values in the blue region (400-500 nm), indicating an unsuitable sun/skyglint correction.

Figure 5.2 - *August* and *April* $R^{Ab}_{rs-QC1}(0^+, \lambda)$

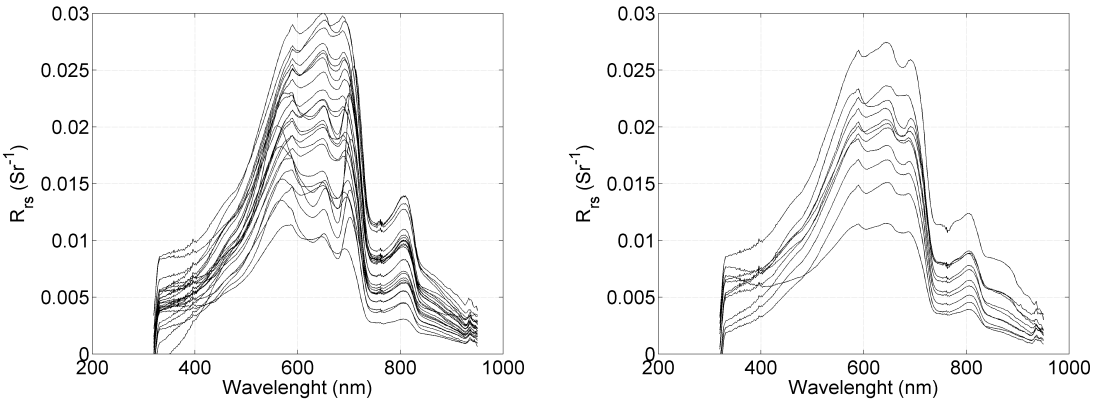

(a) *August* (b) *April*

The residual correction ($R^{Ab}_{rs-RC}(0^+, \lambda)$) is presented in Figure 5.3. As discussed in section 4.3.1.1, this correction used $R^{Ab}_{rs-\rho_{sky}}(0^+, 920)$ to normalize all spectra and account for cloud glint and illumination variation. Before normalizing, however, a filtering procedure discarded all spectra with negative values in 920 nm. Based on this criteria, no stations were removed. Although the assumption of 920 nm as a background is not completely suitable, since the signal in that wavelength can be related to some noise inherent to detector variability, the Residual Correction presented a satisfactory result, with no negative values in the visible region (400 to 700 nm).

Figure 5.3 - *August* and *April* R_{rs-RC}

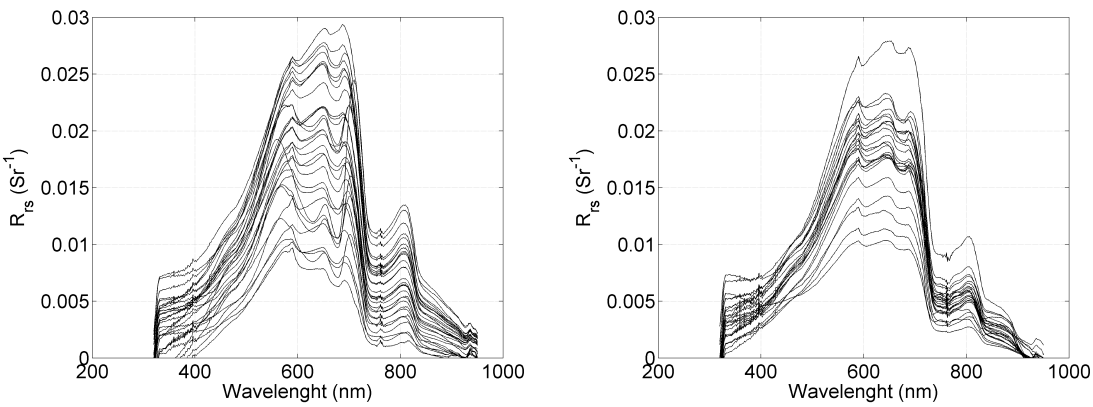

(a) *August* (b) *April*

The second criteria (QC2) to account for cloud glint and illumination variability (CV < 20 % in casts) removed one sampling station in both *August* and *April* campaigns (Figure 5.4). QC2 criteria resulted in $R^{Ab}_{rs-QC2}(0^+, \lambda)$ similar to $R^{Ab}_{rs-RC}(0^+, \lambda)$, regardless of one spectra in *August*. This similarity suggests the following: (1) QC2 was not effective enough to account for biased spectra, or, (2)$R^{Ab}_{rs}(0^+, \lambda)$ was not

sensitive to QC2.

Figure 5.4 - *August* and *April* $R^{Ab}_{rs-QC2}(0^+, \lambda)$

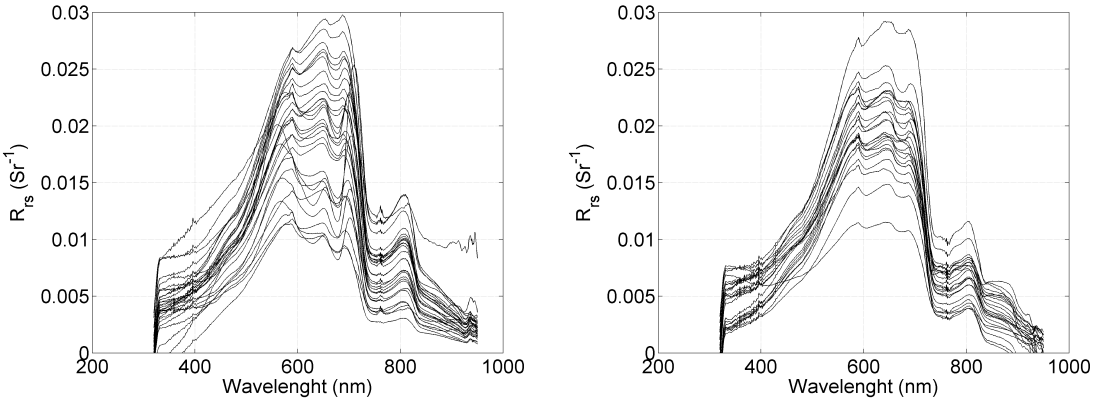

(a) *August* (b) *April*

Statistical indexes were calculated at each step, first taking R^{Ab}_{rs-NC} as reference for Mobley (2015) correction and then taking $R^{Ab}_{rs-\rho_{sky}}$ for the remaining corrections. The correction with the highest impact on R^{Ab}_{rs-NC} was then chosen.

Statistical Indexes analysis are presented in Figure 5.5. The greatest difference was observed between Non-Corrected $R^{Ab}_{rs-NC}(0^+, \lambda)$ and $R^{Ab}_{rs-\rho_{sky}}(0^+, \lambda)$ (blue curve), reaching almost -100 % (UPD) in *April* and a RMSE that reaches ≈ 0.01. The higher impact of sun/skyglint correction reinforces the need of this correction. Among the three tested filtering procedures (apart of sun/skyglint correction) the Residual Correction resulted in the largest differences when compared to $R^{Ab}_{rs-\rho_{sky}}(0^+, \lambda)$, reaching more than 20 % in the blue and infrared regions. QC1 and QC2 had a lower impact when compared to the residual correction, although differences could be as big as 5 to 10%.

Figure 5.5 - Above Water Corrections Statistical Indexes

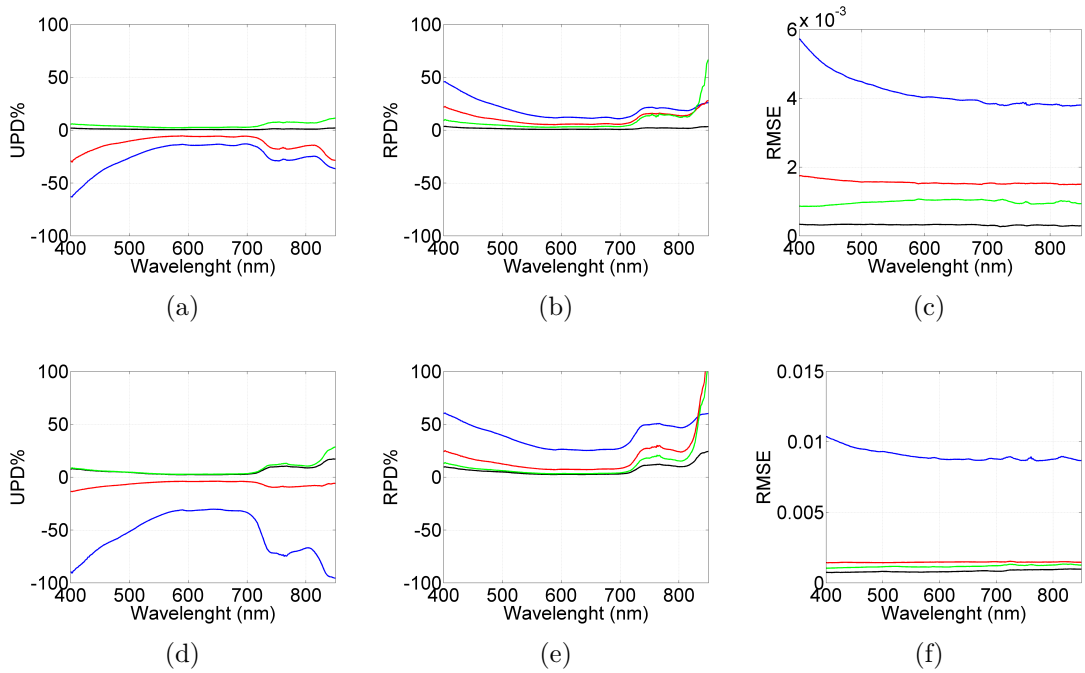

UPD(%), RPD(%) and RMSE for *August* (a,b,c) and *April* (d,e,f). Color Code (x_{test} and x_{ref}): Blue ($R^{Ab}_{rs-\rho_{sky}}(0^+,\lambda)$ and $R^{Ab}_{rs-NC}(0^+,\lambda)$); Red ($R_{rs-RC}$ and $R^{Ab}_{rs-\rho_{sky}}(0^+,\lambda)$); Black ($R^{Ab}_{rs-QC1}(0^+,\lambda)$ and $R^{Ab}_{rs-\rho_{sky}}(0^+,\lambda)$); Green ($R^{Ab}_{rs-QC2}(0^+,\lambda)$ and $R^{Ab}_{rs-\rho_{sky}}(0^+,\lambda)$)

Tests results indicate that sun/skyglint and the Residual Correction have the highest impact on measured $R^{Ab}_{rs-NC}(0^+,\lambda)$. Therefore, $R^{Ab}_{rs-RC}(0^+,\lambda)$ was used as input for Inverse Models (Chapter 7) testing. As QC1 and QC2 corrections did not present large differences in relation to $R^{Ab}_{rs-\rho_{sky}}(0^+,\lambda)$ and caused the discard of a significant number of measured spectrum they were not applied in the modeling process.

5.1.2 In-Water Approach

The use of a fixed depth approach (section 4.3.1) in very turbid shallow waters is mainly affected by sampling strategy and by the sink/depth rate applied to radiometric instrumentation. Figure 5.6 shows an example of downwelling irradiance (E_d) and upwelling radiance (L_u) profiles. It is noteworthy that light decays rapidly, losing $\approx 50\%$ of the signal in the first 50 cm.

The fixed depth approach, clearly, does not lead to continuous profiles, what decreases the quality of water column characterization. Instead, it leads to "punctual measurement clouds" which, due to the fast light decay with depth, dropping it quickly approaches towards zero, limiting the number of measurements for k-function calculation. Also the closer the values are from zero, the higher the uncertainty.

Regarding k-function calculations (section 4.3.1.2), Linear and Non-Linear approaches are mostly driven by measurements close to the surface. Regarding the Non-Linear approach, it seems that the curvature of the fitted exponential is mainly based on measurements closer to the surface (mostly above one meter depending on turbidity). The curvature also depends on wavelength. This is particularly essential for the blue range where the decay at its maximum, and for some stations, the decay is abrupt (blue dots of figure 5.6) making the calculation of k-functions impossible. The impact of deeper measurements on the Linear approach was, apparently, higher. When the logarithm transformation was performed (Equation 4.7), "measurement clouds" close to zero (deeper values) changed the slope what directly impacts on k-function calculation.

For the Weighted and Standard approaches, the effect of deeper measurements are related to the uncertainties within these measurements, where uncertainties are higher. The Weighted approach smooths k-function values. Extreme values within the water column, which could be due to measurement errors are eliminated. However, when those extreme values are related to true water column variability they are also lost. The same logic describes the Standard approach used in this work. The median of all k-functions using Standard approach for each profile also reduces variability.

Figure 5.6 - Example of Irradiance (E_d) and Radiance (L_u) profiles

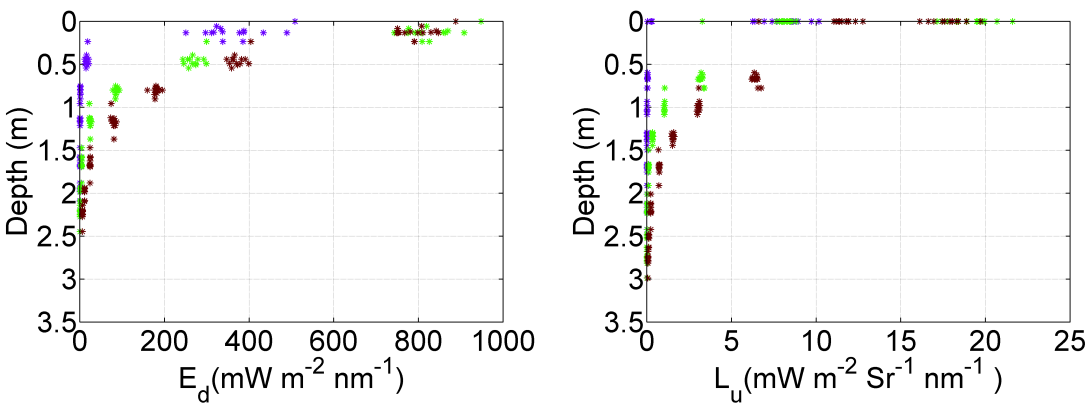

(a) (b)

Station from *April* field campaign. Color represent real visible wavelengths. Color code : Blue - *440 nm*; Green - *550 nm* ; red/brown - *676 nm*. Wavelengths were arbitrary chosen

Figure 5.7 presents the statistical indexes comparing Weighted, Standard and Linear

approaches, for *February*, *August* and *April*, taking the Non-Linear approach as reference (Section 5.1.2) . Linear approach presents the smallest differences (overall UPD and RPD $< 5\%$; RMSE <0.5) for most of the spectra, with a larger difference toward the green to blue range (500 to 550 nm). The Weighted approach presents RPD and RMSE similar to Linear approach, and an increase in the overall UPD, which indicates no bias between Linear and Weighted approaches, but a considerable difference between them. The standard approach presents the largest difference with the highest overall UPD, RPD and RMSE.

The comparison among seasons presented, as expected, higher statistical indexes for *February*, which agrees with the presence of the highest concentration of Optical Active Components (OAC) (Table A.2). However, the differences between seasons for each approach does not exceeds 5% in the $\approx$ 550 to 750 nm range, being much higher outside of it.

It is worth mentioning that the statistical indexes (figure 5.7) are somehow unexpected, especially due to the similarities amongst them. That could be explained by two factors: (1) homogeneity of the water column in most of the stations (better discussed in Chapter 6) which leads to similar low k_d variability; (2) k_d calculations driven by measurements closer to the surface, mainly the first meter depth. This is, in some way, relevant to shallow turbid lakes since any approach chosen to calculate k_d would have similar errors. However this similarity could also be related to the lack of measurements imposed by the choice of depth intervals for the fixed depth approach, which does not capture details of the water column variability.

Regarding k_{lu} calculations, figure 5.6 shows that the decay is similar to E_d. However, when compared to Irradiance, radiance values are much lower, causing an increase on measurement uncertainties, as observed in the statistical indexes below 550 nm and above 750 nm. That fact constrains the analysis of k_{lu} to the 600 to 700 nm interval. Differently from k_d statistical indexes, there is no pattern indicating which approach is the most similar to Non-Linear, used as reference. From UPD it is not possible to come up with a conclusion regarding the most stable approach, but RPD and RMSE shows that, despite of *April*, where the linear approach presents the lower values, *February*, *August* and *All Samples* are similar. Again, the similarity of those approaches are unexpected and could also be explained for the above mentioned reasons.

Figure 5.7 - Statistical Indexes comparing Non-Linear, Linear,Weighted and Standard for K_d (a,b,c) and K_{lu} (d,e,f) . $K_{d-NonLin}$ and $K_{lu-NonLin}$ were taken as reference.

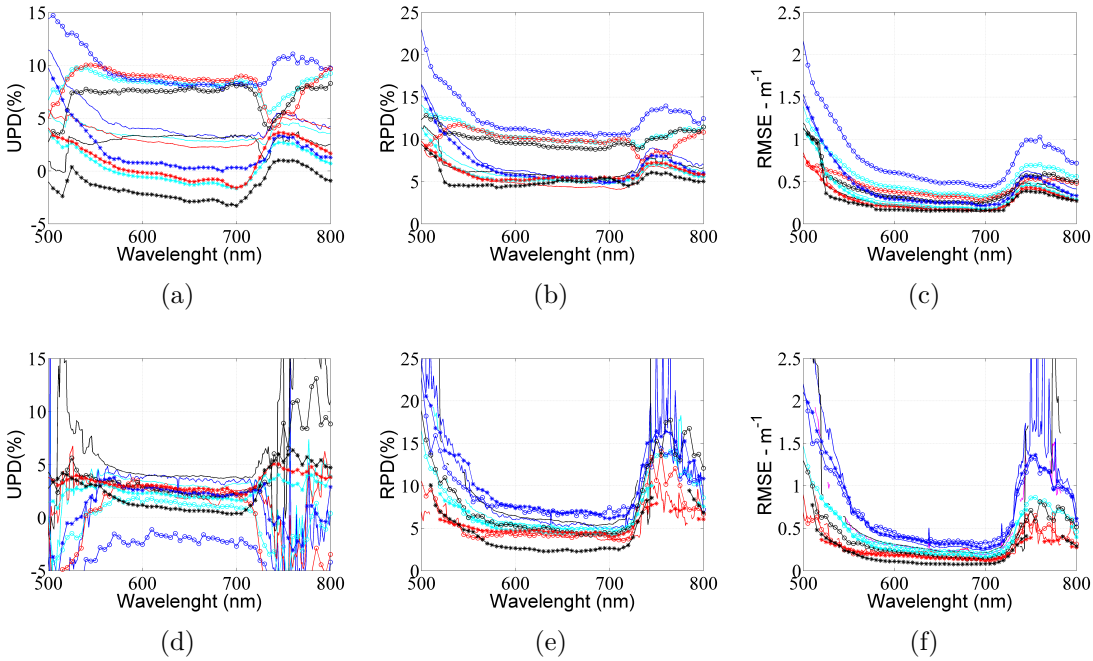

Symbol code: solid line: $K_{Ponderate}$, "o": $K_{Standard}$, "*": K_{Linear}. Color code : Black - All Samples; Blue - *February*; Red - *August*; Cyan - *April*

Figures 5.8 and 5.9 summarizes the results of the comparison of number of depth used to calculate K_d and K_{lu}, respectively (Section b). There is almost no difference between Linear and Non-Linear approaches when using measurements below 3 meters depth (Black), which is somehow expected, since, at larger depths almost no light is available. Meaningful differences were found when using measurements up to one (Blue) and two (Red) meters depth. For Non-linear Approach, K_{lu} (Figure 5.9 a, b, c) is slightly more affected by the choice of depths than K_d (Figure 5.8 a, b, c) although both k-functions presents low overall indexes (UPD $< 5\%$, RPD $< 6\%$ and RMSE < 0.2). The linear approach, on the other hand, is considerably affected by the choice of measurements in the water column. Specially for K_{lu}, UPD and RPD reaches 10% or higher, in the 550 to 700 nm interval, despite the fact that RMSE remain below 0.5 m^{-1}.

Regarding the differences among seasons, the choice of depths in the water column seems negligible for 2 meters (Red) but meaningful for 1 meter (Blue). For Non-Linear K_d (Figure 5.8 a, b, c), *August* (Symbol: "$-$") presented the highest overall

UPD although *April* (Symbol: "$*$") presented the highest RPD and RMSE. Non-Linear K_{lu} (Figure 5.9 a, b, c) reinforces *April* as the most affected by the choice of measurements in the water column. Possible explanations are the use of fixed depth approximate interval for each field campaign and the concentration of OACs. In *April*, radiometric measurements were performed within shorter measurement depth interval ($\approx$ 30 cm between measurements) which includes more observations in the 0 to 1 meter depth interval. Also, the lower concentration of OACs (Table A.2) decrease E_d and L_u decay rate and therefore deeper measurements become relevant to k-functions calculation.

Different from the Non-Linear approach, the effect of choice of measurements in the water column for 2 meters (Red curves) is not negligible for the Linear approach. Overall differences (UPD >0.5 % and RPD > 1% are observed for K_d and K_{lu}. But similar to the Non-Linear approach, the largest differences are observed within the 0 to 1 meter depth interval. Also, similar to the Non-Linear approach, *April* presents the highest statistical indexes.

Figure 5.8 - Depth comparison for Non-Linear (a,b,c) and Linear (d,e,f) K_d

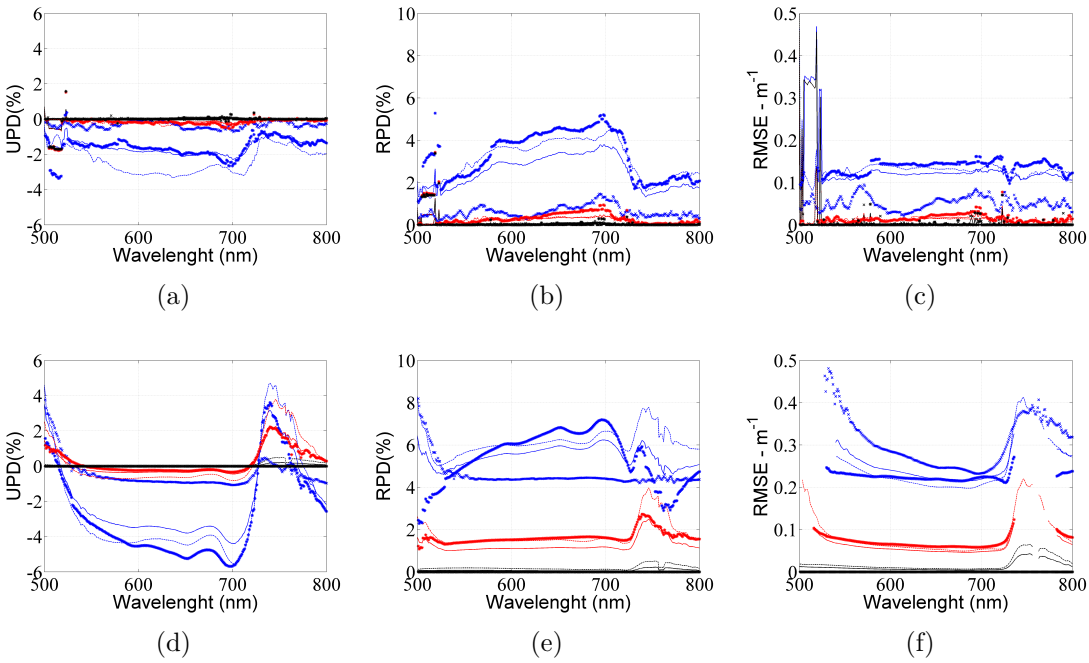

K_d using All measurements at all depths was taken as reference. Symbol code : Solid Line - All Samples; "x" - *February*; "–" - *August*; "*" - *April*; Color code : Blue - All Measurements above 1 meter depth; Red - All Measurements above 2 meter depth; Black - All Measurements above 3 meter depth;

Figure 5.9 - Depth comparison for Non-Linear (a,b,c) and Linear (d,e,f) K_{lu}

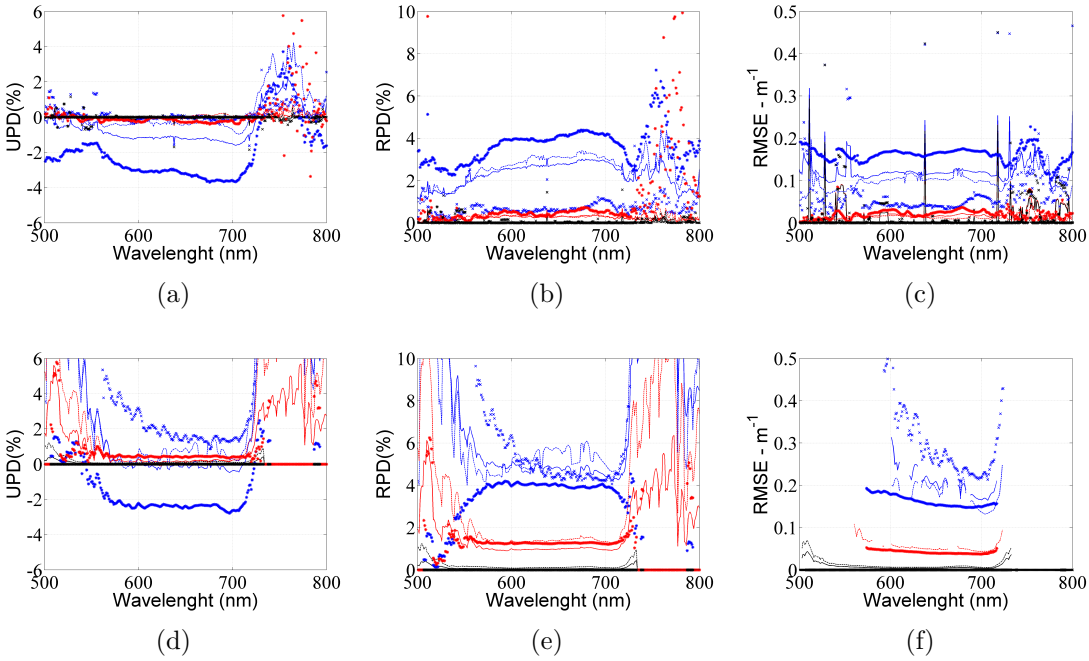

K_{lu} using All measurements at all depths was taken as reference. Symbol code : Solid Line - All Samples; "x" - *February*; "–" - *August*; "*" - *April*; Color code : Blue - All Measurements until 1 meter depth; Blue - All Measurements until 2 meter depth; Black - All Measurements until 3 meter depth;

As previously discussed, the choice of approach, as well as the selected depth interval used to calculate k-functions, directly influences the calculation of $E_d(0-)$ and $L_u(0-)$. Figure 5.10 presents the statistical indexes for modeled R_{rs} from Non-Linear and Linear approaches described in section 5.1.2c. Similar to K_{lu}, below 550 nm and above 700 nm, statistical indexes present higher values (positive and negative) mainly due to errors driven by the fixed depth approach. In the 600 to 700 nm interval, UPD presents values lower than 5% and similar for all seasons. RPD otherwise, shows a high bias, with differences larger than 30% in the 600 to 700 nm interval and 100% outside of that interval. RMSE shows even larger differences. Those indexes show a significant bias between Linear and Non-Linear approaches to estimate $E_d(0-)$ and $L_u(0-)$ and therefore to model $R_{rs}(0-)$.

Figure 5.10 - Comparison of $R_{rs}(0^-)$ derived from Linear and Non-Linear K-functions approaches

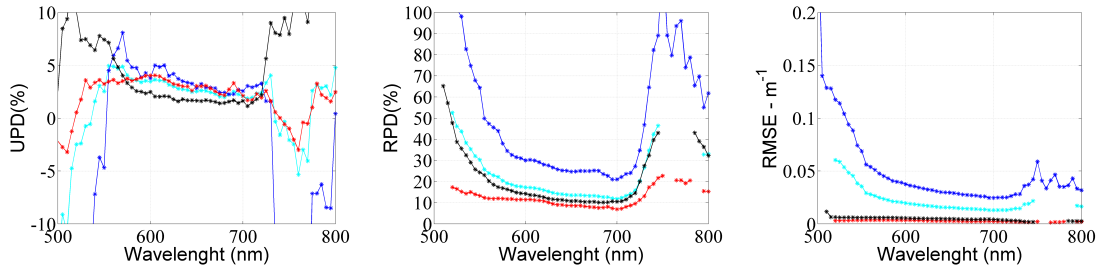

(a) (b) (c)

$R_{rs-NonLin}$ was taken as reference. Color code : Black - All Samples; Blue - *February*; Red - *August*; Cyan - *April*

Figure 5.11 shows the results for the impact of computing approaches (Non-Linear and Linear K-function) on derived $R_{rs}^{Iw}(0^-, \lambda)$ as discussed in section 5.1.2. Figure 5.11 suggests that the Non-Linear approach, despite of the local spikes, displays higher stability than Linear approach for the fixed depth dataset. Similar K_d and K_{lu} for 1 meter depth interval, presented the highest indexes for *April*.

Figure 5.11 - Depth comparison $R_{rs}(0-)$ from Non-Linear (a,b,c) and Linear (d,e,f) K-function approaches

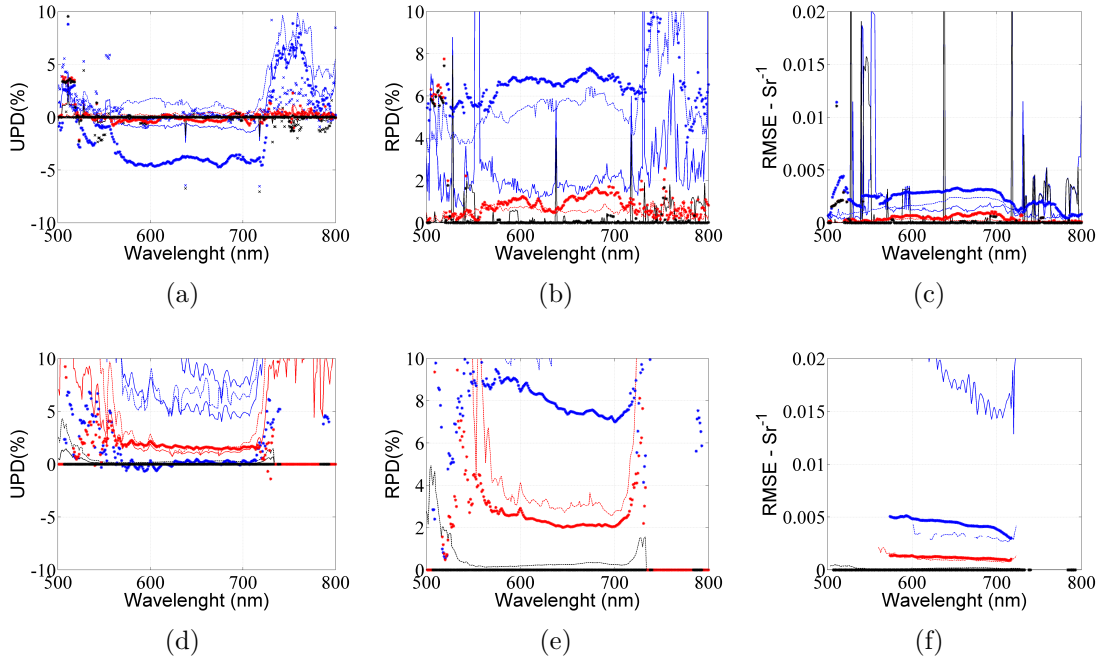

$R_{rs}(0-)$ using All measurements at all depths was taken as reference. Symbol code : Solid Line - All Samples; "x" - *February*; "–" - *August*; "*" - *April*; Color code : Blue - All Measurements until 1 meter depth; Blue - All Measurements until 2 meter depth; Black - All Measurements until 3 meter depth;

Despite the fact that the different approaches have impact on the k-functions, their differences are commonly below 10 % in the 550 to 750 nm, what is reasonably acceptable. The differences on k-functions and estimated $R_{rs}^{Iw}(0^-)$ computed with different number of measurements in the water column are also below 10 %. Based on those analysis, the Non-Linear Approach, in the 500 to 800 nm interval, seems to be the best approach to derive k-functions and $R_{rs}^{Iw}(0^-)$.

The Linear approach seems to be more affected by the fixed depth approach adopted in this study. Due to the rapid decay of $E_d(0^-, \lambda)$ or $L_u(0^-, \lambda)$, the measurements are confined in two "big data clouds", one close to the "surface" and a second one close to "zero". This behavior is somehow biased and do not represent the complete water column. The Non-Linear approach fits an exponential to measured data, and although influenced by the decay of Radiance and Irradiance, it better represents the water column K-functions and $R_{rs}^{Iw}(0^-)$.

5.1.3 Comparing Above and In Water R_{rs} Approaches

The results from the comparison between $R_{rs}^{Ab}(0^-,\lambda)$ and $R_{rs}^{Iw}(0^-,\lambda)$ are presented in Figure 5.12. Indexes are considerably high reaching 60% RPD, 60% UPD and 0.02 RMSE in the 550 to 700 nm interval. Below 550 nm and above 700 nm differences reach extreme values, mostly due to, already discussed, underestimation of $L_u(0^-)$ (Section).

$R_{rs-RC}^{Ab}(0^-,\lambda)$ (Black) is the correction with the largest agreement with Non-linear R_{rs} ($R_{rs-NonLin}^{Iw}(0^-,\lambda)$) having an overall UPD below 30% in the 550 to 700 nm interval. $R_{rs-NC}^{Ab}(0-)$ (Red) presents the highest overall UPD, RPD and RMSE. All above water corrections cause a decrease in $R_{rs-NC}^{Ab}(0^-,\lambda)$ values, which increases the agreement to $R_{rs-NonLin}^{Iw}(0^-,\lambda)$. Also the underestimation of $Lu(0^-,\lambda)$ causes a decrease in $R_{rs-NonLin}^{Iw}(0^-,\lambda)$ contributing to larges discrepancies between $R_{rs-RC}^{Ab}(0^-,\lambda)$ and $R_{rs-NonLin}^{Iw}(0^-,\lambda)$.

Figure 5.12 - Comparison of Above Derived $R_{rs}^{Ab}(0^-,\lambda)$ and In-Water Non-Linear derived $R_{rs}^{Iw}(0^-,\lambda)$ for *August* + *April* (All samples from *August* and *April*)

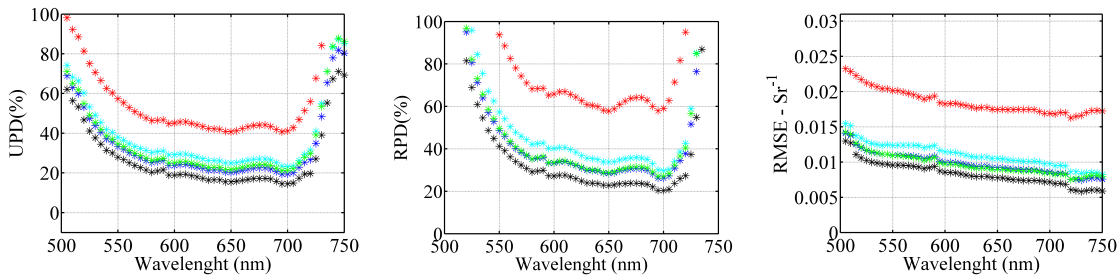

(a) (b) (c)

Non-Linear R_{rs} was taken as reference. Color Code for tested R_{rs}^{Ab}: Red = $R_{rs-NC}(0^-,\lambda)$, Blue = $R_{rs-\rho_{sky}}^{Ab}(0^-,\lambda)$, Black = $R_{rs-RC}^{Ab}(0^-,\lambda)$, Cyan = $R_{rs-QC1}^{Ab}(0^-,\lambda)$, Green = $R_{rs-QC2}^{Ab}(0^-,\lambda)$

Shading effects, illumination variation, sun/skyglint effects and underestimation of $Lu(0-)$ in In-Water R_{rs} calculations and also bidirectional effects are the main reasons for the discrepancies between $R_{rs-RC}^{Ab}(0^-,\lambda)$ and $R_{rs-NonLin}^{Iw}(0^-,\lambda)$. $R_{rs-RC}^{Ab}(0^-,\lambda)$ and $R_{rs-NonLin}^{Iw}(0^-,\lambda)$ are affected by shading effects since all measurements were performed close to the vessel, but with different error sources. Regarding $R_{rs-RC}^{Ab}(0^-,\lambda)$ only L_w is affected since E_s was measured using a pole on the top of the vessel, which prevents any influence from shading. Lw is also corrupted

for platform reflection both directly and indirectly from the water surface, into the sensor's field of view. Non-linear $R_{rs}(0-)$, on the other hand, is corrupted by shading effects which obstruct L_u and E_d profiles simultaneously and at an specific geometry. Bidirectional effects also affects mainly above water measurements, especially due to the high anisotropy caused by particle size and IOPs dependency (PARK; RUDDICK, 2005; LEE et al., 2004; RUDORFF, 2013). Although (LOISEL; MOREL, 2001) showed not a drastic variability for high loaded TSM waters, further investigations should be addressed in future studies.

5.2 In-Situ IOPs

5.2.1 ACS and Hydroscat Corrections - Hydrolight Experiments

The results regarding the Absorption Tube Scattering Correction and Sigma Correction (section 4.4.2) are presented in the following. Figure 5.13a presents an example of different types of correction methods on the effects of the *absorption tube scattering* on both, ACS and Hydroscat measurements for a given sampling station measured in *February*. Overall, the *Zaneveld* (Section 4.3.2.1) correction provides the largest underestimation of absorption providing unrealistic values mainly in the 700 to 750 nm interval. This effect is also observed in the *Flat* correction with values dropping to zero in the 730 to 750 nm interval which is not expected in mineral rich waters. *Kirk* and *Rottgers* corrections present more acceptable values mainly in the infrared range since, for that spectral region, absorption is not zero for turbid waters. The *absorption tube scattering* effect on the sigma corrected Hydroscat measurement (figure 5.13b) reinforces the need of that correction, mainly due to its impact on the slope of b_{b_p} spectra.

Figure 5.13 - Absorption Tube Scattering Correction Effect on ACS Absorption and Backscattering Measurements for a selected station from *February*

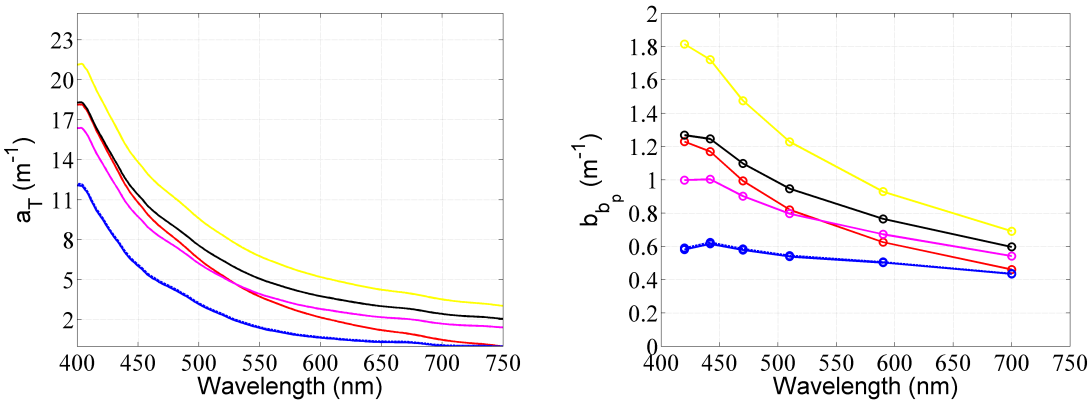

(a) ACS - Absorption (b) Hydroscat - Backscattering

Yellow - Non Corrected; Blue - Zaneveld Correction; Red - Flat Correction ; Black - Kirk Correction; Magenta - Rottgers Correction;

Regarding the Sigma Correction, the influence of K_{scat} (Equation 4.16) variability on b_{b_p} is exemplified on figure 5.14 for the same sampling station and season. The difference between the solid black curve ($K_{scat} = 0.4$) and the red curve ($K_{scat} \approx 0.1$) decreases from $\approx 1.4\ m^{-1}$ in the 420 nm to $\approx 0.2\ m^{-1}$ in 700 nm. That shows the meaningful impact of K_{scat}, specially on the b_{b_p} slope, which shows the necessity to examine the influence of Hydroscat corrections on IOPs dataset.

Figure 5.14 - Sigma correction parameter K_{scat} variability for a selected station from *February*

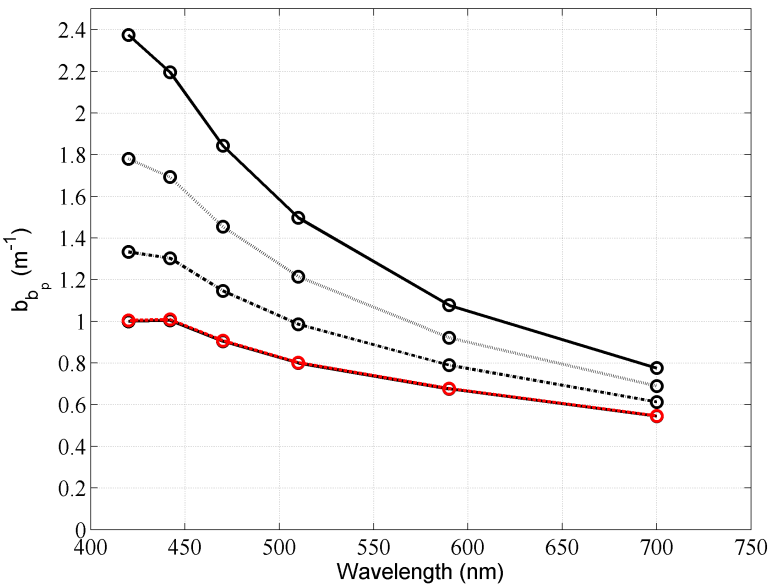

(a) Variability of K_{scat} in the 0.1 to 0.4 interval with 0.1 step. Red represents the *Doxaran* correction. Line code - Dashed (–) $K_{scat} = 0.1$, Dashed/Dotted (.-) $K_{scat} = 0.2$, Two Points/Grey (:) $K_{scat} = 0.3$, Solid $K_{scat} = 0.4$

The results of the Hydrolight experiments, described in section 4.4.2 are presented for each field campaign in the Appendix C Figures C.1, C.2 and C.3. The comprehensive inspection of those figures that allowed to pinpoint the the most consistent set of corrections for ACS/Hydroscat data are synthesized in Table 5.1.The inspection criterion was to select a pair of correction for each AOP, within each season, according to the quality of the statistical indexes for the overall spectra. Table 5.1 analysis is focused in two sets of variables: (1) $K_d(\lambda)$; (2) $R(0^-, \lambda)$ and $R_{rs}(0^-, \lambda)$ comparisons.

The background for this division is the fact that K_d is directly proportional to absorption and backscattering ($K_d \propto$ (a + b_{b_p})) (MOBLEY, 1994; KIRK, 2010) but the absorption dominates that proportionality. Therefore K_d analysis is useful in the identification of optimal scattering corrections for the absorption tube. $R(0^-, \lambda)$ and $R_{rs}(0^-, \lambda)$ are, on the other hand, proportional to $(b_b/(a + b_b))$ and therefore, backscattering has a much higher impact on the proportionality.

Results (Figure 5.1) shows that *Rottgers* correction provided the most consistent closure for the *absorption tube scattering correction* whereas *Doxaran* correction had a better performance for the majority of the comparisons (7 out of 12). Based on these analysis, the pair *Rottgers/Doxaran* was chosen for processing ACS/Hydroscat IOPs, and from now on, all the results are based on those corrections.

Table 5.1 - Best ACS/Hydroscat correction for each field campaign for the tested AOPs. Color in the table are colors from curves in Appendix C.

Season	AOP	ACS/Hydroscat Correction	Color of Each Correction
February	$R(0^-)$	Rottgers/Doxaran	Magenta
		0.18/Doxaran	Cyan
	$R_{rs}(0^-)$	Rottgers/Doxaran	Magenta
		0.18/Doxaran	Cyan
	K_d	Rottgers/0.03	Green
		Rottgers/0.4	Yellow
August	$R(0^-)$	Rottgers/Doxaran	Magenta
		0.18/Doxaran	Cyan
	$R_{rs}(0^-)$	Rottgers/0.4	Yellow
		Zaneveld/0.03	Red
	K_d	Rottgers/0.03	Green
		Rottgers/Doxaran	Magenta
April	$R(0^-)$	Rottgers/Doxaran	Magenta
		Rottgers/0.4	Yellow
	$R_{rs}(0^-)$	Zaneveld/0.03	Red
		Rottgers/0.4	Yellow
	K_d	Rottgers/0.03	Green
		Rottgers/Doxaran	Magenta

Hydrolight closure experiment, sometimes, resulted in mismatches as high as 100% for the Irradiance Reflectance (RPD >90 % in February) with RMSE of up to 6 (No-Units) Appendix C. For August and April those indexes (UPD, MRPD and RMSE) are lower but could still can reach 50 % (Kd-UPD >50% in August and Kd-UPD >60% in April). Careful closure experiment results usually agree within 20-30% (MOBLEY, 1994; MOBLEY et al., 2002; TZORTZIOU et al., 2007). Those results highlight the hindrance involving the acquisition of consistent optical measurements using commercial technology in turbid environments, where inorganic particulate concentrations are very high. However, the current analysis improved the results discussed in Sander de Carvalho et al. (2015) and suggests that a common correction

applied to all field campaigns are more appropriate and general than tuning one specific correction for each station, as previously suggested.

5.2.2 Lisst Experiments

Figure 5.15 presents the comparison between ACS and LISST Attenuation Coefficients in 670 nm. Although, theoretically, those instruments are not comparable due to differences in the acceptance angle (0.93° for the ACS and ≈ 0.0269° for the LISST), Boss et al. (2009) shows that the ratio $\frac{c_{ACS}}{c_{LISST}}$ can reach 0.4 for Ocean Case 2 waters (Martha's Vineyard Coastal Observatory) and, although depending on the shape of the VSF, the acceptance angle effects can be higher for turbid Curuai Lake Waters. For most of the stations (12), for replicas, the $\frac{c_{ACS}}{c_{LISST}}$ ratio presents values below 0.4 (blue flat line). Among those stations,the $\frac{c_{ACS}}{c_{LISST}}$ ratio is below 0.33 for eight stations and only for three of them $\frac{c_{ACS}}{c_{LISST}}$ is below 0.25. Therefore, the measurements for both instruments are within the expected $\frac{c_{ACS}}{c_{LISST}}$ values. Table 5.2 shows that, as expected, indexes are very high reaching RPD values up to 156 %.

Figure 5.15 - Comparison ACS and LISST (670 nm) - *April*

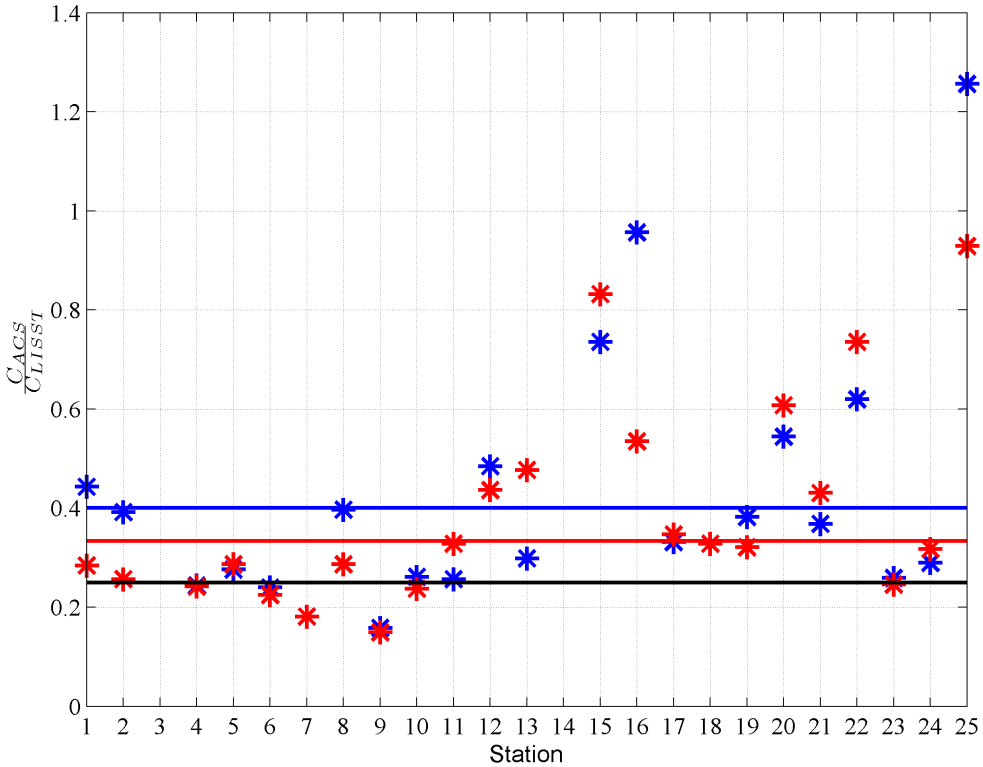

Color code : Blue-First Set of Samples; Red-Second Set of Samples. Solid lines indicate 0.4 (Blue), 0.33 (Red) and 0.25 (Black)

Table 5.2 also shows consistency between replicas with UPD of $\approx$ 5%, RPD of $\approx$ 16% and RMSE of $\approx$ 4 m^{-1}. As mentioned before the comparison of LISST and ACS is somehow biased due to acceptance angle effects, but also consistent with literature. That supports the quality of the Particle Size Distributions (PSD) derived from LISST measurements. It is worth mentioning however, that errors could arise from particle type, inversions strategies and presence of bubbles in the measurement chamber. Those aspects will be further discussed in Chapter 6.

Table 5.2 - LISST Statistical Indexes

Replicas	Indexes		
	UPD	RPD	RMSE
LISST First and Second Set of Samples	-5.026	16.840	4.027
LISST First Set and c_{ACS}	74.176	144.298	13.666
LISST Second Set and c_{ACS}	78.198	156.535	14.606

5.2.3 Forward Models Performance

Polynomial Fitting using *Morel* and *Gordon* model approximations (Equations 3.36, 3.35, 3.37) was performed to relate AOPs ($R^{Iw}_{rs-NonLin}$ and R^{Ab}_{rs-RC}) to IOPs (Rudick/Doxaran corrected a_T and b_{b_p} from ACS/Hydroscat) for *August* + *April* dataset. The fitting results are summarized in Figure 5.16. It is worth mentioning that Park and Ruddick fourth order polynomial model (PARK; RUDDICK, 2005) was also tested but results were out of range in relation to the coefficients presented in RuddickWebsite (2015) and therefore are not discussed.

The polynomial fit for f/Q and f'/Q per wavelength (Figure 5.16a) shows that f/Q and f'/Q'varies with wavelength and are similar in shape and magnitude along the spectra, except for the 400 to 500 nm interval, where errors are substantial (section 5.1.3). As simulated by Loisel and Morel (2001), values of f/Q and f'/Q are approximately within the 0.08 to 0.13 range for type II waters. The values in Figure 5.16a, however, are much higher for all wavelengths except beyond 700nm. Although the comparison between f/Q, f'/Q and the values from Loisel and Morel (2001) is not completely adequate due to errors in both,R_{rs} and IOPs measurements, it is worth saying that this difference is unexpectedly small.

Figure 5.16b shows that none of the R_{rs}s used as input to Gordon second order model (Equation 3.37) provided g_0 and g_1 values similar to those of the literature (0.089 and 0.125 (LEE et al., 2011)). Moreover, the computed g_0 and g_1 vary widely along the wavelengths, depending on the input R_{rs}s.

Figure 5.16 - Results for Polynomial Fitting applied for Morel's and Gordon's First and Second Order models.

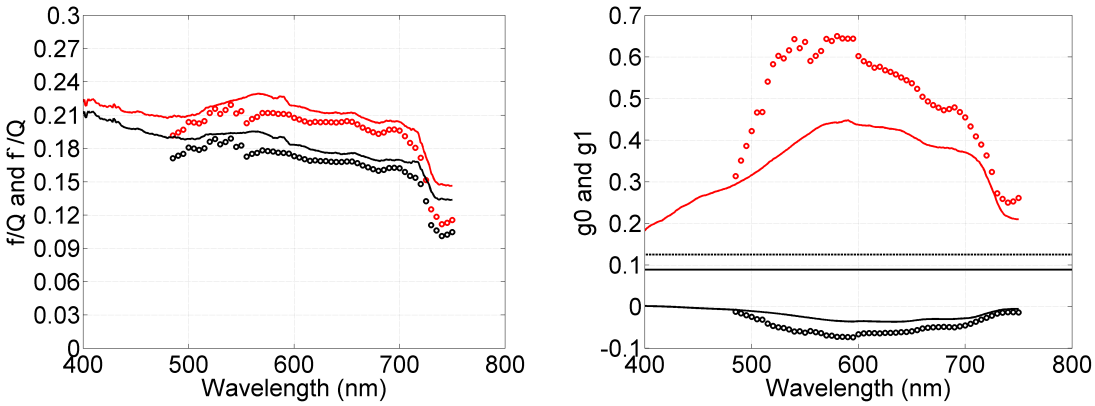

(a) (b)

Figure (a) presents results for Morel's and Gordon's First order models and Figure (b) presents results for Gordon's Second Order models. Solid Lines represent fitting with $R_{rs}^{Ab}(0^-, \lambda)$ and "o" symbol represent fitting with $R_{rs}^{Iw}(0^-, \lambda)$. Figure (a) Color code: Black: Morel Model f/Q (Equation 3.36), Red - First Order Gordon Model f'/Q (Equation 3.35). Figure (b) Color code: Black "g0" and Red "g1". Straight lines show the Lee et al. (2011) (0.08 and 0.12)values

The median coefficients (f/Q, f'/Q', g_0 and g_1) computed using all sampling stations in *August* and *April* are summarized in Table 5.3. They are the output of the Non-Linear fitting applied to Gordon and Morel modeling and resulted in the same conclusions as the analysis of figure 5.16 in the following aspects: (1) f/Q and f'/Q' are similar to literature values and independent of models and R_{rs}s choice. (2) g_0 and g_1 using R_{rs}^{Iw} is completely out of the literature range, whereas for R_{rs}^{Ab}, the median is near the literature range. That's to say that measured values were able to provide better estimates of f/Q and f'/Q' than g_0 and g_1.

Table 5.3 - Derived coefficients for R_{rs}/IOPs models by Non-Linear Fitting

		$R_{rs}^{Iw}(0^-, \lambda)$ (500-700 nm)		$R_{rs}^{Ab}(0^-, \lambda)$ (400-750 nm)	
	Coefficient	Median	Std	Median	Std
$R_{rs} = f/Q \cdot (b_b/a)$	f/Q	0.15	0.07	0.18	0.03
$R_{rs} = f'/Q \cdot (b_b/a + b_b)$	f'/Q	0.17	0.09	0.21	0.04
$R_{rs} = g_0 \cdot (b_b/a + b_b) + g_1 \cdot (b_b/a + b_b)^2$	g_0	0.04	1.29	0.19	0.06
	g_1	0.73	7.24	0.18	0.38

This analysis show that the poor performance of both Polynomial and Non-Linear Fitting between AOPs (R_{rs}^{Iw} and R_{rs}^{Ab}) and IOPs (ACS a_T and b_{b_p}) may be related,

mainly, to measurement errors. First, the poor performance of the polynomial fitting, g_0 and g_1, indicates that both R_{rs}^{Iw} and R_{rs}^{Ab} are controlling the AOP/IOP relationship. This is specially true for g_1 whose shape follows the spectral behavior of R_{rs}, with a maximum in the green range decreasing towards the infrared. The spectral dependence of g_0 is not as noticeable but still varies with wavelength, reaching a minimum in the green region. Second, it seems that, independent of the selected first order modeling, it provides an estimate of f/Q and f'/Q coefficients closer to range reported in the literature, having a much better performance than the second order model for the data available.

5.3 Laboratory Measurements Uncertainty

Particle absorption coefficient (a_p) phytoplankton absorption (a_ϕ) and Non-Algal Particles absorption (a_{nap}) were analyzed only for *April*. Out of 25 stations sampled in *April*, 5 from a_{nap} and 9 from a_ϕ were discarded due to negative values.

Statistical indexes comparing (a_p), (a_ϕ) and (a_{nap}) replicas are presented in figure 5.17. Indexes show very high values for the particle absorption coefficient (a_p) with a UPD higher than 10%, RPD higher than 30% for all wavelengths and up to 1.3 m^{-1}. Despite the large bias, with an RPD that reaches 30% for longer wavelengths, the Non-Algal Particles absorption (a_{nap}) presented the best agreement with a UPD lower than 5% UPD and RMSE ≤ 0.5. Phytoplankton absorption (a_ϕ) reaches UPD and RPD values higher than 25% and 80% respectively and a RMSE reaching up to 0.7 m^{-1}.

Several reasons explain the large differences between replicas. (1) the filtering procedure performed with a manual pump, in a high TSM concentration environment and using a 47 mm diameter filter could explain the a_p UPD values, specially in the infrared region where a_p values are lower. (2) a_p RPD shows a bias which could not be explained by sampling, and might be related to the absorption measurement method. The position of the filter in the spectrophotometer might create a persistent error, that would increase with lower absorption values, observed in larger wavelengths.

Regarding the pigment extraction, following Tassan and Ferrari (1995), the 10% solution of NaClO was used, since it is supposed to be more effective for turbid inland waters. However, the variability of phytoplankton species could affect pigment extraction time. Some phytoplankton absorption features are therefore observed in a_{nap} spectra. Another reason for the high discrepancies observed are related to the

NaClO solution used for pigment extraction. NaClO might remove material out of the filter surface depending on the time of sample exposure to the solution which can cause change in absorption coefficient. Both reasons might also contribute for corrupting the samples (with zeroed values), removing them from the statistical analysis.

The method suggested by Bricaud et al. (2010) resulted in discrepancies between Replicas, depending on the wavelength. For a_{nap} and $a_{nap-fit}$ (Black curve) UPD values are almost identical, but from 400 to 600 nm RPD and RMSE are different. For RPD values are higher for $a_{nap-fit}$ (40 % and below 20 % for a_{nap}) which changes above 600 nm. For RMSE the difference is very high being $a_{nap-fit}$ higher for all spectra. For $a_{\phi-fit}$, difference of statistical indexes are higher for UPD and lower for RPD and RMSE. $a_{\phi-fit}$ is negatively higher for UPD and RPD is lower for all spectra. RMSE is almost the same being slightly lower for a_{nap}. Those statistics show that the applicability Bricaud et al. (2010) method is questionable for this dataset when comparing Replicas and will not be considered in further analysis.

Figure 5.17 - Statistical Indexes for Laboratory Spectrophotometer Absorption Particulate Material, Non-algal Particles and Phytoplankton (a_p, a_{nap}, a_ϕ) - *April*

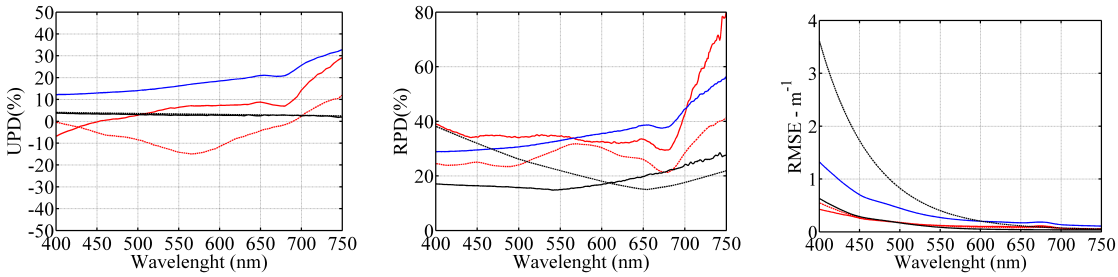

(a) (b) (c)

Solid Line : Blue - a_p; Black - a_{nap}; Red - a_ϕ;. Dashed Line : Modeled by Bricaud et al. (2010) and colors represent the same optical components. First set of measurements were taken as reference for statistical indexes calculations.

Figure 5.18a presents the comparison of a median of ACS total absorption coefficient (a_{T-w}) from 0.5 to 1 meter depth and both, first and second set of samples for the Laboratory total absorption, for each station of *April* field campaign. UPD and RPD indexes (Figure 5.18b and c) show that differences start from ≈ 40% and 50% for UPD and RPD respectively in the blue range raising up to 120 % and % 200 in the NIR range, being ACS absorption higher than both Laboratory set of samples

although RMSE (Figure 5.18d) is higher in the blue range. The higher values for ACS absorption are somehow expected since even with the most suitable correction (*Rottgers*), overestimation of absorption is still an issue. However it is important to point out that in the characteristic Chla peak region in (676 nm), there is an abrupt decrease of both UPD and RPD indexes, indicating that at this wavelength there is an agreement between both measurement techniques. Figures 5.18b, c and d shows almost no difference for the comparison of ACS and Laboratory first and second set of samples.

Figure 5.18 - Comparison of Total Absorption Coefficients from ACS (a_{T-w}) and Laboratory ($a_{T-w} = a_p + a_{cdom}$) for *April*

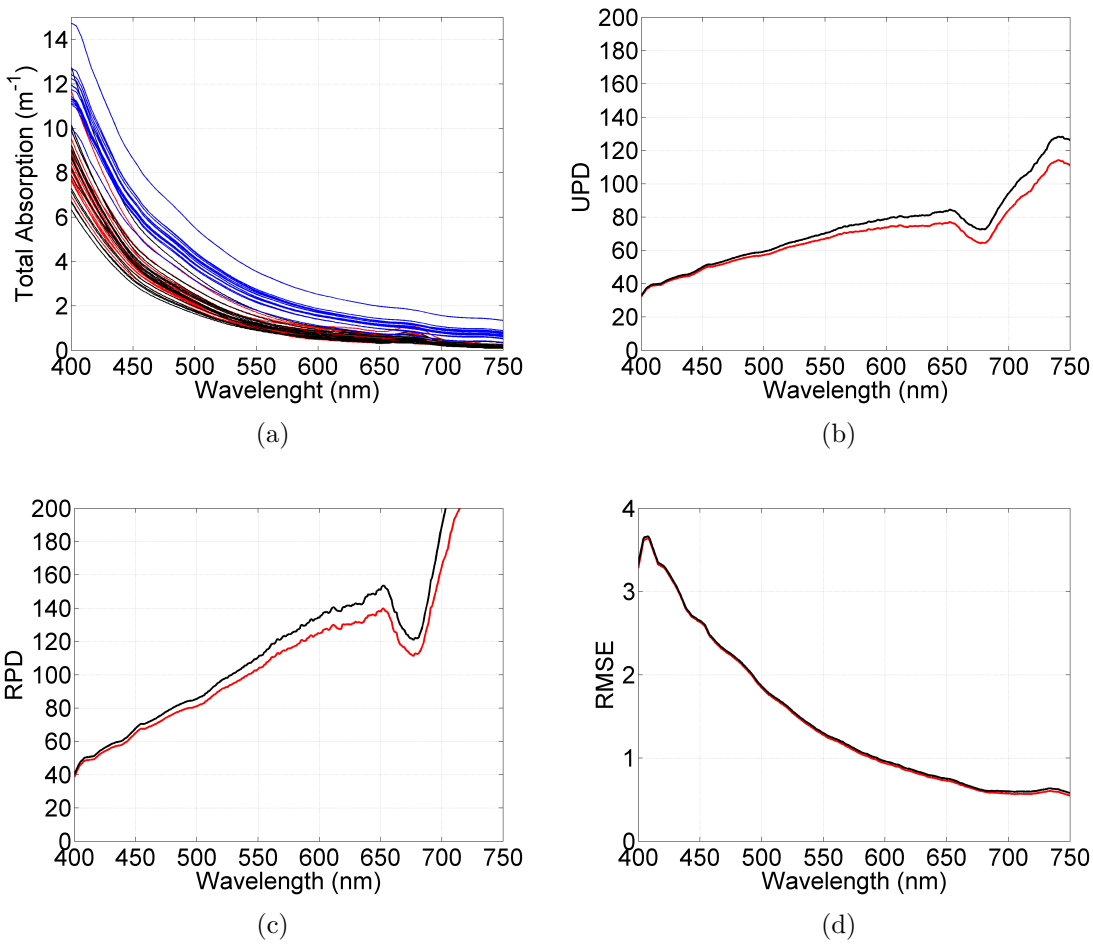

ACS (a_{T-w}) was corrected by Rottgers (a_{rott}) correction. Color code (a) Blue: ACS Absorption, Red: First set of samples of Laboratory Absorption, Black: Second set of samples of Laboratory Absorption. For the statistical indexes calculations (using all samples of *April*) in figures (b), (c), (d) (Red = First set of samples, Black: Second set of samples) Laboratory Absorption was taken as reference.

Table 5.4 presents the statistical indexes for TSM, TSIM, TSOM and Chla replicas. For suspended material, UPD are lower than ± 10 % for all field campaigns but RPD are significantly higher, reaching values up to 58 % in *February*. This suggests a systematic bias between the samples which might indicate problems with concentration determination, particularly for TSOM and TSIM. RMSE shows a reasonable good agreement, reaching its highest value for TSM in *February* (5.451 $mg \cdot L^{-1}$). The same behavior is observed for Chla replicas, which shows higher RPD for all field campaigns. Both, UPD and RMSE show a good agreement for replicas being lower than ≈ 5 % and 1.2 ($\mu g L^{-1}$) respectively.

Table 5.4 - Indexes for Biogeochemical Variables - Replicas

Stations	Index	TSM ($mg \cdot L^{-1}$)	TSOM ($mg \cdot L^{-1}$)	TSIM ($mg \cdot L^{-1}$)	Chla ($\mu g L^{-1}$)
All Seasons	UPD	2.381	3.788	1.126	4.501
	RPD	12.394	35.436	17.149	10.093
	RMSE	3.548	1.884	3.076	1.070
September	UPD	1.886	3.335	0.667	3.469
	RPD	10.596	31.467	15.085	8.937
	RMSE	3.714	2.854	3.520	1.310
February	UPD	0.195	7.335	-2.926	5.130
	RPD	8.181	58.656	11.121	8.909
	RMSE	5.451	2.741	4.794	1.071
August	UPD	-0.832	-2.883	1.714	3.448
	RPD	10.499	16.024	14.584	8.657
	RMSE	1.206	0.830	0.944	0.994
April	UPD	9.075	7.663	5.423	5.030
	RPD	19.969	30.714	27.805	13.343
	RMSE	2.274	1.475	1.824	1.157

6 CURUAI LAKE BIO-OPTICAL VARIABILITY

This chapter presents the results for the bio-optical characterization of Curuai Lake as previously presented in section 4.5. Seasonal variations of biogeochemical variables, AOPs and IOPs are presented and discussed following the description of section 4.5.1. Results for Laboratory absorption measurements as well as LISST particle size distribution, measured only in *April* are also presented as described in section 4.5.2.

6.1 Seasonal variations of biogeochemical variables

The seasonal and inter-seasonal variability of biogeochemical parameters in each season and among them is presented in Table A.2 (Appendix A) and includes all stations for which they were available. Figure 6.1 gives an insight on the spatial and seasonal variability of TSM, DOC and Chla concentrations.

Figure 6.1 - TSM, DOC and Chla Variability among stations

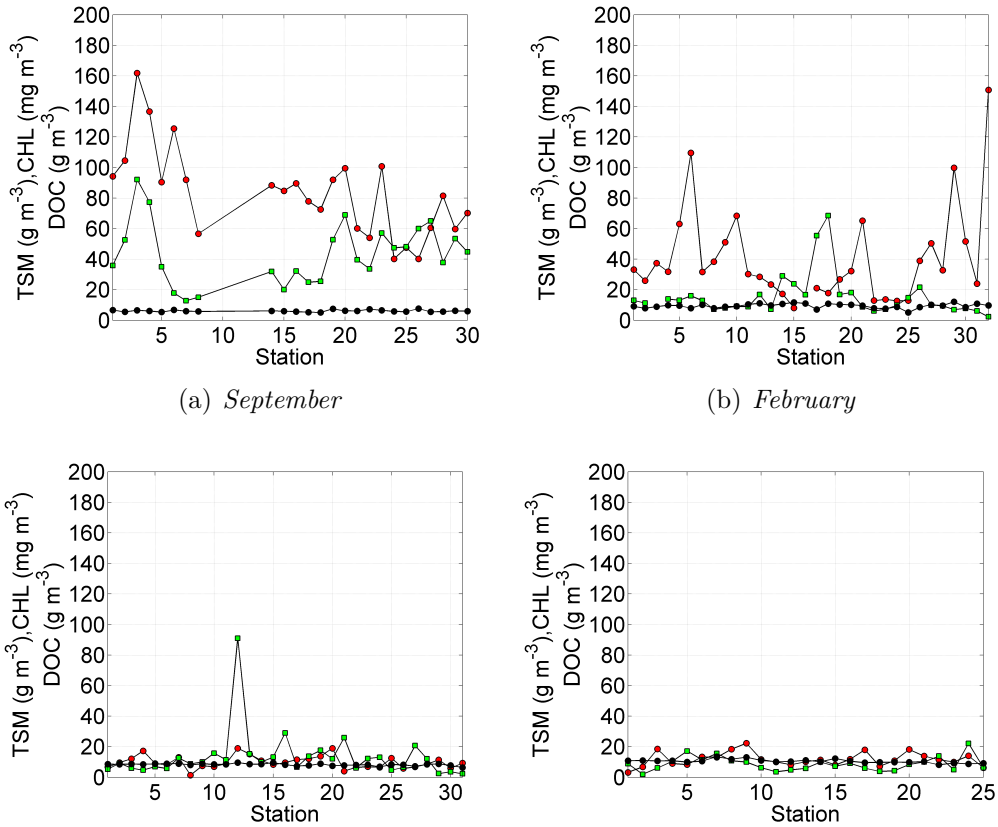

(a) *September* (b) *February*

(c) *August* (d) *April*

Color code: Red:TSM; Black:DOC; Green:Chla

The analysis of Figure 6.1 highlights the following Curuai Lake biogeochemical variables characteristics: (1) the lowest concentrations of all biogeochemical variables occur in *April* (*High Water Period*) and *August* (*Receding Water Period*); (2) in *August*, the spatial variability of Chla is larger than that observed in *April*, with spikes of concentration above 20 mgm^{-3}; (3) DOC is almost constant in time and space; (4) *September* (*Low Water Period*) presents the highest spatial variability of both Chla and TSM and the highest concentration; (5) *February* (*Rising Water Period*) TSM has also high spatial variability but average concentrations are much lower than in *September*. Chl-a concentrations are also low, but with a some spikes of very high concentration.

TSM concentration (Table A.2 Appendix A) exhibits the highest absolute variability in *February* when the standard deviation reaches 31.5 gm^{-3}. The same variability is observed in its fractions (TSIM and TSOM) with a CV of 90.6% for TSIM. TSOM presents a high CV in all seasons, but with median values lower than those of TSIM indicating that IOPs are likely to be driven by inorganic particle concentration. This assumption is also reinforced by TSOM/TSM (Figure 6.2), which for *August* and *April* are around 0.4 and lower than that of *All Samples*, *September* and particularly *February*. Similar to TSM, Chla concentration (Table A.2) presents a high CV, likely due to ephemeral blooms of phytoplankton which can be observed specially in *August*. *September*, however, presents the highest median Chla concentration values (39.6 μgL^{-1}). Dissolved Material (DTC, DOC e DIC) presents the lowest variability with the highest CVs in *February* ($DIC = 30\%$). Median and Mean values are somehow similar among seasons and the ratio DOC/DTC (Figure 6.2) is also stable, being slightly lower in *February*.

It is important to highlight that those values are consistent with Novo et al. (2004), Bonnet et al. (2008), Barbosa et al. (2009), Lobo et al. (2012), Ferreira et al. (2012) previous studies. In *September* and *February* biogeochemical variables concentrations can be as high as those reported for very turbid Chinese (MA et al., 2006; WU et al., 2011; WU et al., 2013), South African (MATTHEWS; BERNARD, 2013) and Australian lakes (CAMPBELL et al., 2011). However, *August* and *April* concentrations are comparable to or even lower than measurements reported in coastal waters (DOXARAN et al., 2009; REYNOLDS et al., 2010; ASTORECA et al., 2012; CHERUKURU et al., 2014; DOGLIOTTI et al., 2015; VANHELLEMONT; RUDDICK, 2015)

Figure 6.2 - Biogeochemical Variables Ratios

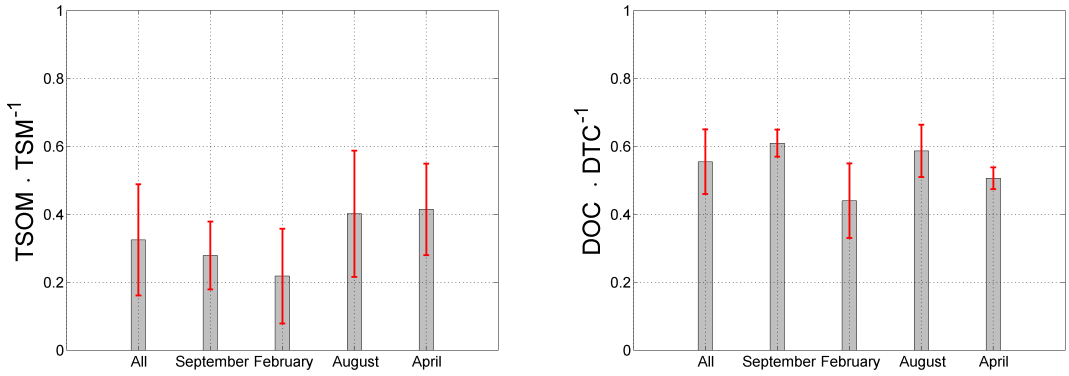

(a) (b)

(a) $^{TSOM}/_{TSM}$ (b) $^{DOC}/_{DTC}$. Grey Bars are the median and red bars are the standard deviation of each ratio

6.2 AOPs Seasonal Inter-comparison

As observed in Appendix E (Figure E.1), k-functions results highlights the bad quality of data mainly in *September* and specially for K_{lu} spectra. It is noteworthy, however, that below 500 nm the error is very high for all seasons, as discussed in section 5.1.3. To come up with an analysis of the spatial variability of diffuse attenuation in Curuai Lake, k-functions spectra were filtered for the 500 to 800 nm interval. Also, in order to compare k-functions among seasons, a specific wavelength (676 nm), was chosen for Table 6.1 analysis.

Figure 6.3 - Diffuse Attenuation Coefficients (K_d and K_{lu}) for the 500 to 800 nm interval. K-function calculated from the Non-Linear Approach

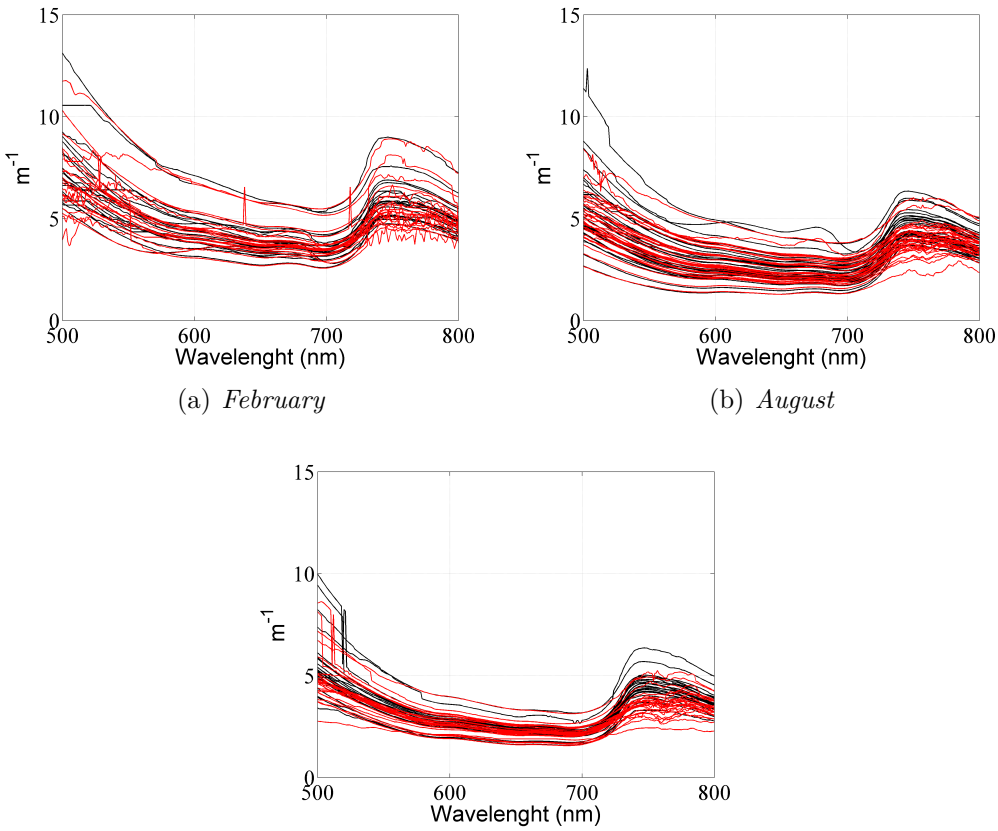

(a) *February*

(b) *August*

(c) *April*

Color Code: Red: K_{lu}; Black: K_d

Both Figure 6.3 and Table 6.1 shows that values of K_d and K_{lu} (K_u is also shown on table 6.1) are similar to each other in each season, which was also confirmed with Hydrolight simulations carried out in this research (section 5.2.1). According to Mobley (1994), under a vertically homogeneous water mass at sufficient depth below the surface, k-function become dependent only on medium composition, being no longer affected by boundary condition, reaching the so called *asymptotic regime*. In this case, all K-functions become identical ($K_d = K_u = K_{lu}$).

Simulations indicated that for Curuai lake, k-function reached this *asymptotic regime* at very shallow depth (10 cm). Table 6.1 reinforces the existence of this regime because Median and Mean k-function values differ less than 2% among themselves. It is important to stress that k-functions measurements under the asymptotic regime become independent of the ambient light field and therefore turns into a reliable

descriptor of the IOPs.

Table 6.1 - Statistics for the Non-Linear K-functions (K_d, K_u and K_{lu},) at 676 nm

Stations	Index	All Samples	September	February	August	April
K_d	Max	14.08	14.08	5.61	4.58	3.26
	Min	1.39	5.34	2.80	1.39	1.61
	Std	3.09	2.25	0.74	0.67	0.37
	Mean	4.24	9.69	3.87	2.54	2.27
	Median	2.96	9.51	3.73	2.39	2.25
	CV (%)	72.90	23.28	19.15	26.35	16.26
K_{lu}	Max	13.88	13.88	5.64	4.01	3.20
	Min	1.37	5.38	2.77	1.37	1.59
	Std	2.92	2.05	0.71	0.61	0.34
	Mean	4.14	9.29	3.88	2.51	2.23
	Median	2.84	9.26	3.68	2.33	2.19
	CV (%)	70.51	22.12	18.26	24.19	15.14
K_u	Max	4.01	-	-	4.01	3.20
	Min	1.36	-	-	1.36	1.63
	Std	0.54	-	-	0.63	0.33
	Mean	2.37	-	-	2.51	2.20
	Median	2.25	-	-	2.33	2.20
	CV (%)	22.67	-	-	25.16	15.06

6.3 IOPs Seasons Inter-comparison

6.3.1 Spectral Dependence of Surface IOPs

February is characterized by the highest median values for all surface IOPs (Figure 6.4) while in *August* and *April*, IOPs present lower values and with less variability, which is consistent to TSM concentrations (Table A.1). When comparing just IOPs, independent of seasons, attenuation, scattering coefficients and therefore the single scattering albedo (ω_0 Calculated as $\frac{b_p}{c_{(p+CDOM)}}$) have a higher variability than the absorption (a_{p+CDOM}).

Figure 6.4 - Total Median Spectral IOPs (Particulate + CDOM) Measured with ACS

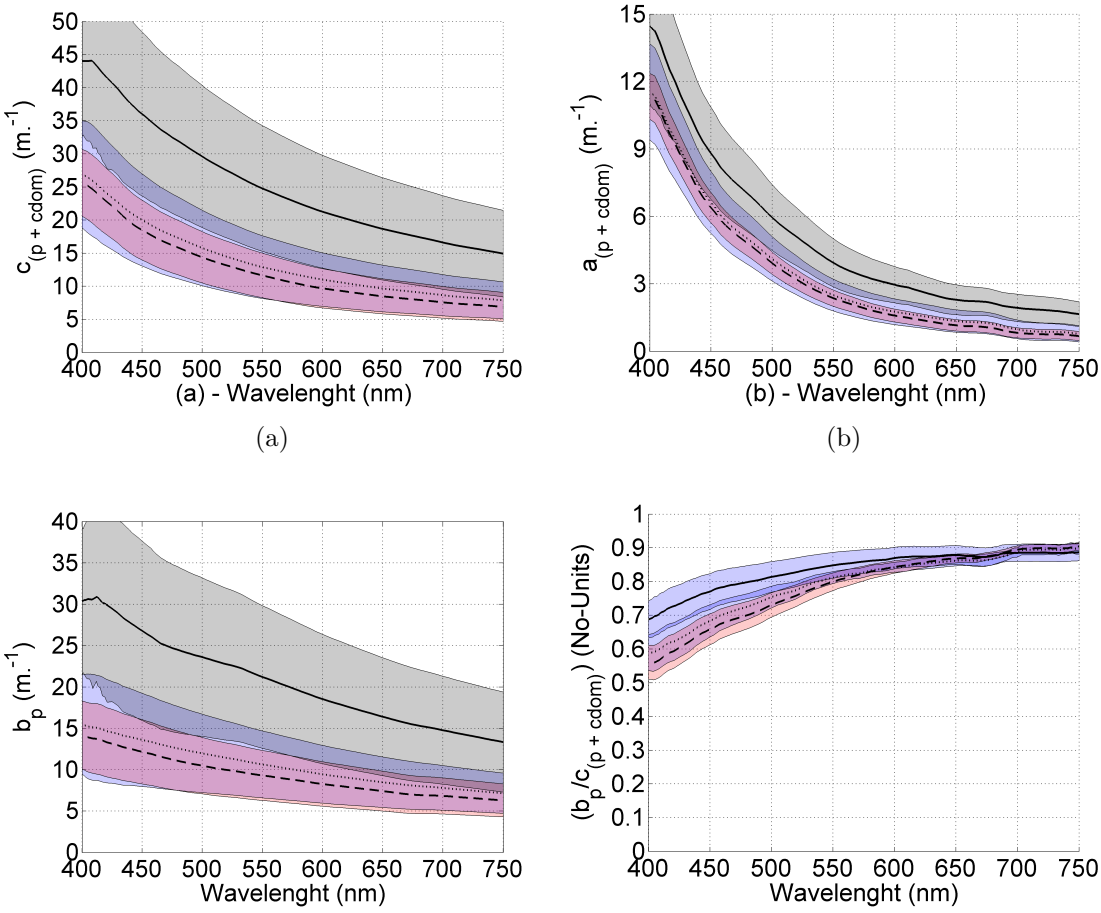

(a) Attenuation coefficient; (b) Absorption coefficient; (c) Scattering coefficient (d) Single Scattering Albedo ($\omega_0 = \frac{b_p}{c_{(Particulate+CDOM)}}$). Solid lines are the median for all stations (for each field campaign) calculated within 0.5 to 1 meter depth. Shades represent one standard deviation. Color Code: Solid Black/Gray Shade- February; Dashed Black/Blue Shade - August; Black Dotted/Red Shade-April.

Particulate backscattering measurements have a similar spectral distribution as particulate scattering (Figure 6.5a). *February* exhibits the highest values and *August* and *April* show similar b_{b_p} spectra. This is also consistent with the variability in biogeochemical parameter concentrations (Table A.1). The particulate backscattering spectra shows unexpected anomalous behavior in the blue-green range similar to that reported by Wu et al. (2013) and which may be related to poor sigma correction, equipment noise or even fluorescence.

Median Backscattering ratios ($^{b_{b_p}}/_{b_p}(HS6/ACS)$) (Figure 6.5b) do not vary among

seasons, particularly at 700 nm, where it ranges from 0.04 to 0.044 (Table 6.2). This small variability suggests relatively small variation in particle size and composition (TWARDOWSKI et al., 2001; BOSS, 2004). b_{b_p}/b_p measured in coastal waters by Boss (2004), McKee and Cunningham (2006), Loisel et al. (2007) and Snyder et al. (2008) despite of few extreme values (0.05 - 0.06 m^{-1}), have mean values lower than those of Curuai Lake. An exception is shown by Cherukuru et al. (2014), which report median values of up to 0.049 for Tasmanian coastal waters. Mineral rich coastal waters presented by McKee et al. (2009) shows that although median values for b_{b_p}/b_p are lower than 0.03, at wavelengths larger than 650 nm, the variability in magnitude is higher and reaches values larger than 0.05.

When compared to turbid Australian lakes (CAMPBELL et al., 2011), Curuai lake presents larger b_{b_p}/b_p than Wivenhoe Dam (0.013-0.014) but similar or even lower than Burdekin Falls (0.039-0.093). This trend is not observed for the Chinese Taihu lake, since Sun et al. (2009), Le et al. (2009a) reported lower median values for all IOPs.

Figure 6.5 - Inter-campaign variability of backscattering

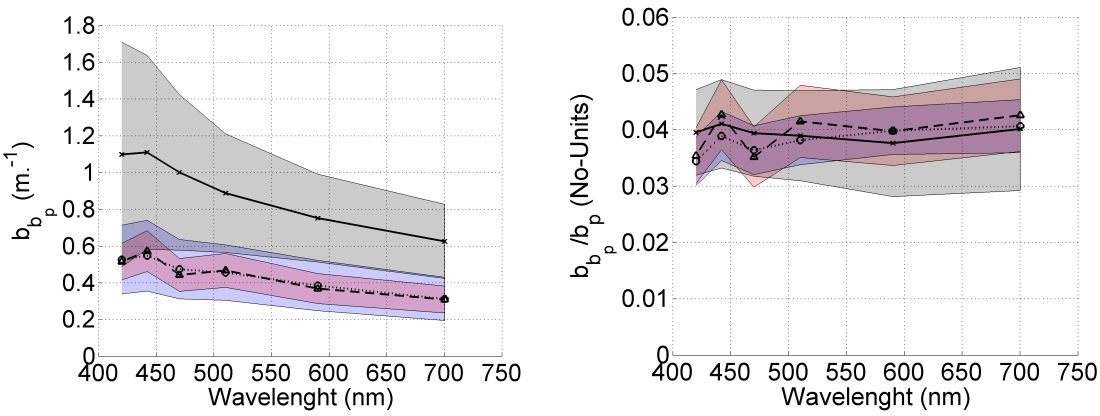

(a) (b)

(a) Median Hydroscat Backscattering and (b) median backscattering ratio ($b_{b_p}/b_p(HS6/ACS)$). Shades represent one standard deviation. Symbol/Color code: [Solid Black Line/Crosses/ Gray Shade] - February; [Dashed Black/Circles/Blue Shade] - August; [Black Dotted/Triangles/Red Shade] - April. In figure-b symbols in 715 nm represents the backscattering ratio calculated from ACS and Symbol/Color code are: Black/Crosses - *February*; Blue/Circles - *August*; Red/Triangles - *April*.

Table 6.2 - ${}^{b_{b_p}}/b_p(HS6/ACS)$ in 700 nm statistics for surface measurements

Statistics	All Stations	*February*	*August*	*April*
Min	0.024	0.024	0.031	0.033
Max	0.069	0.069	0.046	0.059
Median	0.042	0.044	0.040	0.044
Mean	0.042	0.040	0.041	0.043
Std	0.008	0.011	0.005	0.006
CV	18.199	27.079	11.585	15.077

Median γ_b (Equation 4.25 Section 4.5.1) varies between its highest value in the series (1.50) in *February* to similar and smaller values in *August* (1.33) and April (1.38) respectively. *August* presented the highest variability (CV = 17.74 %) and *February* the highest value of all seasons (1.81). γ_b was maximum in *April* (1.71) and significantly higher than that of *February* and *August* (Table 6.3).

The selection of wavelength ranges to avoid absorption effects in γ_b (550 nm to 750 nm) and γ_{b_b} (510, 590 and 700 nm) provided the same range of values when using the entire spectra. Two reasons can provide explanation: (1) the interval used was not sufficient to remove the absorption effect or (2) for smaller particles, the particulate absorption effects on scattering decrease when the particle size increases, i.e., when the proportion of fine particles grows (DOXARAN et al., 2009).

The temporal variability in the γ_b agrees with the temporal variability of hydrological/biogeochemical patterns reported by Barbosa et al. (2009) and Rudorff et al. (2014a). According to them, in the mid-rising period (represented by *February*) the Amazon River discharge to Curuai is not sufficient to maintain larger particles in suspension; therefore γ_b indicates the presence of smaller suspended particles. On the other hand, in *August* and *April*, with overbank flow (RUDORFF et al., 2014a), the higher discharge to Curuai allows the suspension of larger particles further into the lake, resulting in smaller γ_b. It is noticeable that the coefficient of variation (CV) for γ_b is very low indicating that the Amazon river drives the distribution of particle type and concentration within the lake as already reported by Bonnet et al. (2008), Rudorff et al. (2014a), Rudorff et al. (2014b).

Particulate Scattering and backscattering slopes are considerably high when compared to those of literature. Slade and Boss (2015) reported γ_b and γ_{b_b} values up to 0.7 and 1.0 for coastal areas respectively (Martha's Vineyard Coastal Observatory (MVCO)). Doxaran et al. (2009), studying mineral rich coastal waters, showed that

the near-infrared particulate scattering coefficient is represented by a simple power-law function, with a spectral slope varying in the range of 0.1 to 1.4. Boss et al. (2013), using a large data set encompassing a wide range of case I water, reported a median γ_b of 0.73.

Compared to other inland waters, Curuai Lake still presents higher scattering and backscattering slope values. Sun et al. (2009) and Shi et al. (2014) reported extremely lower γ_b values for Taihu lake. On the other hand, high values were reported for coastal areas in Tasmania ($\gamma_{b_b} = 0.76$ to 2.01) (CHERUKURU et al., 2014). As discussed by Slade and Boss (2015), the slope of the attenuation coefficient (γ_c) is linearly related to γ_b with the latter being slightly smaller (see their figure 11) suggesting that Curuai lake values are comparable to Campbell et al. (2011) ($\gamma_c = 1.14$ to 1.57), Strömbeck and Pierson (2001) ($\gamma_c = 1.52$ to 2.84), Herlevi (2002) and Paavel et al. (2007) ($\gamma_c = 0.13$ to 2.53).

Table 6.3 - Exponent γ_b and γ_{b_b} calculated for scattering and backscattering coefficients for all stations (for each field campaign) calculated within 0.5 to 1.0 meters depth

Campaign	IOPs	Min	Max	Median	Mean	Std	CV
February	γ_b	0.94	1.81	1.50	1.47	0.21	14.21
	γ_{b_b}	0.87	1.43	1.08	1.10	0.17	15.38
August	γ_b	0.74	1.67	1.33	1.30	0.23	17.74
	γ_{b_b}	0.85	1.57	1.09	1.14	0.16	13.92
April	γ_b	1.10	1.80	1.38	1.37	0.13	9.78
	γ_{b_b}	0.97	1.71	1.35	1.33	0.17	12.72

6.3.2 Relationships between IOPs and biogeochemical parameters

IOPs provided good predictions for TSM and TSIM (Table D.1-Appendix D) that are consistent with previous studies (HILL et al., 2011; ASTORECA et al., 2012; BOSS et al., 2009). Attenuation and Scattering coefficients ($c_{particulate+CDOM}$ in 660 nm and b_p in 700 nm) were the best predictors of TSM and TSIM, with scattering coefficient being slightly better (Figure 6.6, and Appendix D). This result contrasts with those of Boss et al. (2009) in which b_{b_p} was the best predictor of TSM. The reason may be related the Hydroscat's large pathlength which, in highly turbid waters, causes larger measurement uncertainties (DOXARAN et al., 2013).

The lack of relationship between TSOM and all IOPs (TableD.3-Appendix D) suggests that the organic fraction contribution to scattering (b_p) might be lower. This finding is similar to Loisel et al. (2009) for ocean waters. The same behavior can be observed for TSM and TSIM in *August* and *April* seasons, which presented higher organic content. R^2 values are lower, when compared to *February*, which has a higher inorganic content. It suggests that inorganic material drives attenuation, scattering and backscattering.

When analyzing only R^2 values (Appendix D), the best fit occurred well using *All Samples*, which suggests low variability of particle type through out the seasons. However, Mass-Specific coefficients ($b^*_{b_p}$, b^*_p, $c^*_{(p+CDOM)}$) derived from the slope of the Type II linear regression for TSM (Table 6.4) varies between seasons. Coefficients are lower for *All Samples* and *February* and increase for *August* and *April*. These results agrees with both OAC measurements (Figure A.1) and Babin et al. (2003b) reports, but does not agree with Wozniak et al. (2010), which reported the existence of higher b^* for lower organic concentration in ocean waters.

Regardless the fact that mass-specific scattering coefficient is dependent on particle type (i.e. index of refraction), it is also influenced by particle size (BABIN et al., 2003b). Assuming that the particle size distribution (PSD) can be described by a Power-law (Junge-like), the increase in b^*_p results in the increase in the slope of the distribution (ξ) (BABIN et al., 2003b). For Curuai Lake, February presents the higher γ_b, which can be roughly related to the slope of the Junge distribution ($\gamma_b = \xi - 3$) and therefore to the dominance of smaller particles. That highlights the influence of particle type (inorganic content), because despite the dominance of smaller particles, which would increase b^*_p, *February* still presents the lowest b^*_p values.

Doxaran et al. (2009) presented results similar to those of Curuai lake ($b^*_p = 0.42$ m^2g^{-1} for *February*) working in estuaries with very high concentrations of mineral particles (Elbe and Gironde Estuaries) with b^*_p of 0.38 (m^2g^{-1}) and 0.36 (m^2g^{-1}) respectively and where $^{TSIM}/_{TSM} > 0.85$. In contrast, Sun et al. (2010) and Sun et al. (2012) presented slightly higher values (0.5 to 0.6) for mineral dominated waters (no $^{TSIM}/_{TSM}$ provided). Shi et al. (2014) results show an increase in b^*_p as $^{TSIM}/_{TSM}$ increases: b^*_p average (0.37) for a 60 % $^{TSIM}/_{TSM}$ ratio (Lake Dianchi) and a b^*_p average (0.70 and 0.66) for a 90% and 80% $^{TSIM}/_{TSM}$ ratio (Lakes Taihu and Chaohu respectively). Therefore, there is no consensus regarding the relationship between $^{TSIM}/_{TSM}$ and b^*_p. The reasons for those differences may be related to other factors such as mineralogy of inorganic particles (index refraction and morphology)

(HILL et al., 2011; BABIN et al., 2003b) as well as uncertainties on optical and analytical measurements in turbid environments (LEYMARIE et al., 2010).

Figure 6.6 - LogLog transformed of Suspended Matter (TSM, TSOM and TSIM) and Selected IOPs (b_{b_p}, b_p, $c_{(p+CDOM)}$)

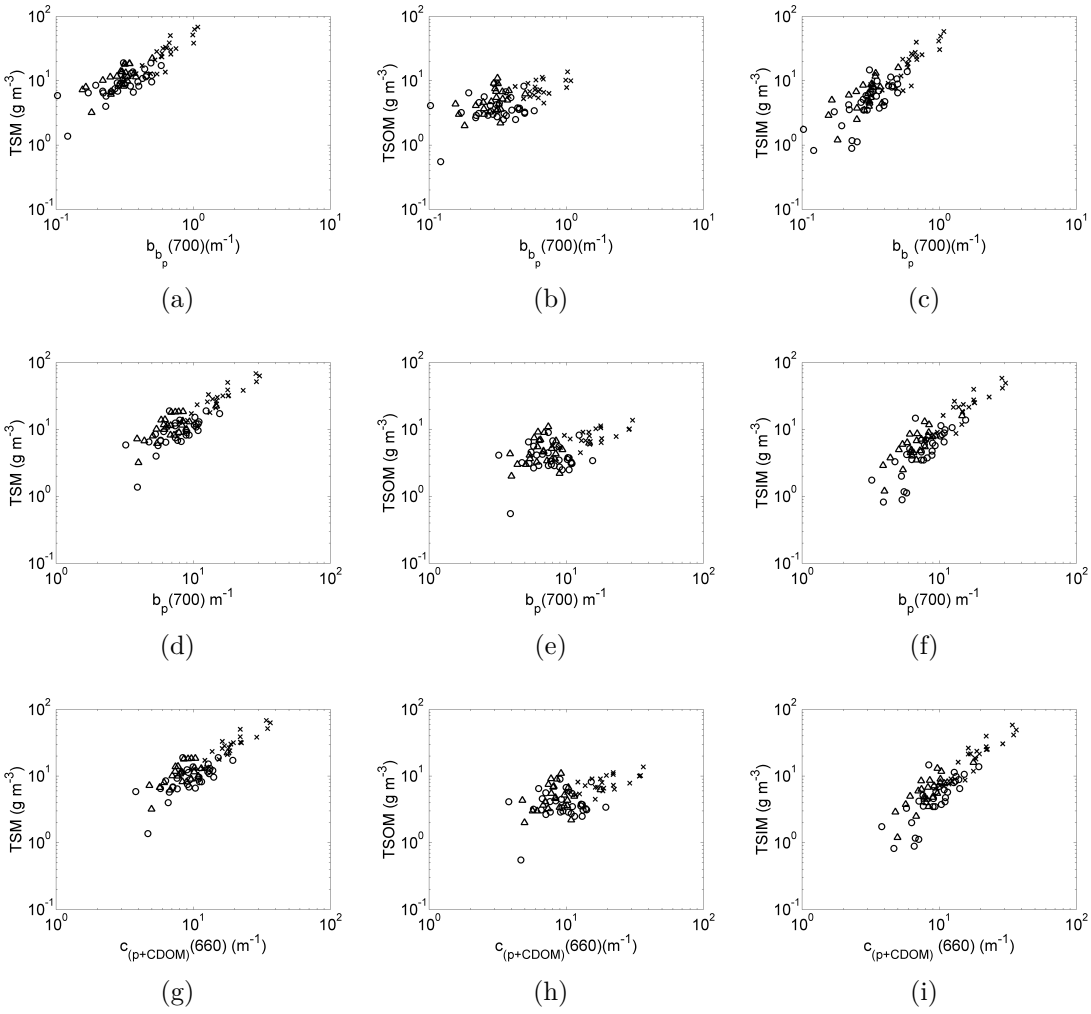

All Samples (N = 79). Symbol Code: "x" *February* Samples (N = 23); "o" *August* Samples (N = 31); "△ " *April* Samples (N = 25).

Table 6.4 - Mass-Specific coefficients for TSM and TSIM calculated from the Type II Linear Regression with Attenuation Coefficient $c^*_{(p+CDOM)}(660)$, Scattering Coefficient $b^*_p(700)$ and Backscattering coefficient $b^*_{b_p}(700)$

Specific IOP	$c^*_{(p+CDOM)}$ (660)	b^*_p (700)	$b^*_{b_p}$ (700)
All Stations	0.52	0.43	0.02
February	0.49	0.42	0.01
August	0.84	0.67	0.03
April	1.80	0.50	0.02

The relationship between Chla concentration and derived phytoplankton absorption ($a_\phi(676)$) from absorption line height at 676 nm (Section 4.5.1) is similar in all seasons ($^1/_{slope} \approx 0.007\ m^2g^{-1}$), despite the very low R^2 presented for April (Figure 6.7, Table 6.5).

Figure 6.7 - Type II Linear Regressions for Chla Concentration Samples and $a_\phi(676)$

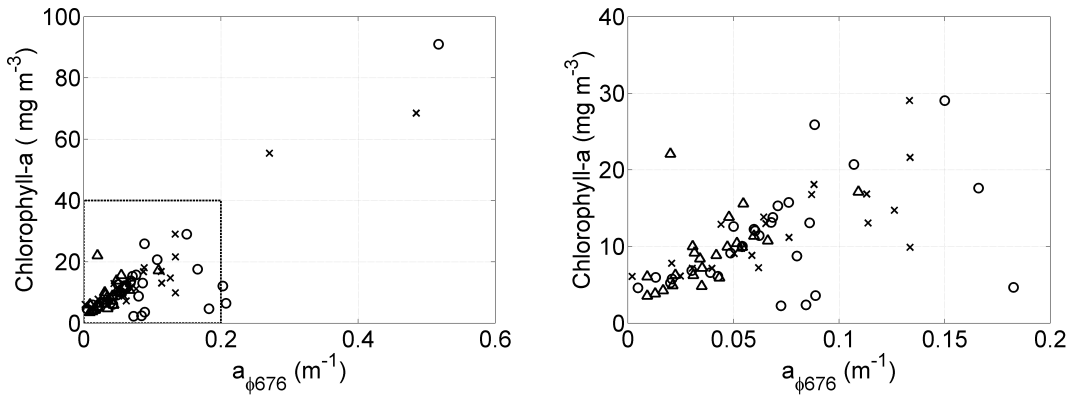

(a) (b)

All samples (N = 79). Symbol Code: "x" *February* Samples (N = 23); "o" *August* Samples (N = 31); "△ " *April* Samples (N = 25). "X" axis scale was changed to highlight differences. Figure (b) is a zoom of the highlighted rectangle in figure (a).

Table 6.5 - Statistics for Chla Concentration and $a_\phi(676)$

Field Campaign	$^1/_{slope}$	R^2	RSME
All Samples (N = 79)	0.007± 0.001	0.74± 0.01	6.76 ± 0.43
February (N = 23)	0.007± 0.001	0.89± 0.03	4.97 ± 1.48
August (N = 31)	0.006± 0.001	0.65± 0.02	8.98 ± 0.30
April (N = 25)	0.006± 0.001	0.07± 0.07	3.90 ± 1.01

Such low $a_\phi(676)^*$ values are not common in open ocean case I waters (BOSS et al., 2013). Those low values are related to Chla concentration; the higher the concentration, the lower is $a_\phi(676)^*$ is mainly due to the packaging effect (BRICAUD et al., 1995) and the low available light. Similar values to Curuai lake are presented for the North Sea (BABIN et al., 2003) (0.004 m^2g^{-1}) and for eutrophic South African lakes (0.005 to 0.03 m^2g^{-1}) (MATTHEWS; BERNARD, 2013). Low values (0.005 m^2g^{-1}) are also reported in Bricaud et al. (1995) for ocean waters.

Figure 6.8 shows that the existence of a relationship between $^{b_{b_p}}/_{b_p}(HS6/ACS)$ and Chla concentration that was observed in coastal waters by Boss (2004) did not occur in Curuai lake. Similarly, $^{b_{b_p}}/_{b_p}(HS6/ACS)$ and $^{TSOM}/_{TSM}$ did not co-vary. There are two hypotheses to explain this lack of relationship : (1) the high turbidity of Curuai waters causes high b_{b_p} which becomes insensitive to variation of $^{TSOM}/_{TSM}$, even for extremes values (20% and 80%); (2) the uncertainties in Hydroscat measurements, mainly due to the pathlength correction, is larger than the b_{b_p} changes with particle concentration.

Figure 6.8 - (a) Backscattering Ratio $^{b_{b_p}}/_{b_p}(HS6/ACS)$ and $^{TSOM}/_{TSM}$ Ratio and (b) Clorophyll- a concentration [Chl-a]/Attenuation $c^*_{(p+CDOM)}(660)$ for All samples.

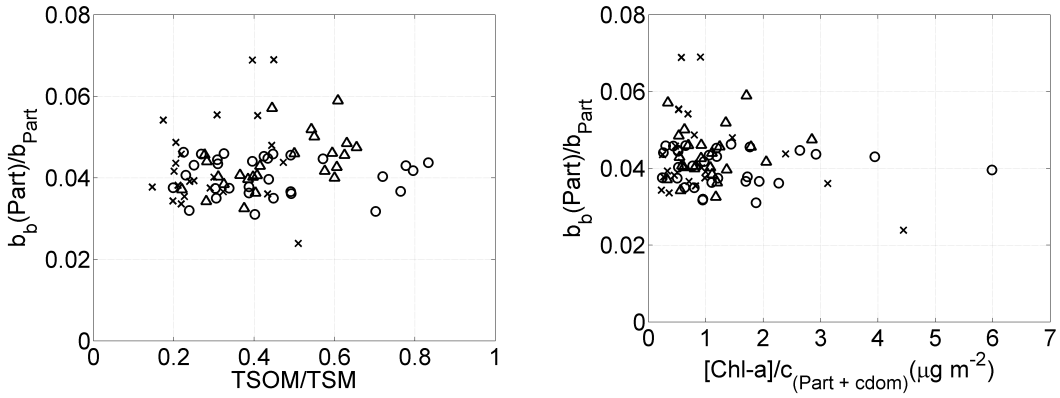

(a) (b)

Symbol Code: "x" *February* Samples (N = 23); "o" *August* Samples (N = 31); "△ " *April* Samples (N = 25). "X" axis scale was changed to highlight differences.

6.3.3 IOPs Profiles

Scattering coefficient b_p vertical profiles are homogeneous, suggesting that the water column was well mixed throughout the seasons (Figure 6.9). Backscattering profiles show similar distributions with higher values closer to the bottom in August (from 4 to 4.5m) probably due to re-suspension. Standard Deviation bars show a large variation, especially in *February*, due to a high spatial variability during this period (Figure 6.1) which is consistent with previous studies (BARBOSA et al., 2009; RUDORFF et al., 2011; RUDORFF et al., 2014a). In *April*, when the Lake is dominated by the Amazon River water, the scattering coefficient shows both smaller magnitude and smaller standard deviation what is consistent with measured OACs (Table A.1). This OAC behavior has already been reported for Amazon Floodplain lakes (MELACK; FORSBERG, 2001; BARBOSA et al., 2009; AFFONSO et al., 2011).

Figure 6.9 - Median Scattering (b_p (700 nm)) Profiles

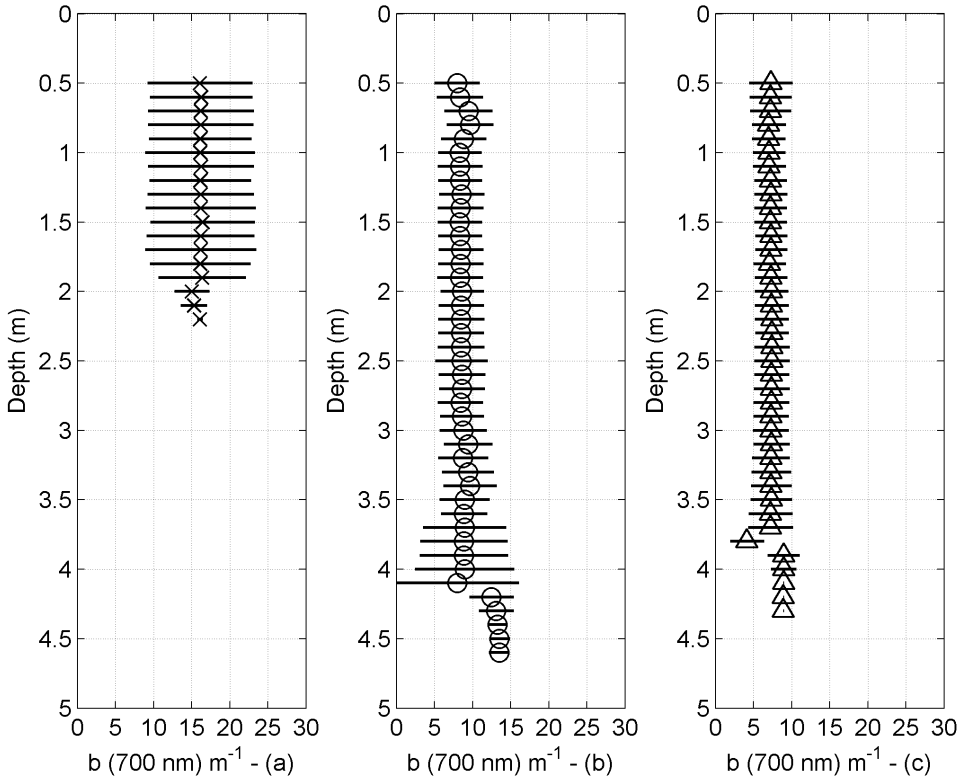

Symbol Code : Symbol Code: "x" *February* Samples (N = 23); "o" *August* Samples (N = 31); "△ " *April* Samples (N = 25).Median Calculated for stations in each Field Campaign (same as for surface analysis) in each depth. Bars represent one standard deviation.

Median profiles for γ_{b_p} (Figure 6.10) are homogeneous as function of depth with values indicating dominance of small particle size from the surface up to the maximum measurement depth. The standard deviation in *February* and *April* is almost constant throughout the profile indicating that Curuai Lake behaves similarly with respect to particle size. In *August* however, when the water leaves the floodplain, the maximum standard deviation is observed at the surface, and decreases with depth. There are at least two explanations for that (1) the degree at which individual lakes which compose Curuai Lake are exposed to the overbank flooding, which may bring less selected suspended particle types; (2) the occurrence of patches of phytoplankton blooms may also contribute to the increase in standard deviation at the surface, as also observed in Figure 6.11.

Figure 6.10 - Median Scattering Gama Factors Profiles

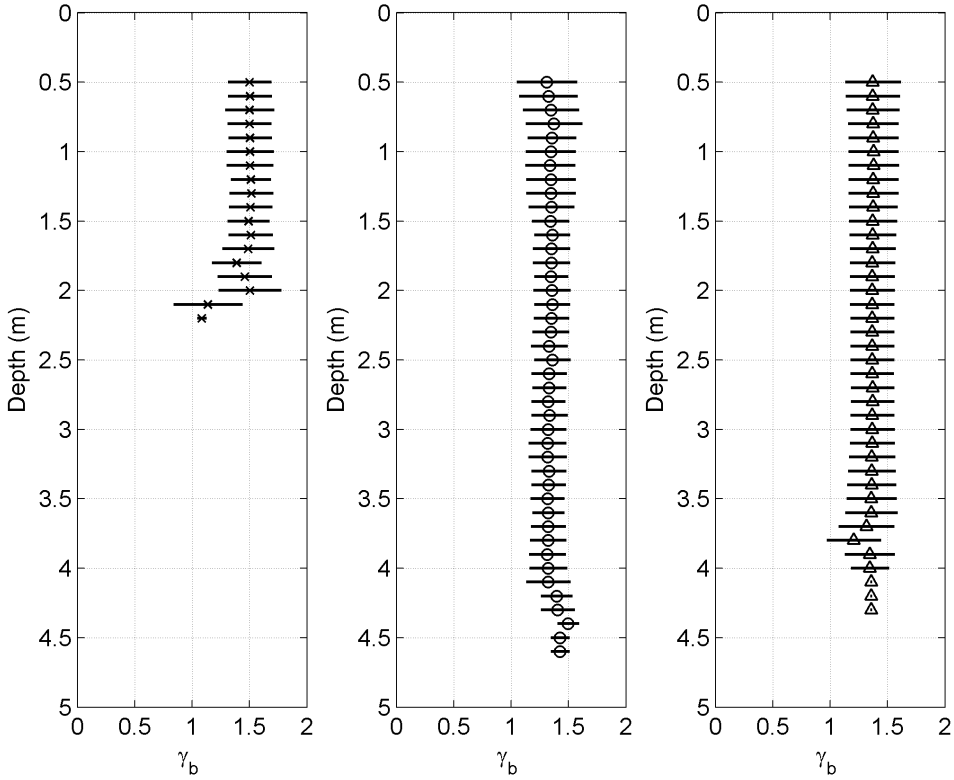

Symbol Code : Symbol Code: "x" *February* Samples (N = 23); "o" *August* Samples (N = 31); "△ " *April* Samples (N = 25).Median Calculated for stations in each Field Campaign (same as for surface analysis) in each depth. Bars represent one standard deviation.

Phytoplankton related Absorption profiles ($a_\phi(676)$) (Figure 6.11) have a depth distribution quite different from those of the scattering coefficient. Absorption coefficient decreases with depth in *August* and *April* and is very erratic in February, when it displays large standard deviation from the surface to the maximum measurement depth, indicating large variability among the now split Curuai floodplain lakes during the mid-rising water level (RUDORFF et al., 2014a). This behavior is in agreement with rising season when the Amazon River incoming water reaches different lakes at different moments depending on their location in the floodplain.

In *April*, during the beginning of overbank flooding, $a_\phi(676)$ indicates higher homogeneity in depth and space. In *August* $a_\phi(676)$ displays high values at surface and decreases with depth suggesting a higher frequency of phytoplankton blooms which is corroborated by in-situ OACs (Table A.1). The August $a_\phi(676)$ standard deviation is larger at the surface and tends to decrease with depth, indicating that

the phytoplankton blooms occur at specific locations in the floodplain where light and nutrient availability triggers primary production despite Curuai lake turbidity.

Figure 6.11 - Median Chlorophyll-a Absorption Profiles

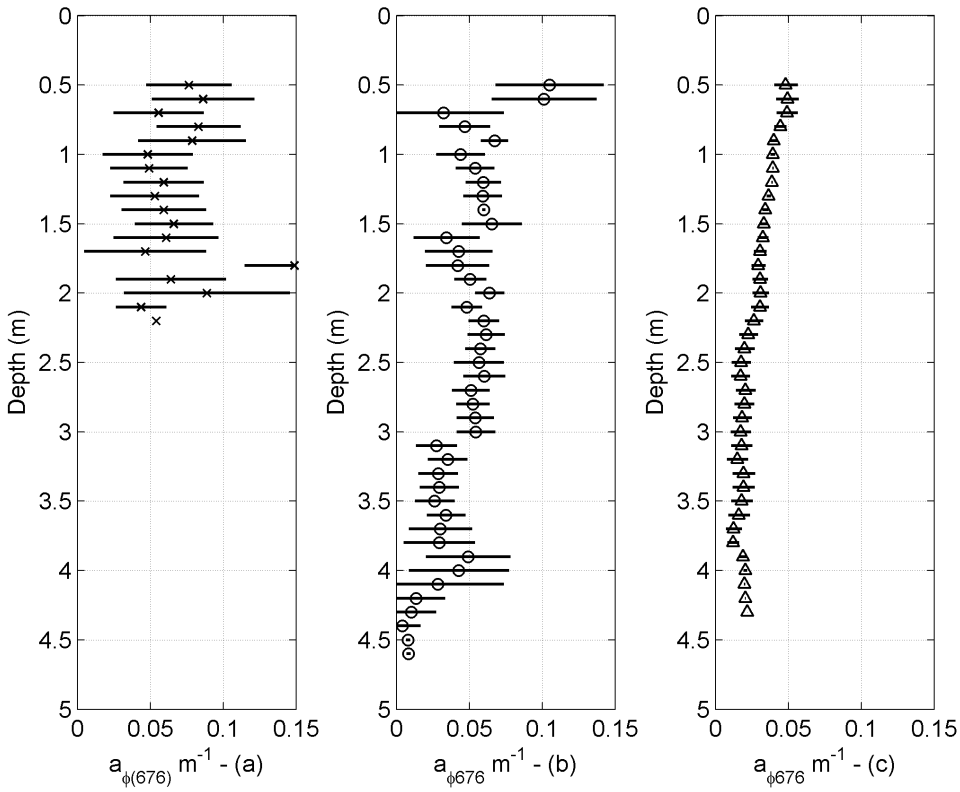

Symbol Code : Symbol Code: "x" *February* Samples (N = 23); "o" *August* Samples (N = 31); "△ " *April* Samples (N = 25). Median Calculated for stations in each Field Campaign (same as for surface analysis) in each depth. Bars represent one standard deviation.

Despite the difficulties of acquiring reliable IOPs in turbid waters, the closure exercise conducted here provided confidence in the measurements when processed using the Rodgers/Doxaran corrections. The use of a single set of corrections for the entire dataset also proved to be the best approach, which despite the remaining uncertainties, allowed consistent characterization of Curuai Lake IOPs. Hence, our work supports the use of the in-situ optical instrumentation in turbid environments such as Amazon lakes, for which they were not designed.

Seasonal pattern of Curuai lake IOPs and TSM/TSIM concentrations were found

to be in close agreement. Scattering coefficient proved to be more variable than absorption, indicating that IOPs are dominated by TSM in all seasons. The absorption coefficient in 676 nm was demonstrated to be a robust chlorophyll- a predictor even in highly turbid conditions. The backscattering ratio indicated that dominant particle type is similar through the seasons. Particle size, however, varies from finer particles during the rising water season (February) to slightly larger particles during the receding water season (August). The lack of significant variability in the spectral shape of scattering, backscattering and attenuation coefficients suggests the dominance of small inorganic particles throughout the seasons, consistent with the findings of Bonnet et al. (2008), Rudorff et al. (2014a) and Rudorff et al. (2014b), which calculated that from 70 to 80 % of Curuai floodplain water comes from the Amazon River.

Relationships between optical and biogeochemical variables were found to be consistent with the literature. The stability of these relationships suggests that it should be possible to design robust overarching algorithms to obtain biogeochemical information using remote sensing of the lake properties.

6.4 The *April* Field Campaign

As discussed in Chapter 4, *April* was the only season for which, besides In-situ (ACS/Hydroscat) and Radiometric measurements, Laboratory Absorption (CDOM (a_{cdom}), Suspended Material (a_p), Phytoplankton (a_ϕ) and Non-Algal Particles (NAP) (a_{nap})) as well as LISST-PSD were measured. Since *April* dataset has all measurements (Table 4.2), it will be used as the main input for Inverse Models assessment (Chapter 7).

6.4.1 Laboratory Measurement Results

Figure 6.12 presents the absorption for CDOM (a_{cdom}) (a), Suspended Material (a_p) (b), Phytoplankton (a_ϕ) (c) and Non-Algal Particles (NAP) (a_{nap}) (d).

Figure 6.12 - Spectrophotometer Absorption Measurements

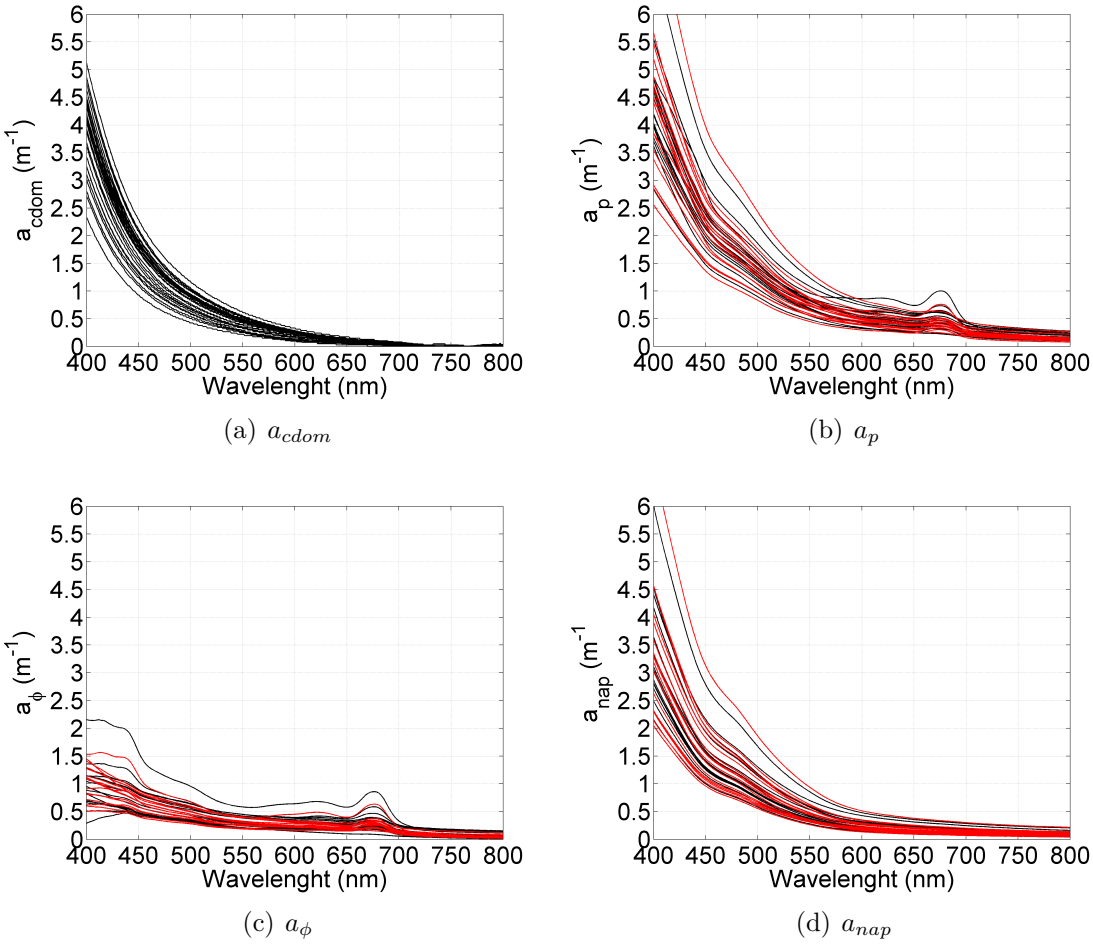

(a) a_{cdom} (b) a_p

(c) a_ϕ (d) a_{nap}

Absorption for: (a) CDOM (a_{cdom}); (b) Suspended Material (a_p); (c) Phytoplankton (a_ϕ); (d) Non-Algal Particles (a_{nap}); Color Code: Red- First Set of Samples; Black: Second Set of Samples;

The absorption by CDOM (a_{cdom}) is much higher (figure 6.12a) than those reported by Babin et al. (2003), Binding et al. (2008) and O'Donnell et al. (2010) but closer to those of Ma et al. (2006), Campbell et al. (2011), Wu et al. (2011). Exponential slopes (Table 6.6) are in close agreement with values reported for coastal and inland waters (from 0.012 to 0.022). The small variation of S_{cdom}, $a_{cdom}(440)$ and DOC concentration suggests homogeneity in DOC distribution in the lake. No significant linear relationship was observed between $a_{cdom}(440)$ and DOC as indicated by very low R^2 values (Not Shown - Birgot et al. (InPress)).

The relationship between CDOM and DOC has been investigated since the 1990's with controversial results (ROCHELLE-NEWALL; FISHER, 2002; YACOBI et al., 2003;

TZORTZIOU et al., 2007). Those studies suggest that both, aquatic system properties (salinity, turbidity, type of DOC) and acquisition factors (wavelength, field and laboratory methods) interfere in this relationship. The lack of relationship in the present study can be explained by the narrow range of dissolved organic matter concentration found across the lake during the high water season, *April*. Also it might be related to fulvic/humic acids ratio, which varies widely in the Amazon region (ERTEL et al., 1986). However, as observed in Table 6.6, due to the high homogeneity of limnological variables during the high water season (AFFONSO et al., 2011), this variability was not observed in *April* resulting in a S_{cdom} CV of only 7%. As the values of S_{cdom} vary inversely with CDOM molecular weight (KIRK, 2010), the slope analysis can be useful for distinguishing between humic and fulvic acids. In April, median S_{cdom} is $\approx$ 15 % higher than the common ocean literature values (0.014) what might suggest a dominance Fulvic acids (ERTEL et al., 1986). Previous studies (RUDORFF et al., 2014a; BONNET et al., 2008) also indicate that during high water the majority source of water in Curuai Lake is the Amazon river which is dominated by Fulvic acids. That reinforces that the lack of relationship between a_{cdom} and DOC is mainly due to the narrow range of dissolved organic matter.

Regarding the suspended solids, a_p spectra (figure 6.12b) appear to be mostly influenced by a_{nap} (figure 6.12d), with exponential shapes characterized by high rate of decay at wavelengths < 500 nm and with a peak caused by a_ϕ in the 650 to 700 nm range. The Type two linear relations between biogeochemical variables (TSM, TSIM, TSOM and Chla) and a_p (Appendix B) shows that the best agreement is presented for Chla and the peak in 676 nm. A stronger agreement is also observed for TSM and TSIM, but independent of wavelength, similar to what is observed when using ACS and Hydroscat measurements.

The variability of a_{nap} in the range between 400 and 500 nm (2.5 to $> 6\ m^{-1}$) can be explained by different proportions of TSM components (TSIM and TSOM) in the lake, which varies from high to low TSOM/TSM ratio for each sampling station (Table A.2 Appendix A). Besides the type of TSM composition, another factor possibly affecting the relationship is the nature of the sediment. Different types of mineral may have different properties of DOC adsorption. The High molecular weight DOC which preferentially adsorb onto mineral surfaces, may explain the high values of NAP absorption coefficients (BINDING et al., 2008). This mineral adsorption process leaves low molecular weight components in solution causing higher concentration of fulvic acids (KIRK, 2010). Similar to what happens to a_p, the highest Linear relationship between a_{nap} and biogeochemical variables (Appendix B) was observed for

TSIM and TSM, independent of wavelength. Very weak relationships were found for both Chla and TSOM.

Table 6.6 presents the slope S_{nap} for a_{nap} replicas. S_{nap} values are comparable to those described in (MA et al., 2006) (table 1 page 4282) for Taihu Lake. Curuai lake S_{nap} range is more similar to that of Taihu Lake than that of coastal oceanic waters described in (BABIN et al., 2003). The narrow range of particle type in Curuai Lake, in *April* explains the low spectral variability of S_{nap}. The ratio between mineral and organic particles ($\frac{TSIM}{TSM} \geq 0.50$) also contributes to the small variability in the slopes.

Table 6.6 - Exponents S_{cdom} and S_{nap}

	Min	Max	Median	Mean	Std	CV
CDOM (S_{cdom})	0.015	0.020	0.016	0.016	0.001	7%
NAP First Set (S_{nap-1})	0.009	0.012	0.010	0.010	0.001	9.5 %
NAP Second Set (S_{nap-2})	0.008	0.015	0.010	0.011	0.001	13.3 %
$S_{(nap+cdom)}$ First Set	0.012	0.016	0.015	0.015	0.001	9.7 %

Characteristic a_ϕ absorption peaks occurs in the red range between 650-700 nm and in the blue range of 430-450 nm for some of the samples, even though they were not well defined in the blue range. The exponential increase in absorption at short wavelengths can be associated with dissolved organic matter, which remains in the filter and affects spectrophotometric measurements (BINDING et al., 2008).

As expected, there is a stronger linear relationship between $a_\phi(676)$ and Chla. The linear relationship between TSOM and a_ϕ is weak, but despite this low value, the existence of a relationship might indicate the presence of organic NAP in a_ϕ. TSM and TSIM presented, as expected, no relationship with a_ϕ (Appendix B).

Specific absorption coefficients are presented in Figure 6.13 and Table 6.7. Ratio a_p/TSM or $a_\phi/Chla$ present extremely high values, not comparable to those reported in literature (MA et al., 2006; CAMPBELL et al., 2011; WU et al., 2011; MATTHEWS; BERNARD, 2013). Babin and Stramski (2004), however, shows that minerogenic particles influence the absorption coefficient resulting in values as high as those of Figure 6.13a. Two factors explain high a^*_ϕ coefficients: *high phytoplankton absorption efficiency* and the *pigment composition of phytoplankton cells*. These effects are mainly due to species types (CIOTTI et al., 2002), cell size (BRICAUD et al., 1995), pigment

content and the physiological state of phytoplankton caused by environment conditions such as temperature, nutrients and light availability (BRICAUD et al., 1995; BABIN et al., 2003; BINDING et al., 2008). The Linear approach (Blue solid and dotted lines), however presents lower a^*_ϕ values. Also it is worth to mention that the T-R method does not completely remove the offset above 700 for a^*_ϕ, indicating problems in the methodology which might be tested in further studies.

The use of a single a^*_ϕ to represent phytoplankton absorption characteristics for the entire lake may be controversial, because it does not account for the variability previously mentioned. Despite that, it might be a viable input for remote sensing algorithms.

Figure 6.13 - Specific Spectrophotometer Absorption Measurements

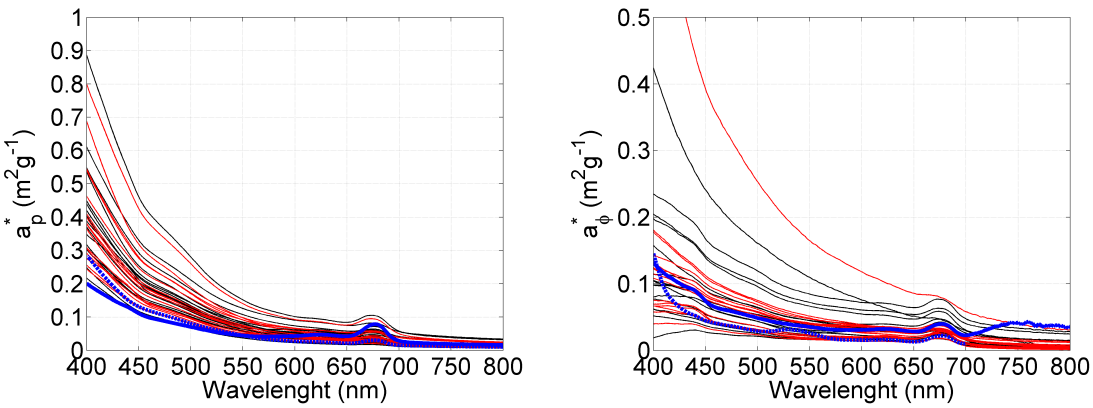

(a) a^*_p (b) a^*_ϕ

Only stations with no zeroed or negative values ploted. Color Code : Red: First Set of Samples and Black: Second Set of Samples for the division a_p over TSM or a_ϕ over Chla; Solid Blue: First Set of Samples and Dotted Blue: Second Set of Samples for the Linear Regression Specific Absorption

Table 6.7 - Specific Absorptions in 676 nm for the division a_p over TSM and a_ϕ over Chla;- Particulate (a^*_p) and Phytoplankton (a^*_ϕ)

	Min	Max	Median	Mean	Std	CV
a^*_p First Set of Samples	0.017	0.105	0.044	0.049	0.023	0.479
a^*_p Second Set of Samples	0.020	0.094	0.038	0.043	0.018	0.418
a^*_ϕ First Set of Samples	0.017	0.076	0.030	0.037	0.018	0.483
a^*_ϕ Second Set of Samples	0.018	0.079	0.031	0.033	0.014	0.429

6.4.2 LISST Results

Figure 6.14 shows the particle number (a) and the volume distribution (b) for *April*. Both displays a bi-modal behavior, with a smaller peak below 10 μm and a second at 15 μm which are similar to previous observations reported by Bouchez et al. (2011) for Solimoes River and by Espinoza Villar et al. (2013) in Madeira river.

Both figures 6.14(a and b) show the presence of artifacts which are more noticeable in figure 6.14b: (1) the volume distribution presents a sharp increase in particle concentration at the minimum diameter (below ≈ 5 μm) followed by a minimum at ≈ 5 μm; (2) a fast increase at the maximum diameter. As discussed by Reynolds et al. (2010) and Agrawal et al. (2008), this sharp increase at the minimum particle diameter might be caused by both, stray light contamination and the presence of particles smaller than the optical measurement range. The artifact at the maximum diameter might be caused by bubbles (Slade and Boss personal communication). The presence of Non-spherical particles in the sample might also cause those artifacts when one uses, as in this present study, the LISST inversion algorithm assuming homogeneous spheres. Therefore in the fitting of Junge distribution, only the 2 to 50 μm diameter interval was used.

Figure 6.14 - Particle Size Distributions for *April*

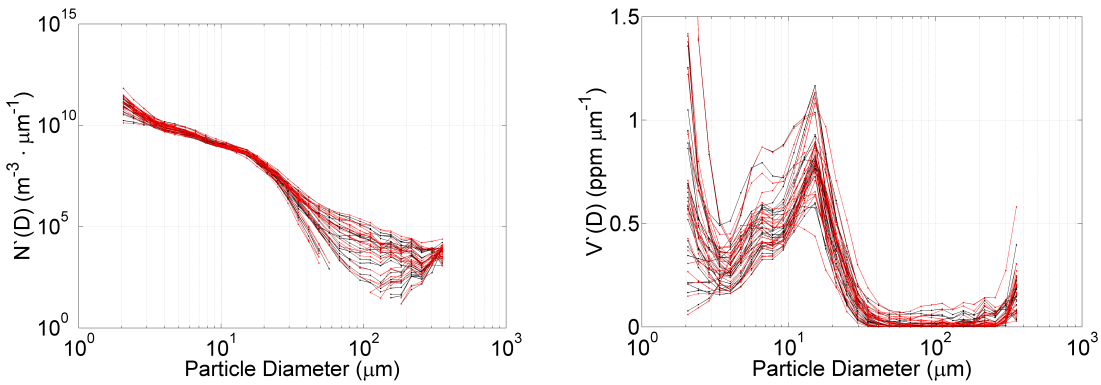

(a) (b)

(a) Particle Volume Distribution (V(D)) and (b) Particle Number Size Distribution ($N'(D)$) (See section 3.1.2). Red: First Set of Samples and Black: Second Set of Samples.

Table 6.8 presents the statistical indexes for the Junge exponent. Median and Mean values are within the range of previous investigations (≈ 4) (LOISEL et al., 2006;

PENG; EFFLER, 2007; REYNOLDS et al., 2010; SLADE; BOSS, 2015), but CV is over 25 % which explains the high range (1.06 to 5.99).

Table 6.8 also allows the comparison of both, scattering and backscattering exponents (γ_b and γ_{b_b} Table 6.3) by applying the approximation $\xi_{psd} = \gamma_X + 3$ (BOSS; PEGAU, 2001; DOXARAN et al., 2009; SLADE; BOSS, 2015). Theoretically, $\gamma_X = \xi_{psd} - 3$ one would expect a linear relationship between ξ_{psd} and γ_X. However, although median γ_X and mean values are (1.279 and 1.111) similar to those in Table 6.3, figure 6.15a shows that the variability of ξ_{psd} is much higher than that of γ_b .

As discussed by Boss et al. (2001) the fitting of a Junge distribution to the PSD depends on both, the reference number concentration N_0 at a reference diameter D_0 and the upper and lower boundaries of the distribution. As shown in figure 6.15b, UPD can exceed 15 %. Previous studies by (PENG; EFFLER, 2007; PENG et al., 2009) show that the power law model is a poor descriptor of the size distribution what may cause the variability of ξ_{psd} indicating the need of more sounder approaches.

Table 6.8 - Statical Indexes for fitted Junge Model Exponent (ξ_{psd})

Exponent	Samples	Min	Max	Median	Mean	Std	CV
ξ_{psd}	First Set	1.060	5.996	4.279	4.155	1.152	27.7 %
	Second Set	0.896	5.937	4.111	4.055	1.143	28.2 %

Figure 6.15 - Comparison of (a) ξ_{psd}/γ_b (b) Junge Model/Measured PSD

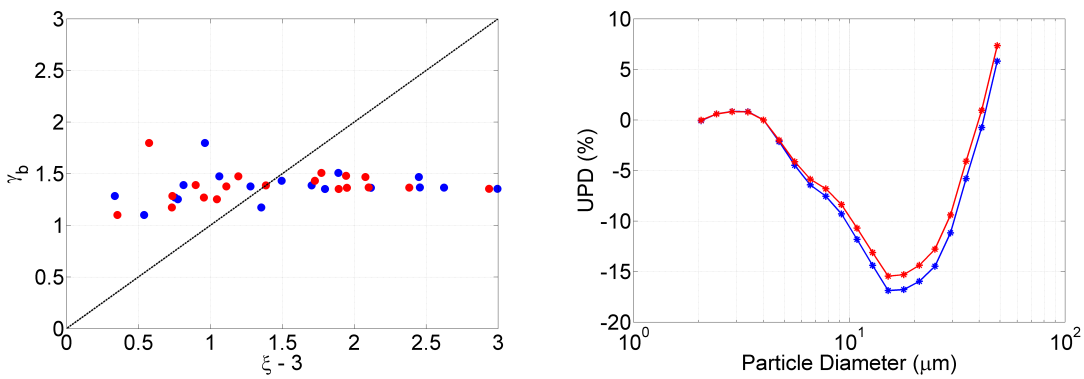

(a) (b)

(a) $\xi_{psd} + 3$ and γ_b plot - Dotted line is the 1:1; (b) UPD calculated comparing Junge Model and Measured PSD. Color Code: Red-First Set of Samples - Blue: Second Set of Samples

7 INVERSE MODELS

In this chapter the results for GIOP, QAA and Nechad semi-analytical algoriths are presented as previously presented in section 4.6. GIOP tests and *Sensitivity Analysis* follows the description of section 4.6.1. Tests of QAA versions (QAA-V5 and QAA-Mishra) follows section 4.6.2 and Nechad algorithm tests follows section 4.6.3.

7.0.1 GIOP

Figure 7.1 shows two indexes used to compare GIOPs outputs and laboratory measurements for the best results as explained in Chapter 4 (Section 4.6.1). They are a combination of b_{bp} Exponent (1.35)(table 6.3), $a_{nap+cdom}$ Exponent (0.015 Table 6.6), Linear Regressed a^*_ϕ (figure 6.13) all from *April* and using the Overconstrained Linear matrix inversion. R^{Ab}_{rs-RC} (figure 5.3) was also used as input. Only the stations selected in section 6.4.1 (Chapter 6) were used for *April* laboratory comparison. ACS/Hydroscat corrected by Rottgers/Doxaran were used and all stations from *August* and *April* included in the comparison.

Figure 7.1 - Statistical Indexes comparing GIOP derived and Laboratory Measured $a_{T-w}(\lambda)$ ($a_{T-w}(\lambda) = a_p(\lambda) + a_{cdom}(\lambda)$), $a_\phi(\lambda)$ and $a_{nap+cdom}(\lambda)$ for *April*

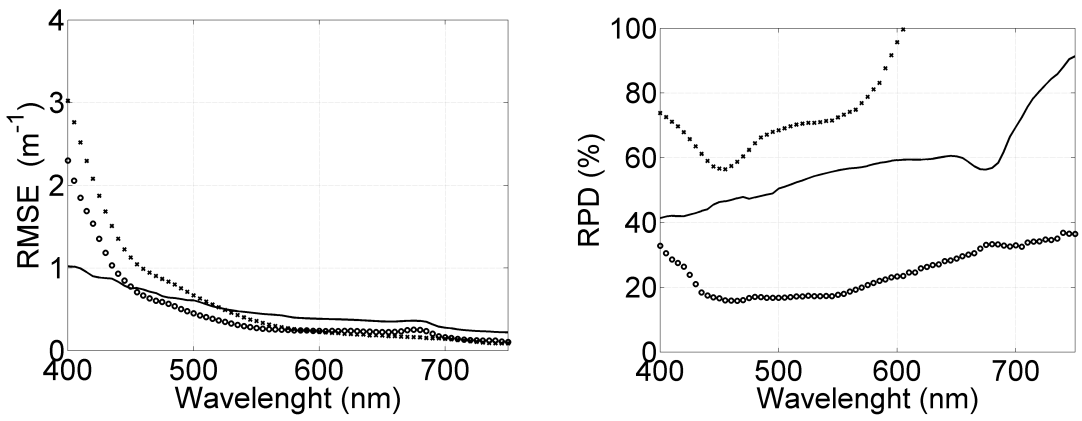

(a) (b)

Symbol Code: $''o''$: $a_{T-w}(\lambda)$, $''x''$: $a_{nap+cdom}(\lambda)$, Solid Line: $a_\phi(\lambda)$. Inputs: b_{bp} Exponent from April (1.35); $a_{nap+cdom}$ Exponent from April (0.016), Linear Regressed a^*_ϕ from April; Overconstrained Linear matrix inversion using QR decomposition.

Figure 7.1 shows that the highest RMSE are at the 400 to 500 interval, reaching up to

2 m^{-1} for $a_{nap+cdom}$ and decreasing with wavelengths. RPD, however, highlights that errors can reach values larger than 100 %, and different from RMSE, increases with wavelength. Total absorption ($a_{T-w}(\lambda)$ which is $a_{T-w} = a_p + a_{cdom} - a_w$) present the lowest RPD values ($\approx$ 20 to 40 %). $a_{nap+cdom}(\lambda)$ RPD are around 30 % in the blue region (400 to 500) but quickly reaches more than 100 % beyond 650 nm. Regarding $a_\phi(\lambda)$, RPD is around 40 % in the blue and increases steadily to 90% with wavelength.This wavelength dependence of RPD may be explained by the following facts: (1) R^{Ab}_{rs-RC} (figure 5.3) becomes insensitive to the components of $a_{T-w}(\lambda)$ ($a_{nap+cdom}(\lambda)$ and $a_\phi(\lambda)$) as the absorption by those components decrease with wavelength or at specific absorption ranges. That explains the presence of a signal of the phytoplankton absorption feature in the red range ($a_\phi(\lambda)$ RPD).(2) On the other hand, backscattering beyond 600 nm becomes a larger proportion of R^{Ab}_{rs-RC} reducing its sensitivity to the components of total absorption ($a_{T-w}(\lambda)$); (3) $a_{nap+cdom}(\lambda)$ approaches zero beyond 600 which might explain the exponential increase in RPD from this point on and (4) $a_\phi(\lambda)$ also approaches zero beyond 700 what increases RPD ($> 60\%$) beyond the phytoplankton absorption feature.

When comparing to ACS/Hydroscat measurements (Figure 7.2), $a_{T-w}(\lambda)$ errors are higher than errors for $a_{T-w}(\lambda)$ presented in Figure 7.1. RMSE reaches 4 m^{-1} in the blue range, particularly in 400 to 410 nm interval and RPD increases from 40 % to 100 % along the wavelengths.

The larger differences found for $a_{T-w}(\lambda)$ ACS are mainly due to differences between $a_{T-w}(\lambda)$ from ACS and $a_{T-w}(\lambda)$ measured in laboratory (Figure 5.18 - Section5.3). As can be noted in Figure 5.18 from Section5.3, RPD between $a_{T-w}(\lambda)$ from ACS and $a_{T-w}(\lambda)$ measured in laboratory reaches 100 % in $\approx$ 600 nm what agrees with Figure 7.2 in which RPD reaches 100 % in 700 nm for *April* (cyan) and around 600 nm for *August* (Red) and *All Samples* (Black) (August+April). It is noteworthy that RMSE (Figure 7.2) is similar for *August* and *April* which might be explained by IOP similarities between those two seasons, as presented in section 6 (Figures 6.4 and 6.5). However, as previously mentioned, RPD reaches 100% in 700 nm for *April* (cyan) and around 600 nm for *August* (Red) what indicates that might be differences between *April* and *August* in absorption values components ($a_{nap+cdom}(\lambda)$ and $a_\phi(\lambda)$).

The differences between *August* and *April* are better observed in b_{bp} comparison (Figure 7.2c/d). RPD errors are lower than 40% and particularly stable in the 400 to 750 nm interval. Different from $a_{T-w}(\lambda)$, b_{bp} RPD for *August* is approximately

twice the values from *April* (40% to 20%), which suggest that b_{bp} Exponent in *April* (1.35) might not be the best input for *August* retrievals. Tests using b_{bp} Exponent from *August* (1.08), however, amounted in poor results. The impact of the choice of the b_{bp} exponent in the inversion (Not shown) was actually very low which might indicate that absorption characteristics dominates the retrieval of AOPs.

Figure 7.2 - Statistical Indexes comparing GIOP derived and ACS/Hydroscat Measured $a_{T-w}(\lambda)$ and $b_{bp}(\lambda)$

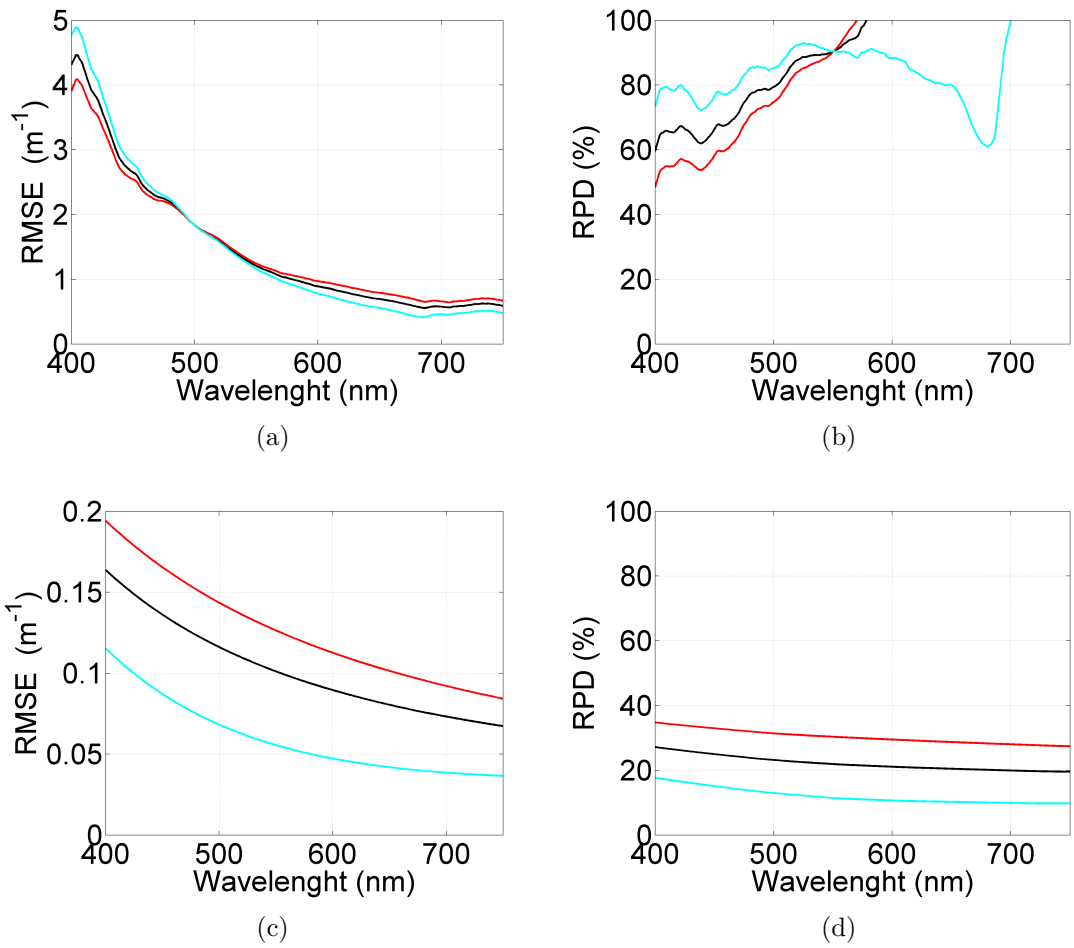

Color code - Black: *All Samples* (= *August* + *April*), Red: *August*, Cyan: *April*. Inputs: b_{bp} Exponent from April (1.35); $a_{nap+cdom}$ Exponent from April (0.016), Linear Regressed a^*_ϕ from April; Overconstrained Linear matrix inversion using QR decomposition.

Table 7.1 shows the results for Chla estimates. As mentioned in chapter 4 (Section 4.6.1), Chla concentration is a direct product of GIOP. GIOP derived Chla were compared to measured Chla in *August*, *April* and *All Samples*. For all the tested

seasons, the results for Chla were poor, reaching RPD > 181% in *April* and RMSE shows that Chla varies $\approx 11\ mgm^{-3}$. For *August* and *All Seasons*, RPD values can be as high as 165% and 172%, respectively, and for $\approx 18\ mgm^{-3}$ for *August* and $\approx 16\ mgm^{-3}$ for *All Seasons*. The impact of each tested GIOP input will be further discussed.

Table 7.1 - Statistical Indexes comparing Measured and Derived TSM/Chl-a - Inputs: b_{bp} Exponent from April (1.35); $a_{nap+cdom}$ Exponent from April (0.015), Linear Regressed a^*_ϕ from April; Overconstrained Linear matrix inversion using QR decomposition.

Chlorophyll-a	All Samples	August	April
RPD (%)	172.81	165.42	181.97
RMSE (mgm^{-3})	15.21	17.73	11.31

The variability of b_{bp} had little impact on Chla estimates, even with the relatively high difference from the tested values (1.03 to 1.50 for February (see Table 6.3)). The same minor impact was observed for $a_{nap+cdom}$ exponent (0.014 to 0.016). The highest impact on Chla estimates was observed for tested a^*_ϕ models, presented in Figure 7.3. The inspection of Figure 7.3 shows that there is a noticeable difference between a^*_ϕ models and measurements in *April*. In the 500 to 650 nm interval, differences are very great. The tested models simulate the characteristic chlorophyll-a absorption peaks in 440 and 676 nm, whilst in the a^*_ϕ measurements no peak is observed in 440 nm and only the 676 peak is presented. *Ciotti* model did not provide good Chla estimates, even when using the highest size factor ($S_f = 1$). With $S_f = 1$, the 676 nm absorption peak is much lower than that measured in *April*. *Ciotti* model might not be suitable for inland turbid waters mainly because it was, parametrized for Case I waters, as emphasized by (CIOTTI; BRICAUD, 2006). Maritorena et al. (2002) model also did not result in good Chla estimates, mainly due to the poor modeling of 676 nm feature, which is essential for Chla retrieval in CDOM rich Curuai Lake waters. Bricaud et al. (1998) model, on the other hand, presented the best results when compared to measured a^*_ϕ. With Chla concentration larger than 7 μgL^{-1} the model approaches measured values at both, 440 nm and 676 nm peaks. The inspection of Table A.2 (Appendix A) shows that the median of *April* is 8.4 μgL^{-1}, which is within the 7 to 10 μgL^{-1} interval used as input to Bricaud et al. (1998) model. The limitation of Bricaud et al. (1998) model, however, is that Chla concentration is needed as input. This input, when using Remote Sensing methods,

is mainly based on empirical relations and might not be adequate when dealing with high and variable Chla environment such as that of Curuai Lake.

Figure 7.3 - Specific Absorption (a^*_{ph}) comparison

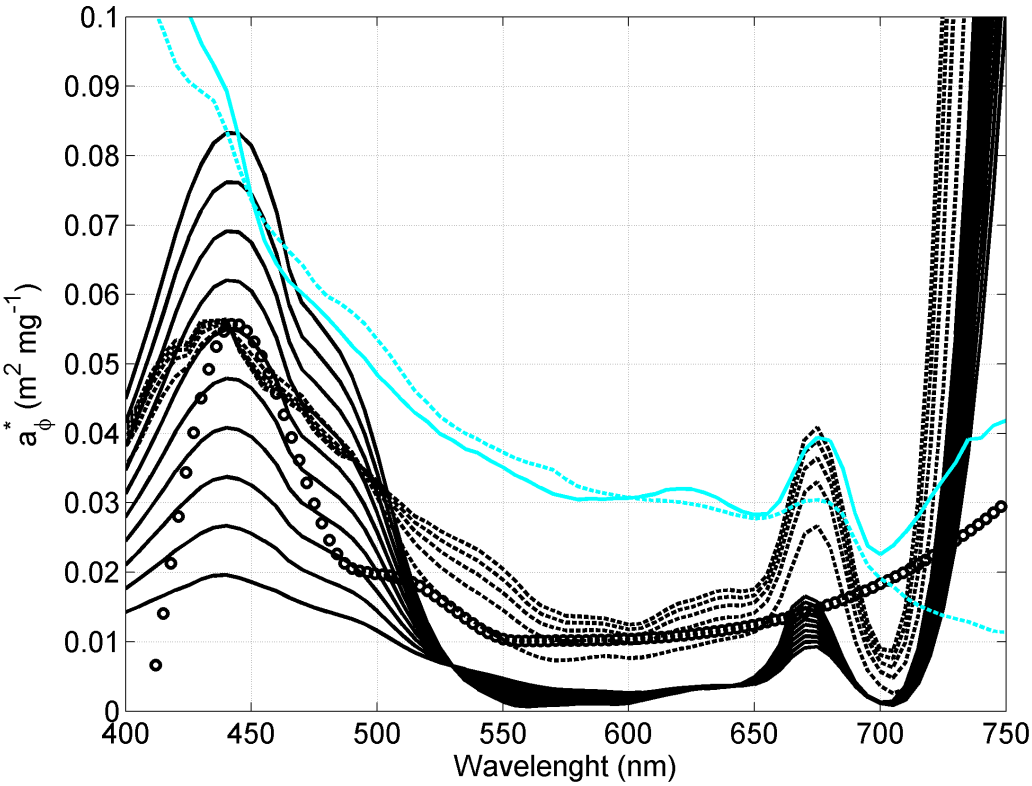

Cyan Solid Line: Median a^*_{ph}, Cyan Dashed Line: Linear Regressed a^*_{ph}. Black Color/Symbol code: Solid Line: Ciotti and Bricaud (2006) model varying the size parameter (S_f in 0:0.1:1); Black Dashed Line: Bricaud et al. (1998) model varying the Chlorophyll- concentration (1:2:10 μgL^{-1}); Black "o": Maritorena et al. (2002) Model.

It is also important to highlight the influence of errors in the measured R^{Ab}_{rs-RC} on IOPs and Chla retrievals. The absence of correction for bidirectional and shading effects would be the first to cause bias IOPs retrievals. Bidirectional effects would cause an increase in b_{b_p} and decrease a_T retrievals, whilst shading effects due to the lack of illumination would cause the inverse, i.e. a decrease in the in b_{b_p} and a increase a_T retrievals. Also, especially for the *April* field campaign some stations were measured with cloudy sky condition, which influences the surface reflectance factors applied for glint corrections. Any glint would increase b_{b_p} artificially, which would lead to a mismatch to the measured IOPs. Also, different from ocean waters

were bubbles affects R_{rs}^{Ab}, for inland waters bubbles are rare. However, a *scum* is sometimes observed in lakes surface, which would also be a source of uncertanties for inverse methods.

The poor results presented in the previous analysis reinforce the need of sensitivity analysis. Sensitivity analysis were carried out based on inputs described in table 4.4, with the variation of b_{b_p} and $a_{nap+cdom}$ Exponents. Only the stations selected in section 6.4.1 (Chapter 6) were used. The 10% criteria (ConvCrit = 0.1), which states that differences between modeled and measured R_{rs} cannot exceed 10% (WANG et al., 2005) did not provided solutions and a 30 % criteria was selected to run the sensitivity analysis (ConvCrit = 0.3) of GIOP.

Figure 7.4 show sensitivity analysis results for all used stations in all wavelengths (400 to 750 nm). From all the possible modeled solutions, which respect the 30 % criteria, for a_{T-w}, a_{ϕ}, $a_{nap+cdom}$, b_{b_p} , figure 7.4 summarizes the median (Black), 5 (Blue) and 95 (Red) percentiles. a_{T-w} (Figure 7.4a) median values (black) are the closest to the 1:1 line, specially when considering values higher than 5 m^{-1}. Below ≈ 2 m^{-1}, solutions deviate from 1:1 line, increasing rapidly when measured a_{T-w} approaches zero. For low a_{T-w} values, median, 5 and 95 percentiles results are similar and close to the 1:1 line. When values increase (Higher values correspond to shorter wavelengths) there is a spread of the median, 5 and 95 percentiles solutions. For a_{ϕ} there is no dominant pattern. From 0 to 1 m^{-1} median, 5 and 95 percentiles solutions are close to 1:1 line and beyond 1 m^{-1} median and 95 percentiles solutions deviate from 1:1 line. The same type of behavior presented a_{T-w} for is observed for $a_{nap+cdom}$ and b_{b_p} (Figure 7.4c/d). Median solutions are the closest to 1:1 line and median, 5 and 95 percentile solutions spread from the 1:1 line with the increase of values. The spread of data could be explained by the impact that the choice of $a_{nap+cdom}$ and b_{b_p} exponents. This choice of exponents has a higher impact on higher values of $a_{nap+cdom}$ and b_{b_p}, specially $a_{nap+cdom}$, which approaches zero for longer wavelengths.

Figure 7.4 - Comparison of Measured and Derived a_{T-w}, $a_{nap+cdom}$, a_{ph} and b_{bp}

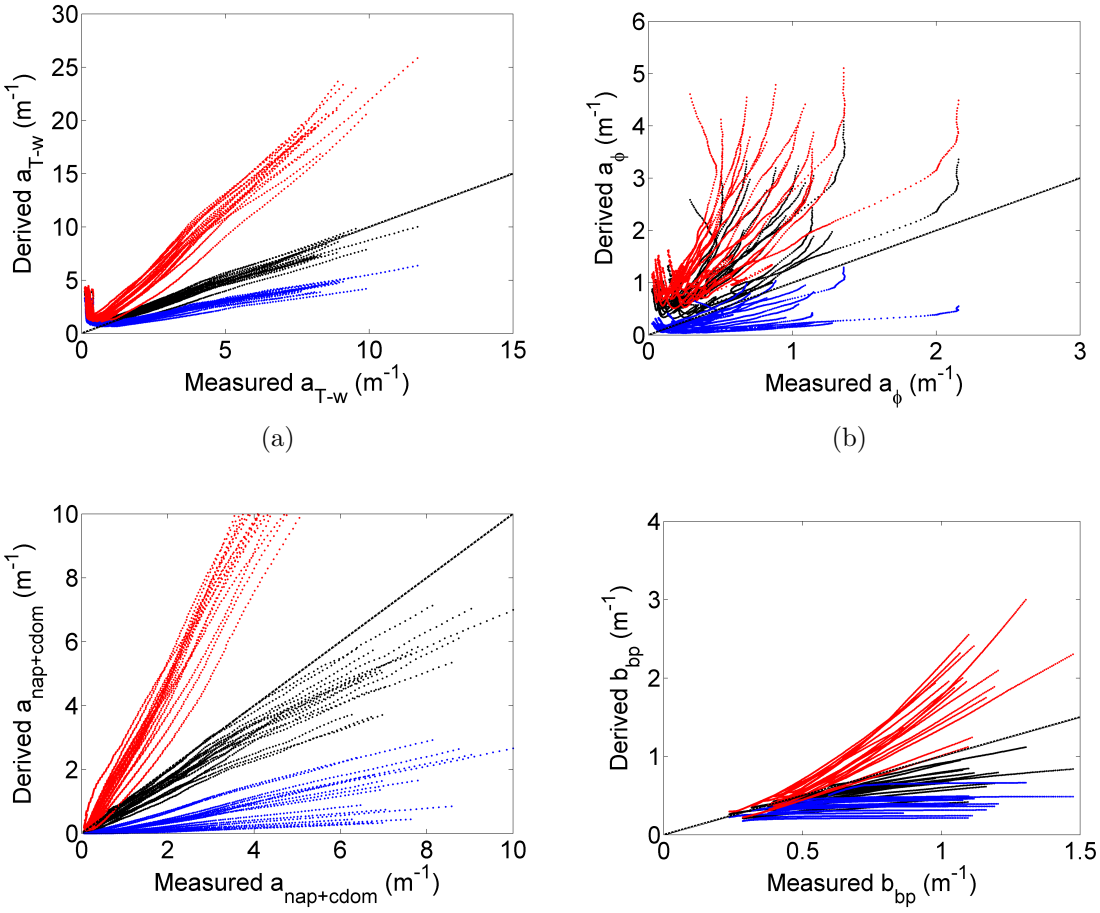

(a) (b) (c) (d)

Color Code: Red: 95(%) Percentiles from the sensitivity analysis solutions; Blue: 5(%) Percentiles from the sensitivity analysis solutions; Black: Median of the sensitivity analysis solutions. Only solutions that follows ConvCrit = 0.3 are presented.

Figure 7.5 shows the median and standard deviation of all $a_{nap+cdom}$ and b_{b_p} exponents resulted from the sensitivity analysis (ConvCrit = 0.3).In figure 7.5a, median $a_{nap+cdom}$ exponents spread around the 1:1 line while in figure 7.5b, median b_{b_p} exponents are more stable with the variation of measured b_{b_p} exponent. Standard deviation for both, $a_{nap+cdom}$ and b_{b_p} exponents, shows that values spans over a wide range. Therefore, accepted solutions (ConvCrit = 0.3) leads to a variety of possible exponents which increase uncertainties and similar to what was discussed by Wang et al. (2005). It is important to highlight that no sensitivity analysis was carried out for a_{ϕ} models, different from Wang et al. (2005), which used the *Ciotti* model and variate its size factor (S_f). As discussed previously, *Ciotti* model did not result in

good estimates of IOPs and therefore $a^*_\phi(\lambda)$ measured in *April* was used. Since $a^*_\phi(\lambda)$ was the main source of variability for GIOP, further analysis should be carried out to achieve better uncertainties estimates.

Figure 7.5 - Comparison of $a_{nap+cdom}$ and b_{b_p} exponents derived from for median solutions presented in Figure 7.4

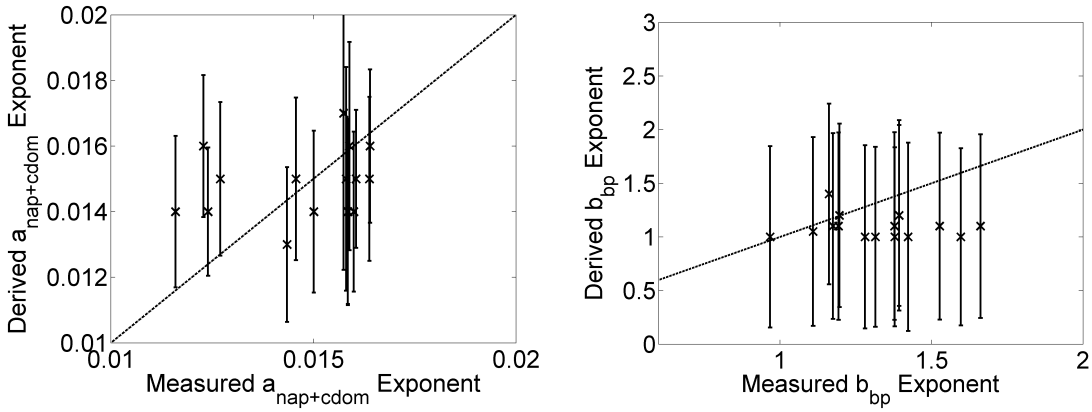

(a) (b)

"x" represent the median of $a_{nap+cdom}$ and b_{b_p}. Bars are the standard deviation of solutions which follows ConvCrit = 0.3

As final recommendations, the GIOP algorithm is directly dependent on the quality of IOPs and R_{rs} inputs. For future studies, a better characterization of IOPs, specially $a^*_\phi(\lambda)$ could improve the results previously obtained. Also, a careful choice of R_{rs} could also contribute for the lower errors in the retrieval of IOPs and Chla.

7.0.2 QAA

Two versions of QAA were tested: QAA-Mishra and QAA-V5 (Section 4.6.2). As described in section 4.6.2, the output of both QAA versions were compared to *April* Laboratory measurements ($a_p(\lambda)$, $a_{nap+cdom}(\lambda)$ and $a_\phi(\lambda)$) and with ACS/Hydroscat $a_T(\lambda)$ and $b_{bp}(\lambda)$ for *August*, *April* and the combination of both (*All Samples*). Since QAA provides $a_T(\lambda)$, which includes absorption by water (a_w), a_w was added to Laboratory ($a_p(\lambda)$ + $a_{cdom}(\lambda)$) and ACS total absorptions. R^{Ab}_{rs-RC} (figure 5.3) was also used as input. Only stations selected in section 6.4.1 (Chapter 6) were used for *April* laboratory comparison. ACS/Hydroscat Rottgers/Doxaran corrections were used and all stations from *August* and *April* included in the comparison.

Figure 7.6 presents QAA-(Mishra and V5) results for *April* dataset. The comparison

of both versions of QAA shows that, for $a_T(\lambda)$, in the 400 nm to 500 nm interval QAA-Mishra (Figure 7.6c/d) outperformed QAA-V5 (Figure 7.6a/b). For the 600 to 700 nm interval, QAA-V5 was slightly better than QAA-Mishra with RMSE lower than 1 m^{-1} and RPD $\approx$ 100 %. Also beyond 700, QAA-V5 presented lower RMSE and RPD ($< 2m^{-1}$ and $\approx$ 100 %), while QAA-Mishra causes a fast increase in RMSE ($\approx 1.5m^{-1} < RMSE <\approx 4.5m^{-1}$) and small rate of increase in RPD ($\approx 150\% < RPD <\approx 170\%$). QAA-V5 underestimation of $a_T(\lambda)$ was demonstrated by Mishra et al. (2014) for high Chla concentration and somehow explains the better results of QAA-Mishra in the 400 to 500 nm interval. However, RPD close to 100% along the spectra shows that, for both approaches, results are poor. For $a_{nap+cdom}(\lambda)$ comparison, in the 400 to 500 nm interval, both approaches reach RMSE larger than 5 m^{-1} and RPD larger than 100 %. In the 500 to 750 nm interval QAA-Mishra is slightly better than QAA-V5 with RMSE reaching values lower than $1m^{-1}$ and $RPD < 50\%$. For $a_\phi(\lambda)$, QAA-V5 outperforms QAA-Mishra in the 400 to 600 interval. RPD and RMSE are below 100% and below 1 m^{-1} respectively for QAA-V5 whilst QAA-Mishra have RPD between 100 and 500 % and RMSE between 1 and 2 m^{-1}.

Figure 7.6 - Statistical Indexes comparing QAA-(Mishra and V5) derived and Laboratory Measured $a_T(\lambda)$ ($a_T(\lambda) = a_p(\lambda) + a_{cdom}(\lambda) + a_w$), $a_\phi(\lambda)$ and $a_{nap+cdom}(\lambda)$ for *April*

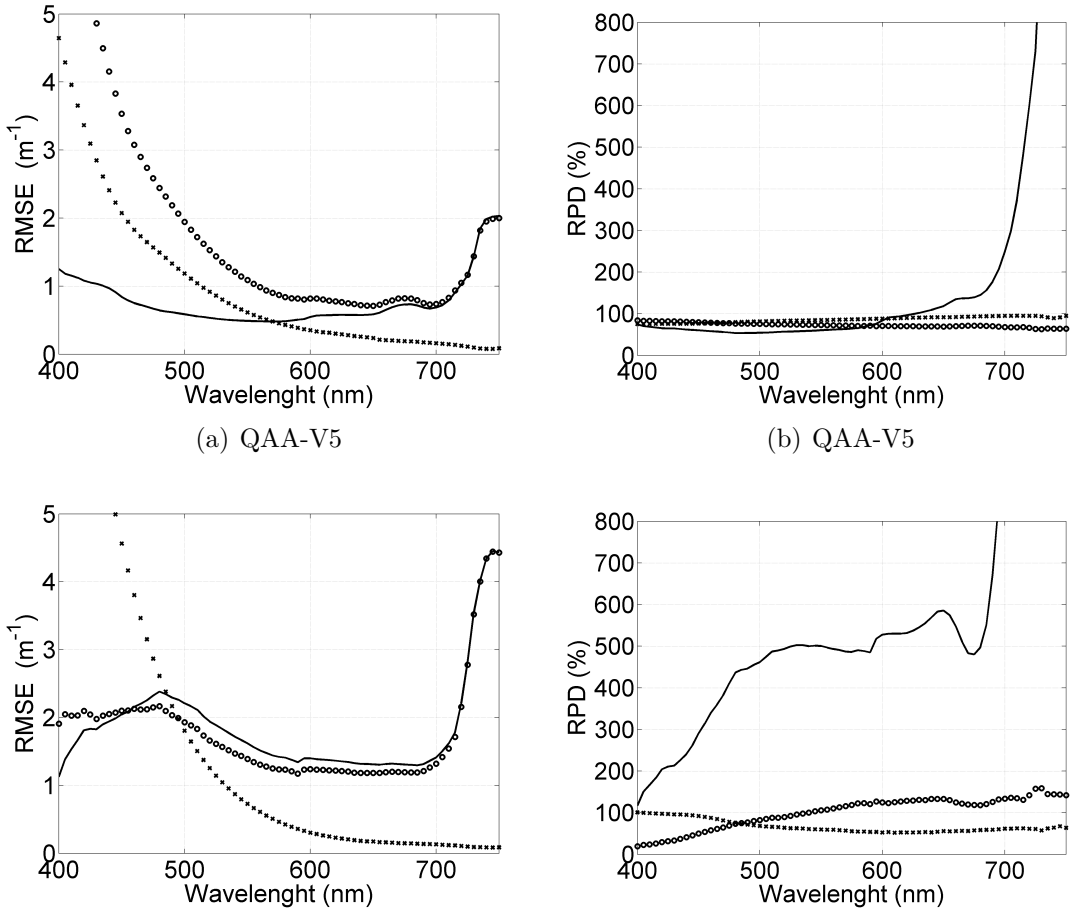

(a) QAA-V5 (b) QAA-V5

(c) QAA-Mishra (d) QAA-Mishra

Symbol Code: $''o''$: $a_T(\lambda)$, $''x''$: $a_{nap+cdom}(\lambda)$, Solid Line: $a_\phi(\lambda)$

The reasons for those poor results regarding the two tested version of QAA are mainly related to both, R^{Ab}_{rs-RC} and QAA steps presented in section 3.3.2.1. Regarding R^{Ab}_{rs-RC}, the shape presented in figure 5.3 is notably different from case I waters for which QAA-V5 was developed (LEE et al., 2002; LEE et al., 2007) and high Chla concentration waters for which QAA-Mishra was tuned. Particularly, the peak in 676 nm is not as noticeable as those presented by Mishra et al. (2014) which might be one of the reasons for the very poor $a_\phi(\lambda)$ presented in figure 7.6. Regarding the steps of QAA, the empirical choice of $a_T(\lambda_0)$ with $\lambda_0 = 555$ for QAA-V5 and $\lambda_0 = 708$ for QAA-Mishra in equations 3.39 and 4.28 might not be suitable for Curuai Lake Waters. Although both assumptions from equations 3.39

and 4.28 caused high RPD, they seem to have distinct impacts on the retrieval of $a_T(\lambda)$. While for QAA-V5, RPD is flat along the spectra, for QAA-Mishra, RPD is lower for shorter wavelengths and higher for longer wavelength. This difference is reinforced by the comparison between QAA $a_T(\lambda)$ and ACS absorption coefficient (figure 7.7). QAA-V5 RMSE (figure 7.7a) is quite similar to Laboratory $a_T(\lambda)$ comparison (figure 7.6a) and QAA-V5 RPD (figure 7.7b) is lower than the comparison to Laboratory $a_T(\lambda)$(figure 7.6b), but also flat along the spectra. QAA-Mishra RMSE shape is quite different from Laboratory $a_T(\lambda)$ comparison (figure 7.7c) whilst RPD (figure 7.7d) have values below 20 % for the 400 to 600 nm interval, and rapidly increases beyond 600 nm reaching 100 % for longer wavelengths, which follows the same behavior of Laboratory $a_T(\lambda)$ comparison. Based on those observations, QAA-Mishra assumption seems more suitable for Curuai Lake $a_T(\lambda)$, at the 400 to 600 nm interval.

Figure 7.7 - Statistical Indexes comparing QAA-(Mishra and V5) derived and ACS Measured $a_T(\lambda)$

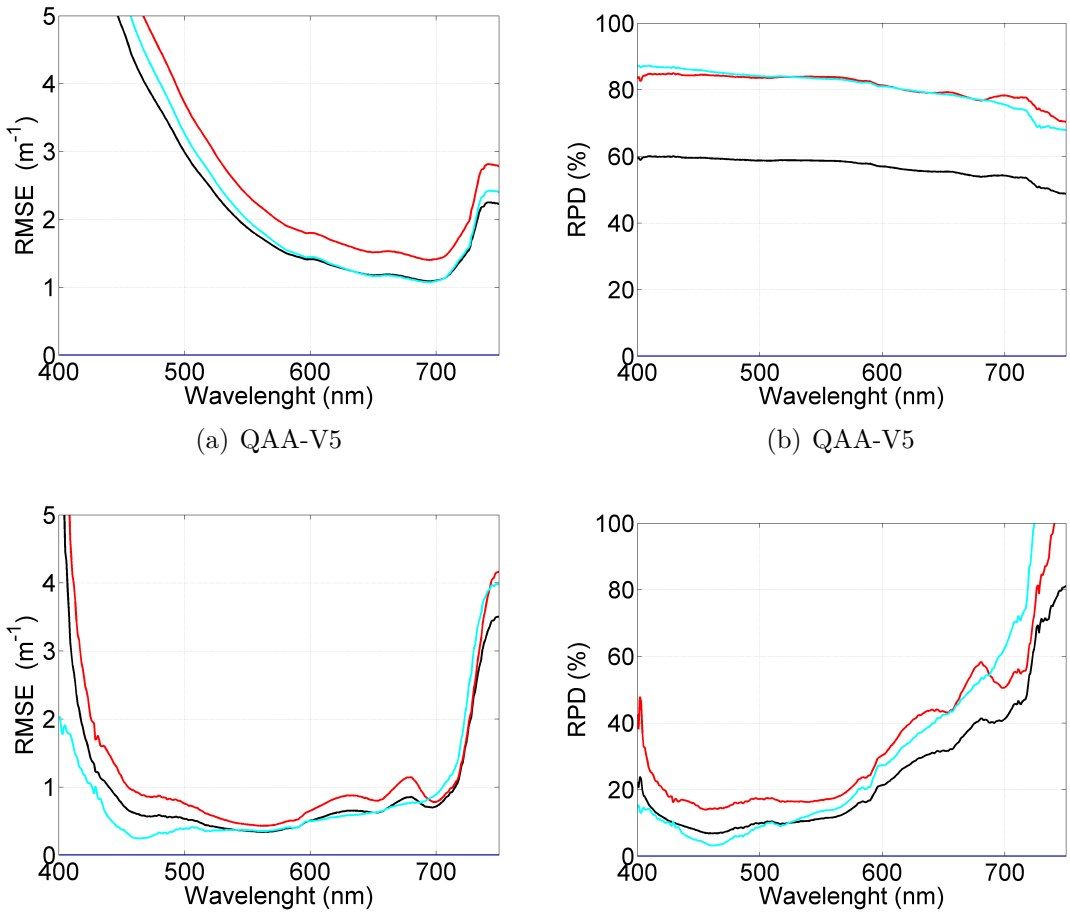

(a) QAA-V5 (b) QAA-V5

(c) QAA-Mishra (d) QAA-Mishra

Color code - Black: *All Samples* (= *August* + *April*), Red: *August*, Cyan: *April*.

Regarding the comparison between *August* and *April* presented in figure 7.7, both seasons presented similar RPD values for QAA-V5, but, *April* presented lower RPD for QAA-Mishra. The similarities between *August* and *April* in the performance of both QAA versions reinforce the IOPs and biogeochemical similarities presented Chapter 6. Another example of this similarity is observed in figure 7.8. RMSE in figure 7.8a presents a decay from $\approx 0.55\ m^{-1}$ to $0.2\ m^{-1}$ in 750 nm for QAA-V5 whilst 7.8c shows that for QAA-Mishra, RMSE is flater along the wavelength. On the other rand, QAA-V5 RPD presented approximately constant values along the spectra in the range between 70 % to 80 % and QAA-Mishra presented RPD starting around 60 % and increasing towards 150% for longer wavelengths. The comparisons among seasons show very low variability and the behavior of RPD is similar to

ACS absorption presented in figure 7.6. The difference between QAA versions for b_{b_T} could result from the influence of $a_T(\lambda_0)$ on the calculation of $b_{b_p}(\lambda_0)$ (section 3.3.2.1). This differences could also be related to the calculation of Y (Equation 3.44).

Figure 7.8 - Statistical Indexes comparing QAA-(Mishra and V5) derived and Hydroscat Measured $b_{bp}(\lambda)$

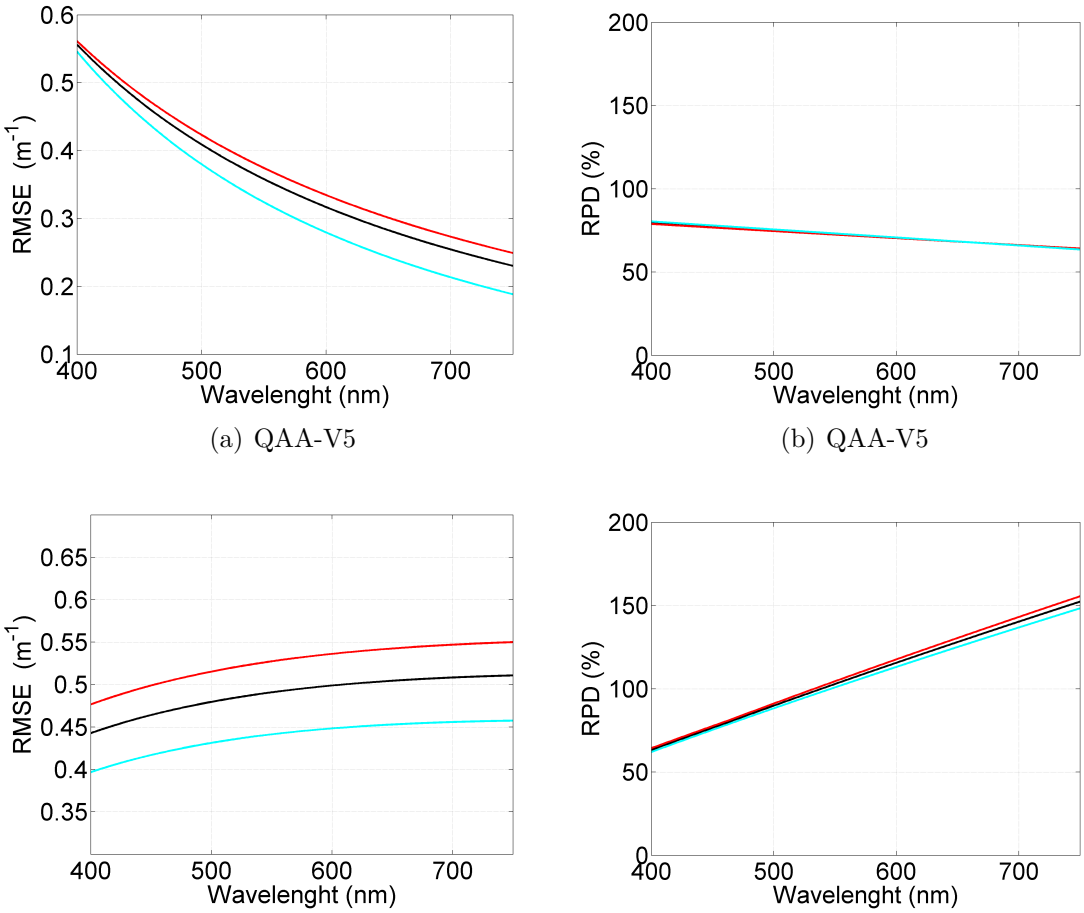

(a) QAA-V5 (b) QAA-V5

(c) QAA-Mishra (d) QAA-Mishra

Color code - Black: *All Samples* (= *August* + *April*), Red: *August*, Cyan: *April*.

The performance of both QAA versions was not satisfactory for Curuai Lake. Although some RMSE/RPD values indicate a reasonable performance ($< 1m^{-1}$ and $<$ 20% respectively) particularly for QAA-Mishra, the general analysis shows a poor performance of both QAA versions. thus there is the need for further studies which would test the set of parameters for the derivation of $a_T(\lambda_0)$, $b_{b_p}(\lambda_0)$ and other pa-

rameters of QAA. As a recommendation, a parametrization of QAA is crucial for future analysis, similar to what was performed by Mishra et al. (2014).

7.0.3 Nechad

The *Nechad* algorithm, which was developed to retrieve TSM concentrations (section 3.3.2.2, Chapter 3.1), was tested for *February*, *August* and *April* (section 4.6.3, Chapter 4). Figure 7.9 shows the comparison of $a_p^*(\lambda)$ and $b_{b_p}^*(\lambda)$, derived from both, measurements taken in *April* and from Nechad et al. (2010) A^p and C^p tabulated parameters (section 3.3.2.2). Two $a_p^*(\lambda)$ were derived from the first set of samples of *April*: The median of $a_p(\lambda)/[TSM]$ and from Linear Regression, as presented in Figure 6.13 in Chapter 6. $b_{b_p}^*(\lambda)$ was also calculated in two different forms: as the median of $b_{b_p}(\lambda)/[TSM]$ and from Linear Regression, similar to the analysis described in section 6.3.2 (Table 6.4), but for each single wavelength in the 400 to 800 nm interval. $b_{b_p}^*(\lambda)$ was calculated for *February*, *August* and *April*, and only Hydroscat median surface measurements were used (Section 4.5.1).

Figure 7.9a shows that both median and Linear fitted measured $a_p^*(\lambda)$, as well as, $a_{nap}^*(\lambda)$, are higher than Nechad et al. (2010) $a_p^*(\lambda)$. The same behavior can be observed in figure 7.9b, in which all measured $b_{b_p}^*(\lambda)$ are higher than Nechad et al. (2010) $b_{b_p}^*(\lambda)$. Nechad et al. (2010) $a_p^*(\lambda)$ is derived from an exponential model ($a_p^*(\lambda) = a_p^*(443) \cdot e^{(-slope_{nap}(\lambda-443))}$) with $slope_{nap} = 0.0123\ m^{-1}$ and $a_p^*(443) = 0.036 m^2 g^{-1}$, which is an average of the specific absorption of non-algal particles (NAP) published by Babin et al. (2003). Nechad et al. (2010) $b_{b_p}^*(\lambda)$ was calculated from $b_{b_p}^*(\lambda) = 0.02 b_{b_p}^*(555) b_p(\lambda)/b_p(555)$ with $b_{b_p}^*(555) = 0.036 m^2 g^{-1}$ (BABIN et al., 2003b). Those theoretical parameters assumed by Nechad et al. (2010) are suitable for Oceanic water and their differences will directly impact the retrieval of TSM concentration.

Figure 7.9 - Comparison of Nechad derived and measured $a_p^*(\lambda)$ and $b_{b_p}^*(\lambda)$.

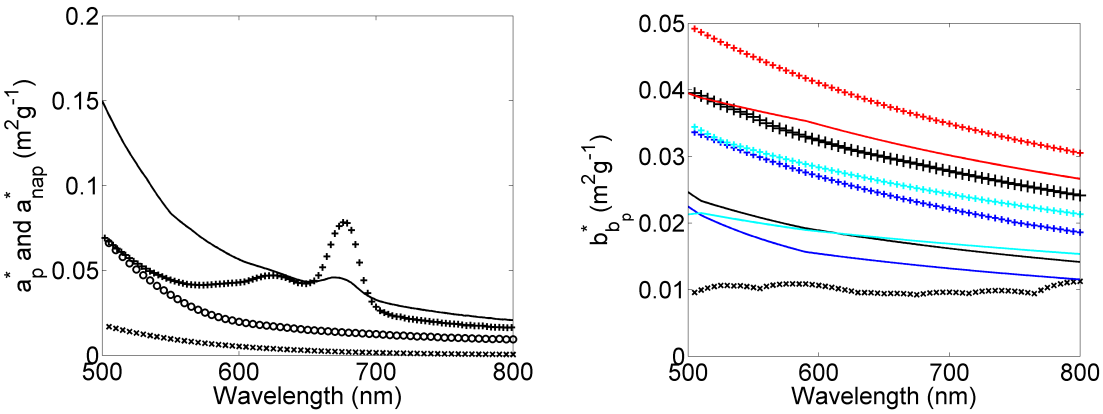

(a) (b)

(a) Symbol code - Solid Line: Median $a_p^*(\lambda)$, $''+''$: Linear Regression $a_p^*(\lambda)$, $''o''$: Linear Regression $a_{nap}^*(\lambda)$, $''x''$: Nechad et al. (2010) $a_p^*(\lambda)$. (b) Symbol code - Solid Line: Linear Regression $b_{b_p}^*(\lambda)$, $''+''$: Median $b_{b_p}^*(\lambda)$, $''x''$: Nechad $b_{b_p}^*(\lambda)$. Color code - Black: *All Samples*, Blue: *February*, Red: *August*, Cyan: *April*.

To test the *Nechad Algorithm*, all combinations of measured specific IOPs (Figure 7.9) were used to calculate A^p and C^p. *Nechad algorithm* TSM output concentration were compared to measured TSM concentrations for *April*. All possible combinations of measured specific IOPs caused an overestimation of TSM. The best TSM estimation occurred when using Linear Regressed $a_{nap}^*(\lambda)$ instead of $a_p^*(\lambda)$, $a_{cdom}(\lambda)$ and $b_{b_p}^*(\lambda)$ from *February* to calculate A^p and C^p. These set of parameters were also used to compare measured TSM to*Nechad algorithm* output TSM for *February*, *August* and the combination of seasons. The statistical indexes for those comparisons are presented in Figure 7.10 for each wavelength. The comparison using tabulated A^p and C^p from Nechad et al. (2010) is also presented.

Statistical indexes for the Nechad model calculated with tabulated A^p and C^p caused, in general, better results than A^p and C^p derived from measurements. The best interval to retrieve TSM is from 700 to 730 nm for all tested seasons; therefore the analysis will be based only on this interval. For $R_{rs-RC}(0^+, \lambda)$ (Figure 7.10a/b), *August* and *All Samples* (*August* + *April*) presented the lowest RMSE/RPD. Using $R_{rs-NonLin}(0^-, \lambda)$ (Figure 7.10c/d), *August* and *April* presented both the lowest RMSE and RPD and *February* presented the highest RMSE and RPD values. For both $R_{rs}(0^-, \lambda)$ and $R_{rs}(0^+, \lambda)$ results were better in *August* then *April* which is somehow unexpected since IOPs from *April* were used to calculate A^p and C^p pa-

rameters. This fact reinforces the similarity between *August* and *April* which was already presented in Chapter 6.

Figure 7.10 - Statistical Indexes comparing measured TSM concentration and derived from both: (1) Nechad model with A^p and C^p tabulated parameters from Nechad et al. (2010) (Dashed Line) and (2) Nechad model with A^p and C^p parameters calculated from $a^*_{nap}(\lambda)$, $a_{cdom}(\lambda)$ and $b^*_{b_p}(\lambda)$ from *February* (Solid Line)

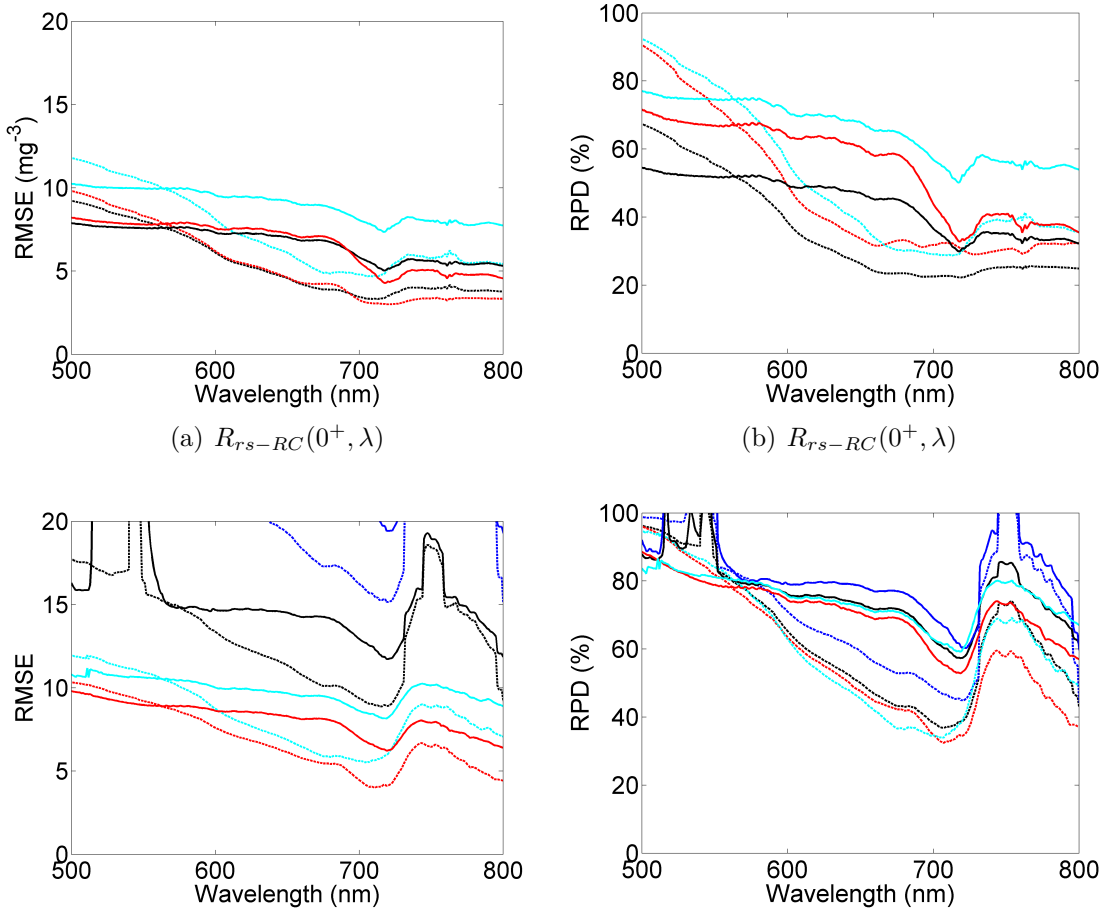

(a) $R_{rs-RC}(0^+, \lambda)$ (b) $R_{rs-RC}(0^+, \lambda)$

(c) $R_{rs-NonLin}(0^-, \lambda)$ (d) $R_{rs-NonLin}(0^-, \lambda)$

Color code - Black: *All Samples*, Blue: *February*, Red: *August*, Cyan: *April*

The poor performance of the Nechad algorithm using A^p and C^p derived from specific measured IOPs raises the question of the quality of measured IOPs and its influence on estimated TSM. A test was performed varying C^p parameter (calculating C^p with tabulated Nechad and Measured parameters alternately). Similar to arguments by Nechad et al. (2010), the influence of C^p in the estimation of TSM is negligible.

However, A^p is decisive for good TSM estimates. A^p depends on a_{cdom} and $b^*_{b_p}$ ($A^p = \frac{A}{\gamma}$ and $A = \frac{a_{np}}{b^*_{b_p}}$ from section 3.3.2.2) and in the 500 to 800 interval the influence of a_{cdom} is minor. Therefore A^p is mainly driven by $b^*_{b_p}$.

Figure 7.11 shows the set of A^p derived from Linear fitting, following the description from section 4.6.3. Four fitted A^p were derived (*February*, *August*, *April* and *All Samples*) using $R_{rs}(0^+, \lambda)$ (Figure 7.11a) and $R_{rs}(0^-, \lambda)$ (Figure 7.11b). C^p was calculated from $a^*_{nap}(\lambda)$ and $b^*_{b_p}(\lambda)$ from *February*. Figure 7.11a shows that A^p fitted for *April* is much higher than A^p fitted for *August*, which is, for instance closer to A^p from Nechad et al. (2010). Figure 7.11b, on the other hand, shows that both, *April* and *August* have higher A^p when compared to A^p from Nechad et al. (2010). Those results suggest that Hydroscat measurements are overestimating b_{b_p}.

Figure 7.11 - Comparison of A^p parameters

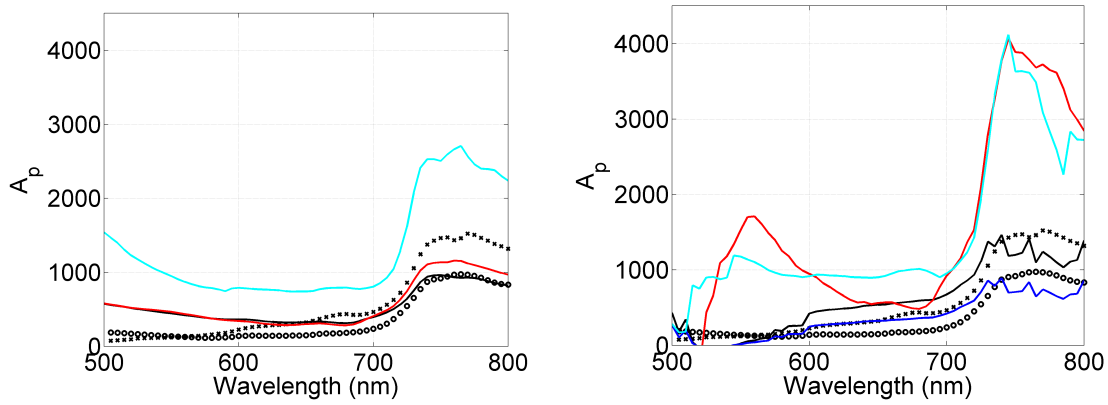

Symbol code: "o": A^p from Nechad et al. (2010), "x": A^p calculated from a_{cdom} (*April*) and $b^*_{b_p}$ from *February*. Solid Lines Color code - Fitted A^p parameters for: Black-*All Samples*, Blue-*February*, Red-*August*, Cyan-*April*.

Figure 7.12 shows the comparison of the Nechad model with parameters A^p and C^p from Nechad et al. (2010) and using fitted A^p parameters showed in figure 7.11 (section 4.6.3). For $R_{rs-RC}(0^+, \lambda)$ (Figure 7.12a/b), models with fitted A^p parameters show lower RMSE/RPD for wavelengths smaller than 600 nm, for all seasons. From 650 nm to $\approx$ 710 nm, Nechad models with A^p and C^p from Nechad et al. (2010) outperformed models with fitted A^p parameters. Beyond 710 nm, only for *April*, models with fitted A^p parameters presented lower RMSE/RPD. For *All Seasons* (*August* + *April*), values for models with fitted A^p parameters are lower just for

wavelengths smaller than 600 nm. For $R_{rs-NonLin}(0^-, \lambda)$ (Figure 7.12c/d), models with fitted A^p parameters presented lower RPD and RMSE at some spectra regions. However, at the 700 to 730 interval, which presented the lowest indexes, only *All Seasons* (*February*+*August*+*April* - Black Color) presented indexes lower than those of Nechad models using tabulated A^p and C^p.

Figure 7.12 - Statistical Indexes comparing Nechad Model calculated with A^p and C^p parameters from Nechad et al. (2010) and calculate from Linear regressed A^p and C^p

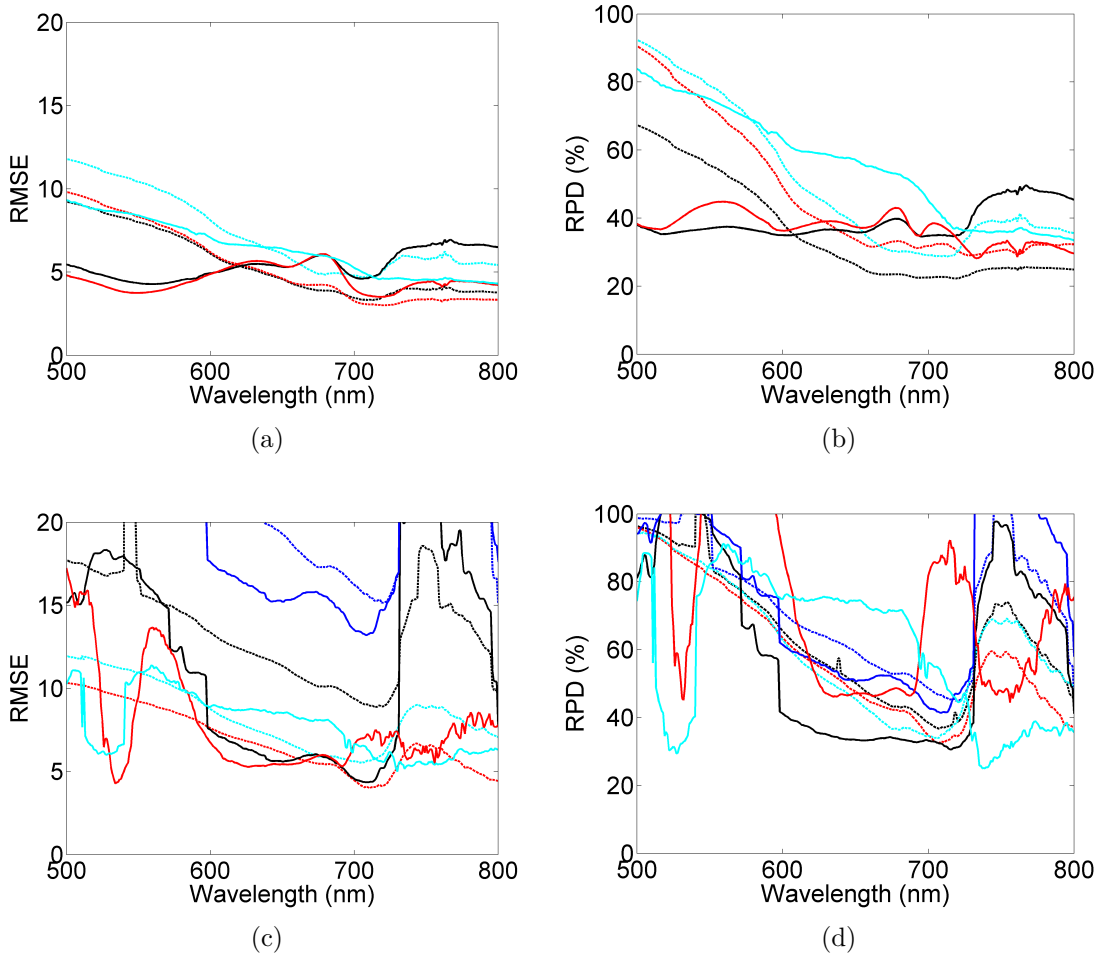

Symbol code - Dashed Line: Nechad Parameters, Solid Lines: Linear regressed parameters Color code - Black: *All Samples*, Blue: *February*, Red: *August*, Cyan: *April*.

Nechad model results suggest that tabulated A^p and C^p parameters perform better than parameters derived from Laboratory and Hydroscat Measurements. The probable reasons for that are twofold: (1) the uncertainties of Hydroscat measurements

are much higher than assumed even after using the most suitable correction (see section 5.2.1) mainly due to improper pathlength correction which is enhanced in very turbid waters; (2) Hydroscat measurements integrates b_{b_p} from 0.5 meter to 1 meter depth which might not represent b_{b_p} at the surface which is the main signal measured by R_{rs}. That suggests that both instrumentation and experimental setup for backscattering measurements should be further investigated before they can be replaced by laboratory measurements provided in tabulated values (BABIN et al., 2003; BABIN et al., 2003b).

As final recommendation, the Nechad algorithm can be used to retrieve TSM with a within a 30 % error, mainly in the NIR region. The best results were found for Nechad parameters but further studies should focuses on representative IOPs estimates, that would clearly improve Nechad Algorithm performances. For now, the use of Nechad parameters is the first guess for the use of this algorithm.

8 CONCLUSIONS AND FINAL CONSIDERATIONS

This research carried out a comprehensive assessment of the protocols for both, acquisition and correction of optical property measurements aiming at the bio-optical characterization as a support to the parametrization of semi-analytical inverse models. This assessment was carried out at Curuai floodplain lake, a cardinal example of thousands of turbid water lakes of the Amazon basin. The main challenge was to select among protocols tuned for Case 1 waters those leading to smaller uncertainties for very turbid waters such as found in Curuai Lake. Both, IOPs and AOPs measurements, were submitted to different correction methods available in literature. Data quality assessment indexes were then analyzed to identify the most suitable protocols for Curuai Lake (Case 2 water). In addition, with the bio-optical characterization which is, up to our knowledge is the first performed in Curuai Floodplain Lake, provided a better understanding on how the seasonal biogeochemical variability impacts lake water optical properties. Optical water property measurements were then used as input for the three selected semi-analytical models, to retrieve both IOPs and biogeochemical variables (Chla and TSM).

Data quality assessment of above water measurements showed that corrections were efficient in minimizing mainly sun/skyglint effects. However, the selected correction (QC1) which accounts for sky cover variability, caused a drastic reduction of R_{rs}^{Ab} dataset and therefore was not further applied. Furthermore, several effects like platform influence, shading and bidirectional effects should be addressed in future studies. Particularly, Lee et al. (2013) proposes a skylight-blocked approach in which R_{rs} is measured far from the Vessel and supposedly eliminates bidirectional effects. This method, however, was not used in case 2 waters yet, but has the potential to be used in future Amazon floodplain Lake studies. The fixed depth method for radiometric profiles was not suitable for Curuai Lake waters because the available light extinguishes in the first meter depth. Depth intervals caused errors in K-function estimates, specially in the shorter wavelengths. Therefore, future studies should focus on measuring continuous profiles, within a low sink depth rate and increasing the number of measurements for each depth. Despite the difficulties using ACS/Hydroscat in turbid water, Rottgers/Doxaran corrections provided reliable measurements, for the proposed corrections but further studies should be carried out to check for the actual accuracy of the measurements. A single set of corrections proved to be the best approach, allowing a consistent characterization of Curuai Lake IOPs. There is, however, a need for a complete characterization of all water column, since for highly turbid waters as Curuai Lake, most of IOPs variability occurs near surface. For

that, ACS/Hydroscat measurement methods should start near the surface. Regarding Laboratory measurement, additional efforts should focus on sample preservation due to the fast degradation caused by high temperatures in the Amazon region. Also, the T-R method should be further tested for highly turbid waters, since the high values presented previously suggest either a miscarried of T-R method or an excessive bleaching, which might also be affecting NAP and therefore, derived phytoplankton absorption.

The observed Curuai Lake biogeochemical variability follows previous studies by (BARBOSA et al., 2009). Measured ACS/Hydroscat IOPs variability are in agreement with biogeochemical variability, being higher for *February* and lower for *August* and *April* (Figure 6.4 and 6.5). In addition while $^{b_{b_p}}/b_p$ small variability along seasons suggests low particle size/composition variability, γ_b indicates smaller particles size for *February* (Table 6.3). The higher correlation between biogeochemical variables and ACS/Hydroscat IOPs was achieved by TSM/TSIM, suggesting that Inorganic suspended matter drives optical characteristics of Curuai Lake. Moreover, specific scattering coefficient (b_p^*) suggests differences in particle type among season. ACS absorption line height was a good proxy for Chla concentration (Figure 6.7 and Table 6.5) (besides with poor results April) showing its suitability for Chla profiles, even for without removing CDOM from total absorption (a_{T-w}). Scattering coefficient (b_p) profiles show a well mixed water column among seasons, while γ_b and a_ϕ^* profiles indicate higher variability of particles size near the surface, specially for *August*, mainly due to occasional phytoplankton blooms along the lake. For *April*, Laboratory absorption coefficients presented high values mainly in the blue range (400 to 500 nm) which is expected for turbid waters dominated by CDOM and NAP. The correlation to biogeochemical variables was not as sound as for ACS/Hydroscat measurements suggesting issues in the laboratory measurement methods. LISST-PSD also present issues in measurements what might explain the low correlation between Junge distribution exponent and measured γ_b. Laboratory and LISST measurements demand further investigation and a larger dataset along the hydrological year to come up with a better quality analysis which could lead to a reliable dataset.

The results for the three Inverse Models were not satisfactory for most of retrieved IOPs and biogeochemical concentration. The best results for GIOP were for total absorption coefficient (a_{T-w}), with RPD of at least 20 % in blue range (Figure 7.1). The reminding IOPs as well as Chla showed higher errors. The main reason for the poor performance of GIOP might be related to the uncertainties in input parameters (R_{rs}^{Ab} and IOPs). Also, the b_{b_p} exponent is a median of b_{b_p} measured at

a highers depths (0.5 to 1 meter) which might not representative of IOPs near the surface and therefore would not be related to measured R_{rs}^{Ab} since light extinguishes above $\approx$ 1 meter depth as shown in Figure 5.6. Further investigation should be carried out in order to understand the main source of error in the current dataset as well as guide future data acquisition. The two versions of QAA tested without any parametrization, presented poor results. That lack of quality in the retrieved optical properties reinforce the need for a parametrization of its empirical steps, based on environment characteristics as currently performed in literature (LE et al., 2009b; MISHRA et al., 2014). The Nechad algorithm shows errors that reach 30 % for TSM estimates which may be considered reasonable. However best results were found for tabulated values (from Nechad et al. (2010)) and again raises the question on the reliability of the measured dataset.

As final recommendations, further investigation are needed in order to tune the current acquisition and corrections protocols to inland turbid waters. This investigation should be focused in the data acquisition near the surface (0.1 meters) and with higher number of measurements in water column. The bio-optical characterization of Curuai Lake should be linked to floodplain temporal and spatial dynamics aiming the better understanding of IOP variability in relation to physicochemical driving forces. At last, inverse models should be further investigated aiming future application to the retrieval of optical components and properties from satellite images. Unfortunately, the quality of the satellite data during the period of each field campaigns (mainly Landsat 8 - OLI) had a significant amount of clouds, what would directly affect the comparison to field data. Despite of the number of works recently performed using Landsat 8, it is not completely suitable for waters AOC retrieval in turbid environments, particularly CDOM and Chla, mainly due to the available set of bands. However, with the efforts of the Remote Sensing community in launching new satellites focused on water (Ocean and Inland) studies (Sentinel 2 and 3), we believe that this study will help on future development of algorithms focused on Amazon waters.

REFERENCES

AFFONSO, A. G.; BARBOSA, C. C. F.; NOVO, E. M. L. M. Water quality changes in floodplain lakes due to the Amazon River flood pulse: Lago Grande de Curuaí (Pará). **Brazilian journal of biology = Revista brasleira de biologia**, v. 71, n. 3, p. 601–10, 2011. ISSN 1678-4375. Available from: <http://www.ncbi.nlm.nih.gov/pubmed/21881783>. 102, 108

AGRAWAL, Y. C.; POTTSMITH, H. Instruments for particle size and settling velocity observations in sediment transport. **Marine Geology**, v. 168, n. 1-4, p. 89–114, aug 2000. ISSN 00253227. Available from: <http://linkinghub.elsevier.com/retrieve/pii/S002532270000044X>. 47

AGRAWAL, Y. C.; WHITMIRE, A.; MIKKELSEN, O. A.; POTTSMITH, H. C. Light scattering by random shaped particles and consequences on measuring suspended sediments by laser diffraction. **Journal of Geophysical Research**, v. 113, n. C4, p. C04023, 2008. ISSN 0148-0227. Available from: <http://doi.wiley.com/10.1029/2007JC004403>. 111

ANTOINE, D.; D'ORTENZIO, F.; HOOKER, S. B.; BÉCU, G.; GENTILI, B.; TAILLIEZ, D.; SCOTT, A. J. Assessment of uncertainty in the ocean reflectance determined by three satellite ocean color sensors (MERIS, SeaWiFS and MODIS-A) at an offshore site in the Mediterranean Sea (BOUSSOLE project). **Journal of Geophysical Research**, v. 113, n. C7, p. C07013, jul 2008. ISSN 0148-0227. Available from: <http://doi.wiley.com/10.1029/2007JC004472>. 49

ASTORECA, R.; DOXARAN, D.; RUDDICK, K. G.; ROUSSEAU, V.; LANCELOT, C. Influence of suspended particle concentration, composition and size on the variability of inherent optical properties of the Southern North Sea. **Continental Shelf Research**, Elsevier, v. 35, p. 117–128, mar 2012. ISSN 02784343. Available from: <http://linkinghub.elsevier.com/retrieve/pii/S0278434312000106>. 90, 97

AUGUSTO-SILVA, P.; OGASHAWARA, I.; BARBOSA, C. C. F.; CARVALHO, L. de; JORGE, D.; FORNARI, C.; STECH, J. L. Analysis of MERIS Reflectance Algorithms for Estimating Chlorophyll-a Concentration in a Brazilian Reservoir. **Remote Sensing**, v. 6, n. 12, p. 11689–11707, 2014. ISSN 2072-4292. Available from: <http://www.mdpi.com/2072-4292/6/12/11689/>. 3

BABIN, M.; DARIUSZ, S.; GIOVANNI, F.; HERVE, C.; ANNICK, B.; GRIGOR, O.; HOEPFFNER, N. Variations in the light absorption coefficients of phytoplankton, nonalgal particles, and dissolved organic matter in coastal waters around Europe. **Journal of Geophysical Research**, v. 108, n. C7, p. 3211, 2003. ISSN 0148-0227. Available from: <http://doi.wiley.com/10.1029/2001JC000882>. 18, 19, 20, 101, 107, 109, 110, 126, 131

BABIN, M.; MOREL, A.; FOURNIER-SICRE, V.; FELL, F.; STRAMSKI, D. Light scattering properties of marine particles in coastal and open ocean waters as related to the particle mass concentration. **Limnology and Oceanography**, v. 48, n. 2, p. 843–859, mar 2003b. ISSN 00243590. Available from: <http://doi.wiley.com/10.4319/lo.2003.48.2.0843>. 98, 99, 126, 131

BABIN, M.; STRAMSKI, D. Variations in the mass-specific absorption coefficient of mineral particles suspended in water. **Limnology and Oceanography**, v. 49, n. 3, p. 756–767, 2004. ISSN 00243590. Available from: <http://www.aslo.org/lo/toc/vol{_}49/issue{_}3/0756.html>. 109

BARBOSA, C. C. F.; Moraes Novo, E. M. L.; MELACK, J. M.; GASTIL-BUHL, M.; FILHO, W. P. Geospatial analysis of spatiotemporal patterns of pH, total suspended sediment and chlorophyll-a on the Amazon floodplain. **Limnology**, v. 11, n. 2, p. 155–166, dec 2009. ISSN 1439-8621. Available from: <http://link.springer.com/10.1007/s10201-009-0305-5http://www.springerlink.com/index/10.1007/s10201-009-0305-5>. 4, 31, 32, 90, 96, 102, 134

BINDING, C. E.; JEROME, J. H.; BUKATA, R. P.; BOOTY, W. Spectral absorption properties of dissolved and particulate matter in Lake Erie. **Remote Sensing of Environment**, v. 112, n. 4, p. 1702–1711, apr 2008. ISSN 00344257. Available from: <http://linkinghub.elsevier.com/retrieve/pii/S0034425707004166>. 107, 108, 109, 110

BIRGOT, P.; BARBOSA, C.; KUTSER, T.; CARVALHO, L. Sander de; FERREIRA, R.; TOMING, K. Mapping inland water carbon content with Landsat 8 data. **International Journal of Remote Sensing**, xx, n. xx, p. x, xx InPress. Available from: <xx>. 107

BOIVIN, L. P.; DAVIDSON, W. F.; STOREY, R. S.; SINCLAIR, D.; EARLE, E. D. Determination of the attenuation coefficients of visible and ultraviolet radiation in heavy water. **Applied Optics**, n. 25, p. 877–882, 1986. 16

BONNET, M. P.; BARROUX, G.; MARTINEZ, J. M.; SEYLER, F.; TURCQ, P. M.; COCHONNEAU, G.; MELACK, J. M.; BOAVENTURA, G.; BOURGOIN, L. M.; LEON, J.; ROUX, E.; CALMANT, S.; KOSUTH, P.; GUYOT, J.; SEYLER, P. Floodplain hydrology in an Amazon floodplain lake (Lago Grande de Curuai). **Journal of Hydrology**, v. 349, n. 2, p. 18–30, January 2008. 90, 96, 106, 108

BOSS, E. Particulate backscattering ratio at LEO 15 and its use to study particle composition and distribution. **Journal of Geophysical Research**, v. 109, n. C1, p. C01014, 2004. ISSN 0148-0227. Available from: <http://doi.wiley.com/10.1029/2002JC001514>. 95, 101

BOSS, E.; COLLIER, R.; LARSON, G.; FENNEL, K.; PEGAU, W. S. Measurements of spectral optical properties and their relation to biogeochemical variables and processes in Crater Lake, Crater Lake National Park, OR. **Hydrobiologia**, v. 574, n. 1, p. 149–159, jan. 2007. ISSN 0018-8158. Available from: <http://www.springerlink.com/index/10.1007/s10750-006-2609-3>. 58

BOSS, E.; PEGAU, W. S. Relationship of light scattering at an angle in the backward direction to the backscattering coefficient. **Applied optics**, v. 40, n. 30, p. 5503–7, oct 2001. ISSN 0003-6935. Available from: <http://www.ncbi.nlm.nih.gov/pubmed/18364835>. 45, 59, 112

BOSS, E.; PICHERAL, M.; LEEUW, T.; CHASE, A.; KARSENTI, E.; GORSKY, G.; TAYLOR, L.; SLADE, W.; RAS, J.; CLAUSTRE, H. The characteristics of particulate absorption, scattering and attenuation coefficients in the surface ocean; Contribution of the Tara Oceans expedition. **Methods in Oceanography**, Elsevier Ltd, v. 7, p. 52–62, 2013. ISSN 22111220. Available from: <http://dx.doi.org/10.1016/j.mio.2013.11.002>. 20, 97, 101

BOSS, E.; SLADE, W. H.; BEHRENFELD, M.; DALL'OLMO, G. Acceptance angle effects on the beam attenuation in the ocean. **Optics express**, v. 17, n. 3, p. 1535–50, feb. 2009. ISSN 1094-4087. Available from: <http://www.ncbi.nlm.nih.gov/pubmed/19188983>. 2, 45, 80, 97

BOSS, E.; TWARDOWSKI, M. S.; HERRING, S. Shape of the particulate beam attenuation spectrum and its inversion to obtain the shape of the particulate size distribution. **Applied Optics**, v. 40, n. 27, p. 4885–4893, 2001. 112

BOUCHEZ, J.; GAILLARDET, J.; FRANCE-LANORD, C.; MAURICE, L.; DUTRA-MAIA, P. Grain size control of river suspended sediment geochemistry: Clues from Amazon River depth profiles. **Geochemistry, Geophysics, Geosystems**, v. 12, n. 3, p. n/a–n/a, mar 2011. ISSN 15252027. Available from: <http://doi.wiley.com/10.1029/2010GC003380>. 111

BOWERS, D.; BINDING, C. E. The optical properties of mineral suspended particles: A review and synthesis. **Estuarine, Coastal and Shelf Science**, v. 67, n. 1-2, p. 219–230, mar 2006. ISSN 02727714. Available from: <http://linkinghub.elsevier.com/retrieve/pii/S0272771405003896>. 19

BRICAUD, A.; BABIN, M.; CLAUSTRE, H.; RAS, J.; TIÈCHE, F. Light absorption properties and absorption budget of Southeast Pacific waters. **Journal of Geophysical Research**, v. 115, n. C8, p. C08009, aug 2010. ISSN 0148-0227. Available from: <http://doi.wiley.com/10.1029/2009JC005517>. xix, 56, 57, 85

BRICAUD, A.; BABIN, M.; MOREL, A.; CLAUSTRE, H. Variability in the chlorophyll-specific absorption coefficients of natural phytoplankton: Analysis and parameterization. **Journal of Geophysical Research**, v. 100, n. C7, p. 13321, 1995. ISSN 0148-0227. Available from: <http://doi.wiley.com/10.1029/95JC00463>. 18, 58, 101, 109, 110

BRICAUD, A.; MOREL, A. Light attenuation and scattering by phytoplanktonic cells: a theoretical modeling. **Applied optics**, v. 25, n. 4, p. 571, feb 1986. ISSN 0003-6935. Available from: <http://www.ncbi.nlm.nih.gov/pubmed/18231215>. 18, 19

BRICAUD, A.; MOREL, A.; BABIN, M.; ALLALI, K.; CLAUSTRE, H. Variations of light absorption by suspended particles with chlorophyll a concentration in oceanic (case 1) waters: Analysis and implications for bio-optical models. **Journal of Geophysical Research: Oceans**, v. 103, n. C13, p. 31033–31044, dec 1998. ISSN 01480227. Available from: <http://doi.wiley.com/10.1029/98JC02712>. 29, 60, 116, 117

BRICAUD, A.; STRAMSKI, D. Spectral absorption coefficients of living phytoplankton and nonalgal biogenous matter: A comparison between the Peru

upwelling areaand the Sargasso Sea. **Limnology and Oceanography**, v. 35, n. 3, p. 562–582, 1990. ISSN 00243590. 18

BUKATA, R.; JEROME, J.; KONDRATYEV, A.; POZDNYAKOV, D. **Optical Properties and Remote Sensing of Inland and Coastal Waters**. Taylor & Francis, 1995. ISBN 9780849347542. Available from: <https://books.google.com.br/books?id=FVpVENnqfLUC>. 1

CAMPBELL, G.; PHINN, S. R.; DEKKER, A. G.; BRANDO, V. E. Remote sensing of water quality in an Australian tropical freshwater impoundment using matrix inversion and MERIS images. **Remote Sensing of Environment**, Elsevier Inc., v. 115, n. 9, p. 2402–2414, sep 2011. ISSN 00344257. Available from: <http://linkinghub.elsevier.com/retrieve/pii/S0034425711001751>. 3, 90, 95, 97, 107, 109

CHERUKURU, N.; BRANDO, V. E.; SCHROEDER, T.; CLEMENTSON, L. a.; DEKKER, A. G. Influence of river discharge and ocean currents on coastal optical properties. **Continental Shelf Research**, Elsevier, v. 84, p. 188–203, 2014. ISSN 02784343. Available from: <http://linkinghub.elsevier.com/retrieve/pii/S0278434314001472>. 3, 90, 95, 97

CIOTTI, A. M.; BRICAUD, A. Retrievals of a size parameter for phytoplankton and spectral light absorption by colored detrital matter from water-leaving radiances at SeaWiFS channels in a continental shelf region off Brazil. **Limnology and Oceanography: Methods**, v. 4, p. 237–253, 2006. ISSN 15415856. 18, 29, 60, 116, 117

CIOTTI, A. M.; LEWIS, M. R.; CULLEN, J. J. Assessment of the relationships between dominant cell size in natural phytoplankton communities and the spectral shape of the absorption coefficient. **Limnology and Oceanography**, v. 47, n. 2, p. 404–417, 2002. ISSN 00243590. 18, 109

CLAVANO, W. R.; BOSS, E.; KARP-BOSS, L. Inherent optical properties of non-spherical marine-like particles – from theory to observation. **Oceanography and Marine Biology: An Annual Review**, v. 45, p. 1–38, 2007. 12

COBLE, P. G. Marine optical biogeochemistry: the chemistry of ocean color. **Chemical reviews**, v. 107, n. 2, p. 402–18, feb 2007. ISSN 0009-2665. Available from: <http://www.ncbi.nlm.nih.gov/pubmed/17256912>. 17

COSTA, M. P. F.; NOVO, E. M. L. a. D. M.; TELMER, K. H. Spatial and temporal variability of light attenuation in large rivers of the Amazon. **Hydrobiologia**, v. 702, n. 1, p. 171–190, oct. 2012. 1

DALL'OLMO, G.; WESTBERRY, T. Significant contribution of large particles to optical backscattering in the open ocean. **Biogeosciences**, n. 1996, p. 947–967, 2009. Available from: <http://www.biogeosciences.net/6/947/>. 17, 19

DOERFFER, R.; SCHILLER, H. The MERIS Case 2 water algorithm. **International Journal of Remote Sensing**, v. 28, n. 3-4, p. 517–535, feb. 2007. ISSN 0143-1161. 23

DOGLIOTTI a.I.; RUDDICK, K. G.; NECHAD, B.; DOXARAN, D.; KNAEPS, E. A single algorithm to retrieve turbidity from remotely-sensed data in all coastal and estuarine waters. **Remote Sensing of Environment**, Elsevier B.V., v. 156, p. 157–168, 2015. ISSN 00344257. Available from: <http://linkinghub.elsevier.com/retrieve/pii/S0034425714003654>. 3, 4, 38, 90

DORON, M.; BABIN, M.; MANGIN, A.; HEMBISE, O. Estimation of light penetration, and horizontal and vertical visibility in oceanic and coastal waters from surface reflectance. **Journal of Geophysical Research: Oceans**, v. 112, n. 6, p. 1–15, 2007. ISSN 21699291. 26

DOXARAN, D.; BABIN, M.; LEYMARIE, E. Near-infrared light scattering by particles in coastal waters. **Optics Express**, v. 15, n. 20, p. 12834, 2007. ISSN 1094-4087. Available from: <https://www.osapublishing.org/oe/abstract.cfm?uri=oe-15-20-12834>. 38

DOXARAN, D.; LEYMARIE, E.; NECHAD, B.; RUDDICK, K. G. An improved correction method for field measurements of particulate light backscattering in turbid waters. CoastalColour and SeaSWIR User Consultation Meeting - 17 Slides. 2013. Available from: <http://www.coastcolour.org/meeting_DARMSTADT_IV_presentations/Doxaran_SeaSWIR_May_2013.pdf>. vii, ix, 97

DOXARAN, D.; RUDDICK, K. G.; MCKEE, D.; GENTILI, B.; TAILLIEZ, D.; CHAMI, M.; BABIN, M. Spectral variations of light scattering by marine particles in coastal waters, from the visible to the near infrared. **Limnology and Oceanography**, v. 54, n. 4, p. 1257–1271, 2009. ISSN 00243590. Available from:

<http://www.aslo.org/lo/toc/vol{_}54/issue{_}4/1257.html>. 58, 59, 90, 96, 98, 112

ERTEL, J. R.; HEDGES, J. I.; DEVOL, A. H.; RICHEY, J. E.; DE NAZARÉ GÓES RIBEIRO, M. Dissolved humic substances of the Amazon River system. **Limnology and Oceanography**, v. 31, n. 4, p. 739–754, 1986. ISSN 00243590. Available from: <http://doi.wiley.com/10.4319/lo.1986.31.4.0739>. 108

Espinoza Villar, R.; MARTINEZ, J.-M.; Le Texier, M.; GUYOT, J.-L.; FRAIZY, P.; MENESES, P. R.; OLIVEIRA, E. D. A study of sediment transport in the Madeira River, Brazil, using MODIS remote-sensing images. **Journal of South American Earth Sciences**, Elsevier Ltd, v. 44, p. 45–54, jul 2013. ISSN 08959811. Available from: <http://linkinghub.elsevier.com/retrieve/pii/S0895981112001630>. 111

ESTAPA, M. L.; BOSS, E.; MAYER, L. M.; ROESLER, C. S. Role of iron and organic carbon in mass-specific light absorption by particulate matter from Louisiana coastal waters. **Limnology and Oceanography**, v. 57, n. 1, p. 97–112, 2012. ISSN 00243590. 19

FARMER, C.; HANSELL, D. Determination of dissolved organic carbon and total dissolved nitrogen in sea water. **Guide to best practices for ocean CO2 measurements.**, PICES Special Publication 3, p. 191, 2007. 47

FERRARI, G. M.; TASSAN, S. A method for the experimental determination of light absorption by aquatic heterotrophic bacteria. **Journal of Plankton Research**, v. 20, n. 4, p. 757–766, 1998. ISSN 0142-7873. Available from: <http://plankt.oxfordjournals.org/cgi/doi/10.1093/plankt/20.4.757>. 49

FERREIRA, R. D.; BARBOSA, C. C. F.; NOVO, E. M. L. d. M. Assessment of in vivo fluorescence method for chlorophyll-a estimation in optically complex waters (Curuai floodplain, Pará - Brazil). **Acta Limnologica Brasiliensia**, v. 24, n. 4, p. 373–386, dec 2012. ISSN 2179-975X. Available from: <http://www.scielo.br/scielo.php?script=sci{_}arttext{&}pid=S2179-975X2012000400005{&}lng=en{&}nrm=iso{&}tlng=en>. 4, 90

FMINSEARCH. **Find minimum of unconstrained multivariable function using derivative free method**. 2015. Available from: <http://www.mathworks.com/help/matlab/ref/fminsearch.html>. 41

FRANZ, B. A.; WERDELL, J. A Generalized Framework for Modeling of Inherent Optical Properties in Ocean Remote Sensing Applications. In: **Proceedings of Ocean Optics**. Anchorage: [s.n.], 2010. p. 1–13. 29

GIARDINO, C.; BRANDO, V. E.; DEKKER, A. G.; STRÖMBECK, N.; CANDIANI, G. Assessment of water quality in Lake Garda (Italy) using Hyperion. **Remote Sensing of Environment**, v. 109, n. 2, p. 183–195, jul 2007. ISSN 00344257. Available from: <http://linkinghub.elsevier.com/retrieve/pii/S0034425707000065>. 18

GIOPSENSITIVITY. **GIOP Sensitivity Analysis Matlab code**. 2005. Available from: <http://misclab.umeoce.maine.edu/software.php>. 61

GLEASON, A. C. R.; VOSS, K. J.; GORDON, H. R.; TWARDOWSKI, M. S.; SULLIVAN, J. M.; TREES, C.; WEIDEMANN, A.; BERTHON, J.-F.; CLARK, D.; LEE, Z. Detailed validation of the bidirectional effect in various Case I and Case II waters. **Optics express**, v. 20, n. 7, p. 7630–45, mar 2012. ISSN 1094-4087. Available from: <http://www.ncbi.nlm.nih.gov/pubmed/22453442>. 3

GLOBALLAKESWEBSITE. **Global Lakes**. 2015. Available from: <http://www.globolakes.ac.uk/>. 2

GORDON, H. R. Inverse methods in hydrologic optics. **Oceanologia**, v. 44, n. 1, p. 9–58, 2002. 23

GORDON, H. R.; BROWN, O. B. Irradiance reflectivity of a flat ocean as a function of its optical properties. **Applied optics**, v. 12, n. 7, p. 1549–51, jul 1973. ISSN 0003-6935. Available from: <http://www.ncbi.nlm.nih.gov/pubmed/20125561>. 21

GORDON, H. R.; BROWN, O. B.; EVANS, R. H.; BROWN, J. W.; SMITH, R. C.; BAKER, K. S.; CLARK, D. K. A semianalytic radiance model of ocean color. **Journal of Geophysical Research**, v. 93, n. D9, p. 10909, 1988. ISSN 0148-0227. Available from: <http://doi.wiley.com/10.1029/JD093iD09p10909>. xx, 22

GORDON, H. R.; BROWN, O. B.; JACOBS, M. M. Computed relationships between the inherent and apparent optical properties of a flat homogeneous ocean. **Applied optics**, v. 14, n. 2, p. 417–27, feb. 1975. ISSN 0003-6935. Available from: <http://www.ncbi.nlm.nih.gov/pubmed/20134901>. 22

GORDON, H. R.; MCCLUNEY, W. R. Estimation of the Depth of Sunlight Penetration in the Sea for Remote Sensing. **Applied Optics**, v. 57, n. 2, p. 589, feb 1975. ISSN 0003-6935. Available from: <http://www.ncbi.nlm.nih.gov/pubmed/20134900>. 57

HERLEVI, A. A Study of Scattering, Backscattering and a Hyperspectral Reflectance Model for Boreal Waters. **Geo-physica**, v. 268, n. 38, p. 113–132, 2002. 97

HILL, P. S.; BOSS, E.; NEWGARD, J. P.; LAW, B. a.; MILLIGAN, T. G. Observations of the sensitivity of beam attenuation to particle size in a coastal bottom boundary layer. **Journal of Geophysical Research: Oceans**, v. 116, n. 2, p. 1–14, 2011. ISSN 21699291. 12, 97, 99

HOGE, F. E.; LYON, P. E. Satellite retrieval of inherent optical properties by linear matrix inversion of oceanic radiance models: An analysis of model and radiance measurement errors. **Journal of Geophysical Research: Oceans**, v. 101, n. C7, p. 16631–16648, jul 1996. ISSN 01480227. Available from: <http://doi.wiley.com/10.1029/96JC01414>. 23, 29, 30

HYDRO-OPTICS, BIOLOGY AND INSTRUMENTATION LABORATORIES. **HydroScat-6 Spectral Backscattering Sensor & Fluorometer - user's manual**: Revision j. 12819 SE 38th St. 434 Bellevue, WA 98006 USA, 2010. 63 p. 45, 46

IIE. **International Institute of Ecology**. 2015. Available from: <XXX>. 47

IOCCG. Remote Sensing of Inherent Optical Properties : fundamentals , tests of algorithms , and applications In: LEE, Z.-P. (ed.). **Reports of the International Ocean-Colour Coordinating Group**, n. 5, p. 123, 2006. 1, 23, 24

JUNK, W. J.; BAYLEY, P. B.; SPARKS, R. E. **The flood pulse concept in river-floodplain systems**. dec. 1989. 110–127 p. Available from: <http://dx.plos.org/10.1371/journal.pone.0028909>. 1

JUNK, W. J.; PIEDADE, M. T.; WITTMANN, F.; SCHONGART, J.; PAROLIN, P. **Amazonian floodplain forests**. 1. ed.. ed. Dordrecht: Springer Netherlands, 2011. 615 p. (Ecological Studies, v. 210). ISBN 978-90-481-8724-9. Available from: <http://link.springer.com/10.1007/978-90-481-8725-6>. 1, 17

KARP-BOSS, L.; AZAVEDO, L.; BOSS, E. LISST-100 measurements of phytoplankton size distribution: evaluation of the effects of cell shape. **Limnology**

and Oceanography: Methods, v. 5, n. Nov, p. 396–406, 2007. ISSN 15415856. 12

KIRK, J. **Light and photosynthesis in aquatic ecosystems**. Cambridge University Press, 2010. ISBN 9781139493918. Available from: <https://books.google.com.br/books?id=DXCl0fw__noC>. 1, 16, 17, 18, 19, 40, 41, 78, 108

KIRK, J. T. O. Monte Carlo modeling of the performance of a reflective tube absorption meter. **Applied optics**, v. 31, n. 30, p. 6463–8, oct. 1992. 44

KNAEPS, E.; RUDDICK, K. G.; DOXARAN, D.; DOGLIOTTI, A.; NECHAD, B.; RAYMAEKERS, D.; STERCKX, S. A SWIR based algorithm to retrieve total suspended matter in extremely turbid waters. **Remote Sensing of Environment**, Elsevier Inc., v. 168, p. 66–79, 2015. ISSN 00344257. Available from: <http://linkinghub.elsevier.com/retrieve/pii/S0034425715300523>. 4

KOSTADINOV, T. S.; SIEGEL, D. A.; MARITORENA, S. Retrieval of the particle size distribution from satellite ocean color observations. **Journal of Geophysical Research**, v. 114, n. C9, p. C09015, sep 2009. ISSN 0148-0227. Available from: <http://doi.wiley.com/10.1029/2009JC005303>. 12

KUTSER, T. The possibility of using the Landsat image archive for monitoring long time trends in coloured dissolved organic matter concentration in lake waters. **Remote Sensing of Environment**, v. 123, n. February, p. 334–338, 2012. ISSN 00344257. 3

KUTSER, T.; PIERSON, D. C.; KALLIO, K.; REINART, a.; SOBEK, S. Mapping lake CDOM by satellite remote sensing. **Remote Sensing of Environment**, v. 94, n. 4, p. 535–540, 2005. ISSN 00344257. Available from: <http://linkinghub.elsevier.com/retrieve/pii/S0034425704003670>. 3

LE, C.; LI, Y.; ZHA, Y.; SUN, D.; HUANG, C.; LU, H. A four-band semi-analytical model for estimating chlorophyll a in highly turbid lakes: The case of Taihu Lake, China. **Remote Sensing of Environment**, Elsevier B.V., v. 113, n. 6, p. 1175–1182, jun 2009. ISSN 00344257. Available from: <http://linkinghub.elsevier.com/retrieve/pii/S0034425709000327>. 95

LE, C. F.; LI, Y. M.; ZHA, Y.; SUN, D.; YIN, B. Validation of a quasi-analytical algorithm for highly turbid eutrophic water of meiliang bay in Taihu Lake, China.

IEEE Transactions on Geoscience and Remote Sensing, v. 47, n. 8, p. 2492–2500, 2009. ISSN 01962892. 26, 135

LEE, Z.; ARNONE, R.; HU, C.; WERDELL, J.; LUBAC, B. Uncertainties of optical parameters and their propagations in an analytical ocean color inversion algorithm. **Applied optics**, v. 49, n. 3, p. 369–81, jan 2010. ISSN 1539-4522. Available from: <http://www.ncbi.nlm.nih.gov/pubmed/20090801>. 22

LEE, Z.; CARDER, K. L.; ARNONE, R. a. Deriving inherent optical properties from water color: a multiband quasi-analytical algorithm for optically deep waters. **Applied optics**, v. 41, n. 27, p. 5755–72, sep. 2002. ISSN 0003-6935. Available from: <http://www.ncbi.nlm.nih.gov/pubmed/12269575>. vii, ix, 1, 4, 5, 22, 23, 24, 26, 28, 29, 60, 61, 122

LEE, Z.; CARDER, K. L.; DU, K. Effects of molecular and particle scatterings on the model parameter for remote-sensing reflectance. **Applied Optics**, v. 43, n. 25, p. 4957, sep 2004. ISSN 0003-6935. Available from: <https://www.osapublishing.org/abstract.cfm?URI=ao-43-25-4957>. 76

LEE, Z.; CARDER, K. L.; MOBLEY, C. D.; STEWARD, R. G.; PATCH, J. S. Hyperspectral remote sensing for shallow waters. 2. Deriving bottom depths and water properties by optimization. **Applied optics**, v. 38, n. 18, p. 3831–43, jun. 1999. ISSN 0003-6935. Available from: <http://www.ncbi.nlm.nih.gov/pubmed/18319990>. 22

LEE, Z.; DU, K.; VOSS, K. J.; ZIBORDI, G.; LUBAC, B.; ARNONE, R.; WEIDEMANN, A. An inherent-optical-property-centered approach to correct the angular effects in water-leaving radiance. **Applied optics**, v. 50, n. 19, p. 3155–67, 2011. ISSN 1539-4522. Available from: <http://www.ncbi.nlm.nih.gov/pubmed/21743515>. 3, 22, 82, 83

LEE, Z.; PAHLEVAN, N.; AHN, Y.-H.; GREB, S.; O'DONNELL, D. Robust approach to directly measuring water-leaving radiance in the field. **Applied optics**, v. 52, n. 8, p. 1693–701, 2013. ISSN 1539-4522. 3, 133

LEE, Z.; WEIDEMANN, A.; KINDLE, J.; ARNONE, R.; CARDER, K. L.; DAVIS, C. Euphotic zone depth: Its derivation and implication to ocean-color remote sensing. **Journal of Geophysical Research: Oceans**, v. 112, p. 1–11, 2007. ISSN 21699291. 24, 61, 122

LEITE, N. K.; KRUSCHE, A. V.; BALLESTER, M. V. R.; VICTORIA, R. L.; RICHEY, J. E.; GOMES, B. M. Intra and interannual variability in the Madeira

River water chemistry and sediment load. **Biogeochemistry**, v. 105, n. 1, p. 37–51, 2011. ISSN 01682563. 1

LEYMARIE, E.; DOXARAN, D.; BABIN, M. Uncertainties associated to measurements of inherent optical properties in natural waters. **Applied optics**, v. 49, n. 28, p. 5415–36, oct 2010. ISSN 1539-4522. Available from: <http://www.ncbi.nlm.nih.gov/pubmed/20885480>. 3, 43, 44, 99

LISST. **LISST - portable**. 2015. Available from: <http://www.sequoiasci.com/wp-content/uploads/2013/06/LISST-Portable_Manual_V3touch_panel_display.pdf>. 46

LOBO, F. D. L.; COSTA, M. P. F.; NOVO, E. M. L. M. Time-series analysis of Landsat-MSS/TM/OLI images over Amazonian waters impacted by gold mining activities. **Remote Sensing of Environment**, Elsevier Inc., v. 157, p. 170–184, 2014. ISSN 00344257. Available from: <http://dx.doi.org/10.1016/j.rse.2014.04.030>. 4

Lobo, F. d. L.; NOVO, E. M. L. D. M.; BARBOSA, C. C. F.; GALVÃO, L. S. Reference spectra to classify Amazon water types. **International Journal of Remote Sensing**, v. 33, n. 11, p. 3422–3442, jun 2012. ISSN 0143-1161. Available from: <http://www.tandfonline.com/doi/abs/10.1080/01431161.2011.627391>. 4, 90

LOISEL, H.; LUBAC, B.; DESSAILLY, D.; DUFORET-GAURIER, L.; VANTREPOTTE, V. Effect of inherent optical properties variability on the chlorophyll retrieval from ocean color remote sensing: an in situ approach. **Optics Express**, v. 18, n. 20, p. 20949, sep 2010. ISSN 1094-4087. Available from: <http://log.univ-littoral.fr/docs/equipe5/loisel/loisel{_}2010{_}205793.pdfhttps://www.osapublishing.org/oe/abstract.cfm?uri=oe-18-20-20949>. 18

LOISEL, H.; MÉRIAUX, X.; BERTHON, J.-F.; POTEAU, A. Investigation of the optical backscattering to scattering ratio of marine particles in relation to their biogeochemical composition in the eastern English Channel and southern North Sea. **Limnology and Oceanography**, v. 52, n. 2, p. 739–752, 2007. ISSN 00243590. 95

LOISEL, H.; MÉRIAUX, X.; POTEAU, a.; ARTIGAS, L. F.; LUBAC, B.; GARDEL, a.; CAILLAUD, J.; LESOURD, S. Analyze of the inherent optical

properties of French Guiana coastal waters for remote sensing applications . **Journal of coastal research**, SI 56, n. ICS2009 (Proceedings), p. 1532–1536, 2009. ISSN 07490208. 98

LOISEL, H.; MOREL, A. Non-isotropy of the upward radiance field in typical coastal (Case 2) waters. **International Journal of Remote Sensing**, v. 22, n. 2-3, p. 275–295, jan 2001. ISSN 0143-1161. Available from: <http://www.tandfonline.com/doi/abs/10.1080/014311601449934>. 22, 27, 76, 82

LOISEL, H.; NICOLAS, J. M.; SCIANDRA, A.; STRAMSKI, D.; POTEAU, A. Spectral dependency of optical backscattering by marine particles from satellite remote sensing of the global ocean. **Journal of Geophysical Research: Oceans**, v. 111, n. 9, p. 1–14, 2006. ISSN 21699291. 111, 112

LOISEL, H.; STRAMSKI, D. Estimation of the inherent optical properties of natural waters from the irradiance attenuation coefficient and reflectance in the presence of Raman scattering. **Applied optics**, v. 39, n. 18, p. 3001–11, jun 2000. ISSN 0003-6935. Available from: <http://www.ncbi.nlm.nih.gov/pubmed/18345226>. 23, 29

MA, R.; PAN, D.; DUAN, H.; SONG, Q. Absorption and scattering properties of water body in Taihu Lake, China: backscattering. **International Journal of Remote Sensing**, v. 30, n. 9, p. 2321–2335, may 2009. ISSN 0143-1161. Available from: <http://www.tandfonline.com/doi/abs/10.1080/01431160802549385>. 3

MA, R.; TANG, J.; DAI, J.; ZHANG, Y.; SONG, Q. Absorption and scattering properties of water body in Taihu Lake, China: absorption. **International Journal of Remote Sensing**, v. 27, n. 19, p. 4277–4304, oct 2006. ISSN 0143-1161. Available from: <http://www.tandfonline.com/doi/abs/10.1080/01431160600851835>. 90, 107, 109

MAFFIONE, R. A.; DANA, D. R. Instruments and methods for measuring the backward-scattering coefficient of ocean waters. **Applied optics**, v. 36, n. 24, p. 6057–67, aug 1997. ISSN 0003-6935. Available from: <http://www.ncbi.nlm.nih.gov/pubmed/18259450>. 41

MARITORENA, S.; SIEGEL, D. a.; PETERSON, A. R. Optimization of a semianalytical ocean color model for global-scale applications. **Applied optics**,

v. 41, n. 15, p. 2705–14, may 2002. ISSN 0003-6935. Available from: <http://www.ncbi.nlm.nih.gov/pubmed/12027157>. 23, 29, 60, 116, 117

MATTHEWS, M. W.; BERNARD, S. Characterizing the Absorption Properties for Remote Sensing of Three Small Optically-Diverse South African Reservoirs. **Remote Sensing**, v. 5, n. 9, p. 4370–4404, sep 2013. ISSN 2072-4292. Available from: <http://www.mdpi.com/2072-4292/5/9/4370/>. 3, 90, 101, 109

MCKEE, D.; CHAMI, M.; BROWN, I.; CALZADO, V. S.; DOXARAN, D.; CUNNINGHAM, A. Role of measurement uncertainties in observed variability in the spectral backscattering ratio: a case study in mineral-rich coastal waters. **Applied optics**, v. 48, n. 24, p. 4663–75, aug 2009. ISSN 1539-4522. Available from: <http://www.ncbi.nlm.nih.gov/pubmed/19696853>. 2, 95

MCKEE, D.; CUNNINGHAM, A. Identification and characterisation of two optical water types in the Irish Sea from in situ inherent optical properties and seawater constituents. **Estuarine, Coastal and Shelf Science**, v. 68, n. 1, p. 305–316, 2006. ISSN 02727714. 3, 95

MEADE, R. H. Suspended sediments of the modern Amazon and Orinoco rivers. **Quaternary International**, v. 21, n. 93, p. 29–39, jan 1994. ISSN 10406182. Available from: <http://linkinghub.elsevier.com/retrieve/pii/1040618294900191>. 1

MELACK, J.; FORSBERG, B. Biogeochemistry of amazon floodplain lakes and associated wetlands. In: **The biogeochemistry of the Amazon basin and its role in a changing world.** New York: Oxford University Press, 2001. p. 235–276. 102

MISHRA, S.; MISHRA, D. R.; LEE, Z. Bio-optical inversion in highly turbid and cyanobacteria-dominated waters. **IEEE Transactions on Geoscience and Remote Sensing**, v. 52, n. 1, p. 375–388, 2014. ISSN 01962892. 1, 4, 26, 61, 121, 122, 126, 135

MISHRA, S.; MISHRA, D. R.; LEE, Z.; TUCKER, C. S. Quantifying cyanobacterial phycocyanin concentration in turbid productive waters: A quasi-analytical approach. **Remote Sensing of Environment**, v. 133, p. 141–151, 2013. ISSN 00344257. 4

MOBLEY, C. **Light and Water**: Radiative transfer in natural waters. [S.l.]: Academic Press, 1994. ISBN 9780125027502. 10, 12, 13, 16, 21, 23, 78, 79, 92

MOBLEY, C. D. Estimation of the remote-sensing reflectance from above-surface measurements. **Applied optics**, v. 38, n. 36, p. 7442–55, dec 1999. ISSN 0003-6935. Available from: <http://www.ncbi.nlm.nih.gov/pubmed/18324298>. xix, 15, 36, 37

_____. Polarized reflectance and transmittance properties of windblown sea surfaces. **Applied Optics**, v. 54, n. 15, p. 4828, may 2015. ISSN 0003-6935. Available from: <https://www.osapublishing.org/ao/abstract.cfm?uri=ao-54-15-4828>. xxi, 15, 16, 36, 37, 50, 63, 66

MOBLEY, C. D.; SUNDMAN, L. K.; BOSS, E. Phase function effects on oceanic light fields. **Applied optics**, v. 41, n. 6, p. 1035–50, feb 2002. ISSN 0003-6935. Available from: <http://www.ncbi.nlm.nih.gov/pubmed/11900122>. 79

MOREL, A. Optical properties of pure water and pure seawater. **Optical Aspects of Oceanography**, Academic Press, p. 1–24, 1974. 60, 61

MOREL, A.; ANTOINE, D.; GENTILI, B. Bidirectional reflectance of oceanic waters: accounting for Raman emission and varying particle scattering phase function. **Applied optics**, v. 41, n. 30, p. 6289–306, oct. 2002. ISSN 0003-6935. Available from: <http://www.ncbi.nlm.nih.gov/pubmed/12396179>. 22, 38

MOREL, A.; BRICAUD, A. Theoretical results concerning light absorption in a discrete medium, and application to specific absorption of phytoplankton. **Deep Sea Research Part A. Oceanographic Research Papers**, v. 28, n. 11, p. 1375–1393, 1981. ISSN 01980149. 18

MOREL, A.; GENTILI, B. Diffuse reflectance of oceanic waters. II Bidirectional aspects. **Applied optics**, v. 32, n. 33, p. 6864–6879, 1993. ISSN 0003-6935. 22

_____. Diffuse reflectance of oceanic waters III Implication of bidirectionality for the remote-sensing problem. **Applied Optics**, v. 30, n. 30, p. 4850, oct 1996. ISSN 0003-6935. 14, 15, 22, 38

MOREL, A.; MARITORENA, S. Bio-optical properties of oceanic waters: A reappraisal. **Journal of Geophysical Research**, v. 106, n. C4, p. 7163, 2001. ISSN 0148-0227. Available from: <http://doi.wiley.com/10.1029/2000JC000319>. 29

MOREL, A.; PRIEUR, L. Analysis of variations in ocean color. **Limnology and Oceanography**, v. 22, n. 4, p. 709–722, 1977. ISSN 00243590. Available from: <http://www.aslo.org/lo/toc/vol{_}22/issue{_}4/0709.html>. 22

MOUW, C. B.; GREB, S.; AURIN, D.; DIGIACOMO, P. M.; LEE, Z.; TWARDOWSKI, M.; BINDING, C. E.; HU, C.; MA, R.; MOORE, T.; MOSES, W.; CRAIG, S. E. Aquatic color radiometry remote sensing of coastal and inland waters: Challenges and recommendations for future satellite missions. **Remote Sensing of Environment**, Elsevier Inc., v. 160, p. 15–30, 2015. ISSN 00344257. Available from: <http://linkinghub.elsevier.com/retrieve/pii/S0034425715000474>. 2, 4, 23, 24

MUELLER, J. L.; FARGION, G. S.; MCCLAIN, C. R.; MUELLER, J. L.; MOREL, A.; FROUIN, R.; DAVIS, C.; ARNONE, R.; CARDER, K.; STEWARD, R. G.; HOOKER, S. B.; MOBLEY, C. D.; MCLEAN, S.; HOLBEN, B.; PIETRAS, C.; KNOBELSPIESSE, K. D.; PORTER, J. **Ocean Optics Protocols For Satellite Ocean Color Sensor Validation ,**. [S.l.], 2003. Revision 4 , Volume III : Radiometric Measurements and Data Analysis Protocols NASA / TM-2003- Ocean Optics Protocols For Satellite Ocean Color Sensor Validation(NASA/TM-2003-21621/Rev-Vol III), n. January. 2, 3, 14, 35, 39, 41

NECHAD, B.; RUDDICK, K.; PARK, Y. Calibration and validation of a generic multisensor algorithm for mapping of total suspended matter in turbid waters. **Remote Sensing of Environment**, Elsevier Inc., v. 114, n. 4, p. 854–866, apr. 2010. ISSN 00344257. vii, ix, xiii, 4, 5, 23, 24, 26, 59, 62, 126, 127, 128, 129, 130, 135

NELSON, N.; COBLE., P. Practical guidelines for the analysis of seawater. In: _____. [S.l.]: CRC, 2009. chapter Optical analysis of chromophoric dissolved organic matter - Chapter 5. 2

NLINFIT. **Matlab Nonlinear regression**. 2015. Available from: <http://www.mathworks.com/help/stats/nlinfit.html>. 56, 58

NOVO, E. M. L. D. M.; FILHO, W. P.; MELACK, J. M. Assessing the utility of spectral band operators to reduce the influence of total suspended solids on the relationship between chlorophyll concentration and the bidirectional reflectance factor in Amazon waters. **International Journal of Remote Sensing**, v. 25, n. 22, p. 5105–5115, nov 2004. ISSN 0143-1161. Available from:

<http://www.tandfonline.com/doi/abs/10.1080/01431160410001709048>. 4, 90

NUSCH, E. Determination of dissolved organic carbon and total dissolved nitrogen in sea water. **Archiv für Hydrobiologie**, v. 14, n. 1, p. 14–36, 1980. 47

ODERMATT, D.; GITELSON, A. A.; BRANDO, V. E.; SCHAEPMAN, M. Review of constituent retrieval in optically deep and complex waters from satellite imagery. **Remote Sensing of Environment**, Elsevier Inc., v. 118, p. 116–126, mar 2012. ISSN 00344257. Available from: <http://dx.doi.org/10.1016/j.rse.2011.11.013http://linkinghub.elsevier.com/retrieve/pii/S0034425711004081>. 4, 23

O'DONNELL, D. M.; EFFLER, S. W.; STRAIT, C. M.; LESHKEVICH, G. a. Optical characterizations and pursuit of optical closure for the western basin of Lake Erie through in situ measurements. **Journal of Great Lakes Research**, v. 36, n. 4, p. 736–746, dec 2010. ISSN 03801330. Available from: <http://linkinghub.elsevier.com/retrieve/pii/S0380133010001930>. 107

OISHI, T. Significant relationship between the backward scattering coefficient of sea water and the scatterance at 120°. **Appl. Opt.**, OSA, v. 29, n. 31, p. 4658–4665, Nov 1990. Available from: <http://ao.osa.org/abstract.cfm?URI=ao-29-31-4658>. 45

OOWB. **Ocean Optics Web Book**. 2015. Available from: <http://www.oceanopticsbook.info/>. 21, 38

PAAVEL, B.; ARST, H.; HERLEVI, A. Dependence of spectral distribution of inherent optical properties of lake waters on the concentrations of different water constituents. **Nordic Hydrology**, v. 38, n. 3, p. 265, 2007. ISSN 13667017. Available from: <http://www.iwaponline.com/nh/038/nh0380265.htm>. 97

PALMER, S. C.; KUTSER, T.; HUNTER, P. D. Remote sensing of inland waters: Challenges, progress and future directions. **Remote Sensing of Environment**, Elsevier Inc., v. 157, p. 1–8, 2015. ISSN 00344257. Available from: <http://linkinghub.elsevier.com/retrieve/pii/S0034425714003666>. 4

PARK, Y.-J.; RUDDICK, K. G. Model of remote-sensing reflectance including bidirectional effects for case 1 and case 2 waters. **Applied optics**, v. 44, n. 7, p. 1236–49, mar. 2005. ISSN 0003-6935. Available from: <http://www.ncbi.nlm.nih.gov/pubmed/15765704>. 22, 23, 76, 82

PEGAU, W. S.; GRAY, D.; ZANEVELD, J. R. V. Absorption and attenuation of visible and near-infrared light in water: dependence on temperature and salinity. **Applied optics**, v. 36, n. 24, p. 6035–46, aug 1997. ISSN 0003-6935. Available from: <http://www.ncbi.nlm.nih.gov/pubmed/18259448>. 16

PENG, F.; EFFLER, S. W. Suspended minerogenic particles in a reservoir: Light-scattering features from individual particle analysis. **Limnology and Oceanography**, v. 52, n. 1, p. 204–216, 2007. ISSN 00243590. Available from: <http://www.aslo.org/lo/toc/vol{_}52/issue{_}1/0204.html>. 111, 112

PENG, F.; EFFLER, S. W.; DONNELL, D. O.; WEIDEMANN, A. D.; AUER, M. T. Characterizations of minerogenic particles in support of modeling light scattering in Lake Superior through a two-component approach. **Limnology and Oceanography**, v. 54, n. 4, p. 1369–1381, 2009. ISSN 00243590. 112

POLYFIT. **Matlab Polynomial curve fitting**. 2016. Available from: <http://www.mathworks.com/help/matlab/ref/polyfit.html>. 56

POPE, R. M.; FRY, E. S. pure water . II . Integrating cavity measurements. **Applied Optics**, 1997. 16, 25, 60, 61

PREISENDORFER, R. **Hydrologic Optics**: 6 volumes: Vol. 1: Introduction, 218 pp; vol. 2: Foundations, 400 pp; vol. 3: Solutions, 246 pp; vol. 4: Imbeddings, 207 pp; vol. 5: Properties, 296 pp; vol. 6: Surfaces. Seattle, WA.: NOAA Pacific Mar. Environ. Lab., 1976. 10

QUICKENDEN, T. I.; IRVIN, J. A. The ultraviolet absorption spectrum of liquid water. **The Journal of Chemical Physics**, v. 72, n. 8, p. 4416, 1980. ISSN 00219606. Available from: <http://link.aip.org/link/JCPSA6/v72/i8/p4416/s1{&}Agg=doihttp://scitation.aip.org/content/aip/journal/jcp/72/8/10.1063/1.439733>. 16

REGRESS. **Matlab regress multiple linear regression**. 2015. Available from: <http://www.mathworks.com/help/stats/nlinfit.html>. 41

REYNOLDS, R. a.; STRAMSKI, D.; WRIGHT, V. M.; WOZNIAK, S. B. Measurements and characterization of particle size distributions in coastal waters. **Journal of Geophysical Research: Oceans**, v. 115, n. 8, 2010. ISSN 21699291. 13, 90, 111, 112

RICHEY, J. E.; MEADE, R. H.; SALATI, E.; DEVOL, A. H.; NORDIN, C. F.; SANTOS, U. D. Water Discharge and Suspended Sediment Concentrations in the Amazon River: 1982-1984. **Water Resources Research**, v. 22, n. 5, p. 756–764, may 1986. ISSN 00431397. Available from: <http://doi.wiley.com/10.1029/WR022i005p00756>. 1

ROCHELLE-NEWALL, E.; FISHER, T. Chromophoric dissolved organic matter and dissolved organic carbon in Chesapeake Bay. **Marine Chemistry**, v. 77, n. 1, p. 23–41, jan 2002. ISSN 03044203. Available from: <http://linkinghub.elsevier.com/retrieve/pii/S0304420301000731>. 107, 108

ROESLER, C. S.; BARNARD, A. H. Optical proxy for phytoplankton biomass in the absence of photophysiology: Rethinking the absorption line height. **Methods in Oceanography**, Elsevier Ltd, v. 7, p. 79–94, 2013. ISSN 22111220. Available from: <http://dx.doi.org/10.1016/j.mio.2013.12.003>. 58

ROESLER, C. S.; PERRY, M. J. In situ phytoplankton absorption, fluorescence emission, and particulate backscattering spectra determined from reflectance. **Journal of Geophysical Research**, v. 100, n. C7, p. 13279, 1995. ISSN 0148-0227. Available from: <http://doi.wiley.com/10.1029/95JC00455>. 23, 29

RöTTGERS, R.; MCKEE, D.; WOZNIAK, S. B. Evaluation of scatter corrections for ac-9 absorption measurements in coastal waters. **Methods in Oceanography**, Elsevier B.V., In press, p. 1–19, dec. 2013. Available from: <http://linkinghub.elsevier.com/retrieve/pii/S2211122013000455>. vii, ix, 44, 45

RUDDICK, K. G.; De Cauwer, V.; PARK, Y.-J.; MOORE, G. Seaborne measurements of near infrared water-leaving reflectance: The similarity spectrum for turbid waters. **Limnology and Oceanography**, v. 51, n. 2, p. 1167–1179, 2006. ISSN 00243590. 23, 38

RUDDICKWEBSITE. **Ruddick Website**. 2015. Available from: <http://odnature.naturalsciences.be/remsem/software-and-data/bidirectional-water-reflectance>. 82

RUDORFF, C. M.; GALVÃO, L. S.; NOVO, E. M. L. D. M. Reflectance of floodplain waterbodies using EO?1 Hyperion data from high and receding flood periods of the Amazon River. **International Journal of Remote Sensing**,

v. 30, n. 10, p. 2713–2720, may 2009. ISSN 0143-1161. Available from: <http://www.tandfonline.com/doi/abs/10.1080/01431160902755320>. 4

RUDORFF, C. M.; MELACK, J. M.; BATES, P. D. Flooding dynamics on the lower Amazon floodplain: 1. Hydraulic controls on water elevation, inundation extent, and river-floodplain discharge. **Water Resources Research**, v. 50, n. 1, p. 619–634, jan. 2014. 1, 4, 32, 96, 102, 104, 106, 108

_____. Flooding dynamics on the lower Amazon floodplain: 2. Seasonal and interannual hydrological variability. **Water Resources Research**, v. 50, n. 1, p. 635–649, jan. 2014. 4, 32, 96, 106

RUDORFF, C. M.; MELACK, J. M.; MACINTYRE, S.; BARBOSA, C. C. F.; NOVO, E. M. L. D. M. Seasonal and spatial variability of CO 2 emission from a large floodplain lake in the lower Amazon. **Journal of Geophysical Research**, v. 116, n. G4, p. G04007, oct 2011. ISSN 0148-0227. Available from: <http://www.agu.org/journals/jg/jg1104/2011JG001699/2011jg001699-t03.txthttp://doi.wiley.com/10.1029/2011JG001699>. 102

RUDORFF, N. d. M. **Ocean colour variability across the Southern Atlantic and Southeast Pacific**. 321 p. PhD Thesis (PhD) — Instituto Nacional de Pesquisas Espaciais (INPE), São José dos Campos, 2013-08-19 2013. Available from: <http://urlib.net/sid.inpe.br/mtc-m19/2013/09.17.14.26>. Access in: 22 set. 2015. 49, 50, 76

Sander de Carvalho, L. A.; Faria Barbosa, C. C.; Leão de Moraes Novo, E. M.; de Moraes Rudorff, C. Implications of scatter corrections for absorption measurements on optical closure of Amazon floodplain lakes using the Spectral Absorption and Attenuation Meter (AC-S-WETLabs). **Remote Sensing of Environment**, Elsevier Inc., v. 157, p. 123–137, feb 2015. ISSN 00344257. Available from: <http://dx.doi.org/10.1016/j.rse.2014.06.018http://linkinghub.elsevier.com/retrieve/pii/S0034425714002387>. 3, 45, 79

SEQUOIA SCIENTIFIC, INC. **HydroLight 5.2 technical documentation**: First printing. 2700 Richards Road, Suite 107, Bellevue, WA, 2013. 110 p. 23

SHI, K.; LI, Y.; ZHANG, Y.; LI, L.; LV, H.; SONG, K. Optical scattering properties of organic-rich and inorganic-rich particles in inland waters. **Journal of Great Lakes Research**, Elsevier B.V., v. 40, n. 2, p. 308–316, jun 2014. ISSN 03801330. Available from:

<http://linkinghub.elsevier.com/retrieve/pii/S0380133014000574>. 2, 97, 98

SIOLI, H. **Hydrochemistry and geology in the Brazilian Amazon region.** New York: Springer-Verlag, 1984. 1, 2

SLADE, W. H.; BOSS, E. Spectral attenuation and backscattering as indicators of average particle size. **Applied Optics**, v. 54, n. 24, p. 7264, aug. 2015. ISSN 0003-6935. Available from: <https://www.osapublishing.org/abstract.cfm?URI=ao-54-24-7264>. 20, 59, 96, 97, 111, 112

SLADE, W. H.; BOSS, E.; RUSSO, C. Effects of particle aggregation and disaggregation on their inherent optical properties. **Optics express**, v. 19, n. 9, p. 7945–7959, 2011. ISSN 1094-4087. 12

SMITH, R. C.; BAKER, K. S. Optical properties of the clearest natural waters (200-800 nm). **Applied Optics**, n. 20, p. 177–184, 1981. 16

SMYTH, T. J.; MOORE, G. F.; HIRATA, T.; AIKEN, J. Semianalytical model for the derivation of ocean color inherent optical properties: description, implementation, and performance assessment. **Applied optics**, v. 45, n. 31, p. 8116–31, nov 2006. ISSN 0003-6935. Available from: <http://www.ncbi.nlm.nih.gov/pubmed/17068554>. 23

SNYDER, W. a.; ARNONE, R. a.; DAVIS, C. O.; GOODE, W.; GOULD, R. W.; LADNER, S.; LAMELA, G.; RHEA, W. J.; STAVN, R.; SYDOR, M.; WEIDEMANN, A. Optical scattering and backscattering by organic and inorganic particulates in U.S. coastal waters. **Applied optics**, v. 47, n. 5, p. 666–677, 2008. ISSN 0003-6935. 95

SPRENT, P.; DOLBY, G. R. The geometric mean functional relationship. **Biometrics**, JSTOR, p. 547–550, 1980. 57

STAVN, R. H.; RICHTER, S. J. Biogeo-optics: particle optical properties and the partitioning of the spectral scattering coefficient of ocean waters. **Applied optics**, v. 47, n. 14, p. 2660–79, may 2008. ISSN 0003-6935. Available from: <http://www.ncbi.nlm.nih.gov/pubmed/18470263>. 20

STRAMSKI, D.; BABIN, M.; WOZNIAK, S. B. Variations in the optical properties of terrigenous mineral-rich particulate matter suspended in seawater.

Limnology and Oceanography, v. 52, n. 6, p. 2418–2433, 2007. ISSN 00243590. 19

STRAMSKI, D.; BRICAUD, A.; MOREL, A. Modeling the inherent optical properties of the ocean based on the detailed composition of the planktonic community. **Applied optics**, v. 40, n. 18, p. 2929–45, jun 2001. ISSN 0003-6935. Available from: <http://www.ncbi.nlm.nih.gov/pubmed/18357311>. 18

STRAMSKI, D.; REYNOLDS, R. a.; KACZMAREK, S.; UITZ, J.; ZHENG, G. Correction of pathlength amplification in the filter-pad technique for measurements of particulate absorption coefficient in the visible spectral region. **Applied Optics**, v. 54, n. 22, p. 6763, aug 2015. ISSN 0003-6935. Available from: <https://www.osapublishing.org/abstract.cfm?URI=ao-54-22-6763>. 2, 48

STRAMSKI, D.; WOZNIAK, S. On the role of colloidal particles in light scattering in the ocean. **Limnology Oceanography**, n. 50, p. 1581–1591, 2005. 17

STRÖMBECK, N.; PIERSON, D. C. The effects of variability in the inherent optical properties on estimations of chlorophyll a by remote sensing in Swedish freshwaters. **The Science of the total environment**, v. 268, n. 1-3, p. 123–37, mar 2001. ISSN 0048-9697. Available from: <http://www.ncbi.nlm.nih.gov/pubmed/11315736>. 97

SULLIVAN, J. M.; TWARDOWSKI, M. S.; DONAGHAY, P. L.; FREEMAN, S. a. Use of optical scattering to discriminate particle types in coastal waters. **Applied optics**, v. 44, n. 9, p. 1667–1680, 2005. ISSN 0003-6935. 46

SULLIVAN, J. M.; TWARDOWSKI, M. S.; ZANEVELD, J. R. V.; MOORE, C. M.; BARNARD, A. H.; DONAGHAY, P. L.; RHOADES, B. Hyperspectral temperature and salt dependencies of absorption by water and heavy water in the 400-750 nm spectral range. **Applied Optics**, v. 45, n. 21, p. 5294, 2006. ISSN 0003-6935. Available from: <http://www.ncbi.nlm.nih.gov/pubmed/16826267https://www.osapublishing.org/ao/abstract.cfm?uri=ao-45-21-5294>. 16, 42

SUN, D.; LI, Y.; WANG, Q.; GAO, J.; LV, H.; LE, C.; HUANG, C. Light scattering properties and their relation to the biogeochemical composition of turbid productive waters: a case study of Lake Taihu. **Applied Optics**, v. 48, n. 11, p. 1979, apr 2009. ISSN 0003-6935. Available from: <http://www.opticsinfobase.org/abstract.cfm?URI=ao-48-11-1979https://www.osapublishing.org/ao/abstract.cfm?uri=ao-48-11-1979>. 3, 95, 97

SUN, D.; LI, Y.; WANG, Q.; LV, H.; LE, C.; HUANG, C.; GONG, S. Partitioning particulate scattering and absorption into contributions of phytoplankton and non-algal particles in winter in Lake Taihu (China). **Hydrobiologia**, v. 644, n. 1, p. 337–349, mar 2010. ISSN 0018-8158. Available from: <http://link.springer.com/10.1007/s10750-010-0198-7>. 98

SUN, D.; LI, Y.; WANG, Q.; LE, C.; LV, H.; HUANG, C.; GONG, S. Specific inherent optical quantities of complex turbid inland waters, from the perspective of water classification. **Photochemical & photobiological sciences : Official journal of the European Photochemistry Association and the European Society for Photobiology**, v. 11, n. 8, p. 1299–312, aug 2012. ISSN 1474-9092. Available from: <http://www.ncbi.nlm.nih.gov/pubmed/22584274>. 98

TASSAN, S. A sensitivity analysis of the 'Transmittance-Reflectance' method for measuring light absorption by aquatic particles. **Journal of Plankton Research**, v. 24, n. 8, p. 757–774, aug. 2002. ISSN 14643774. Available from: <http://plankt.oxfordjournals.org/content/24/8/757.shorthttp://www.plankt.oupjournals.org/cgi/doi/10.1093/plankt/24.8.757>. 48, 49

TASSAN, S.; FERRARI, G. M. An alternative approach to absorption measurements of aquatic particles retained on filters. **Limnology and Oceanography**, v. 40, n. 8, p. 1358–1368, 1995. ISSN 00243590. Available from: <http://cat.inist.fr/?aModele=afficheN&cpsidt=2992977http://doi.wiley.com/10.4319/lo.1995.40.8.1358>. 48, 84

TRIOS. **Trios Sensors**. 2015. Available from: <http://trios-science.com/>. 35, 39

TWARDOWSKI, M. S.; BOSS, E.; MACDONALD, J. B.; PEGAU, W. S.; BARNARD, A. H.; ZANEVELD, J. R. V. A model for estimating bulk refractive index from the optical backscattering ratio and the implications for understanding particle composition in case I and case II waters. **Journal of Geophysical Research**, v. 106, n. C7, p. 14129, 2001. ISSN 0148-0227. Available from: <http://doi.wiley.com/10.1029/2000JC000404>. 12, 95

TZORTZIOU, M.; SUBRAMANIAM, A.; HERMAN, J. R.; GALLEGOS, C. L.; NEALE, P. J.; HARDING, L. W. Remote sensing reflectance and inherent optical properties in the mid Chesapeake Bay. **Estuarine, Coastal and Shelf Science**, v. 72, n. 1-2, p. 16–32, mar 2007. ISSN 02727714. Available from: <http://linkinghub.elsevier.com/retrieve/pii/S0272771406004379>. 79, 107, 108

VANHELLEMONT, Q.; RUDDICK, K. G. Advantages of high quality SWIR bands for ocean colour processing: Examples from Landsat-8. **Remote Sensing of Environment**, Elsevier B.V., v. 161, p. 89–106, 2015. ISSN 00344257. Available from: <http://linkinghub.elsevier.com/retrieve/pii/S0034425715000577>. 90

VOLTEN, H.; HAAN, J. F. D.; HOVENIER, J. W.; SCHREURS, R.; VASSEN, W.; DEKKER, a. G.; HOOGENBOOM, H. J.; CHARLTON, F.; WOUTS, R. Laboratory measurements of angular distributions of light scattered by phytoplankton and silt. **Limnology and Oceanography**, v. 43, p. 1180–1197, 1998. ISSN 0024-3590. 18, 19

WANG, M.; SON, S.; HARDING, L. W. Retrieval of diffuse attenuation coefficient in the Chesapeake Bay and turbid ocean regions for satellite ocean color applications. **Journal of Geophysical Research**, v. 114, n. C10, p. C10011, oct 2009. ISSN 0148-0227. Available from: <http://doi.wiley.com/10.1029/2009JC005286>. 2

WANG, P.; BOSS, E.; ROESLER, C. S. Uncertainties of inherent optical properties obtained from semianalytical inversions of ocean color. **Applied optics**, v. 44, n. 19, p. 4074–85, jul 2005. ISSN 0003-6935. Available from: <http://www.ncbi.nlm.nih.gov/pubmed/16004055>. 1, 23, 30, 60, 118, 119

WERDELL, J.; FRANZ, B. a.; BAILEY, S. W.; FELDMAN, G. C.; BOSS, E.; BRANDO, V. E.; DOWELL, M.; HIRATA, T.; LAVENDER, S. J.; LEE, Z.; LOISEL, H.; MARITORENA, S.; MÉLIN, F.; MOORE, T. S.; SMYTH, T. J.; ANTOINE, D.; DEVRED, E.; D'ANDON, O. H. F.; MANGIN, A. Generalized ocean color inversion model for retrieving marine inherent optical properties. **Applied optics**, v. 52, n. 10, p. 2019–37, 2013. ISSN 1539-4522. Available from: <http://www.ncbi.nlm.nih.gov/pubmed/23545956>. vii, ix, xv, 1, 4, 5, 18, 23, 24, 28, 29

WET LABS, INC. **Spectral Absorption and Attenuation Meter - AC-S - users guide**: Revision j9. Philomath, OR 97370, 2009. 35 p. 41, 42, 44

WETZEL, R. G.; LIKENS, G. E. **Limnological Analyses.** New York: Springer-Verlag, 2000. 48

WHITMIRE, A. L.; PEGAU, W. S.; KARP-BOSS, L.; BOSS, E.; COWLES, T. J. Spectral backscattering properties of marine phytoplankton cultures. **Optics Express**, v. 18, n. 14, p. 15073–15093, 2010. ISSN 10944087. Available from:

<http://www.opticsinfobase.org/abstract.cfm?URI=oe-18-14-15073>. 18, 19

WOZNIAK, S. B.; STRAMSKI, D.; STRAMSKA, M.; REYNOLDS, R. a.; WRIGHT, V. M.; MIKSIC, E. Y.; CICHOCKA, M.; CIEPLAK, A. M. Optical variability of seawater in relation to particle concentration, composition, and size distribution in the nearshore marine environment at Imperial Beach, California. **Journal of Geophysical Research: Oceans**, v. 115, n. 8, p. 1–20, 2010. ISSN 21699291. 20, 98

WU, G.; CUI, L.; DUAN, H.; FEI, T.; LIU, Y. Absorption and backscattering coefficients and their relations to water constituents of Poyang Lake, China. **Applied optics**, v. 50, n. 34, p. 6358–68, dec 2011. ISSN 1539-4522. Available from: <http://www.ncbi.nlm.nih.gov/pubmed/22192987>. 3, 90, 107, 109

_____. Specific absorption and backscattering coefficients of the main water constituents in Poyang Lake, China. **Environmental monitoring and assessment**, v. 185, n. 5, p. 4191–206, may 2013. ISSN 1573-2959. Available from: <http://www.ncbi.nlm.nih.gov/pubmed/22976118>. 90, 94

YACOBI, Y. Z.; ALBERTS, J. J.; TAKÁCS, M.; MCELVAINE, M. Absorption spectroscopy of colored dissolved organic carbon in Georgia (USA) rivers: The impact of molecular size distribution. **Journal of Limnology**, v. 62, n. 1, p. 41–46, 2003. ISSN 11295767. 107, 108

ZANEVELD, J. R. V.; KITCHEN, J. C.; MOORE, C. C. The Scattering Error Correction of Reflecting-Tube Absorption Meters. In: JAFFE, J. S. (Ed.). [s.n.], 1994. v. 2258, p. 44–55. Available from: <http://proceedings.spiedigitallibrary.org/proceeding.aspx?articleid=969574>. 44

ZHANG, X.; HU, L. Scattering by pure seawater at high salinity. **Optics Express**, v. 17, n. 15, p. 12685, jul. 2009. ISSN 1094-4087. Available from: <https://www.osapublishing.org/oe/abstract.cfm?uri=oe-17-15-12685>. 45

ZHU, W.; YU, Q.; TIAN, Y. Q.; BECKER, B. L.; ZHENG, T.; CARRICK, H. J. An assessment of remote sensing algorithms for colored dissolved organic matter in complex freshwater environments. **Remote Sensing of Environment**, Elsevier Inc., v. 140, p. 766–778, jan 2014. ISSN 00344257. Available from: <http://linkinghub.elsevier.com/retrieve/pii/S0034425713003830>. 4

ZIBORDI, G.; BERTHON, J.-F.; DALIMONTE, D. An Evaluation of Radiometric Products from Fixed-Depth and Continuous In-Water Profile Data from Moderately Complex Waters. **Journal of Atmospheric and Oceanic Technology**, v. 26, n. 1, p. 91–106, jan. 2009. ISSN 0739-0572. 35

Appendix A

A.1 Descriptive Statistics of the Biogeochemical used for IOP relationships

Table A.1 - Descriptive Statistics of the Surface Optically Active Substances used for IOP relationships (23, 31 and 25 Stations for *February*, *August* and *April* respectively)

Stations	Index	TSM ($mg \cdot L^{-1}$)	TSOM ($mg \cdot L^{-1}$)	TSIM ($mg \cdot L^{-1}$)	Chl-a ($\mu g L^{-1}$)
February	Min	6.1	12.7	7.0	4.5
	Max	68.5	68.4	58.4	13.8
	Median	12.9	28.4	21.5	7.3
	Mean	16.7	30.7	22.8	7.9
	Std	15.4	15.5	13.9	2.3
	CV	119.6	54.4	64.6	31.6
August	Min	2.3	1.4	0.8	0.6
	Max	91.0	19.0	14.7	9.0
	Median	13.4	9.8	5.8	4.0
	Mean	10.1	9.0	5.1	3.4
	Std	15.8	4.1	3.7	1.8
	CV	156.7	45.9	71.5	51.0
April	Min	1.9	3.2	1.2	2.0
	Max	22.1	22.3	16.0	11.0
	Median	8.7	11.7	6.6	5.2
	Mean	8.4	11.4	6.0	4.6
	Std	4.7	4.6	3.4	2.3
	CV	55.7	40.0	56.9	49.6

Table A.2 - Descriptive Statistics of the Surface Optically Active Substances - All Samples

Stations	Index	DTC ($mg \cdot L^{-1}$)	DIC ($mg \cdot L^{-1}$)	DOC ($mg \cdot L^{-1}$)	TSM ($mg \cdot L^{-1}$)	TSIM ($mg \cdot L^{-1}$)	TSOM ($mg \cdot L^{-1}$)	Chl-a ($\mu g L^{-1}$)	Pheophytin ($\mu g L^{-1}$)
All Samples	Max	13.4	7.0	7.7	161.9	137.2	42.0	92.1	38.7
	Min	5.1	1.4	2.9	1.4	0.8	0.6	1.9	0.1
	Std	1.4	1.2	1.0	36.0	28.7	8.8	19.4	7.9
	Mean	9.4	4.3	5.1	35.2	25.1	10.0	19.6	6.5
	Median	9.5	4.1	5.0	17.9	10.3	6.7	12.2	3.3
	CV	14.4	28.7	18.7	102.4	114.2	87.9	99.4	121.6
September	Max	11.7	4.9	7.5	161.9	120.8	42.0	92.1	38.7
	Min	8.9	2.8	5.1	40.2	19.6	15.1	12.7	6.2
	Std	0.7	0.5	0.6	29.4	25.1	7.6	19.9	8.8
	Mean	10.0	3.9	6.1	83.3	59.2	24.1	43.3	18.5
	Median	9.7	3.7	6.0	84.8	60.4	22.8	39.6	17.1
	CV	7.5	7.5	10.6	35.3	42.4	31.7	46.1	47.4
February	Max	12.1	7.0	7.0	150.8	137.2	17.4	68.5	9.0
	Min	5.1	1.5	2.9	8.1	2.1	4.5	2.3	1.0
	Std	1.5	1.5	0.9	31.5	28.9	3.1	13.8	1.6
	Mean	9.4	4.9	4.4	40.7	32.0	8.7	15.4	3.9
	Median	9.6	5.2	4.2	31.8	25.0	7.8	11.2	3.6
	CV	15.7	29.9	19.9	77.4	90.6	36.0	89.9	41.4
August	Max	9.6	4.2	7.0	19.0	14.7	9.0	91.0	5.5
	Min	6.4	1.4	3.5	1.4	0.8	0.6	2.3	0.1
	Std	0.7	0.7	0.7	4.1	3.7	1.7	15.7	1.6
	Mean	8.3	3.3	5.0	9.8	5.8	4.0	13.4	2.1
	Median	8.4	3.4	4.9	9.0	5.1	3.4	10.0	1.6
	CV	8.6	22.0	14.8	42.2	63.0	44.0	117.8	73.5
April	Max	13.4	6.9	7.7	22.3	16.0	11.0	22.1	11.5
	Min	8.2	4.0	4.1	3.2	1.2	2.0	1.9	0.8
	Std	1.2	0.7	0.8	4.6	3.4	2.3	4.7	1.9
	Mean	10.5	5.2	5.3	11.7	6.6	5.2	8.7	2.9
	Median	10.3	5.3	5.0	11.4	6.0	4.6	8.4	2.8
	CV	11.6	12.7	14.3	38.9	52.0	44.3	53.6	65.8

Appendix B

B.1 Absorption Measurements and its respectively Statistical Indexes for is relation to biogeochemical components for *April*

Figure B.1 - Statistical Indexes for Particulate Absorption a_p and TSM/TSOM/TSIM Linear Fitting

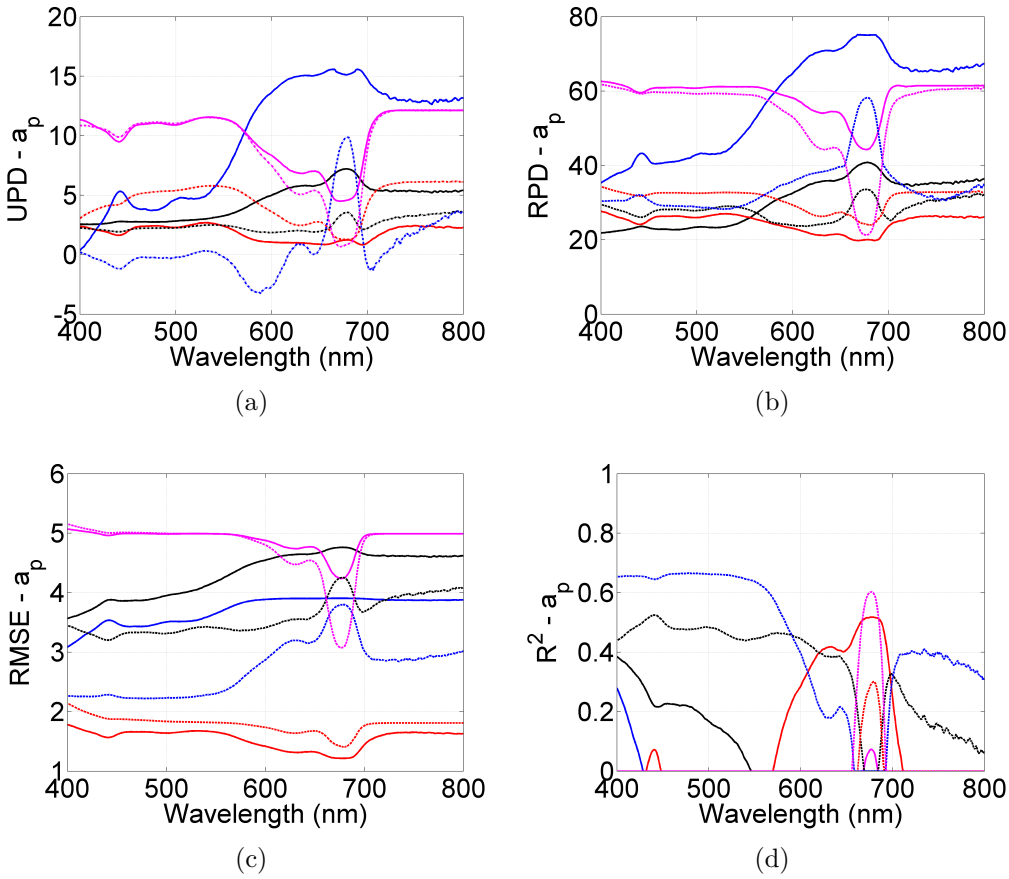

Color code: Black-TSM; Red-TSOM; Blue-TSIM; Magenta-Chla. Symbol code: Solid Line- First set of Samples; Dashed Line- Second set of Samples.

Figure B.2 - Statistical Indexes for Particulate Absorption a_{nap} and TSM/TSOM/TSIM Linear Fitting

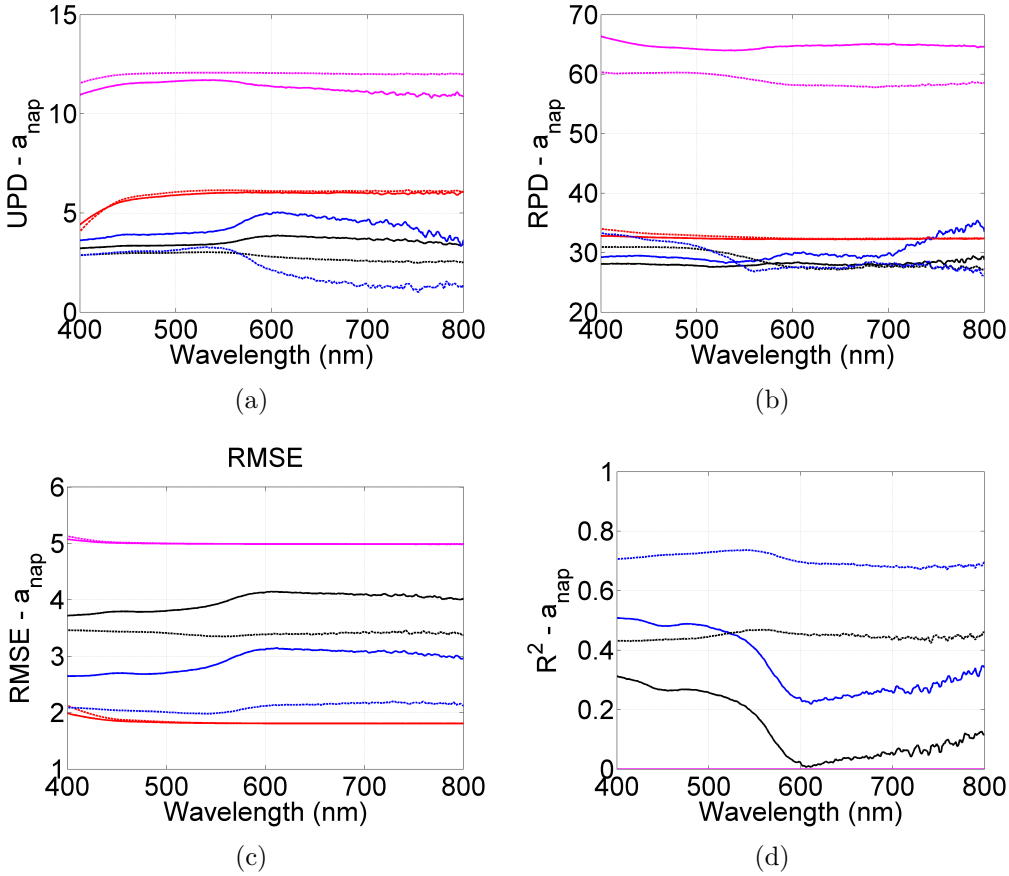

Color code: Black-TSM; Red-TSOM; Blue-TSIM; Magenta-Chla. Symbol code: Solid Line- First set of Samples; Dashed Line- Second set of Samples.

Figure B.3 - Statistical Indexes for Particulate Absorption a_ϕ and TSM/TSOM/TSIM Linear Fitting

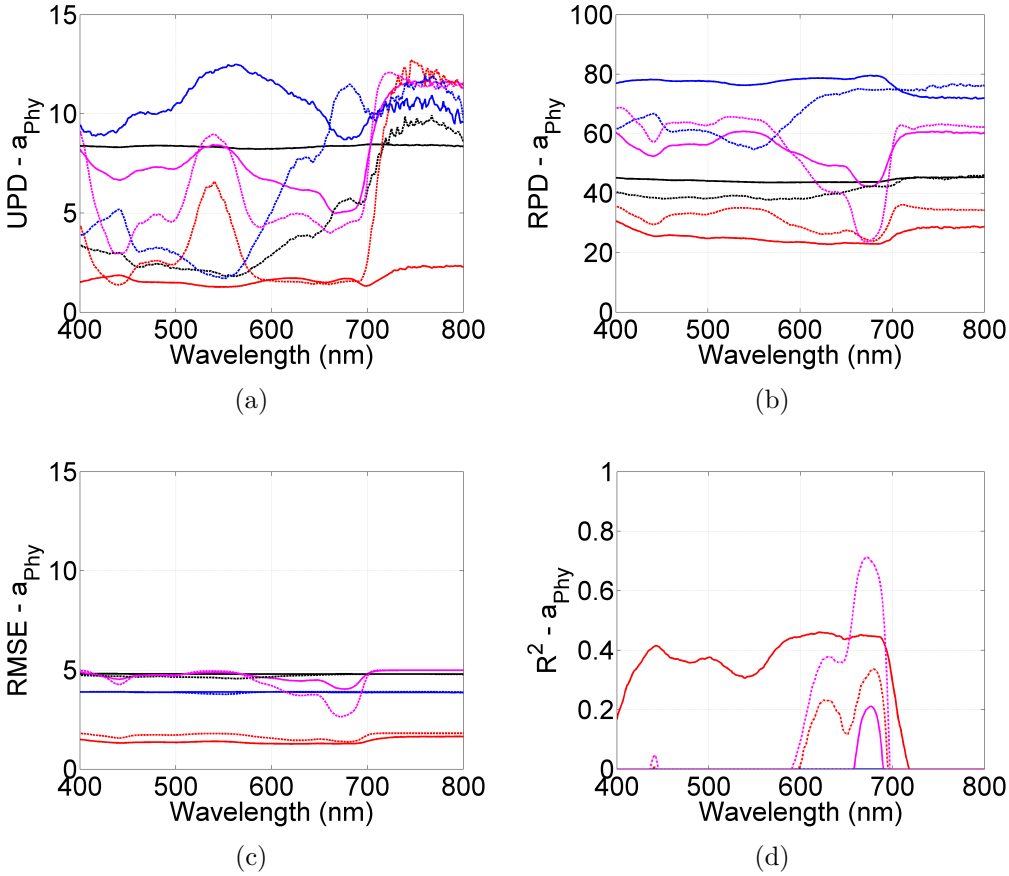

Color code: Black-TSM; Red-TSOM; Blue-TSIM; Magenta-Chla. Symbol code: Solid Line- First set of Samples; Dashed Line- Second set of Samples.

Appendix C

C.1 Results for Hydrolight Experiments

Figure C.1 - Hidrolight Experiment - *February*

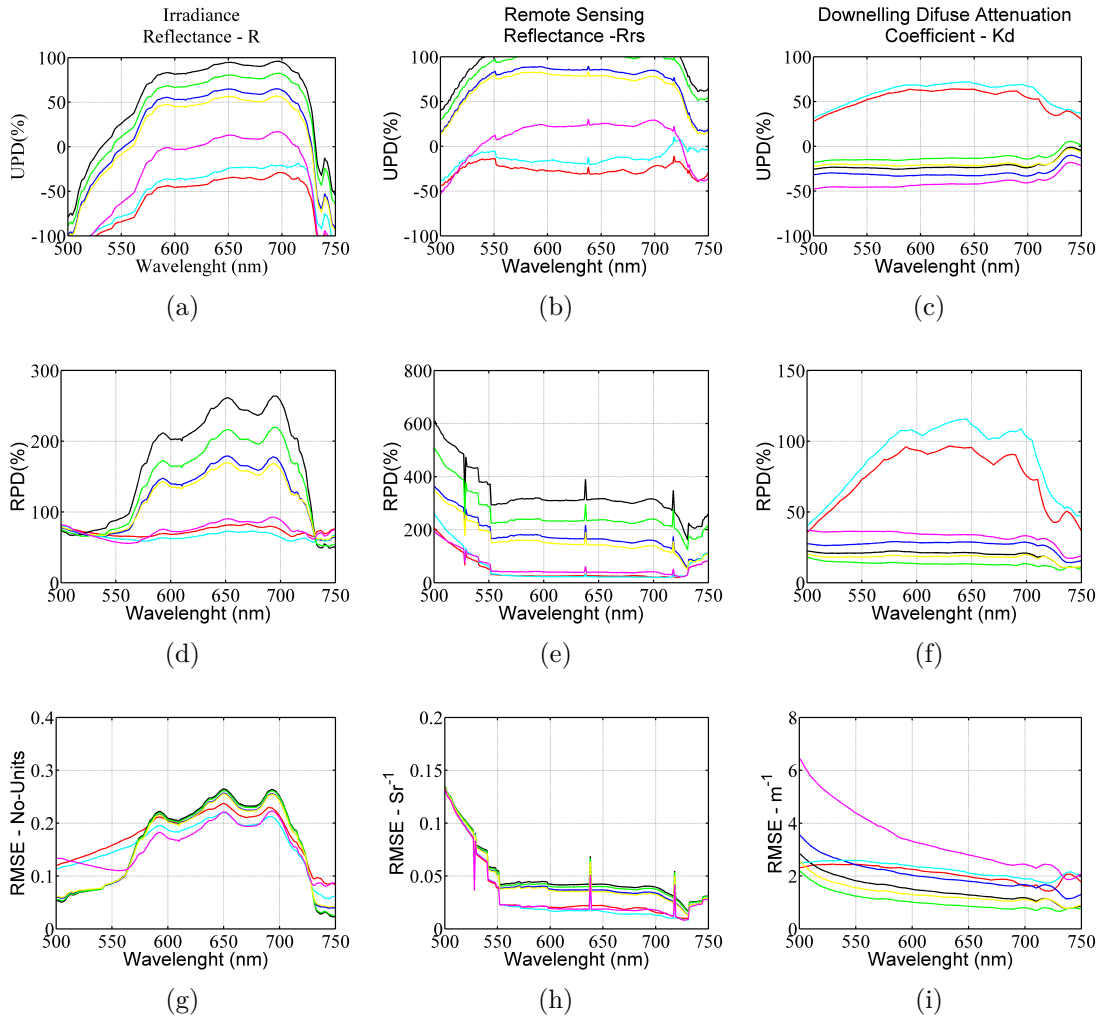

Comparison Measured AOPs and Hydrolight Derived AOPs for February field campaign. Red - Zaneveld/0.03; Blue - Zaneveld/Doxaran; Black - 0.18/0.03; Cyan - 0.18/Doxaran; Green -Rottgers/0.03; Yellow - Rottgers/0.4; Magenta - Rottgers/Doxaran. The *name/name* stand for the combination *Scattering Correction/Hydroscat Correction*

Figure C.2 - Hidrolight Experiment - *August*

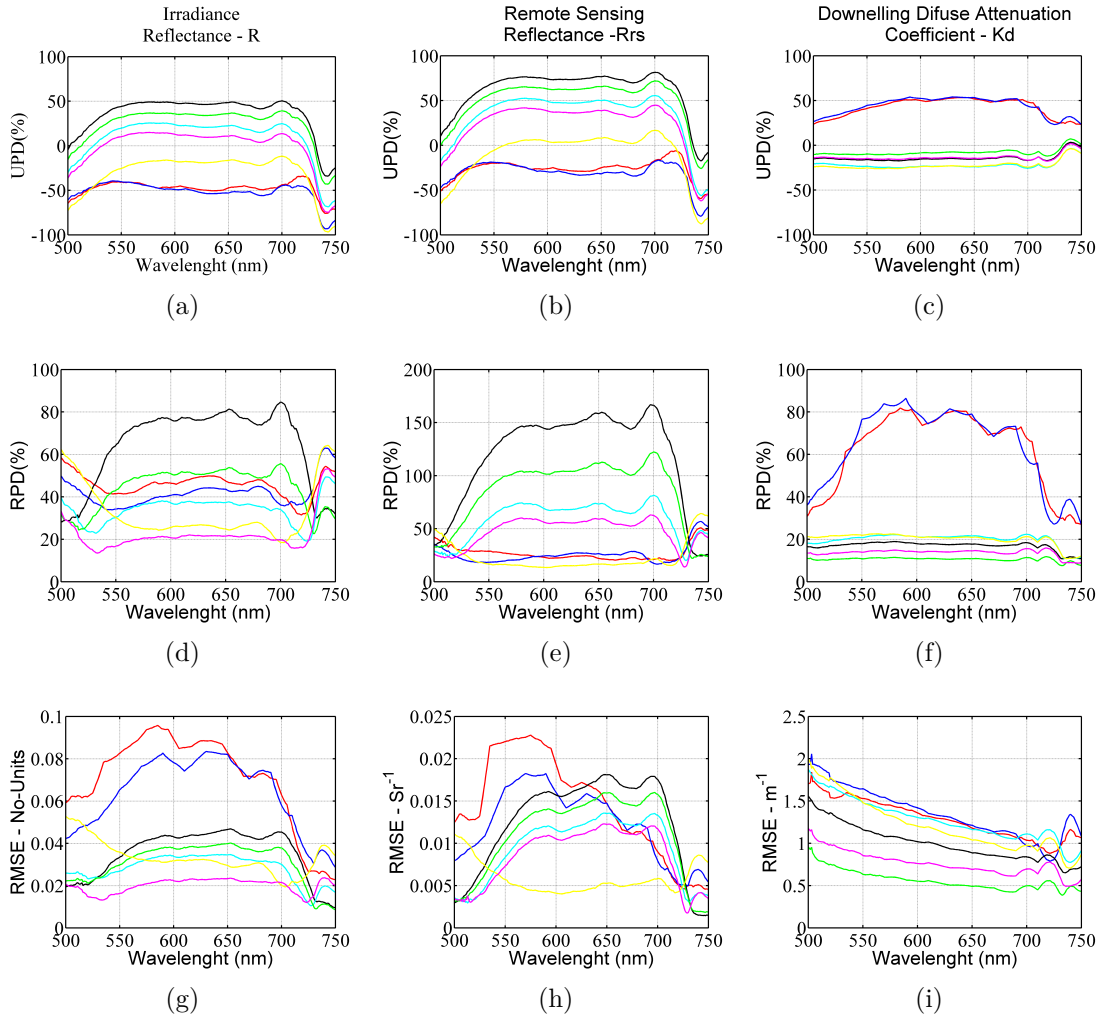

Comparison Measured AOPs and Hydrolight Derived AOPs for August field campaign.

Red - Zaneveld/0.03; Blue - Zaneveld/Doxaran; Black - 0.18/0.03; Cyan - 0.18/Doxaran; Green -Rottgers/0.03; Yellow - Rottgers/0.4; Magenta - Rottgers/Doxaran. The *name/name* stand for the combination *Scattering Correction/Hydroscat Correction*

Figure C.3 - Hidrolight Experiment - *April*

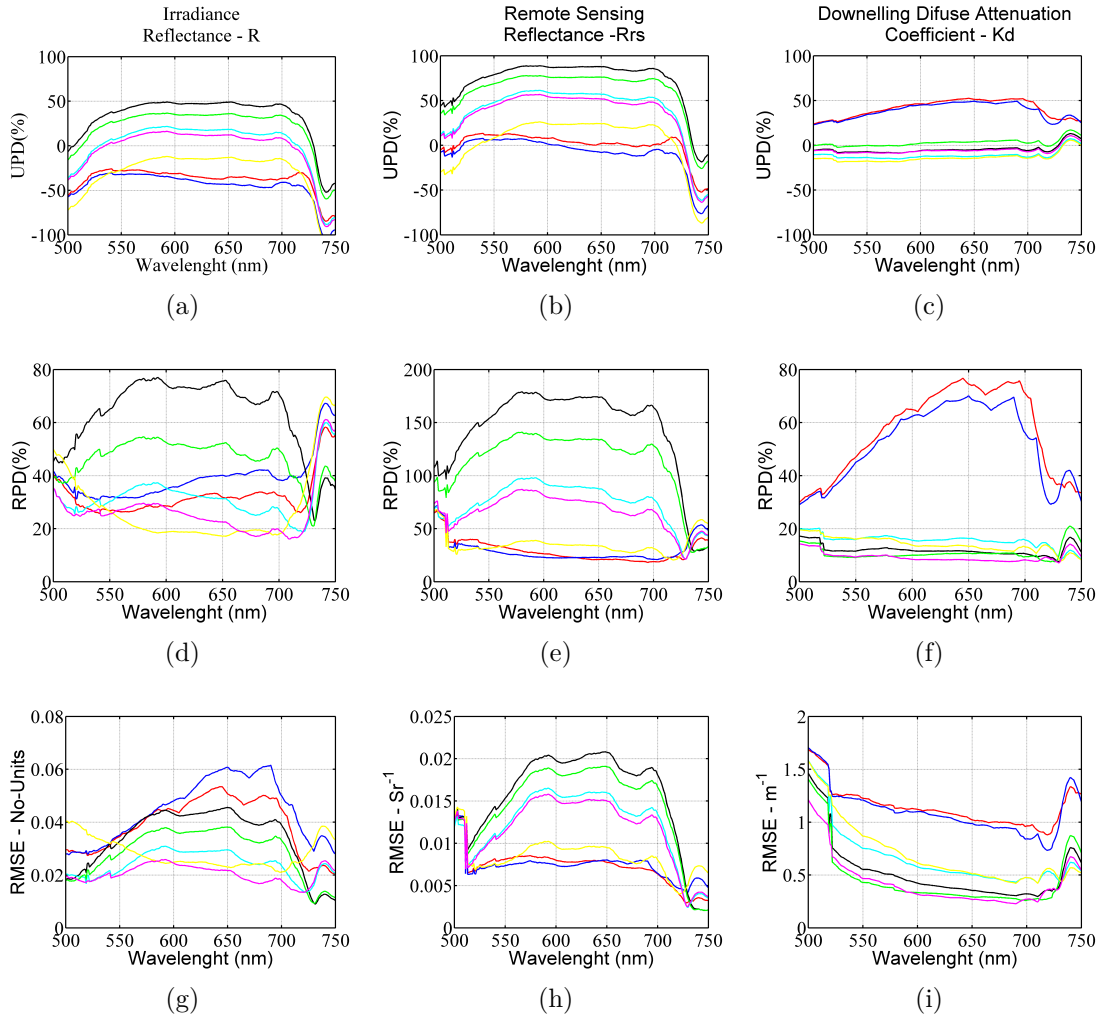

Comparison Measured AOPs and Hydrolight Derived AOPs for April field campaign.

Red - Zaneveld/0.03; Blue - Zaneveld/Doxaran; Black - 0.18/0.03; Cyan - 0.18/Doxaran; Green -Rottgers/0.03; Yellow - Rottgers/0.4; Magenta - Rottgers/Doxaran. The *name/name* stand for the combination *Scattering Correction/Hydroscat Correction*

Appendix D

D.1 Statistical Indexes for TSM, TSIM and TSOM and IOPs

Table D.1 - Statistical Indexes for TSM and IOPs. For UPD, RPD and RMSE, TSM was taken as reference.

Statistics	IOPs	All Stations (N = 79)	*February* (N = 23)	*August* (N = 31)	*April* (N = 25)
R^2	$\left(b_p^*(700)\right)$	0.78	0.70	0.37	0.40
	$\left(b_{b_p}^*(700)\right)$	0.85	0.85	0.38	0.37
	$\left(c_{(p+CDOM)}^*(660)\right)$	0.84	0.85	0.38	0.39
UPD	$\left(b_p^*(700)\right)$	31.34	-1.46	1.03	-0.07
	$\left(b_{b_p}^*(700)\right)$	-2.86	0.04	1.23	1.92
	$\left(c_{(p+CDOM)}^*(660)\right)$	-4.41	0.16	0.89	1.72
RPD	$\left(b_p^*(700)\right)$	35.36	26.26	27.83	29.25
	$\left(b_{b_p}^*(700)\right)$	30.31	14.16	28.92	25.59
	$\left(c_{(p+CDOM)}^*(660)\right)$	30.36	14.49	28.82	25.22
RMSE	$\left(b_p^*(700)\right)$	5.92	8.15	3.05	3.28
	$\left(b_{b_p}^*(700)\right)$	5.01	5.77	3.13	3.42
	$\left(c_{(p+CDOM)}^*(660)\right)$	5.09	5.84	3.17	3.39

Table D.2 - Statistical Indexes for TSIM and IOPs. For UPD, RPD and RMSE, TSIM was taken as reference.

Statistics	IOPs	All Stations (N = 79)	*February* (N = 23)	*August* (N = 31)	*April* (N = 25)
R^2	$\left(b_p^*(700)\right)$	0.80	0.75	0.45	0.37
	$\left(b_{b_p}^*(700)\right)$	0.86	0.83	0.51	0.62
	$\left(c_{(p+CDOM)}^*(660)\right)$	0.85	0.83	0.52	0.62
UPD	$\left(b_p^*(700)\right)$	-0.90	-5.89	-31.03	-4.24
	$\left(b_{b_p}^*(700)\right)$	10.93	0.05	-13.17	1.43
	$\left(c_{(p+CDOM)}^*(660)\right)$	-67.13	0.36	-15.83	0.97
RPD	$\left(b_p^*(700)\right)$	61.37	33.08	54.10	39.67
	$\left(b_{b_p}^*(700)\right)$	45.59	21.02	42.19	30.54
	$\left(c_{(p+CDOM)}^*(660)\right)$	47.12	20.30	42.86	30.60
RMSE	$\left(b_p^*(700)\right)$	4.89	6.72	2.57	2.50
	$\left(b_{b_p}^*(700)\right)$	4.12	5.64	2.50	2.05
	$\left(c_{(p+CDOM)}^*(660)\right)$	4.17	5.58	2.50	2.05

Table D.3 - Statistical Indexes for TSOM and IOPs. For UPD, RPD and RMSE, TSOM was taken as reference.

Statistics	IOPs	All Stations (N = 79)	*February* (N = 23)	*August* (N = 31)	*April* (N = 25)
R^2	$\left(b_p^*(700)\right)$	0.05	0.00	0.00	0.00
	$\left(b_{b_p}^*(700)\right)$	0.28	0.46	0.00	0.00
	$\left(c_{(p+CDOM)}^*(660)\right)$	0.28	0.42	0.00	0.00
UPD	$\left(b_p^*(700)\right)$	18.29	35.21	20.77	53.89
	$\left(b_{b_p}^*(700)\right)$	18.07	42.43	52.87	56.59
	$\left(c_{(p+CDOM)}^*(660)\right)$	18.79	47.18	38.45	61.65
RPD	$\left(b_p^*(700)\right)$	13.56	29.59	20.96	64.89
	$\left(b_{b_p}^*(700)\right)$	10.67	39.52	20.25	62.73
	$\left(c_{(p+CDOM)}^*(660)\right)$	11.13	46.97	11.14	66.62
RMSE	$\left(b_p^*(700)\right)$	2.24	2.13	1.72	2.17
	$\left(b_{b_p}^*(700)\right)$	2.37	1.73	2.99	2.83
	$\left(c_{(p+CDOM)}^*(660)\right)$	2.41	1.81	3.54	2.96

Appendix E

E.1 Measured AOPs

Figure E.1 - Diffuse Attenuation Coefficients (K_d and K_{lu}) for the 400 to 800 nm interval

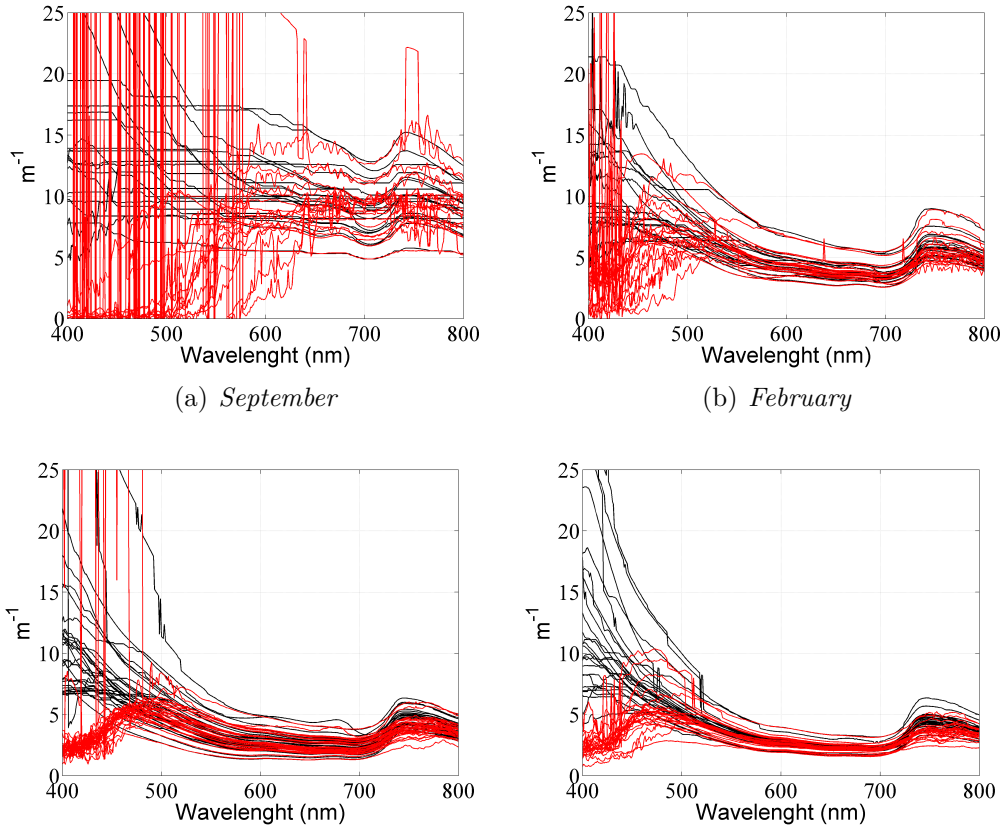

(a) *September* (b) *February*

(c) *August* (d) *April*

Color Code: Red: K_u; Black: K_d